Designing Nanostructures for Application in Electronic Devices

A THESIS

Submitted in partial fulfillment of the
requirements for the award of the degree
of

DOCTOR OF PHILOSOPHY

By

Suryakant Mishra

DISCIPLINE OF PHYSICS
INDIAN INSTITUTE OF TECHNOLOGY INDORE
March 2018

INDIAN INSTITUTE OF TECHNOLOGY INDORE

CANDIDATE'S DECLARATION

I hereby certify that the work which is being presented in the thesis entitled "**Designing Nanostructure for Application in Electronic Devices"** in the partial fulfillment of the requirements for the award of the degree of **DOCTOR OF PHILOSOPHY** and submitted in the **DISCIPLINE OF PHYSICS, INDIAN INSTITUTE OF TECHNOLOGY INDORE**, is an authentic record of my own work carried out during the time period from January 2015 to March 2018 under the supervision of Dr. Rajesh Kumar, Associate Professor, Discipline of Physics, and Dr. Pankaj R. Sagdeo, Associate Professor, Discipline of Physics, IIT Indore.

The matter presented in this thesis has not been submitted by me for the award of any other degree of this or any other institute.

Signature of the student with date
Suryakant Mishra

This is to certify that the above statement made by the candidate is correct to the best of our knowledge.

Signature of Thesis Supervisor #1	Signature of Thesis Supervisor #2
Date:	Date:
Dr. Rajesh Kumar	**Dr. Pankaj R. Sagdeo**

Suryakant Mishra has successfully given his Ph.D. Oral Examination held on……………………..

Signatures of Thesis Supervisors	Signature of External Examiner	Convener, DPGC
Date:	Date:	Date:

Signature of PSPC Member #1	Signature of PSPC Member #2	Signature of chairman (OEB)
Date:	Date:	Date:

Dedicated

To

My Parents & Wife

Acknowledgement

This thesis is the last step toward the end of my journey for the completion of PhD degree. This journey was not possible without the constant support, motivation and encouragement of some people.

First and foremost I would like to thanks my family specially my wife Aarti for her tireless efforts to make it possible. I am deeply indebted to my supervisors Dr. Rajesh Kumar and Dr. Pankaj Sagdeo whose stimulating motivation and valuable ideas kept me on track during this journey. Dr. Rajesh Kumar has been a tremendous mentor for me during PhD. His constant support, valuable advices, constructive criticism and extensive discussion helped me in accomplishing my PhD. Moreover, his principles, noble thoughts, politeness and simplicity always influenced me and will always help me in becoming a good person. I sincerely thank Dr. Pankaj Sagdeo for sharing his deep knowledge. His keen interest in research and deep understanding of the subject always encouraged me to become a good research scientist.

I would like to express my gratitude to Prof. Pradeep Mathur. He always goes out of the way to help students of IIT Indore. His energy and enthusiasm towards research always motivated me.

I would like to express my sincere gratitude to my parents, my brothers for all the sacrifices they made on my behalf. My mother and father were always been a source of encouragement and inspiration to me throughout my life. My friends like brothers Ayank and Prabhat were always with me during my hard times. This thesis was not possible without their moral support and help.

I would like to specially thank Dr. J. Jayabalan (RRCAT), for his constant help during the experiments. I would like to express my gratitude towards my seniors Dr. Shailendra Saxena for his constant support and motivation. Dr. Swarup Roy & Dr. Harimohan Rai always provided me his guidance and support to complete this Ph.D degree.

I take this opportunity to sincerely acknowledge my PSPC member Dr. Ashisha Kumar and Dr. Sudeshna Chattopadhyay for constructive evolution throughout. Thanks specially Dr. Preeti Bhobe and Dr. Vinod Kumar for their constant support during the research work.

I want to thank whole Physics department which was like a family to me in these three years. I never felt alone due to pleasant atmosphere of the department. I want to express my sincere gratitude to late Mrs. Khusboo mam for her supportive and generous nature.

Writing PhD thesis without the help of colleagues is not possible. I sincerely thank my friends Vikash, Priyanka, Kamal, Tulika, Preetam, Haardik, Devesh, Simran, Anjali, Anchal, Anil, Rupnayan, Pooja, Deepika and Manu for providing friendly and fruitful environment in lab. In particular, I want to thank specially Mr. Haardik with whom I started my PhD work, I am always admire his supportive nature.

I cannot forget to thank some of my best buddies who were always there in my bad and good times during this period Dr. Thaksen, Dr. Bahusaheb, Dr. Rohit, Dr Prakhar Garg, Dr. Rituraj, Ambikesh, Siddharth, Madan and Dharmendra. I would thank Dr. Sonam for her valuable suggestions.

I sincerely thank Dr. N.P. Lalla, Dr. Vasant Sathe and Dr. U.P. Deshpande for providing me experimental facilities with constant guidance. I would like to specially thank various research groups working across India like Prof. T. Pradeep's, S. Ogale's and K.V Adarsh's groups for their constant support during the experiments. I thank SIC facility of IIT Indore, most specifically Mr. Kinny Pandey, Mr. Nitin Upadhyay, and physics staff Mr. Ujwal Kulkarni for their support. Thanks to NIT Jaipur central facility center for the experimental facility.

I want to express my gratitude towards Dr. Shilpa, Dr. P. Matkar and other staff members of IIT dispensary who kept me physically fit.

Last but not least, I want to thank all staff members of IIT Indore for providing all comfort and convenience. Besides this, several people have knowingly and unknowingly helped me in successful completion of my thesis. I also acknowledge MHRD for providing me financial assistance.

Suryakant Mishra

Abstract

A worldwide great investment, in terms of scientists' time and money, in the field of nanoscience and nanotechnology has delivered its promises upto a great extent especially in the field of optoelectronics, materials science and energy. In current scenario, new nanomaterials need to be designed by adopting a dual approach in making electronic devices power efficient and can be used for multiple potential application which can minimize electronic garbage, which is very hard to dispose. An electrochromic device is one of the important members of electronics and lot of efforts are going on in developing novel materials to be used for such kind of power efficient device applications. Devices based on electrochemical activity show interesting behavior by controlling nanoscale architecture of the active material when used as the working electrode. Among these, electrochromism, of new nanomaterials fabricated as electrodes, is one such promising technology which has various potential application in the current era of advancement from automobile to smart buildings to display system and many more. Hence, primary focus has been to develop novel and multifunctional materials on one hand, and sustainable technologies on the other several approaches have been explored to develop conducting polymer nanostructures. Keeping this in mind the work presented in this thesis having primary objectives of develop an understanding on electrochemical approach towards device fabrication and understanding device operational mechanism. Along with the operation, explore new techniques to track molecular changes within the electrochromic device like: in-situ spectroscopies to probe the device behavior under its operational condition. Explore the possibility of nanostructures of organic and inorganic material which can be incorporated in the device for better performance. As far as structure is concern understanding the growth mechanism of various nanostructures involving hydrothermal and electrodeposition methods along with high temperature and pressure treatment so that the electrochromic device parameters can be optimized. Apart from electrochromic device incorporation of these nanostructures in other areas of electrochemical based application such as energy storage and sensing. Other than this field emission is also one of the application we have gone through it.

In an attempt to understand the color switching mechanism of organic electrochromic devices, live spectroscopy has been done to probe the internal mechanism of the device. Role of redox reactions taking place at the electrode/electrolyte interface has been identified using Raman and UV-Vis spectroscopies which have been carried out during the device operation. The origin of color change has been attributed to the bias induced redox switching between its dication and free radical forms which have different optical properties from each other. Raman spectra collected from negative and positive electrodes of the device reveal that blue color species (free radical) are present at the negative electrode which is created due to reduction of the dicationic form. In-situ UV-Vis spectra reveals that the navy blue color of the device under biased condition. Absorption modulation has been reported from the device with good ON/OFF contrast of the device. After understanding the fundamental mechanism of color switching within the electrochromic device we have prepared a new electrochromic gel (EC-Gel) combine of ethyl viologen (EV) - graphene nanoflake (GNFs) - tetrathiafulvalene (TTF) show faster and efficient electrochromism. A prototype flexible electrochromic device has been fabricated using the above-mentioned EC-Gel as active layer which shows overall improved coloring efficiency.

After successfully understanding pure organic electrochromic devices, we have deigned inorganic core-shell nanorods made of TiO_2/Co_3O_4 exhibits improved electrochromic properties. The core shell hetrostructure shows better performances as compared to the individual nanostructures of either of the metal oxides. The structures grown on FTO coated glass substrate using hydrothermal electrodeposition technique. The core-shell electrode exhibit high stable and power efficient bias induced color change between transparent (sky blue) and opaque (dark brown) state with coloration efficiency of $\sim 90 cm^2/C$. Improvement in electrochromic performance is likely due to increased surface area and modified charge dynamics within the core-shell heterojunction with solid foundation of single crystalline nanorods. Additionally, these core-shells also exhibit porous morphology and strong adhesion to the surface of transparent conducting glass electrode gives rise to superior cyclic stability in both, energy storage and electrochromic application. After understanding pure organic and pure inorganic electrochromic devices, we have demonstrated hybrid core-shell nanostructures based on transition metal oxide as core and conducting polymer as shell to improve electrochromic properties. Nickel oxide nanopetals (NiO-NPs) transition metal used as backbone templates for polyaniline (PANI) conducting polymer as shell shows efficient and stable electrochromic performance.

Apart from electrochromic applications, we have also explored various other applications such as energy storage to field emission to glucose sensing of the same multifunctional nanostructures used in electrochromic application. The core-shell nanostructures have been grown on an FTO coated glass substrate by preparing TiO_2 nanorods through hydrothermal reaction followed by growing Co_3O_4 shell layer by electrodeposition shows high specific and areal capacitance. A power efficient and stable field emission (FE) has been observed from ultrathin nanothorns covered nickel oxide (NiO) nanopetals (NPs) where three orders of magnitude improved electron FE, in terms of threshold and turn-on fields, has been observed. Glucose sensing properties of mesoporous well-aligned, dense nickel oxide (NiO) nanostructures (NSs) in nanopetals (NPs) shape grown hydrothermally on the FTO coated glass substrate has been demonstrated.

LIST OF PUBLICATIONS

(A) Peer reviewed journals (thesis)

1) **Suryakant Mishra**, H. Pandey, P. Yogi, S. Saxena, S. Roy, P. R. Sagdeo, Rajesh Kumar. "Interfacial redox centers as origin of color switching in organic electrochromic device" **Optical Materials**, 2017, 66, pp 65-71

2) **Suryakant Mishra**, H. Pandey, P. Yogi, S. Saxena, S. Roy, P. R. Sagdeo, Rajesh Kumar. "Live spectroscopy to observe electrochromism in viologen based solid state device" **Solid State Communications**, 2017, 261, pp 17-20

3) **Suryakant Mishra**, P. Yogi, S. Saxena, S. Roy, P. R. Sagdeo, Rajesh Kumar. "Fast electrochromic display: tetrathiofulvalen and graphene nanoflakes as facilitating agent" **Journal of Materials Chemistry C**, 2017, 5, pp 9504-9512

4) **Suryakant Mishra**, P. Yogi, S. Saxena, J. Jayabalan, P. Behera, P. R. Sagdeo, Rajesh Kumar. "Significant field emission enhancement in ultrathin nano-thorn covered NiO nano-petals" **Journal of Materials Chemistry C**, 2017, 5, pp 9611-9618

5) **Suryakant Mishra**, P. Yogi, P. R. Sagdeo, Rajesh Kumar. "The synthesis of NiO Nanopetals, structural characterization, and their glucose sensing application" **Nanoscale Research Letters**, 2018, pp 13-16

6) **Suryakant Mishra**, P. Yogi, P. R. Sagdeo, Rajesh Kumar. "TiO_2/Co_3O_4 Core-Shell Nanorods: Bi-functional Role in Better Energy Harvestation & Electrochromism" **ACS Applied Energy Materials**, 2018, 1(2), pp 790–798

7) **Suryakant Mishra**, P. Yogi, S. Saxena, S. Roy, P. R. Sagdeo, Rajesh Kumar. "Construction of Well Aligned Highly Dense Cobalt Nanoneedles for Efficient Device Application" **Advances in Materials and Processing Technologies**, 2017, pp 627-631

8) **Suryakant Mishra**, S. Lambora, P. Yogi, Pankaj R. Sagdeo, Rajesh Kumar. "Organic Nanostructures on Inorganic ones: An Efficient Electrochromic Display by Design" **ACS Applied Nano Materials**, 2018, 1(7), pp 3715-3723

9) **Suryakant Mishra**, P. Yogi, A. Chaudhary, D. Pathak, S. Saxena, A. Krylov, P. R. Sagdeo, Rajesh Kumar. "Color Perseverance and its Correlation with Gradual Spectroscopic Variations in Electrochromism" communicated

(B) Peer reviewed journals (other than thesis)

10) **Suryakant Mishra**, P. Yogi, S. Saxena, V. Kumar, Rajesh Kumar. "Fano Scattering: Manifestation of Acoustic Phonons at the Nanoscale" **J. Phys. Chem. Letters**, 2016, 7 (24), pp 5291-5296

(C) Peer reviewed journals (As a contributory author)

1) P. Yogi, D. Poonia, **Suryakant Mishra**, S. Saxena, S. Roy, V. Kumar, P. R. Sagdeo, Rajesh Kumar. “Spectral Anomaly in Raman Scattering from p-Type Silicon Nanowires” **J. Phys. Chem. C**, 2017, 121 (9), pp 5372-5378
2) S. Saxena, P. Yogi, **Suryakant Mishra**, H.M. Rai, V. Mishra, K. Warshi, S. Roy, P. Mondal, P. R. Sagdeo, Rajesh Kumar. “Pseudo-symmetric Raman line-shape: graveyard for Fano and quantum effects” **Phys. Chem. Chem. Phys.**, 2017, 19, 31788 – 31795.
3) S. Roy, S. Saxena, **Suryakant Mishra**, P. Yogi, P. R. Sagdeo, Rajesh Kumar. “Ecofriendly gold nanoparticles lysozyme interaction: thermodynamical perspectives” **Journal of Photochemistry & Photobiology, B: Biology**, 2017, 174, pp 284-290.
4) S. Roy, S. Saxena, **Suryakant Mishra**, P. Yogi, P. R. Sagdeo, Rajesh Kumar. “Evidence of bovine serum albumin-viologen herbicide binding interaction and associated structural modifications” **Journal of Molecular Structure**, 2017, 1139, pp 447-454
5) P. Yogi, S. Saxena, **Suryakant Mishra**, H. M. Rai, R. Late, V. Kumar, B. Joshi, P. R. Sagdeo, Rajesh Kumar. “Interplay between Phonon Confinement and Fano Effect on Raman line shape for semiconductor nanostructures: Analytical study” **Solid State Communications**, 2016, 230, pp 25-29
6) S. Saxena, P. Yogi, P Yadav, **Suryakant Mishra**, H. Pandey, H. M. Rai, V. Kumar, P. R. Sagdeo, Rajesh Kumar. “Role of Metal Nanoparticles on porosification of silicon by metal induced etching (MIE)” **Superlattices and Microstructures**, 2016, 94, pp 101-107.
7) S. Roy, **Suryakant Mishra**, P. Yogi, S. Saxena, P. R. Sagdeo, Rajesh Kumar. “Synthesis of Conducting Polypyrrole-Titanium Oxide Nanocomposite: Study of Structural, Optical and Electrical Properties” **J. Inorg. Organomet. Polym.**, 2017, 27, pp 1-7.
8) S. Roy, S. Saxena, **Suryakant Mishra**, P. Yogi, P. R. Sagdeo, Rajesh Kumar. “An insight of spirooxindole-annulated thiopyran - DNA interaction: Spectroscopic and Docking Approach of these biological materials” **Advances in Materials and Processing Technologies**, 2017, 3, pp 339-352
9) S. Roy, **Suryakant Mishra**, P. Yogi, S. Saxena, V. Mishra, P. R. Sagdeo, Rajesh Kumar. “Polypyrrole Vanadium Oxide Nanocomposite: polymer dominates crystallinity and oxide dominates conductivity” **Applied Physics A**, 2018, 124:53
10) S. Roy, S. Saxena, **Suryakant Mishra**, P. Yogi, P. R. Sagdeo, Rajesh Kumar. “Spectroscopic Evidence of Phosphorous Heterocyclic - DNA Interaction and its Verification by Docking Approach” **Journal of Fluorescence**, 2017, pp 1-8

11) M. Tanvar, P. Yogi, S. Lambora, **Suryakant Mishra**, S. Saxena, P. R. Sagdeo, A. Krylov, Rajesh Kumar. “Generalization of Phonon Confinement Model for Interpretation of Raman Line-Shape from Nano-Silicon” **Advances in Materials and Processing Technologies**, 2017, pp1-7

12) P. Yogi, A Choudhary, D.K. Pathak, S. Saxena, **Suryakant Mishra**, Pankaj R. Sagdeo, Rajesh Kumar. “Porous Silicon’s fractal nature revisited” **Superlattices and Microstructures**, 2018, 120, pp 141-147.

13) P. Yogi, D Poonia, P Yadav, **Suryakant Mishra**, S. Saxena, Pankaj R. Sagdeo, Rajesh Kumar. “Tent-Shaped Surface Morphologies of Silicon: Texturization by Metal Induced Etching” **Silicon**, 2018.

14) P. Yogi, M. Tanvar, S. Saxena, **Suryakant Mishra**, D.K. Pathak, A. Choudhary, P. R. Sagdeo, Rajesh Kumar. “Quantifying the short-range order in amorphous silicon by Raman scattering” **Analytical Chemistry**, 2018, 90 (13), pp 8123-8129.

15) S. Jain, **Suryakant Mishra**, T Sarma. “Zn^{2+} Induced Self-Assembled Growth of Octapodal Cu_xO-ZnO Microcrystals: Multifunctional Applications in Reductive Degradation of Organic Pollutants and Non-Enzymatic Electrochemical Sensing of Glucose” **ACS Sustainable Chemistry & Engineering**, 2018, 6 (8), pp 9771-9783.

Contents

Chapter 2: Experimental Details

Chapter 3: Electrochromic Devices Based on Organic Materials

Chapter 4: Inorganic Core-Shell Hetero Nanostructured Junction: Efficient Electrochromism

Chapter 5: Hybrid Core/Shell Nanostructures: Improved Electrochromism

Chapter 6: Special Nanostructures: Applications beyond Electrochromism

Chapter 7: Conclusions and Future Scope

Appendix

List of Figures

List of Tables

Abbreviations

Ethyl viologen	EV
Nanostructures	NSs
Nanopetals	NPs
Nanohemisphericals	NHs
Tetrathiafulvalene	TTF
Optical Density	OD
Color Contrast Ratio	CCR
Graphene Nanoflakes	GNFs
Poly Ethylene Oxide	PEO
Indium Tin Oxide	ITO
Cross Bar Geometry	CBG
Open Face Geometry	OFG
Fluorine doped Tin Oxide	FTO
X-Ray diffraction	XRD
Commission Internationale de l’Eclairge	CIE
Scanning Electron Microscopy	SEM
Transmission Electron Microscopy	TEM
X-Ray Photoemission Spectroscopy	XPS
Charge coupled device	CCD
Energy Dispersive X-Ray	EDX
Cyclic Voltammetry	CV
Electrochromic Displays	ECDs
Graphene Oxide	GO
Electrochromic Gel	EC-Gel
Photo Luminescence	PL
Ultra Violet Visible Spectroscopy	UV-Vis
Working Electrode	WE
Counter Electrode	CE
Glassy carbon electrode	GCE

Reference Electrode	RE
Saturated Calomel Electrode	SCE
Polyaniline	PANI
Atomic Force Microscopy	AFM
Diffuse Reflectance Spectroscopy	DRS
Chronoamperometry	CA
Fast Fourier Transform	FFT
Charge/Discharge	CD
Field Emission	FE
Brunauer–Emmett–Teller	BET

Chapter 1

Introduction

In electronics, device science and technology at ‘nano’ level is a fastest growing multidisciplinary field as it attracts interest from the areas of bio-sciences to physical sciences to chemical science to engineering science as well as interdisciplinary sciences. Tremendous interest and investment is made in research and development around the world for the development of nanotechnology based devices. At nanoscale, atoms and molecules interact and assemble into structures and possess unique properties, which depend on the size of the structures and not observed in their bulk forms. Nanoscience is one of the thrust areas that may contribute in making India a developed country by year 2020.

1.1 Nanoscience in various fields

Nanoscience have played significance roll nearly in all research fields from physical science to biomedical, chemical to engineering etc. In nanoscience, nanostructures of various materials are vital parameters; some of the NSs of various inorganic as well as organic materials are shown below.

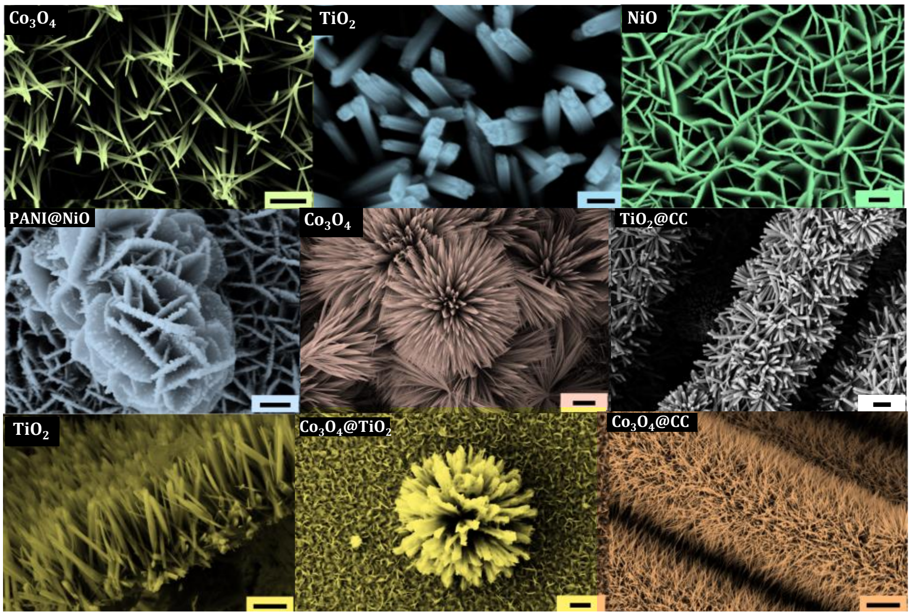

Figure: 1.1 Various morphologies of the some nano-materials (scale bar 500nm).

1.1.1 Chemical science

Nanotechnology plays one of the vital roles in chemical science as can be understood through its usage in meeting the needs of as basic item as clean drinking water through rapid, low-cost detection and treatment of impurities in water. Thin film membrane with nanopores for energy-efficient desalination. A molybdenum disulphide (MoS_2)[1] membrane filters two to five times more water than current conventional filters. In recent report Geim and coworker developed graphene based membrane which is useful to convert salty see water into drinking water[2]. Nanoparticles are being developed to clean industrial water pollutants in ground water through chemical reactions that makes the pollutants harmless. In new research, nanofabric "paper towel" has been developed woven from tiny wires of potassium manganese oxide that can absorb 20 times its weight in oil for cleanup applications[3]. Researchers have also placed magnetic water-repellent nanoparticles in oil spills and used magnets to mechanically remove the oil from water[4]. The filters contain nanoscale pores that trap particles larger than the size of the pores and an additional charcoal layers that remove odors. Nanotechnology-enabled sensors and solutions are now able to detect and identify chemical or biological agents in the air and soil with much higher sensitivity than ever before. Above examples only list a few whereas the application of 'nano' in chemical science is plenty which is being used to develop technology to makes one's life easier worldwide.

1.1.2 Physical science

In the field of physical science, various physical phenomena, which were not observable in bulk materials can be detected in their NSs. In the past, one of the important physical phenomena in the materials is to probe the non-radiative transitions and for the same, low frequency Raman spectroscopy on the nanostructures of the various materials has been proved to be a handy technique. The non-radiative transition from silicon NSs can be observed by an indirect technique with the help of Raman spectroscopy. In nanomaterials, different physical properties are observed as compared to their bulk counterpart mainly due to quantum confinement effect and increased reactivity[5–7]. When the first is a solely a physical phenomenon, then latter also leads to various changes in associated chemical properties including increased chemical activity, catalysis etc. The quantum confinement effect is helpful in understanding various optical, electronic and electrical properties of nanomaterials. The confinement effect induces the energy levels to become quantized when reduced to sufficiently small sizes. Electrons, holes, phonons and other bound state entities, confined inside these low dimensional materials give rise to special properties to these nanostructures as compared to their bulk form. Various microscopic interactions also show different nature when take place at nanoscale that includes interaction between the interaction of confined phonons and intra-band quasi-continuum[8]. This interaction, observed through Raman spectroscopy, is named as "Fano scattering" and is useful in getting information about non-radiative transitions.[1]

1.1.3 Bioscience

Nanotechnology has given a new direction to the bioscience from diagnosis to treatment. Nanomaterials help in detecting signals from the effective tissue while diagnosis and also are helpful in targeted drug delivery, one of the biggest promises that nanotechnology has committed. It covers the biological mapping of interior body parts. Most of the work based on the photo acoustic tomography (PAT) by the absorbent inside the body parts[9–11]. Intensity of these acoustic signals is very important for mapping various defects inside the body cell. Optical light used to harvest the acoustic signal and can be detected by the ultrasonic transducer detectors. Movement of these detectors or array of the detector around the body parts enables 3D mapping of these bio-molecular cell. Most of the R&D is focused on propagation of optical light toward biomolecules inside the body to improve depth of penetration of optical light. Various optical arrangement have been carried out recently to improve focal length like waveguide arrangement, endoscopy (using biodegradable optical fibers), laser pulsing, two photon arrangement etc. in further advancement in the same special gel made up off biodegradable nanoparticles, which serve the purpose of propagating light within the body by proper matching the refractive index[9–11]. Gel is composed of biodegradable NPs, which modulate the refractive

---

[1] *Mishra et al.,* **J. Phys. Chem. Lett.**, (2016), 7, pp 5291–5296

index of surroundings the cell and can control the amount of light propagation.

1.1.4 Engineering (electronic devices)

Various electronic devices are now flexible, bendable, foldable, rollable, and stretchable contributing in and around all the sectors and are being integrated into a variety of products, including wearable gadgets for medical and aerospace applications[12–16]. Flexible electronics have been developed using, for example, semiconductor nanomembranes for applications in smartphone and e-reader displays[12–16]. Other nanomaterials like graphene and cellulosic nanomaterials are being used for various types of flexible electronics to enable wearable sensors, photovoltaics that can be incorporated onto clothing and electronic paper that can be rolled up[17–19]. Making flat, flexible, lightweight, non-brittle, highly efficient electronics opens the door to countless smart products. Using magnetic random access memory (MRAM), computers will be able to "boot" almost instantly[20,21]. MRAM is enabled by nanometer-scale magnetic tunnel junctions and can quickly and effectively save data during a system shutdown or enable resume-play features. Ultra-high definition displays and televisions are now available that use quantum dots to produce more vibrant colors while being more energy efficient[22,23]. In electronic devices, ECD is one of the potential components for advancement of the electronics. Current work focuses on the ECDs, which are capable of showing modulations in their optical properties by appropriate external electrical stimuli[24].

This chapter deals with the introduction of the electrochromism ingredient. Materials showing electrochromic properties come from both organic as well as inorganic as have been discussed here along with the various parameters, which affect this. Apart from the previously developed concepts, recent advancement in the field of smart electrochromic displays and their various other potential applications are also included here. Furthermore, it has also been explored that how various kinds of NSs of both organic as well as inorganic electrochromic active materials can play crucial role in fabricating energy efficient and multitasking device.[2,3]

1.2 Electrochromism

Electrochromism is a phenomenon of the reversible changes in the optical properties of any material[25–27]. Different electrochromic behavior is observed in reflection, transmission and absorption modes with external electrical stimuli. The potential applications of electrochromic material are in reflective type displays and anti-glare glasses of automobile or transmissive type smart windows used in energy efficient buildings[25]. Generally, electrochromism in any material is perceived due to change in the electronic states of a molecule which alters the optical properties on the application of electrical bias. In other words, electrochromism arises due to reversible change between two redox states of a chemical species with distinguishable optical spectrum. This was first discovered by Deb with his coworkers in 1969 when performing experiments on WO_3[28].

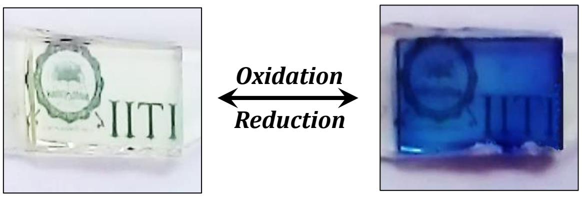

Figure: 1.2 Electrochromic display made using viologen derivatives[29].

Electrochromism can be exhibited by several organic (conjugated polymers) and inorganic (transition metal oxides) compounds which usually have reversible redox state. Both organic and inorganic groups of EC materials have their own merits and demerits, which are addressed accordingly during the device

---

[2] *Mishra et al.,* **J. Mater. chem. C**, (2017) 5, 9504-9512

[3] *Mishra et al.,* **ACS Appl. Energy Mater**., (2018) 1, pp 790–798

fabrication. As compared to the emissive materials (like LED), color can appear in a transmissive style through the coating on a transparent electrode or a reflective style when viewed in an external light. Transmission or reflection makes it possible to fabricate EC display that can be of a paper-like display with appropriate engineering, unlike the usual electronic displays. As far as science is concerned, material understanding and device composition need to be established for making an ECDs with an 'appropriate' quality.

1.2.1 Device geometry paradigms

An EC material, along with other necessary constituents, needs to be fabricated in the form of a device to achieve a predefined performance thus is very critical when it comes to design one. An ECD composed of a redox couple must be present between two electrodes to ensure the operation of the device. During the operation one of the species get oxidized and the other gets reduced for the completion of the whole process. ECD must switch its mode reversibly from the bleached state to the colored state and vice versa. Device shown in Figure 1.2 is a fundamental geometry of an ECD. In electrochromism, two conditions are mandatory: first, both the redox couples must be transparent; second, at-least one of them is electrochromic active. The material which is more active in both the materials is called primary and always nearer to the working electrode. On the other side there will be a redox supporting agent which can be electrochromic active or otherwise. In addition to this, an electrolyte separator may be sandwiched between both redox agents, which is an ionic conductor for the transportation of the ions from one electrode to the other one. At the same time, the given electrolyte must have negligible electronic conduction to avoid short circuit of the device. All the above-mentioned layers are usually sandwiched between two transparent conducting electrodes speed of the coloration/decoloration of the device depends upon the nature of constitutes present within the device.

Electrochromic device can broadly be of two types:

- Single layer EC device: Only one electrochromic active species present
- Double layer EC device: Both redox layers electrochromic active

Single layer ECD have less number of redox states compared to the double layer EC device. Transmittance of the single layer ECD is higher in its neutral state. A double layer ECD offer color tuning capability during operation with small electrical potential window. Other components of the device include the following:

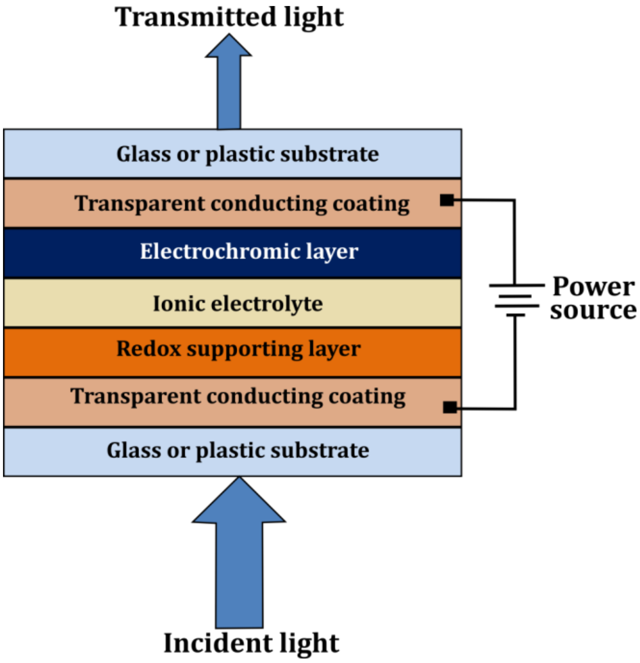

Figure: 1.3 Layered geometry of a typical electrochromic display.

Transparent conducting electrode (TCE): These are generally indium tin oxide (ITO) or fluorine doped tin oxides (FTO) based material coated either on a glass or a quartz substrate where in case of flexible device, polyethylene terephthalate (PET) is used as substrate for the device fabrication.

Electrochromic active layer: This layer is made up of electrochromic active materials, which respond during the application of bias on the device.

Ionic conductor electrolyte: Electrolytic layer generally placed in between the layer of active material and redox supporting material. It must be an ionic conductor but electronic insulator to avoid short circuit.

Redox supporting layer: This layer is generally used to support the redox reaction of the electrochromic layer. It may be electrochromic active and participate in the electrochromism.

1.2.2 Color perceived

In case of metals mostly its nanoparticles prominent spectroscopic feature overserved due to surface Plasmon resonance, which gives rise to a sharp and intense absorption band in the visible range. The physical origin of the absorption is a collective resonant oscillation of the free electrons of the metals. The color perceived to our eyes, are result of the light that reaches the eye after it gets reflected and/or transmitted by the object along with the eyes nonlinear sensitivity of different wavelengths.

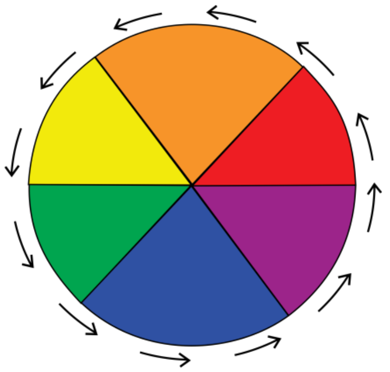

Figure: 1.4 Color-wheel to check various color-combinations.

In this regards complementary color system easily allows one to relate the maximum color absorbed. This can be understood using the famous color wheel (Figure 1.4). One can understand this by an example, in transmission mode film that is green in color do have minimum absorption in the green wavelength spectrum (560- 600 nm), this absorption minimum will be prepared by two higher absorption bands. Absorption in the red region (650-700) and in the blue region (350-450) will be high to perceive green color. Therefore for the appearance of green color, blue and red will be the complementary colors. Accordingly, the absorption of red and green yields their complementary which is blue color[30]. In the context of electrochromism, during the operation of an ECD, if blue color is perceived the explanation of the same can be given as follows. It is important to reiterate the fact that the color perceived depends on the visible wavelength that reaches the eye by whatever means. It is the combination of wavelengths reaching eyes decide the resultant color. While correlating the color combination in Figure 1.4 with the observed blue color, concept of additive primary colors (RGB or Red-Green-Blue) and subtractive primary colors (CMY or Cyan-Magenta-Yellow) will be used.

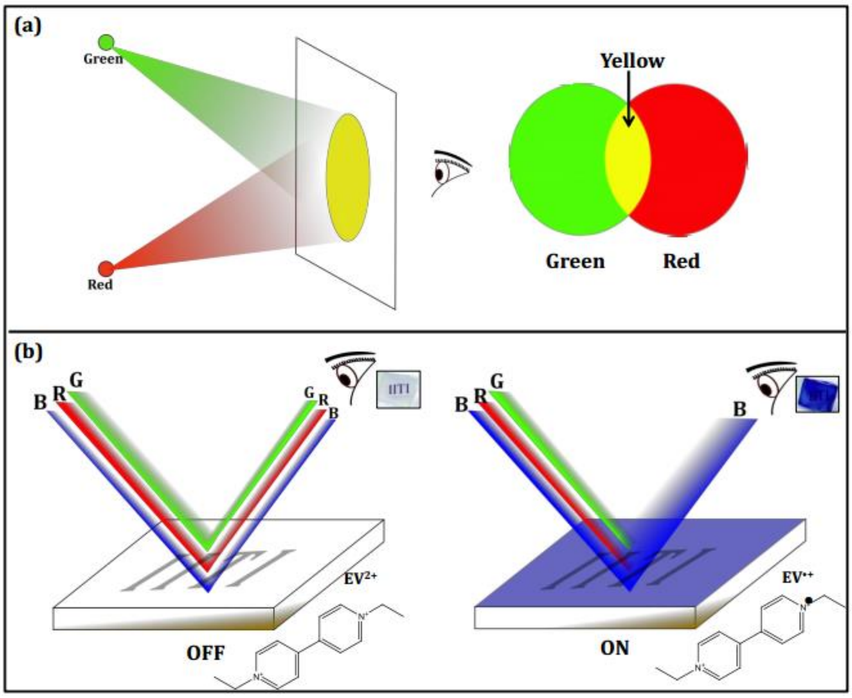

Figure: 1.5 (a) Color combination (b) Schematic presentation of blue color perceivance of the fabricated electrochromic display with the actual images given in inset of the figure.

If an ECD show absorption maxima in yellow (560-590nm), which is the combination of red and green colors as depicted schematically in Figure 1.5a. This can be visualized from the Figure 1.5b, initially in the OFF state of the device white light coming from the 'IITI' can be seen but in the ON state of the device it absorbs yellow (green + red) color and the 'IITI' perceived blue to the eyes. If whole of this experiment perform on a non-reflecting surface like black paper, no change in color is expected to appear.

1.2.3 Reflective ECDs

Electrochromism is not limited to visible color changes, but can be extended to encompass materials that exhibit radiation modulation in the visible regions. This has provided the impetus for developing device that can operate at broader wavelengths region, with long lifetimes and fast switching times.

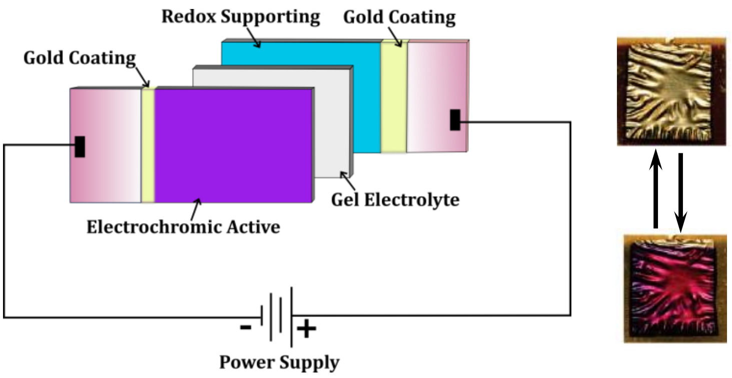

Figure: 1.6 Schematic illustration of reflection based electrochromic display and their corresponding actual images[30].

Reflective devices are another type of devices having structure commonly utilized eternal light for the modulation into various other wavelength radiations. This device type, there are two structures most often reported based on specular reflectance. The reflective-type of devices operate with one of the electrodes as the reflector. As shown in Figure 1.6, the working and counter are electrodes arranged in such a manner that the working electrode is forward facing and the counter electrode is hidden/transparent behind. The working electrode should be porous, to allow for ion diffusion during switching of the device. Relatively high reflective contrasts have been obtained with this type of device as the counter electrode is hidden/transparent and the optical properties of the counter material do not affect the device contrast, only providing charge balancing. As such, a larger variety of materials can be utilized at the counter electrode, such as the same material at the working electrode, with the only two requirements being a sufficient charge density during switching and electrochemical stability within the switching voltage of the device. Another advantage of this device type is that the most often used electrode material is a gold-coated porous membrane. Given that gold has a large IR reflectivity, these devices are advantageous platforms for characterizing the IR electrochromic switching properties and utilization for space,[31,32] thermal, and optical telecommunications applications[33].

1.2.4 Various parameters of electrochromism

1.2.4.1 Contrast ratio (CR)

Optical contrast is used to quantify the color change in an ECDs by defining CR. CR can refer either to a specific wavelength or to the overall white light. For reflective device, CR is given by the following definition:

$$\boldsymbol{CR = \frac{R_0}{R_X}}$$

where, R_x and R_0 are the intensity of light reflected from the opaque and the bleached state respectively.

In the case of transmissive devices, contrast ratio is given as

$$\boldsymbol{CR = \frac{T_0}{T_X}}$$

Where, T_x is the light intensity of transmitted light in the opaque state and To is the intensity of light transmitted through the bleached state when the device is in the same media.

1.2.4.2 Optical density (OD)

The Optical density (OD) is an expression of the optical transmittance of an element at a given wavelength and is expressed as

$$\boldsymbol{OD = log_{10}\left(\frac{1}{T}\right)}$$

where, T is the transmittance.

1.2.4.3 Coloration efficiency (η)

Coloration efficiency is defined as the change in optical properties like transmittance and absorbance by a certain amount of injected charge per unit area (unit cm^2/C). Coloration efficiency is also known as electrochromic efficiency, which is also used for the comparison of the efficient electrochromic layers.

$$\boldsymbol{\eta}(\boldsymbol{cm^2/C}) = \frac{\boldsymbol{\Delta OD}}{\boldsymbol{Q}}$$

where, $\boldsymbol{\Delta OD}$ change in optical density and Q is the charge required during the device operation respectively. More details about this will be discussed in relevant chapters later on.

1.2.4.4 Switching time

Response time is another important parameter to check device performance, which gives the information about the time taken by the device to switch form its one state to the other. The switching speed of ECDs depends upon the composition like ionic conductivity of the electrolyte, ion diffusion in the active layers and accessibility of the ions to the electroactive sites, applied field intensity, film thickness and conductivity of the transparent electrode.

1.2.4.5 Cycling life

As can be understood, an indeed ECD should be able to switch between its ON and OFF states infinitely. Limited by the materials' performance, cycle life needs to be defined to say how many times an ECD can be turned ON and OFF. Cycling counts of the ECDs from colored to bleach and vice-versa give the information about the life of the fabricated device. During repeated cycling, device failure eventually occurs, resulting from physical changes of the device or some chemical side reactions or higher applied field. The device life decreases if strong changes in electrode composition like permanent deposition on the electrode of the material during cycling, so it is preferable not to switch the ECDs at their maximum capacity.

1.2.4.6 Stability

In ECDs stability, electrochromic material plays the crucial role. Multiple redox switching of one material kills the device performance. Applied field and environmental condition also play an important role for consistent performance. Therefore, ECDs with good environmental and redox stability are required for future applications.

1.2.5 Electrochromism as optical memory

ECD can also be applicable as optical memory can be defined as the propensity of the material to retain its redox or colored state upon removing the external bias (open circuit). Electrochromism generally see their colored state bleach rapidly in the absence of applied voltage as the ions can freely diffuse and exchange electrons (self-erasing mechanism)[34]. In contrast, the primary requirement of minimizing self-erasing effect is that material should be well-adhered onto the electrodes, with proper selection of the redox supporting agent on the counter electrode.

1.2.6 Electrochromic materials

The active material used in an ECDs must exhibit a combination of properties that includes high coloration efficiency, high optical contrast, long-term redox and photo stability and fast switching kinetics. Based on the above-mentioned properties electrochromic materials can be divided into following two categories.

1.2.6.1 Inorganic electrochromic compounds

Transition metal oxides have long been used in ECDs, where they are almost always the active electrochromic electrode (Figure 1.7). Reversible color changes in tungsten bronzes have been studied for more than hundred years,[35,36] and Deb's demonstration of electrochromism in tungsten oxide launched nearly 50 years of ongoing electrochromic research[28,37]. Conventional electrochromic oxides tend to be deposited in the form of thin-film by physical vapor processes like sputtering, and they typically operate via an electrochemical ion intercalation and redox process. Although metal oxides based ECDs are the current state of the art in smart windows, improvements in cost, durability, spectral control like color contrast, tuning and switching time still need to be done. Recent advances in nanostructured metal oxides, and their combination with the organic counterpart are promising signs of progress in this area. Materials, which changes its color upon reduction are referred as cathodically electrochromic, whereas those change color upon oxidation are called anodically electrochromic.

(a) Cathodic electrochromic and their nanostructures

Tungsten oxide, in both crystalline and amorphous form, is easily the most ubiquitous solid-state electrochromic material. Edge- and corner-sharing WO_6 octahedral in WO_3 form periodic structures with open tunnels of interstitial sites, which facilitate ion motion and intercalation. When WO_3 is cathodically electrochromic material, on the application of the negative potential intercalation of the cations (H^+ or Li^+) starts and compensated by injected electrons, which reduce tungsten cations from W^{6+} to W^{5+}[36]. Concurrently, the material changes from a clear, transparent state to dark blue.

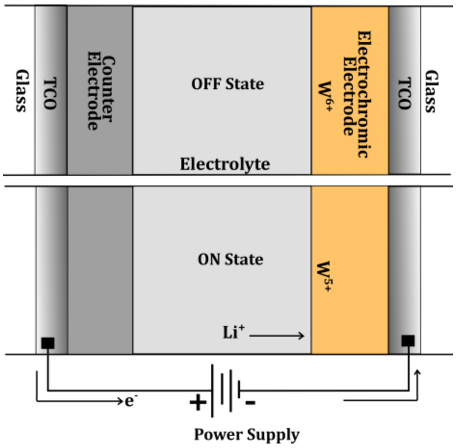

Figure: 1.7 Schematic presentation of ionic movement within the electrochromic device[27].

The other cathodically coloring transition metal oxides, including TiO_2, Nb_2O_5, and MoO_3, also have edge- and corner-sharing MO_6

octahedral and intrinsically empty d-bands and color by related mechanisms upon charge injection[38]. However, the cathodic metal oxides aside from WO_3 have met with limited success because of low coloration efficiency and poor durability. Nanostructures of the same show highly improvement in the performance. Recently, various nanostructures like nanocrystals, nanorods and nanoflakes display enhanced coloration efficiencies, charge capacities, and optical contrast compared with crystalline thin films, with greater enhancement for decreasing particle sizes[39,40]. Nanocrystalline WO_3 is an attractive electrochromic material because crystalline WO_3 is much more durable than the amorphous form when parotic electrolytes are used,[41] and the small length scales for ion diffusion into the nanocrystals enable short switching times that are not possible in dense crystalline WO_3 thin films. Furthermore, electrochromic nanomaterials may be compatible with solution processing methods, which can confer significant benefits for cost and manufacturability. Other cathodically coloring oxides, namely TiO_2 and MoO_3, exhibit similar performance enhancements at the nanoscale[40,42].

(b) Anodic electrochromic and their nanostructures

Materials, which show electrochromic behaviors on the anode is called anodically electrochromic. Metal oxides like NiO, IrO_2, and V_2O_5 show electrochromic nature in their oxidation state and are transparent in their initial reduced state. Where NiO is just a reciprocal of WO_3 change in its color in just opposite potential window and the perceive color is also similar. Nanostructured versions of the anodically coloring oxides display interesting electrochromic behavior by pseudocapacitive mechanisms, which can be exploited for fast switching and prolonged cycle life by avoiding ion intercalation. Deb and coworkers first discovered pseudocapacitance in electrochromic NiO nanoparticles in 2005[43]. Their NiO nanoparticles, dispersed in a Ta_2O_5 proton-conducting matrix, achieved coloration efficiencies comparable to thin films, but with greater charge capacity and optical modulation that increased with smaller particle sizes. Likewise, gyroidal structures of NiO and V_2O_5, prepared by block copolymer templated electrodeposition, display pseudocapacitive electrochromism with exceptionally fast switching, deep optical modulation, and high charge capacity[44,45].

1.2.6.2 Organic electrochromic compounds

(a) Electrochromic polymers

Conjugated polymers of thiophenes, pyrroles, anilines, furans and carbazoles are electrochromic active (some are shown in Figure 1.8), because electrochemical doping can alter their π-conjugated electronic structures to induce a change in bandgap and optical contrast[46,47]. Their electrochromism is synthetically tunable with changes to the monomer type, conjugation length, substitution groups/side chains, stereoregularity, and steric effects. Thiophenes, aniline, pyrroles and their derivative are of particular interest because of their facile chemical and electrochemical synthesis, suitable bandgaps and low redox potentials.

In the past decades, a great amount of effort has been put on their structural and bandgap engineering. Synthesizing various derivatives of these with different functional groups, with various fused aromatic rings, or with segments that can be polymerized into random, alternating, or block copolymers. Numerous different color changes can be found in the literature; for example, poly(thiophene) can change color from red in the neutral state to blue in the oxidized state. Reynolds et al. [48] synthesized a donor acceptor copolymer electrochrome, consisting of 3,4-bis(2-ethylhexyloxy)thiophene donor and 2,1,3-benzothiadiazole acceptor moieties, which showed a black-to-transmissive color switching, meeting the need for color neutrality that is a highly desirable feature for window applications. PProDOP and PProDOT color both cathodically and anodically and can be used as either working or counter electrodes in ECDs to produce new color states.

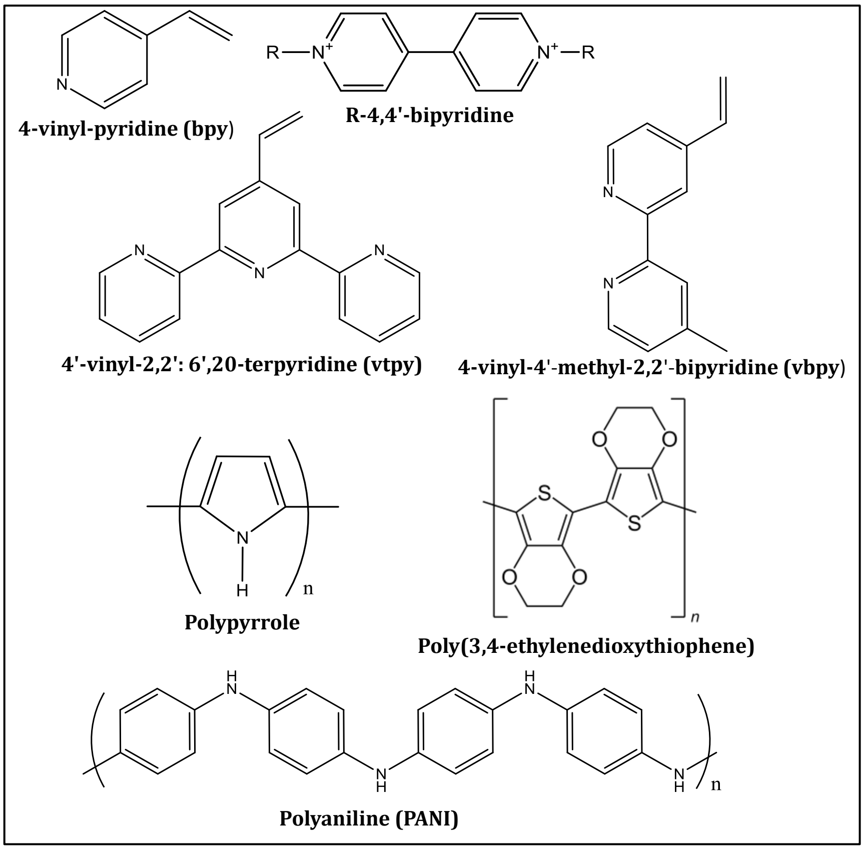

Figure: 1.8 Organic compounds and polymers which show electrochromic behaviors.

PEDOT:PSS and polyaniline electrodes in a device exhibits an optical modulation of 72% at 580 nm, a switching time of 160 ms, and a color efficiency of 338 cm^2/C, which is approximately four times greater than crystalline WO_3. However, devices based on electrochromic polymers generally lack a clear and highly transparent state, but are important for smart window applications. Their electrochemical and photochemical durability upon cycling is generally inferior to those for the inorganic materials, which is often attributed to redox irreversibility.

(b) Non-polymeric electrochromic materials

Electrochromism can also be found in a wide range of other materials, including small organic and inorganic molecules and conjugated polymers. Compared with metal oxides, most of these materials offer color tuning, high coloration efficiency, good color contrast and simple solution processibility Their photochemical and electrochemical stability can be problematic, as faded optical contrast and yellowing arising from side reactions and sometime irreversible redox process.

Viologens are a class of 4,4-bipyridine compounds that exhibit reversible redox chemistry between a colorless dicationic form (V^{2+}) and a blue radical cationic ($V^{+\cdot}$) form. It is worth mentioning here that the radical cation ($V^{+\cdot}$) can be further reduced into a yellow neutral form (V^0). However, this reaction does not show good reversibility. The well-established substitution chemistry on the two nitrogen atoms in viologens has allowed researchers to tune the color of viologen radical cations; for example, alkyl groups give a deep blue color, whereas 4-cyanophenyl groups induce an intense green color[36]. Recent work on viologens and their devices emphasizes the development of novel substitution groups, counter anions, and redox agents to lower the reduction potential and improve switching rate, coloration efficiency, and color neutrality. Studies related to electrochromic performance of viologens and their derivatives have been used reported in the current thesis. Various attempts have been taken to improve the performance of the material. These materials have been studied not only in their material form but also by making a proto-type device. Other than electrochromism, specially designed nanomaterials have been tested for applicability in energy storage, field emission display and sensing. The driving force for such a diverse study can be emphasized by looking at the multifunctional importance as has been summarized below.

1.3 Other applications of functional nanomaterials

1.3.1 Nanomaterials in energy storage

Increasing power and energy needs in applications ranging from next-generation plug-in hybrid electric vehicles and modern consumer electronics to micro- and nano-electro-mechanical systems, recent research and development has focused on new electrode materials for advanced energy storage devices[49–55]. Various power storage devices such as supercapacitors, also known as electrochemical capacitors, have attracted great interest due to a number of desirable properties, including fast charging and discharging, long cycle life, and the ability to deliver up to ten times more power than conventional batteries[56–60]. Additionally, these capacitors play an important role in complementing fuel cells in future all-electric vehicles based on clean and renewable energy media[61]. Three major types of materials are well established for the application in supercapacitors: carbonaceous materials, metal oxides/hydroxides, and conducting polymers[62]. Carbon-based materials store charge electrostatically from the reversible adsorption of ions onto their surfaces, leading to high power delivery at the cost of low energy density. By contrast, metal oxides/hydroxides and conducting polymers store charge in a faradic or redox-type process similar to batteries. To improve the performance of these materials, attempts at novel electrode design by confining there size are being made. Materials presenting high pseudocapacitence (metal oxides) are incorporated directly into highly conductive nanostructured carbons (carbon nanotubes,[63,64] mesoporous carbons,[65] carbon aerogels,[66] graphene,[67] etc.) or conducting polymers,[68] with the component contacts either at the nanoscale or microscale. By combining unique properties of individual constituents, improved performance has been demonstrated in such an electrode. Some effort has also been directed at the search for hybrid pseudocapacitive materials such as mixed metal oxides and binary metal oxide/ hydroxides. Due to the lack of well-defined micro-/nanostructures, electrochemical performance for this kind of electrode material has been largely unsatisfactory and the possible synergistic effect between individual constituents has so far not been well understood. A key challenge in this direction is to build an integrated smart architecture, in which structural features and electrical activities of each component are fully manifested, the interface/chemical distributions are homogeneous at the nanoscale and a fast ion and electron transfer is guaranteed.

1.3.2 Nanomaterials for field emission

Field emission (FE), a quantum mechanical tunneling phenomenon is of great interest, due to its application in devices such as microwave device, x-ray source etc.[69,70] One dimensional (1D) materials such as nanotubes, rods, wires and needles are having high aspect ratio that provide local electric field enhancement[71] which is a favorable condition for FE. Similarly two dimensional (2D) materials such as nanosheets, wells, plates have novel and unique physical and chemical properties[72]. High surface area to volume ratio with nanoscale thickness makes them suitable for a given applications by exploiting the appropriate property of the NSs[73]. Nanosheets, another 2D materials, can get arranged like flower petals (nanopetals) [74]. If these NSs (wires or petals) are well aligned, very good FE is theoretically possible irrespective of the material however, the FE efficiency and ease with which FE can take place may vary and makes a topic of research as has been investigated covering a variety of materials in their different nano forms[75]. Carbon, in the form of nanotubes and nanoflakes, has been established as a landmark material for field emission[76–81]. In-spite of being one of the well-studied systems, carbon NSs based FE devices are not available commercially[77]. This has forced scientists to start quest for another material that are good field emitters, parallely, if not as an alternative to the carbon based field emitters. Nickel based materials[82] and different oxides[83,84] are amongst materials which have been studied in search for good field emitting materials other than elemental nanomaterials like carbon[81] and silicon[71].

1.3.3 Nanomaterials based sensors

Electrochemical methods have often been used for sensor analysis of liquid samples, relying on the direct transformation of an electrical signal into the target analyte concentration, based on known theoretical principles of electrode processes. Unlike other transduction mechanisms, which usually consider the homogeneous solution, the electrochemical processes occur at the electrode−solution surface. Two main groups of electrochemical processes can be used for sensor development: potentiometric and volt-amperometric methods. In the first case, no current flows in the electrochemical cell and the electrode potential is measured. In the second case, the interesting phenomenon is the current flowing in the cell due to the oxidation and reduction processes at the electrodes. Both methods require dedicated electronic setups, making use of high input impedance amplifiers.

1.4 Objectives

Main objectives of the presented work are as follows

- Develop the understanding on electrochemical approach towards device fabrication and understanding device operation mechanism.
- Understanding parameters involved in fabrication of electrochromic device based on organic as well as inorganic materials.
- Explore the possibility of nanostructures of organic and inorganic material, which can be incorporated in the device for better performance of an electrochromic device.
- Understanding the growth mechanism of various nanostructures involving hydrothermal and electrodeposition methods along with high temperature and pressure treatment so that the electrochromic device parameters can be optimized.

- Incorporation of these nanostructures in the electrochromic device and observe its effect on overall efficiency and various other device parameters.
- Explore the possibilities, beyond electrochromism, for application of the prepared nanostructures in other areas like field emission display, energy storage and sensing.

1.5 Organization of the thesis

All the research work carried out during the Ph.D. has been reported chapter-wise as follows:

- **Chapter 1 (Current chapter)** Gives the introduction of the relevant topics related to the thesis work and defines the objective of the thesis
- **Chapter 2** Deals with the details of experimental methodology used for the experimental work carried out in the thesis along with details of various experimental parameters and procedures followed for the fabrication of the nanostructures and devices. It also summarizes various equipments used for various measurements carried out during the research work.
- **Chapter 3** Presents the work related to electrochromic device prepared using organic compounds including their nanostructures. Different parameters of the device such as color contrast ratio, cyclability, coloration efficiency, device fabrication steps and optical density modulation are discussed in detail.
- **Chapter 4:** Deals with pure inorganic material based special kind of nanostructures used in electrochromism.
- **Chapter 5:** Discusses the study of combined from of organic and inorganic materials' nanostructures and their performance in electrochromism.

- **Chapter 6:** Discusses various other applications beyond electrochromism of the prepared nanostructures. It includes energy storage, field emission and glucose sensing.
- **Chapter 7:** Summarizes all the conclusions drawn based on research work reported above. This also includes future works available to be explored along with the current challenges with of electrochromic commercial applications.

Chapter 2

Experimental Details

This chapter provides information about synthesis of samples, studied for the thesis work, and techniques used for their characterization. Details of the instruments used for the characterization from microscopy to spectroscopy like FESEM, HRTEM, AFM, optical Microscope and UV-Vis, Raman, PL, XRD, XPS spectroscopy etc. have been provided. Information about the electrochemical workstation (galvanostat) involved for the characterization and their various techniques such as liner sweep voltammetry (LSV), cyclic voltammetry (CV), chronopotentiommetry (CP), and chronoamperometric (CA) has also been provided. Broadly the details have been covered under two categories, microscopy and spectroscopy as will be discussed as follows.

2.1. Microscopic techniques

2.1.1 Field emission scanning electron microscope (FESEM)

Morphological study of samples can be done very precisely by FESEM. In FESEM the electrons interact with the specimen atoms and produce signals containing information about sample's surface, topography, morphology, composition and other properties.

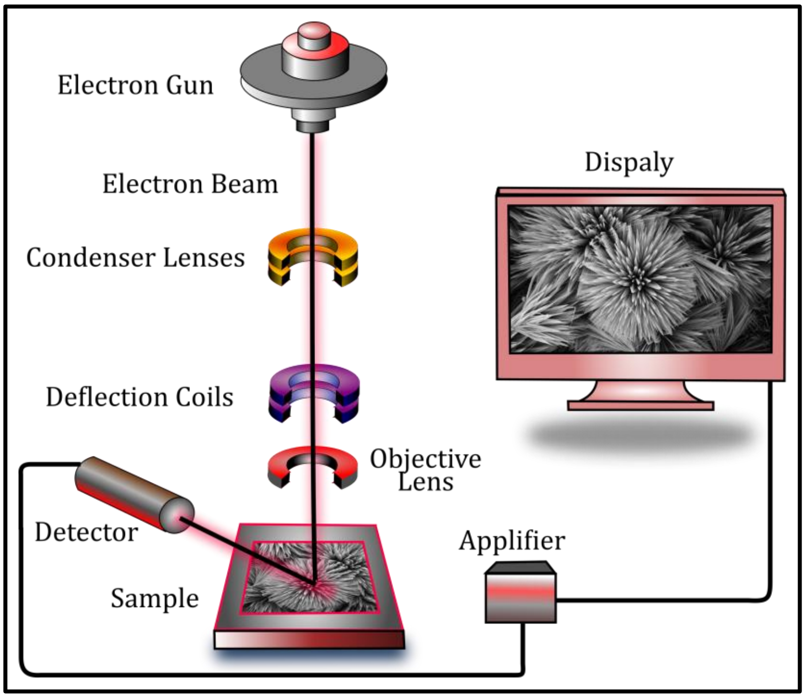

Figure: 2.1 Schematic illustration of scanning electron microscope.

During the interaction electrons, it leads to emission of secondary electrons (SEs), backscattered electrons (BSEs), auger electrons, X-rays, etc. In FESEM, (i) SEs and (ii) BSEs used for the generation of images. When incident electron beam enters the specimen, secondary electrons are produced from the emission of the valence electrons of the constituent atoms of specimen. Due to lower energy of secondary electrons (energy<50 eV), are extremely abundant and yield (the number emitted per primary electron) is dependent on the accelerating voltage. Where backscattered electrons (energy>50 eV) are generated by elastic scattering and yield depends on atomic number Z, so information from a relatively deep region is contained in the back scattered electrons. The back scattered electrons are sensitive to the composition of the specimen. This feature can be used to observe the topography of the surface. Along with SEs & BSEs there are X-rays also emitted having energies correspond to the energy difference between the outer and inner shell electrons.

2.1.1.1 Electron gun: Mostly tungsten or combination of tungsten with iridium is used for the source of electron by heating the filament. In Field emission electron microscopy, a cold cathode of tungsten with fine tips of nm size is used for the emission of electron at high vacuum (10^{-8} Torr).

2.1.1.2 Condenser lens: Condenser lens used to control the diameter of the electron beam by varying the current. Lesser the current of condenser lens smaller the diameter of the electron beam and vice versa. Where narrow beam has the advantage of high resolution at the same time this have high signal to noise ratio. In case of large beam diameter situation reversed.

2.1.1.3 Deflection coils: The use of the deflection coil is to deflect electron beam to scan the sample. The digital image of the sample on the computer screen is formed through the multiple scan of the beam on the sample. Higher the scanning speed higher will be the noise and lesser the resolution of the image. In case of small region scanning of the sample, it show high-resolution image on constant window size. Deflection coils is made up of upper and lower coils, which prevent the formation of a circular shadow at low magnification

2.1.1.4 Objective lens: This is the lowest portion of the column attached with electron gun. This lens is used to focus on the object from short distance.

2.1.1.5 Detector: Detector use to detect the secondary emission form the object where it records the velocity and angle of the emission (SEs & BSEs) from the surface. This detector combines of the Corona to attract electrons and strike on the florescent screen, which generate photons. A transducer is used to transform this signal to video signal which is amplified, and then send for the display.

2.1.1.6 Display: Display synchronized with the scan movement of the electron beam show the digital picture which reflects the real time structure of the sample. Obtain digital image can be further processed for more some other surface analysis.

Model used: Field emission scanning electron microscope (FESEM, Supra 55 Zeiss) [85].

2.1.2 Transmission electron microscope (TEM)

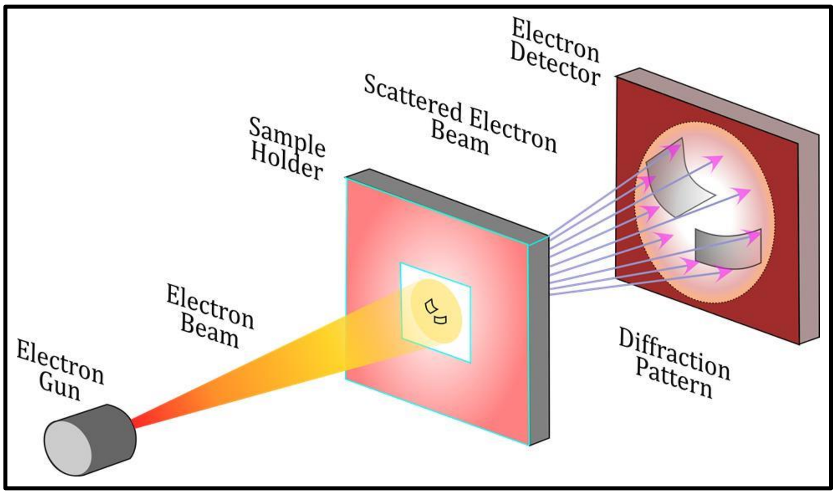

Figure: 2.2 Schematic illustration of transmission electron microscope.

The transmission electron microscope (TEM) operates on the same basic principles as the optical microscope but uses electrons instead of light. In optical microscope wavelength of light is one of the limitation to see the objects. In TEM, electrons beam use as light source and their much lower wavelength makes it possible to get a high resolution thousand times better than optical microscope. Electrons that travel through vacuum in the column of the microscope focus the electrons into a very thin beam using electromagnetic lenses. The electron beam travels through the specimen and depending on its density, some of the electrons are scattered and disappear from the beam. At the bottom of the microscope the unscattered electrons hit a fluorescent screen and form a shadow image of the specimen.

Most of the parts of the TEM are similar to SEM except some.

- TEM uses broad static beam of electrons in comparison with SEM, which uses focused and very fine point beam.
- In SEM, line-by-line scanning is used over the sample surface in a rectangular raster pattern, where in TEM transition of electron beam is required through the sample.
- In SEM, accelerating voltage of election beam is lesser (<50kV) comparatively, whereas in TEM, around 200kV is used to penetrate the sample by the beam.
- There is no restriction of the sample size in SEM but in case of TEM, specimen need be thin, small in size, non-magnetic.

TEM geometry can be divided in to three parts: 1) Electron Gun; 2) Sample Holder; 3) Detector screen. The final image viewed by projection onto a phosphorescent screen, which gives off photons when irradiated by the electron beam. A film camera is located beneath the phosphorescent screen. The screen raised in order to expose a special photographic film with a thicker emulsion layer than light film. An alternative to photographic film is digital capture with a computer digitizing and archiving charge coupled device (CCD) camera. The operator can adjust variable bias, recognition of aberrations, image drift, photography, specimen contrast, resolution, even illumination, and filling the anti-contaminators with liquid nitrogen before using the TEM.

Model used: High-resolution transmission electron microscope (HRTEM 200 KV FEI TECNAI G220 microscope) [86].

2.1.3 Atomic Force Microscope (AFM)

Atomic force microscopy is one of the versatile and powerful microscopies for the analysis of nanostructures. Atomic force microscope is useful not only in the imaging by plotting three-dimensional topography of the nanostructures, but it also provides various types of surface measurements like density of state calculation bandgap calculation and I-V measurement at the atomic level. It is capable of generating images at angstrom scale resolution with height information, with minimum sample preparation efforts.

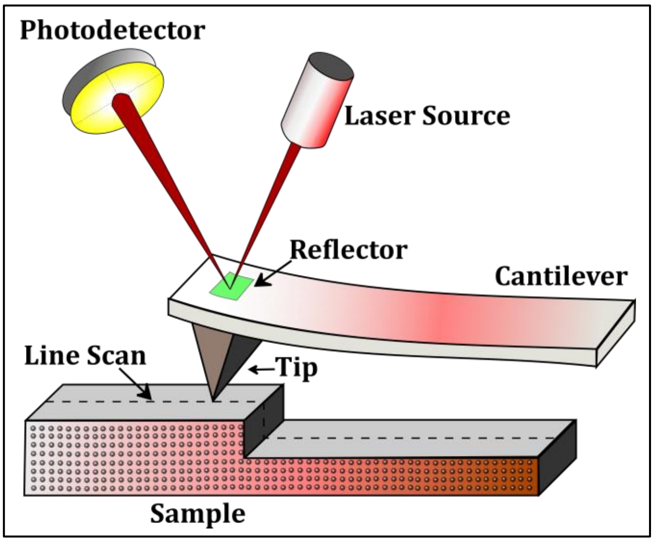

Figure: 2.3 Schematic illustration of atomic force microscopy

2.1.3.1 Principle: Morphological analysis of any material can be done using AFM by scanning the tip attached cantilever over the surface of the sample. As the tip approaches the surface, the close-range, attractive force between the surface and the tip cause the cantilever to deflect towards the surface. However, as the cantilever is brought even closer to the surface, such that the tip makes contact with it, increasingly repulsive force takes over and causes the cantilever to deflect away from the surface.

2.1.3.2 Detection: A laser beam used to detect cantilever movement towards or away from the surface. By reflecting an incident beam from the flat top of the cantilever, can detect slight changes in cantilever make larger change in the direction of the reflected beam. A position-sensitive photo diode (PSPD) used to track these changes. Thus, tip passes over a raised surface feature by the deflection of cantilever causes subsequent change in direction of reflected beam, recorded by the PSPD.

2.1.3.3 Imaging: Imaging is one of the important part in AFM microscopy. AFM images the topography of a sample surface by scanning the cantilever over a region of interest. The raised and lowered features on the sample surface influence the deflection of the cantilever, which is monitored by the PSPD. By using a feedback loop to control the height of the tip above the surface thus maintaining constant laser position the AFM can generate an accurate topographic map of the surface features.

Model used: Atomic Force Microscope (AFM Bruker Multi-Mode 8-HR) [87].

2.1.4 Optical microscope

In optical microscope, visible light employed to closely view a sample through the magnifying lens arrangement. An optical microscope, also sometimes known as a light microscope, it uses series of lenses to magnify and focus visible light to enlarge the specimen. The lenses are placed between the sample and the viewer’s eye to magnify the image so that it can be examined in detail.

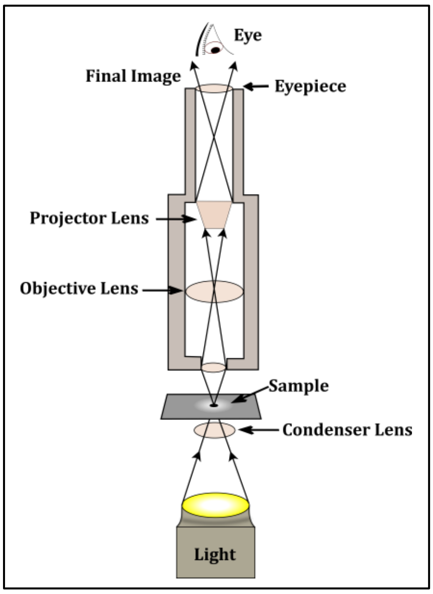

Figure: 2.4 Schematic illustration of optical microscope.

2.1.4.1 Eyepiece: Eyepiece or ocular lens is a cylinder containing two or more lenses; its function is to bring the image into focus for the eye. The eyepiece is inserted into the top end of the body tube.

2.1.4.2 Objective: Objective (optics) lens used at the lower end of a typical compound optical microscope, there are one or more objective lenses that collect light from the sample. The objective is usually in a cylinder housing containing a glass single or multi-element compound lens.

2.1.4.3 Condenser: The condenser is a lens designed to focus light from the illumination source onto the sample. The condenser may also include other features, such as a diaphragm and/or filters, to manage the quality and intensity of the illumination.

2.1.4.4 Light Source: Most microscopes, however, have their own adjustable and controllable light source – often a halogen lamp, although illumination using LEDs and lasers are becoming a more common provision.

Model used: Optical Microscope (Radical Model RXL-4T) [88].

2.2. Spectroscopies

2.2.1 Raman spectroscopy

To understand the inelastic scattering using monochromatic light source often near IR, visible or UV range is known as Raman effect. It describes the excitation of photons to virtual energy states and the resultant loss (stokes) and gain (anti-stokes) of energy that occurs because of the interaction of light with vibrational modes associated with chemical bonds within the sample.

2.2.1.1 Source: The selection of excitation source depends upon the suitability of the specimen, sensitivity and resolution required. Wavelength and spot size are the main parameters to choose the type of laser. When choosing a laser source, it is also important to consider whether the experiment requires the use of pulsed rather than continuous-wave lasers. For example, a pulsed laser would be required in a stimulated Raman spectroscopy system, as the more intense electric field strength of the laser pulse energy can contribute to the increased frequency of Raman scattering events. The line width of the laser is also an important consideration, as it has a direct influence on the spectral resolution, regardless of spectrometer configuration. Laser wavelength is critical during the experiment design, fluorescence contribution in Raman spectrum can be avoided by exciting the sample with a wavelength that falls outside its profile.

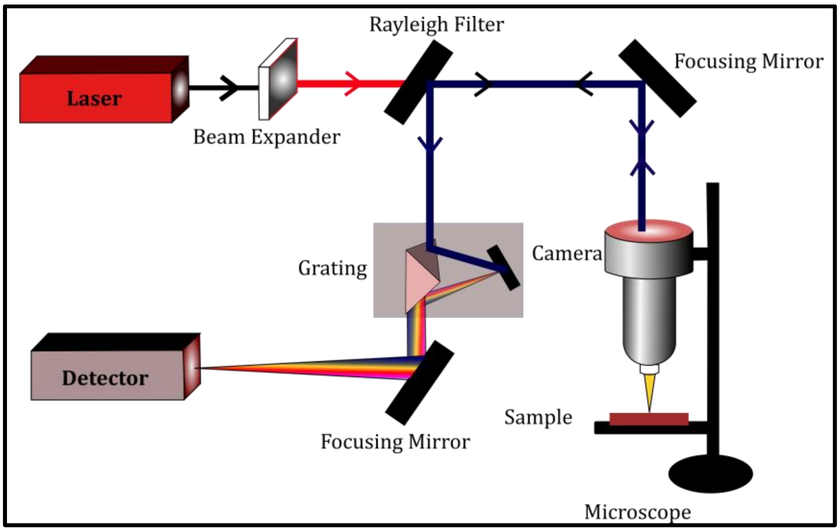

Figure: 2.5 Schematic illustration of Raman spectroscopy

2.2.1.2 Rayleigh filter: To optically filter Rayleigh scattering which is more intense than the Raman scattering a monochromator is used. Rayleigh filters must be selected for the specific wavelength of the laser.

2.2.1.3 Microscope: Microscope is one of the important as well as crucial parts in the micro- Raman spectroscopy. The objective lens throughput depends on its magnification and numerical aperture (NA). Objective lens having high-magnification and high NA value provides higher resolution, with shorter working distance compatible to thin samples where low-magnification/ moderate-NA provide lower resolution, with longer working distance suited for bulky sample.

2.2.1.4 Detector: Detector of Raman spectroscopy must be very sensitive which is capable to sense the molecular structure of the molecule with weak scattering. Charge-coupled devices (CCDs) integrated detector is generally used in the Raman spectroscopy due to its high quantum efficiency and less signal to noise ratio. Where CCDs are composed of thousands of pixels, which are connected to multichannel array can collect charge from scattered photons. The collected charge is directly proportional to the intensity of Raman scattering.

2.2.1.5 Gratings: Diffraction grating are used for the dispersion of the Raman scattered light. Gratings are generally used with Rayleigh filters, which differ by the number of grooves (per mm) or lines (per mm) on the surface. Higher the groove frequency higher the spectral resolution at the cost of reduced spectral intensity and range.

Model used: Raman spectrophotometer (Horiba Jobin Yvon LabRAM HR) [89].

2.2.2 UV-Vis spectroscopy

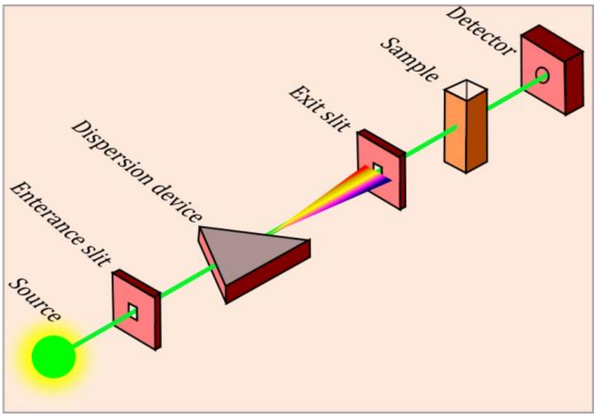

Figure: 2.6 Schematic block diagram of UV-Vis spectroscopy.

Xenon lamp is used as the source of white light in the system. Here in this set up dispersion device is used to disperse white light into multiple wavelength which pass through the exit slit works as grating to select monochromatic wavelength. Beam coming out of the grating slit splits in two parts, one is taken as reference and other one goes on to the sample. At last output is compared with the reference beam and data gets collected. Since output photons comes through scattering from the samples so there is an integrating sphere detector.

Model used: Spectrophotometer (Agilent Cary 60) [90].

2.2.3 X-ray diffraction (XRD)

X–rays diffraction (XRD) is one of the most suitable and reliable tool to probe the structure of a material as the wavelength of X-rays (it is of the order of Å) is comparable to the interatomic distances. The non-destructiveness is an additional advantage of XRD method. In XRD, an X-ray falls on the material at some incidence angle, gets diffracted through different set of atomic planes present in the crystal structure.

2.2.3.1 X-ray source: X-rays are generated in a cathode ray tube by heating a filament to produce electrons, accelerating the electrons toward a target by applying a voltage, and bombarding the target material with electrons produce X-ray spectra. These spectra consist of several components, the most common being K_α and K_β, where K_α again subclassified into $K_{\alpha 1}$ and $K_{\alpha 2}$. Copper is the most common target material for single-crystal diffraction, with Cu-K_α radiation = 1.5418Å.

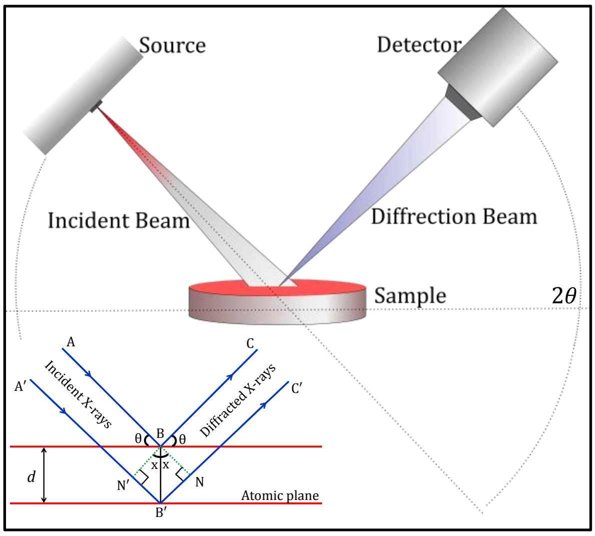

Figure: 2.7 Schematic illustration of X-ray diffractometer.

2.2.3.2 X-ray detector: The position of the detector and sample is placed in such a manner it satisfies the Bragg's Equation. The geometry of an X-ray diffractometer is such that the sample rotates in the path of the collimated X-ray beam at an angle θ while the X-ray detector is mounted on an arm to collect the diffracted X-rays and rotates at an angle of 2θ. A detector records and processes this X-ray signal and converts the signal to a count rate which is then output to a computer device. The instrument used to maintain the angle and rotate the sample is termed a goniometer. For typical powder patterns, data is collected at 2θ from ~5° to 70°, angles that are preset in the X-ray scan.

Model used: X-ray diffraction (Rigaku SmartLab X-ray diffractometer using monochromatic Cu-Kα radiation λ= 1.54 Å) [91].

2.2.4 X-ray photoelectron spectroscopy (XPS)

XPS is a spectroscopic technique used to measure surface elemental composition, chemical state and electronic state of the elements present in the specimen.

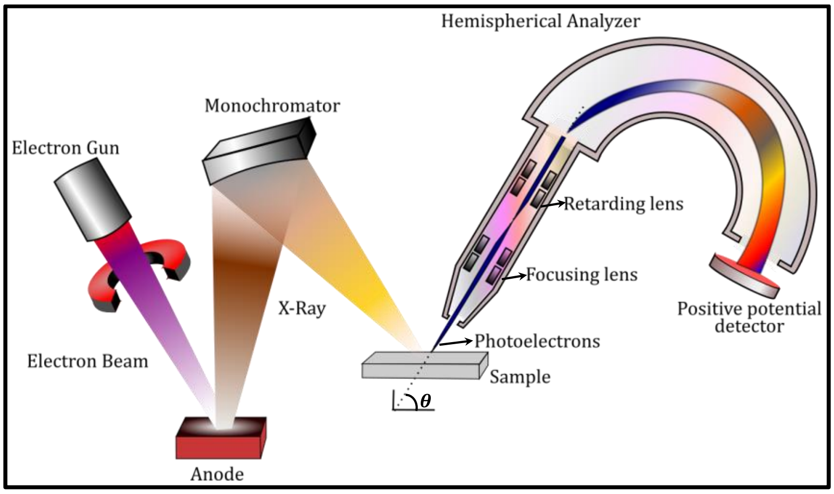

Figure: 2.8 Schematic illustration of X-ray photospectroscopy.

2.2.4.1 Electron gun: The said XPS system is equipped with Al Kα (1486.6 eV) X-ray source. Prior to XPS measurements the surface of the sample was properly cleaned using in built argon ion sputtering gun. Working pressure of 5 x 10^{-9} Torr, the pass energy

~20 eV and the dwell period 0.1 sec maintained. The energy resolution of the XPS system is 0.85 eV. Any ionizing radiation causes Auger-electron emission, because an Auger transition is possible after an atom is ionized in an inner shell. Heavy particle bombardment has been used to excite Auger electrons. Electron guns have the advantages of easy construction and maintenance, high beam intensity, and capability of focusing and x–y deflection. High spatial-resolution <10 nm is obtained by instruments with a field emission cathode and an elaborate electron beam column. Because a focused electron beam of high energy impinging on anode metal surface creates characteristic X-rays, it is often use as point source for spatially resolved XPS.

2.2.4.2 Anode: The most common anode metals used for X-ray generation are Mg and Al, often as a twin anode for alternative use. The characteristic Mg K’ radiation at 1253.6 eV and the Al K ’ radiation at 1486.6 eV possess sufficiently high energies for core level excitation as well as a sufficiently low line width (below 1 eV) to yield XPS spectra with fairly good resolution. For efficient irradiation, usual sources are operated from 500 W to 1 kW power, at 5–15 keV anode voltage.

2.2.4.3 Monochromator: Monochromator is used for better energy resolution and removal of the Bremsstrahlung background with satellite peaks. Monochromator, which selects a narrow line from the natural emission are made of usually a bent quartz crystal or several pieces of them.

2.2.4.4 Hemispherical analyzer: The concentric hemispherical analyzer used due to its superior energy resolution and areal transmission properties consists of two concentric hemispheres. The outer sphere is put on a negative potential against the inner hemisphere, and the mean radius describes an equipotential plane that connects entrance and exit slits. For an electron with some energy traveling from entrance to exit, the condition has to be fulfilled. Concentric hemispherical analyzers have an input lens that defines the analyzed area. Useful compromise between large transmission and high resolution is possible by a higher aperture angle. The main purpose of the input lens is retardation of the electrons to reduce their energy before they enter the analyzer. This reduced (and constant) energy is called the pass energy. Lower pass energy means a lower absolute energy resolution. Thus, angle-resolved XPS is possible without tilting the sample.

2.2.4.5 Positive potential detector: The hemispherical analyzer is energy dispersive systems, which can used simultaneously to detect electrons arriving at different locations in the dispersion plane. Therefore, parallel multichannel detection of a certain energy range (usually about 10% of the pass energy) enabled in the detector. In some XPS system in a variety of ways, for example, by using a channel plate for amplifying the electron current, resistive plate as a position-sensitive and phosphorescence screen used for the mapping.

Model used: X-ray Photoelectron Spectrometer (ESCA System, SPECS GmbH, Germany with Al-K$_\alpha$ radiation 1486.6 eV) [92].

2.3 Electrochemistry

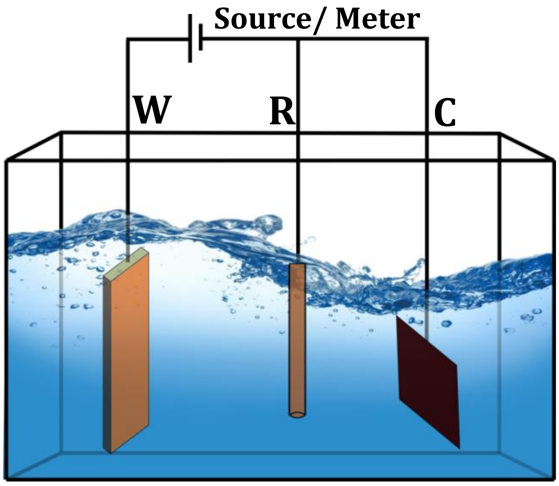

Figure: 2.9 Schematic illustration of electrochemical cell.

An electrochemical cell is an instrument that produces an electric current from energy released by a spontaneous redox reaction. Electrochemical cells have two conductive electrodes (the anode and the cathode). The anode is defined as the electrode where oxidation occurs and the cathode is the electrode where the reduction takes place. In between these electrodes is the electrolyte, which contains ions that can freely move. Along with the mentioned two electrodes there is one more reference electrode use to check accurate potential on the working electrode.

2.3.1 Liner sweep voltammetry

In linear sweep voltammetry (LSV) a fixed potential range is employed much like potential step measurements. However in LSV the voltage is scanned from a lower limit to an upper limit as ramp signal with some given scan rate (V/second).

2.3.2 Cyclic voltammetry

The potential of the working electrode is measured against a reference electrode which maintains a constant potential, and the resulting applied potential produces an excitation signal. Cyclic voltammetry (CV) is very similar to LSV. In this case the voltage is swept between two values (V_1 and V_2) at a fixed rate, however now when the voltage reaches V_2 the scan is reversed and the voltage is swept back to V_1. In the forward scan potential first scans negatively, starting from a greater potential V_1 and ending at a lower potential V_2, The potential extreme V_2 is call the switching potential, and point where the voltage is sufficient enough to have caused an oxidation or reduction of an analyte. The reverse scan occurs from V_2 to V_1, and is where the potential scans positively. It is important to note that some analytes undergo oxidation first, in which case the potential would first scan positively. This cycle can be repeated, and the scan rate can be varied. The slope of the excitation signal gives the scan rate used.

2.3.3 Chronopotentiommetry

Galvanostat uses a three electrode configuration, in which a current is applied between the auxiliary and working electrodes, and the potential of the working electrode (measured with respect to the reference electrode) is monitored. The basis of controlled current experiments is that a redox (electron transfer) reaction occurs at the surface of the working electrode in order to support the applied current. Common applications of the galvanostat include constant current stripping potentiometry and applications. One advantage of all constant current techniques is that the ohmic drop due to solution resistance is also constant, as it is equal to the product of the current and the solution resistance.

2.3.4 Chronoamperometry

Chronoamperometry is used to study the kinetics of chemical reactions, diffusion processes, and adsorption. In this technique, a potential step is applied to the electrode and the resulting current vs. time is observed.

Model used: Electrochemical workstation (Keithley 2450-EC) [93].

2.4 Experimental set-ups used for material/device characterization

To track molecular changes within the device two spectroscopic technique used with some special arrangements in the sample holder.

2.4.1 In-situ UV-Vis spectroscopy

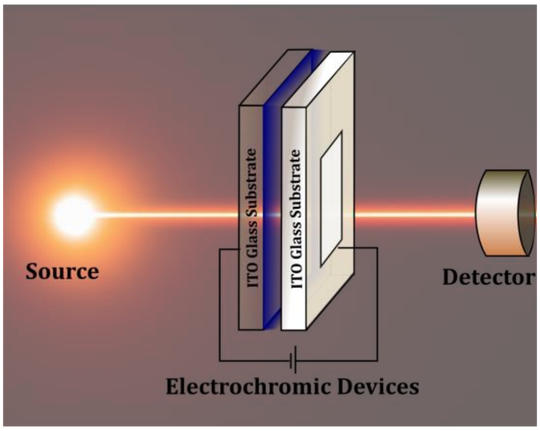

Figure: 2.10 Set-up for carrying out in-situ UV-Vis spectroscopy of the electrochromic device.

2.4.2 In-situ spectroelectrochemistry

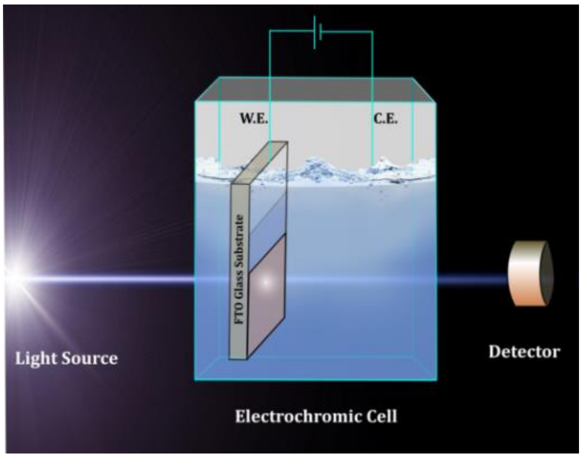

Figure: 2.11 Electrochemical cell set-up for carrying out in-situ UV-Vis spectroscopy.

2.5 Synthesis techniques and recipe

2.5.1 Ethyl viologen (EV) + Poly ethylene oxide (PEO) Gel Preparation

Commercially available chemicals from Alfa Aesar and Sigma Aldrich were used. Polyethylene oxide (PEO, Alfa Aesar, MW = 100 000), Ethyl viologen diperchlorate (98%, Sigma Aldrich), Sodium borohydride ($NaBH_4$, Alfa Aesar), and Acetonitrile (ACN, anhydrous, 99.8%, Sigma Aldrich) were used as received. Gel used in fabrication of electrochromic devices was prepared in the solution form by mixing 4 wt. % ethyl viologen diperchlorate [$EV(ClO_4)_2$] in acetonitrile and 5 wt. % PEO in acetonitrile. The PEO solution was filtered through a 0.45 μm PTFE filter before adding the viologen solution.

2.5.2 Device geometries used

Open face geometry (OFG) device prepared by spin coating method initially 3μl gel (PEO+EV) dropped in-between E_1 & E_2 gold electrodes and then spin the device upto 2000 rpm for 1 second. By spinning the device it uniform and dry the film present on the electrodes. Cross bar geometry (CBG) device has been fabricated by placing a film of gel (EV+PEO) between two transparent conducting ITO electrodes. The gel film was deposited on an ITO substrate using spin coating. After spin coating, second ITO electrode was laminated face to face on the spin coated substrate. The extreme part of both the electrodes was painted by silver glue for making connection with external power supply.

2.5.3 Graphene nanoflakes preparation

Graphene oxide has been synthesized from natural graphite powder by the modified Hummers method[94]. Before going for GO preparation, an extra step of preoxidation of graphite powder was performed. The 2g graphite powder was put into 75 °C solution of 8 mL concentrated H_2SO_4, 3g of $K_2S_2O_8$, and 3g of P_2O_5. The resultant precipitate in the solution was allowed to cool to room temperature over a period of 10 hours. The solution was then carefully diluted with distilled water, filtered, and washed until the rinse water became neutral. The product was dried at ambient temperature over 24 hours. This preoxidized graphite was then put into cold (0°C) concentrated H_2SO_4 (45mL). $NaNO_3$ (1g) was added. $KMnO_4$ (6g) was added successively with continues stirring while maintaining mixture temperature below 12 °C for next 1 hour. The mixture stirred at room temperature for 6 h and left for overnight. DI water around 90 mL was added to the mixture which improves temperature to 75°C, wait for 15 min, then end the reaction by adding large amount of DI water (300 mL) and 30% H_2O_2 solution (5 mL), within few second color of the mixture changed into light yellowish. Finally the mixture was filtered and swilled with DI water.

2.5.4 EV+ GNFs+ Tetrathiafulvalene (TTF) gel preparation

Polyethylene oxide (PEO, MW = 100,000) and ethyl viologen diperchlorate (EV) were purchased from Sigma-Aldrich and used as received. GNFs were prepared by the above mention revised hummer method. Step-wise recipe to prepare the EC-Gel is as follows from step 1 to 6 in the device fabrication section.

2.5.5 Electrode/electrochromic-gel/electrode fabrication

Step 1: Prepare solution of 4wt% EV diperchlorate in acetonitrile: solution A (say)

Step 2: Prepare solution of 3wt% TTF in acetonitrile: solution B (say)

Step 3: Prepare solution of 5wt% PEO in acetonitrile: solution C (say)

Step 4: Prepare GNFs powder as per details given sample preparation section.

Step 5: 5 ml of solution A + 3 ml of solution B + 5 ml of solution C + 0.06 mg of GNFs powder (designated "electrolyte"): Solution D (say)

Step 6: Solution D mixed properly using vortex for 10 minutes.

Step 7: Filter solution after *step 6* through a 0.75 μm PTFE filter: Solution E (say).

Step 8: Affix a transparent double-sided tape, pattern with desired text, on an FTO coated glass.

Step 9: Spin coat solution E with 1000 rpm for 120 sec on substrate prepared in *step 8*.

Step 10: Stack second FTO coated glass on to the film coated substrate prepared in *step 9*. The double-sided tape, used in *step 8*, will keep the two FTO coated substrates attached with each other with EC-Gel (solution E) layer sandwiched as patterned on the tape. The two FTO coated glass allows the biasing of the device.

2.5.6 Synthesis of single crystalline - TiO_2 nanorod array

Single-crystalline TiO_2 nanorods were grown on the FTO coated glass substrate using hydrothermal method with some modifications in previous reports[95]. 15 ml concentrated HCl, diluted in equal volume of deionized water, was stirred at room temperature for 10 min followed by addition of 400 μl of titanium n-butoxide (used as received from Sigma Aldrich). After stirring the resultant solution for another 10-12 min, it was transferred to a teflon-lined stainless steel autoclave of volume 50 ml. FTO coated glass substrate of size 1 × 2 cm^2, cleaned with the solution of acetone, methanol, IPA and DI water, were placed inside using an appropriate arrangement with conducting side facing towards the bottom of autoclave. The hydrothermal process was carried out at 150°C for 9h in an electric oven and then was allowed to cool down to room temperature under normal conditions. After washing properly with DI water and drying in ambient air, a TiO_2 nanorods array film was uniformly grown on the FTO glass substrate.

2.5.7 Synthesis of TiO_2/Co_3O_4-Core/Shell nanorod array

Co_3O_4 shell over TiO_2 core nanorod array were synthesized by the electrodeposition methods[96]. Self-sustainable TiO_2 nanorod array fabricated on FTO substrate, grown in the above step, was used as the working electrodes provide the scaffolding for the Co_3O_4 nanostructures facile electrodeposition. Electrolyte for electrodeposition was prepared by dissolving 0.81 g $Co(NO_3)_2$ into 10 ml DI water. The electrodeposition of Co_3O_4 was carried out using three electrodes chemical cell with Ag/AgCl as reference and Pt foil was used as the counter electrode. Chronopotentiommetry technique was used at the constant current of -0.3mA, for the deposition. During the deposition, constant current was maintained for 5 minutes. Finally, the samples were washed with distilled water and annealed for two hours at 200^0C inside an electric oven.

2.5.8 Synthesis of NiO nanopetals

In the synthesis of nickel oxide nanopetals, nickel nitrate used with potassium persulfate as oxidizing agent and small amount of ammonium solution to prepare precursor solution. For this, 0.3g of $Ni(NO_3)_2$ along with 0.05g of $K_2S_2O_8$ in 35ml of DI water mixed my magnetic stirrer for 15 minutes in between add 1.2ml of NH_4OH prepared solution placed inside the Teflon line autoclave. After placing hydrothermal reactor into the electric oven for five hours at the temperature of 150°C it is cooled down to environmental condition. Deposited film on FTO electrode was later rinsed with deionized water and dried in air with nitrogen gun. After cleaning, the NiO-NPs film was annealed at 250°C for three hours, results in uniform and well aligned NPs array on FTO coated glass.

2.5.9 Synthesis of NiO nanopetals/PANI nanohemispheres core-shell

NiO-NPs deposited in previous section on FTO substrate used as electrode for the electropolymerization of aniline. Galvanostat used with three-electrode electrochemical system for electropolymerization of aniline. The NiO-NPs deposited FTO electrode used as the working electrode with Pt-wire & Hg/HgCl as counter & reference electrodes respectively. Electrolytic solution was prepared with 0.182ml of aniline in 20ml of DI water with 1ml of perchloric acid. Before applying 0.01 mA of constant current for 1 hour for the polymerization of aniline, five 10 seconds pulses of 0.1 mA was applied to prepare the hemispherical shaped nanostructures. After the polymerization, working electrode taken out from the electrolyte solution, washed with ultrapure water, dried under the atmospheric condition to obtain the finished electrode for various characterization and later to be used in electrochromic device. The whole process has been summarized as a schematic representation in Figure 1 which also shows how NHs of PANI shell cover a NP of NiO to result in a typical morphology of core-shell hybrid nanostructures.

2.5.10 NiO/PANI- core/shell NSs based device fabrication

Step 1: Cleaned, by ultrasonication, FTO electrode of size (2x1 cm^2) patterned by double-sided tape.

Step 2: In this step, hydrothermal method is used to grow NiO-NSs of previous step fabricated electrode.

Step 3: Electrode of *step 2* is used for the electro-polymerization of aniline.

Step 4: Second layer of double-sided tape is peeled-off from the electrode fabricated in *step 3*.

Step 5: Finally second transparent electrode stack on the working electrode made in *step 4*.

Step 6: This is final step, which is about the operational state of the device.

2.6 Various software, involved during the characterizations

- Atomic Force Microscope high resolution nanostructures analysis by using "WSxM" software [97].
- SEM images analysis by ''Image J" software [98].
- XPS spectra were fitted with "XPSPEAK41" software [99].
- Schematics drawing prepared by MS-office "Visio" software [100].

Chapter 3

Electrochromic Devices Based on Organic Materials

In this, chapter two types of organic electrochromic device has been discussed where first one is very simple with ethyl viologen (EV) alone used as electrochromic active material. In an attempt to understand the color switching mechanism of organic electrochromic devices, live spectroscopy of a viologen based device has been carried out. Role of redox reactions taking place at the electrode/electrolyte interface have been identified using Raman and UV-Vis spectroscopies and both are carried out during the device operation. In-situ Raman and transmission/absorption studies establish the origin of bias induced color change, between a transparent and navy blue color, in this simplest electrochromic device.[4,5] The second, an improved version of the previous one, device has been fabricated by composing graphene nanoflakes (GNFs) and Tetrathiafulvalene (TTF) as redox supporting agent along with EV in the form of a gel. Device composed of this (EV-GNFs-TTF) gel demonstrates faster and efficient electrochromism. Redox activity of EV-TTF pair result in such a fast bias induced color switching. Besides acting as an electrolyte, GNFs also facilitates achieving faster bleaching time by allowing reversing the redox process quickly.[6] Both of these devices will be discussed separately in detail in the following sections.

---

[4] *Mishra et al.,* **Optical Materials**,(2017), 66, 65-71

[5] *Mishra et al.,* **Solid State Comm.**,(2017), 266, 17-20

[6] *Mishra et al.,* **J. Mater. chem. C**,(2017), 5, 9504-9512

3.1 The basic electrochromic device (ITO/EV/ITO)

Electrochromic effects are observed as a result of redox processes either in the form of a solid-state device or in an electrochemical cell[25–27,30]. Origin of this property lies in the fact that many materials show multiple redox states with different optical properties (e.g. absorption/transmittance). One particularly intriguing class of materials in this context is bipyridinium species,[27] which are formed upon N,N-diquaternization of 4,4′-bipyridine, also known as viologens. Scheme 1 shows the molecular structures of ethyl viologen.

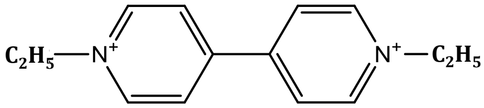

Scheme 1: Ethyl Viologen molecule

Viologen, a known herbicide, is an organic compound having potential application in flexible electrochromic devices due to its activity in reversible redox reaction and excellent electron accepting nature. In other words, viologens, are reducible materials used in solid-state electrochromic devices, which may undergo one- or two-electron reductions[101–104]. Ease of processing and have stimulated intensive research into the electrochromic properties of viologens. The current research has been undertaken to better understand viologen's electrochromism and to simplify the device design for realization of a solid-state electrochromic device as well as understanding it's operation mechanism.

Controlling the often complex stoichiometry of metal oxides, another class of electrochromic materials, is a complication when fabricating electrochromic devices based on these materials[105,106]. In addition, many metal oxides lack sufficient transparency for use in a wide range of applications. In contrast, viologen based materials are solution processable and flexible electrochromic devices can be made. In order to achieve an electrochromic response in the solid state, a matrix to allow ionically conduction is required along with redox counter-reaction. Lithium perchlorate in polyethylene oxide (PEO) has been used successfully as a solid electrolyte for organic electronics in general and thin film transistors in particular[107–112]. Ethyl viologen in PEO matrix can be a good choice for making viologen based electrochromic devices for testing purposes. Thus, ethyl viologen diperchlorate ($EV(ClO_4)_2$) can be a good candidate because it contains EV^{2+} which is a good electron acceptor and also contains perchlorate ion which itself can act as supporting ion. Its solution in an appropriate solvent is transparent and does not absorb visible light until gets reduced to form radical cationic form $EV^{\bullet+}$ after accepting an electron. In the reduced state it shows absorption peaks at 396 and 606 nm which predicts blue color of the device[113]. Radical cations play an important role in the optical property of any material. Some molecules do not show any absorption in the visible region but it's free radical exhibits higher absorption in this wavelength range[114]. Viologen is one of them which shows absorption in its radical cationic state which makes viologen eligible to be categorized as an electrochromic material[115]. Radical cation of viologen can be obtained by chemical, electrical and optical methods and are sensitive to environment[116]. The advantage with viologen is that it shows reversible switching between both the redox states mentioned above. In other words, $EV^{\bullet+}$ can go back to EV^{2+} by oxidation, which again show no absorption in the visible region and make device transparent (or bleached). A solid state electrochromic device can be made using viologen by appropriately controlling the redox process using an electric bias.

The present section is based on simple electrochromic device fabrication and understanding the device operation mechanism. Two simple geometries of the device have been fabricated (Figure 3.1) to study the fundamental reason of color change using in-situ UV-Vis and Raman spectroscopies without focusing on fabricating an actual working device. In the simplest geometry, the EV (in an appropriate matrix) has been sandwiched between two ITO electrodes on glass substrate to get the device in cross-bar geometry (CBG) (Figure 3.1a 3D representation). Another device have been fabricated by drop casting EV in between two gold electrodes separated by few microns where both the electrodes are on the same plane and can be called open face geometry (OFG) (Figure 3.1b cross-section representation). With the given geometries in place, the bias is applied as per following protocol.

The biasing polarity protocol:

- *Positive potential V means,* E_1 *become positive with respect to* E_2 *electrode.*
- *Negative V means* E_1 *terminal to be negative with respect to* E_2*.*

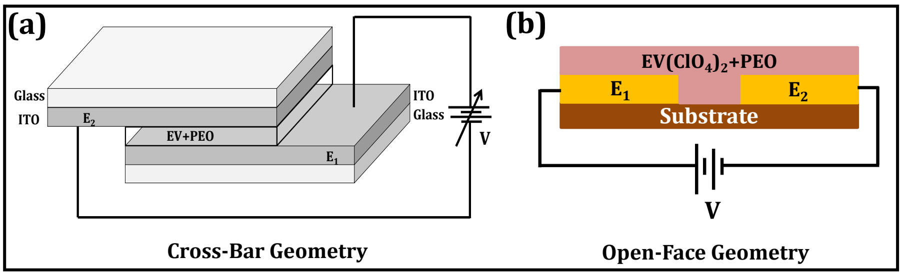

Figure 3.1: (a) Cross-bar geometry (CBG) device and (b) open face geometry (OFG).

OFG device was used for in-situ Raman spectroscopy on specific electrode to check the molecular changes occurring on the application of bias. By Raman spectroscopic experiments on OFG device and result clearly reveals connection between electrochemical doping and Raman peak position as will be discussed below in detail. Both UV-Vis and Raman spectroscopic data reconcile the correlation between charge carriers and color changes in viologen base devices. The free radical cation has been depicted as the fundamental charged species responsible for the color changing properties in ethyl viologen. Appropriate control experiments have been carried out to validate the conclusions. All the synthesis of the gels, material involved and steps followed during the device fabrication has been discussed in detailed manner in chapter 2.

3.1.1 Device mechanism

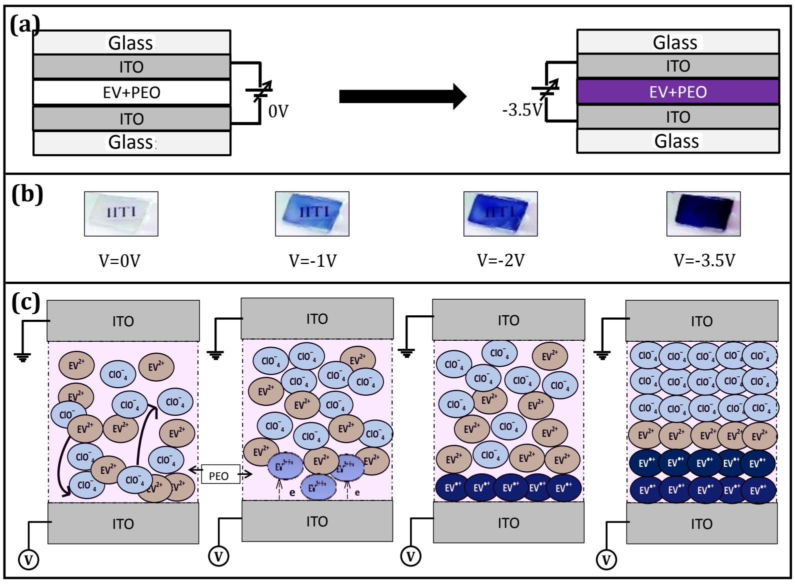

Figure 3.2: (a) Schematic representation of CBG device connecting through the external biasing arrangement (b) Actual photographs of device at different bias, (c) Schematic model of change in redox state of viologen inside the device as a result of applied bias.

Figure 3.2 is the combined schematic presentation of internal and external mechanism of CBG device. Figure 3.2a shows cross sectional schematic view of CBG device with its biasing arrangement. Figure 3.2b shows the corresponding bias dependent actual photographs of CBG device for various applied voltages. Figure 3.2b shows that when external potential is 0 V, device is in its OFF state which corresponds to the transparent state and thus the text ‘IITI’ written below can be seen through the device clearly in Figure 3.2b. The transparency of the complete device reduces and becomes opaque after the application of -3.5 V bias as shown in Figure 3.2b. Color change in viologen is a well reported phenomenon[117] and is often assigned to the different absorption/transmission properties exhibited by viologen species in its different oxidation states. Typical optical properties of chemically reduced viologen show that blue color originates due to the presence of $EV^{\bullet+}$ species which can be obtained by chemically reducing EV^{2+} (present in ethyl viologen diperchlorate) which is transparent. Alternatively, similar redox change can be induced in the material in the form of a solid state device as a result of electrical bias which provides the basis for an electronic electrochromic device. Mechanism responsible for bias induced color change as shown in Figure 3.2b can be understood as follows which is also schematically presented in Figure 3.2c, Initially EV^{2+} and ClO_4^- species (in PEO matrix) are randomly distributed in between the two ITO electrodes in the absence of bias (V=0). When we apply negative potential (V = -1V) on the device, current starts flowing through the device and exchange of electron take place. Electrons are injected from the electrode which is connected with the positive terminal of the battery, first layer of EV^{2+} in the immediate vicinity of electrode start receiving these electrons and get reduced to $EV^{\bullet+}$ which initiates color change. By the formation of $EV^{\bullet+}$, which shows higher absorption of green color, will make the device opaque (ON) for this color window near the interface. As higher voltages are applied more reduction takes place and large number of $EV^{\bullet+}$ gets generated which results in opaque device as soon as a complete interfacial layer of blue species ($EV^{\bullet+}$) line-up along the electrode/electrolyte interface. It is worth mentioning here that without such lineup process it is very difficult to get complete opaque state of the device because finite amount of light will be able to pass through the device if the redox species are randomly distributed inside the device. Movement of perchlorate & EV^{2+} ions, under the influence of bias, help the above-mentioned process to takes place. As a result, complete opaque nature of device is obtained with arrangement of ions in the device as shown in the case of V = -3.5V bias case in Figure 3.2c. Evidence of presence of color centers near the electrodes-electrolyte interface (not necessarily throughout the device) can be seen using Raman spectroscopy as will be discussed later on. The "blue" color visible as a result of bias in Figure 3.2b has only qualitative meaning and needs more scientific approach to identify the presence of different wavelength components in the transmitted light when the device is seen in the visible light. Perceived color by human eye must be cross checked with scientific results (with optical tools) before making any conclusion. To understand the color changing phenomena in CBG device the best suitable technique is UV-Vis spectroscopy. From UV-Vis spectra one can understand the actual wavelength of light which is more affected by the reduction of viologen molecule.

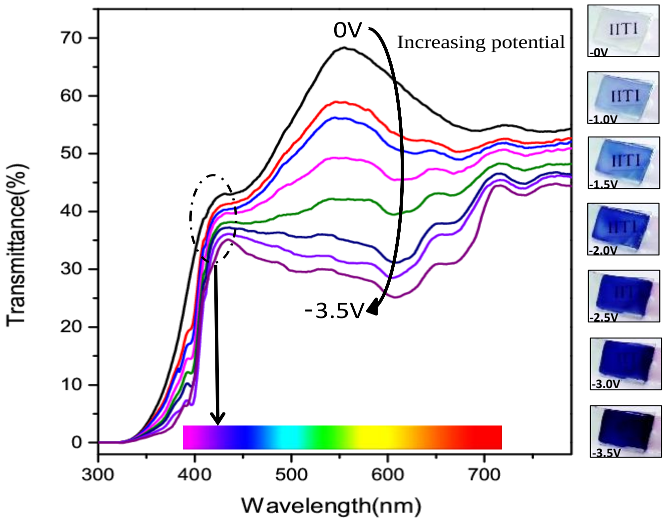

Figure 3.3: In-situ UV-Vis transmittance spectrum of the CBG device with changing bias from 0 to -3.5V. Inset showing color appearance of the device at various potential.

Figure 3.3 shows transmission spectra with respect to change in bias voltage using UV-Vis spectroscopy. The transmission spectrum under zero bias condition has been recorded as reference data, to see any variation in it after bias application. Under no bias condition, only ITO and EV^{2+} (in PEO matrix) species are present and a peak appears around 560 nm. The peak around 560 nm gets suppressed as the biasing potential is increased and finally it changed into a valley shaped curve for a voltage of -3.5 V. It can be noticed from Figure 3.3 that there is not much change in %T at the wavelengths of blue (~425 nm) and red (~725 nm) colors as compared to the wavelengths in between these two. The device exhibited a minimum transmittance in the visible region at around 590 (orange-yellow) nm with a transmittance at -3.5V is ~22 %. As a result, the counter color of orange-yellow, i.e. blue, is observable to the visible eye. This also means that blue color of the device in ON state is not due to the enhancement of blue wavelength but due to suppression of other colors in the visible range in terms of transmittance. We have also tested the effect of electric field on material more of this discussed in Appendix A.1.

It is clearly observed from the transmittance spectrum corresponding to -3.5V that transmission is suppressed in the range of 500 to 700 nm. Also, from the color wheel (Figure 1.4, chapter 1) we can say the counter color of most suppressed color in transmission spectra will be the color of the film[118]. The simple analysis of UV-Vis spectra allows one to understand the origin of the color appearance of the electrochromic device. This also may enable one to understand that transmission (T %) corresponding to a given wavelength may be tuned by appropriately enhancing/suppressing the %T spectra at other wavelengths. Relative %T corresponding to different wavelengths decide the exact color of appearance and can be obtained from 1976 format of CIE (Commission Internationale de l'Eclairge

International Commission on Illumination) color calculator (Osram Sylvania) [119].

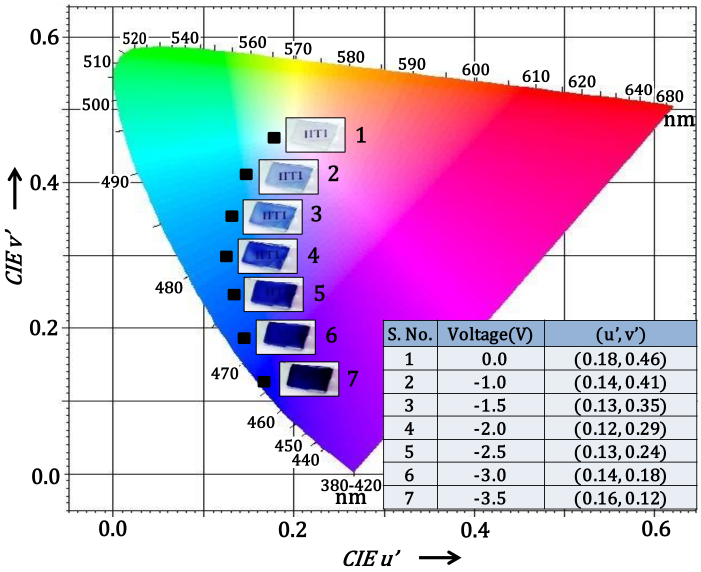

S. No.	Voltage(V)	(u′, v′)
1	0.0	(0.18, 0.46)
2	-1.0	(0.14, 0.41)
3	-1.5	(0.13, 0.35)
4	-2.0	(0.12, 0.29)
5	-2.5	(0.13, 0.24)
6	-3.0	(0.14, 0.18)
7	-3.5	(0.16, 0.12)

Figure 3.4: CIE chart fitting of device color at different intensity. Inset table contain colors coordinates with applied bias.

Figure 3.4 shows the CIE color calculator chart with the photograph of the actual device on various states. The CIE color calculator has been used here to calculate CIE coordinates corresponding to the device appearance color for a given applied bias. Initially at zero bias (OFF) device is transparent hence it allows the white light to pass through. As the applied bias voltage increase, only blue color spectrum passes through it as compared to green and red. According to color appearance, related point is observed on different coordinate of the chart as shown in Figure 3.4. Finally it gets saturated at dark blue color and their corresponding coordinate on CIE chart are (0.16, 0.12). Hence except blue color, device absorbs all colors in its ON state. The CIE chart is very useful as it says that if somehow the material, to be used in device, is tuned in such a way that the color corresponding to coordinates (0.5,0.5) is allowed to transmit from the device a red color appearance will be observed. If one identifies the species responsible for appearance of one particular color corresponding to a given coordinate, the same can be used to make a devise giving that particular color. Before implementing this idea, it is very important to understand the species responsible for a particular color's appearance. This investigation can be done using Raman scattering experiments.

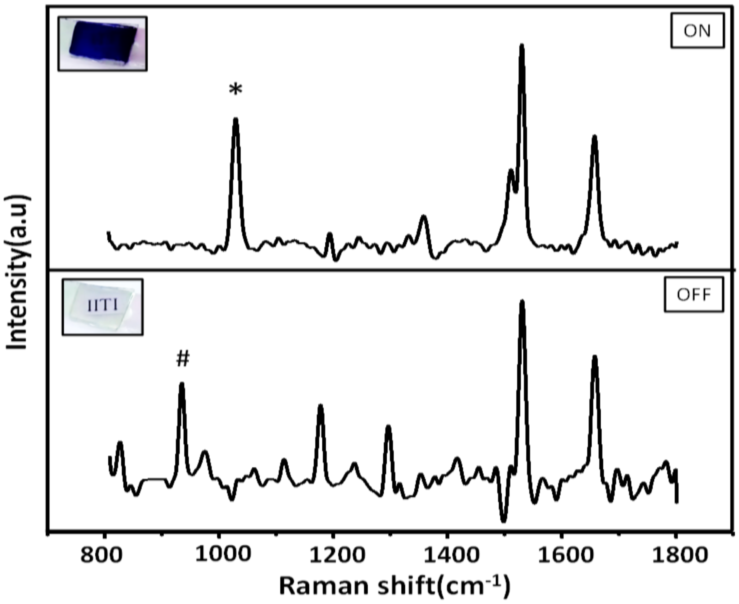

Figure 3.5: In-situ Raman spectra in ON and OFF state of device in cross-bar geometry. Insets show actual photographs of the device in its ON and OFF states.

Figure 3.5 shows Raman spectra of the device in the OFF and ON states. Raman spectrum of the device in its OFF state is similar to the $EV(ClO_4)_2$+PEO mixture in powder. This means that the device contains the EV^{2+} form of viologen in the OFF state. Raman spectrum of the device in the ON state is different from its OFF state as evident from Figure 3.5. Raman peak at 934 cm^{-1} (marked with #) corresponding to EV^{2+} in OFF state disappears under biased condition along with appearance of a peak ~ 1028 cm^{-1} (marked with *) corresponding to $EV^{\bullet +}$ as reported by Liu et al.[101]. This certainly means that the species present in the ON and OFF states, giving rise to the Raman peaks, are different. It is also likely that the peaks appearing in the ON state are obtained as a result of reduction of the species present in the OFF state. To confirm this, Raman spectra in Figure 3.5 have been compared with the Raman spectra from EV^{2+} and $EV^{\bullet+}$ as obtained by chemically reducing the $EV(ClO_4)_2$ using $NaBH_4$ which is shown in Appendix-A.2. Raman spectra from this device for intermediate voltages have also been recorded (Appendix-A.3) to see gradual change in species as seen through appearance and disappearance of Raman peaks. With the above study of Raman peaks' position one can conclude that the OFF device contains EV^{2+} whereas the ON device contains $EV^{\bullet+}$ in majority which means that EV^{2+} reduces to $EV^{\bullet+}$ as a result of applied bias most likely at the –ve (negative) electrode (please see Appendix-A.4). To probe electrolyte-electrode interface reaction at the negative electrode CBG geometry cannot be employed for spatial Raman spectroscopy.

To confirm this, in-situ Raman spectroscopy has been carried out in suitably designed device in OFG given in Figure 3.6. Device in OFG was prepared by drop casting the active material (EV+PEO) on a pre-fabricated electrode system where two gold electrodes are a few microns (~10 μm) apart. A drop of prepared sample in the gap completes electrical circuit and device will start working like electrochemical cell. Top view of the finished device using optical microscope is shown in Figure 3.6a without and with bias applied. The polarity scheme of the power supply to apply bias is shown in Figure 3.6b, which shows the cross-sectional schematic of the device. A color change on electrode E_1 as a result of negative bias on this electrode can be seen which is similar to the bias induced color change in Figure 3.3. This can be appreciated by comparing the Raman spectra obtained from points X and Y in Figure 3.6a and Appendix-A.4. Alphabets X, Y, Z on the microscopic images indicate the positions from where the Raman signals were collected. Raman spectra with laser post size 721nm (532nm) recorded from points X, Y and Z (Figure 3.6c) to compare the effect of bias on the present chemical species in the device. These points have been chosen for Raman measurements so that a comparison can be done between Raman signal from a virgin device (point X), negative terminal (point Y, where reduction is possible) and positive terminal (point Z) under biased condition.

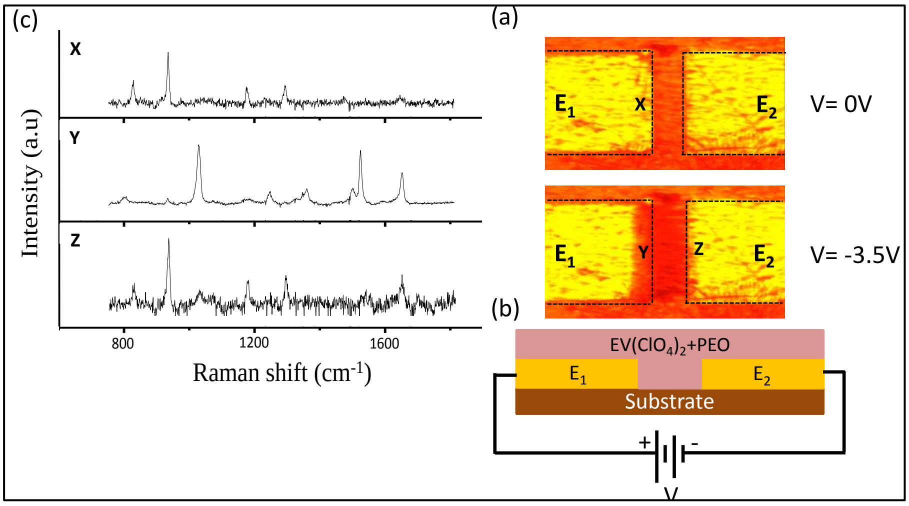

Figure: **3.6** (a) Optical image (using optical microscope) of OFG with and without bias (b) Schematic cross section view of OFG device with biasing arrangement. (c) In-situ Raman spectra recorded on the various position of the OFG device.

Figure 3.6c shows Raman spectra at different position of OFG device under different biasing condition. Microscopic image in Figure 3.6b of OFG device shows color change only on the negative electrode of the device. During the electrochemically reduction, intensity of color between E_1-E_2 and on E_1 electrode changed which attributes reduction of EV^{2+} molecule. The corresponding Raman scattering studies have been done on E_1 and E_2. Raman spectrum in Figure 3.6c (X) was recorded from the E_1 terminal of an unbiased device, which shows major peak at 932 cm^{-1}, the peaks corresponding to EV^{2+}. Raman spectra in Figure 3.6c (Y) & 3.6c (Z) have been recorded under bias of -3.5V on E_1 and E_2 respectively. Some additional peaks appear on the E_1 electrode in biased condition, spectrum in 3.6c (Y) shows two prominent peaks corresponding to reduced viologen, which are at 1028 and 1528 cm^{-1}. With biasing potential, peak intensity increases as the applied potential, shows the formation of more free radical cations ($EV^{\bullet+}$) can be visualize in Appendix A.3. There is no change in the spectrum recorded on E_2 where +ve terminal of the power supply is connected.

From the above in-situ Raman study of neutral and chemically reduced form of $EV(ClO_4)_2$ as well as in the both the device form shows this change of color is due to variation in absorption spectrum of EV^{2+}, $EV^{\bullet+}$ and EV^0. Raman spectrum from chemically reduced form of $EV(ClO_4)_2$ shows peaks at 1028 and 1528 cm^{-1} which are signatures of $EV^{\bullet+}$ species.(These peaks are marked by stars in Appendix-A.2). It is now safe to conclude that the blue color observed in Figure 3.3 as a result of applied bias is due to the $EV^{\bullet+}$ species being generated at the negative terminal as a result of reduction of EV^{2+}. It is also important to mention here that Raman peak at 934 cm^{-1} corresponds to the Cl-O stretching mode of ClO_4 ions in the device in OFF state[120,121]. The Appearance of the ring breathing mode to 1028 cm^{-1} in ON state, as compared to OFF state, indicates that the addition of one electron to the LUMO results in a weakening of the ring C-C[122]. By combining the data in Figures 3.3, 3.5 & 3.6, one can see that the Raman spectrum from the dark region on the device (marked as point Y on E_1 electrode in Figure 3.6a) shows the presence of $EV^{\bullet+}$ species whereas the virgin device shows the signature of stable EV^{2+}.

To confirm results obtained from the Raman spectroscopy, we have done FTIR of EV solution in acetonitrile without and with bias condition (Appendix-A.5). The appearance of solution was seen to change from transparent to blue as a result of bias. Some of the new peaks appeared in FTIR (star signed) due to bias induced change in the species present in the solution. The bias induced changes observed in FTIR spectra are in consonance with the Raman spectrum. This validates our model, described in Figure 3.2c, that presence of blue color centers near the electrode-electrolyte interface is sufficient enough to show completely opaque (Blue) device. Therefore, the Raman spectra permit the conclusion that the mechanism of bias induced color change in the electrochromic device is due to formation of free radical cation from viologen dication.

3.1.2 Device performance

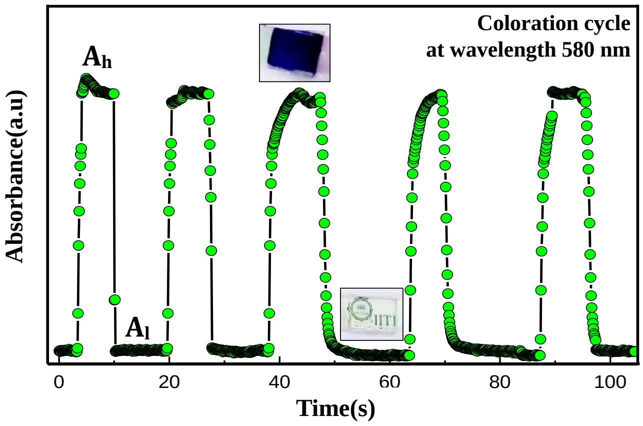

Figure: 3.7 Coloration and de-coloration cycle between ON and OFF states of device. Inset shows corresponding images of the device

Above discussion confirms the origin of color change in the electrochromic device. It will be interesting to see how fast and how many times the electrochromic device be turned ON and OFF[123]. Figure 3.7 shows ON and OFF cycles in terms of normalized absorbance corresponding to 580 nm which has been studied within a specific time period with manual switching power supply. Initially at 580 nm, with no bias absorbance is in its lowest value, A_l which reaches the highest value A_h by applying potential (-3.5V) making it opaque for this wavelength. Figure 3.7 show that device can be turned ON and OFF five times in ~100 seconds. It is worth mentioning here that it takes more time in returning to OFF state after removal of the applied bias because the returning to OFF state depend on the natural oxidation of viologen. A 50% transparency in the second cycle onwards has been considered as OFF state whereas ON state corresponds to 100 % transparency.

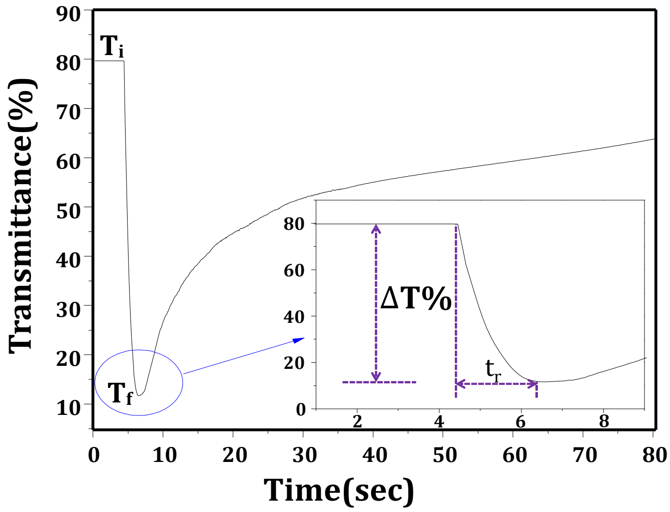

Figure: 3.8 Transmission response of the device during the operation

Additionally, contrast between the ON and OFF states can be calculated by defining color contrast ratio (CCR) using the following equation. [120–122]

$$\boldsymbol{CCR}(\%) = \frac{\boldsymbol{T_i - T_f}}{\boldsymbol{T_i}}\mathbf{x100} \tag{3.1}$$

Here T_i and T_f are the initial and final values of transmittance of the device at wavelengths 580 nm (Figure 3.8). Transmittance changing from 80% to 12% which gives ΔT= 68% with the help of Eq. 3.1 we have find out CCR=85%. It is worth mentioning here that viologen alone in the device having 85% contrast ratio which is quite high among all other known organic and inorganic materials especially in the present situation where counter ion (to support redox reaction of viologen) is absent. This contrast is expected to improve in the complete device as will be discussed below. Inset of the Figure 3.8 also shows that it takes approximately 1.5 seconds to switch between the ON and OFF states of the device. An electrochromic device with 85% CCR is a very good device with an ability to switch in 1.5 seconds which can be improved if an external method is used for turning OFF the device of course by modifying the device composition and geometry appropriately.

Now we have established by in-situ UV-Vis and Raman studies of viologen based electrochromic devices that the electrochromism originates from the redox changes taking place at the electrode-electrolyte interface. In-situ spectroscopic investigations suggest that switching in redox states of a few layers of viologen present at electrode-electrolyte interface is sufficient to turn the device opaque. Raman spectra from the ON device reveal the presence of viologen free-radical which is solely responsible for the change in optical properties of the device. Above device shows poor electrochromism as there was no counter ion to support the redox induced color change and it had to rely on the bias and most likely the atmospheric moisture. Now for further improvement in the device we have incorporated various other materials in the form of electrochromic gel, which improves the overall performance of the device. The new gel is combination of viologen as electrochromic active material and tetrathiafulvalene (TTF) as redox supporting agent along with nanoflakes of graphene. Graphene nanoflakes (GNFs) used as supporting channel to shuttles the ions flow in between of both anchored molecule within the device.

3.2 Fast electrochromic device (ITO/EC Gel/ITO)[7]

As mentioned earlier, ethyl viologen, in the EV^{2+} state is stable and colorless, whereas radical cationic form ($EV^{+\bullet}$) of the same show a different absorption and appears blue. Due to this redox induced

---

[7] *Mishra et al.,* **J. Mater. chem. C**,(2017), 5, 9504-9512

color switching, viologen and its derivatives based electrochromic displays (ECDs) are fabricated in combination with counter ion, like polythiophene, ferrocene etc., as one of the constituents. These counter ions are required and chosen appropriately to facilitate the reduction of viologen when biased to initiate the redox process (reduction of viologen and oxidation of counter ion). Recently, graphene (and graphene based materials) have been found playing a role in electrochromism[124–126] either by acting as an alternative to electrolyte or as a supporting material to be used with the electrode and have received good response in achieving better speed[127,128]. This is possible mainly due to its charge transport properties, which enables it to be used in graphene-based ECD and solar cells where graphene is used as transparent electrodes. However, graphene supports the EC switching of viologen with improvement in speed but compromises on the overall transparency of the device and hence the switching contrast. Like polythiophene, TTF is transparent and an electron donor material[129] making it an eligible material to be used as counter ion in combination with viologen. The Viologen-TTF combination has not yet been explored for EC purposes. The excellent functionality of graphene oxide (GO) as an alternative for electrolyte can be explored, along with viologen-TTF, by synthesizing it as GNFs to make it transparent to be suitable for application in EC display. Based on the study of viologen-graphene as EC material and TTF as electron-donor it can be hypothesized that the *"viologen-graphene-TTF"* combination may prove to be a better device composition with faster (due to GNFs) and transparent (due to TTF) ECD. The reduction potential of $TTF^{+\bullet}/TTF$ is more positive than that of $EV^{2+}/EV^{+\bullet}$ which facilitates lesser power consumption[130]. Overall the role of these substances has to be elucidated, it seems reasonable to expect that their great tendency to form charge-transfer complexes with EC-gel can assist electron-transfer processes as can be appreciated using redox reactions (next section) involved during the device operation.

Current section of this chapter is based on this electrochromic gel (EC-Gel) consisting of EV, TTF and graphene nanoflakes which have been used in an attempt to fabricate an efficient and faster electrochromism with better color contrast. During the color switching, it is expected that TTF will support the viologen reduction, at the negative electrode, by getting oxidized and leave electrons to the positive electrode for the circuit to be completed. The color of the device will be sustained if this redox process is continued and the “reduced viologen-oxidized TTF” is withheld inside the device. Power required to withhold this state decides the power consumption of the device and must be minimum for an ideal ECD. The above discussed redox process needs to be completely reversible while achieving the initial state of the device which was transparent. As can be understood, the coloring process is expected to be faster because applied bias helps in achieving the colored state. On the other hand the bleaching process is expected to be a bit slower as the reduced-viologen & oxidized-TTF have to go back to their respective initial states where the GNFs’ role is expected to be handy. It is likely that the electrons released by reduced viologen will stay on the GNFs and can be ballistically transferred to oxidized TTF for consumption. This way a faster bleaching is expected from GNF containing EC-Gel as compared to the one without it. Redox activity of each component has been established here by means of cyclic voltammetry measurements along with appropriate control experiments. The interaction of EV and TTF with GNFs has been studied by fluorescence quenching method[131]. Electrochemical studies demonstrate how GNFs play key-role in the control of electron capture, transport and discharge through one molecule to other. Absorption/Transmission characteristic in UV-Vis region has been studied to understand the color change properties of the EC-Gel based ECD. Stability and repeatability has also been studied for 2500 color-bleach cycles along with power efficiency of the ECD. A comparison of performance from the current device with the already reported devices has been done in support of the claims regarding the speed and efficiency.

3.2.1 EC-gel constitutes

Following redox reactions involve during the device operation:

$$EV^{2+} + e^{-} \rightarrow EV^{+\bullet} \qquad \text{(R-3.1)}$$

$$EV^{+\bullet} + GNF \rightarrow EV^{2+} + GNF(e^{-}) \qquad \text{(R-3.2)}$$

$$TTF - e^{-} \rightarrow TTF^{+\bullet} \qquad \text{(R-3.3)}$$

$$TTF^{+\bullet} + GNF(e^{-}) \rightarrow TTF + GNF \qquad \text{(R-3.4)}$$

As the experiments have been designed according to literature based hypothesis it is better to discussed prior to analysis of actual experiments. It will be realized later that the entire hypothesis mentioned above are true and the performance of device is in line with the hypotheses. Figure 3.9 schematically illustrates the ECD consisting of EC-Gel sandwiched in between transparent electrodes. The width of EC-Gel (EV/graphene/TTF) layer has been shown exaggerated to show the transport process easily. In the EC-Gel, viologen and TTF have been used as cathodic EC active and as anodic species respectively whereas GNFs are used instead of an electrolyte as will be discussed later. The unbiased device is transparent due to Viologen and TTF being in their natural states. With a negative voltage applied (with the polarity sign as depicted in Figure 3.9b) viologen will starts getting reduced by accepting one electron from the electrode (R-3.1), depicted as left dotted line in Figure 3.9a and at the same time TTF will get oxidized by losing one electron to the electrode (R-3.3). Under this condition, device goes into opaque state (transmittance suppression) due to change in optical absorption of the chemical species in this bias state. It is important to understand here that this opaque phase can be retained only if a voltage remains applied so that the viologen and TTF continue to stay in their corresponding redox states responsible for opacity.

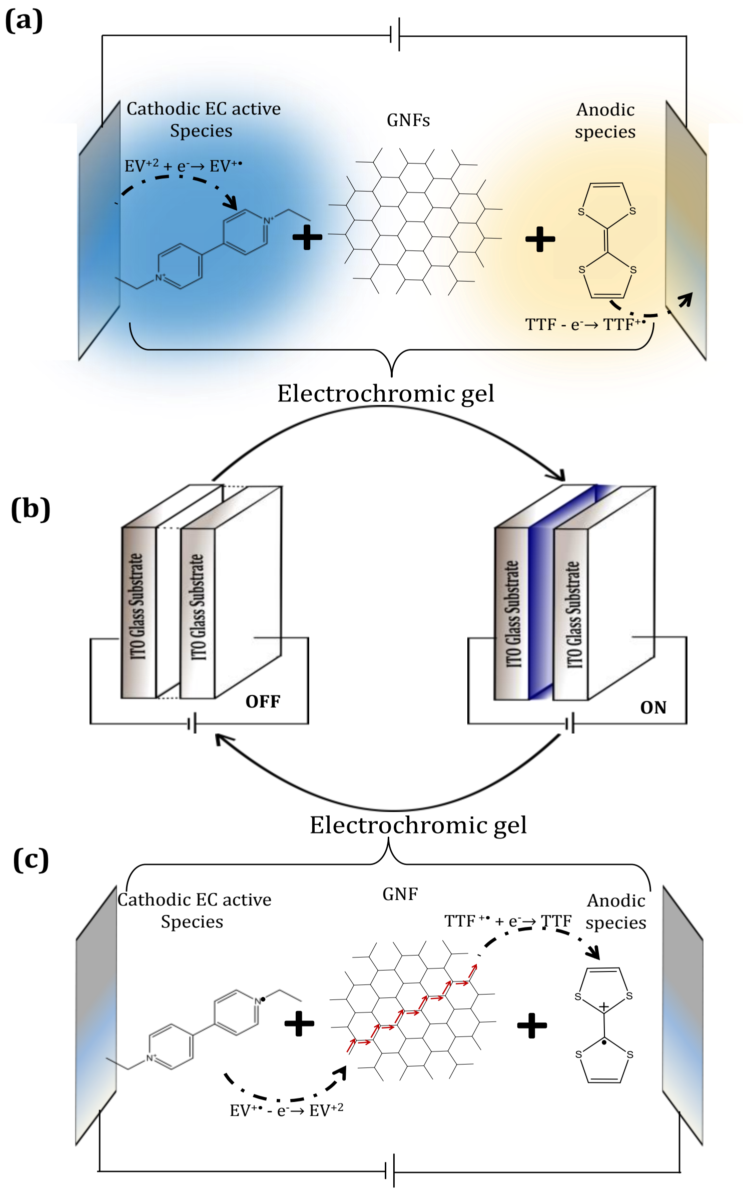

Figure 3.9: Schematic illustration of EC display showing (a) electron movement for coloring process under a bias, (b) circuital arrangement and (c) electron movement for decoloring process after removal of the bias.

When the bias is removed, the redox process breaks and both the species revert-back to their previous states and after the complete reversal a transparent state will be achieved. The time taken to go back to the transparent state is decided by the ease with which the reduced viologen loses electrons (hence gets oxidized) only to get accepted by the oxidized TTF to get reduced (R-3.2) & (R-3.4)). If left unaddressed this process can be delayed and result in a slow switching process. Introduction of GNFs can address this dilatory process, also known as bleaching. Due to unique conducting nature of graphene, electrons move ballistically through it to improve bleaching time (time taken to switch from transparent to opaque states) of the display. It appears that the sandwiched sheets of GNFs play a key role in the EC display by facilitating the charge transport necessary for reversed redox process. It draws electrons and allow their shuttling toward counter molecule which allows electrons from $EV^{+\bullet}$ to get transferred to GNF and stored within its network (R-3.2). During the bleaching process, the movement of electrons (generated due to oxidation of $EV^{+\bullet}$) from EV to TTF through the graphene (R-3.4) is depicted in Figure 3.9c. The apparent role of graphene and other constituents needs to be investigated further to establish not only a better EC device composition but also to get best performance out of it using gel-containing electrochromic device. This will be discussed in detail later on.

The microstructures of the GNFs, fabricated for being used in the ECD in the current study, have been studied using electron-microscopy & diffraction. The SEM images (Figure 3.10a & 3.10b) of GNFs, electrodeposited on a gold film electrode, allow one to clearly distinguish small flakes of GNFs, which have been broken from the large sheets lying on the electrode. It is evident from the SEM images that shape and size of flakes are uniform with each flake having an averages size of ~500nm. The transmission electron micrographs (TEM) (Figure 3.10c & 3.10d) of the GNFs reveal presence of thin sheets (along with folded sheets at many places) which is having uniform thickness. Single graphene sheet as well as nanoflakes, consisting of multiple graphene sheets agglomerated together, can be seen as identified using selected area electron diffraction (SAED) (Figure 3.10e & 3.10f) in the form of ring like and spotty patterns.

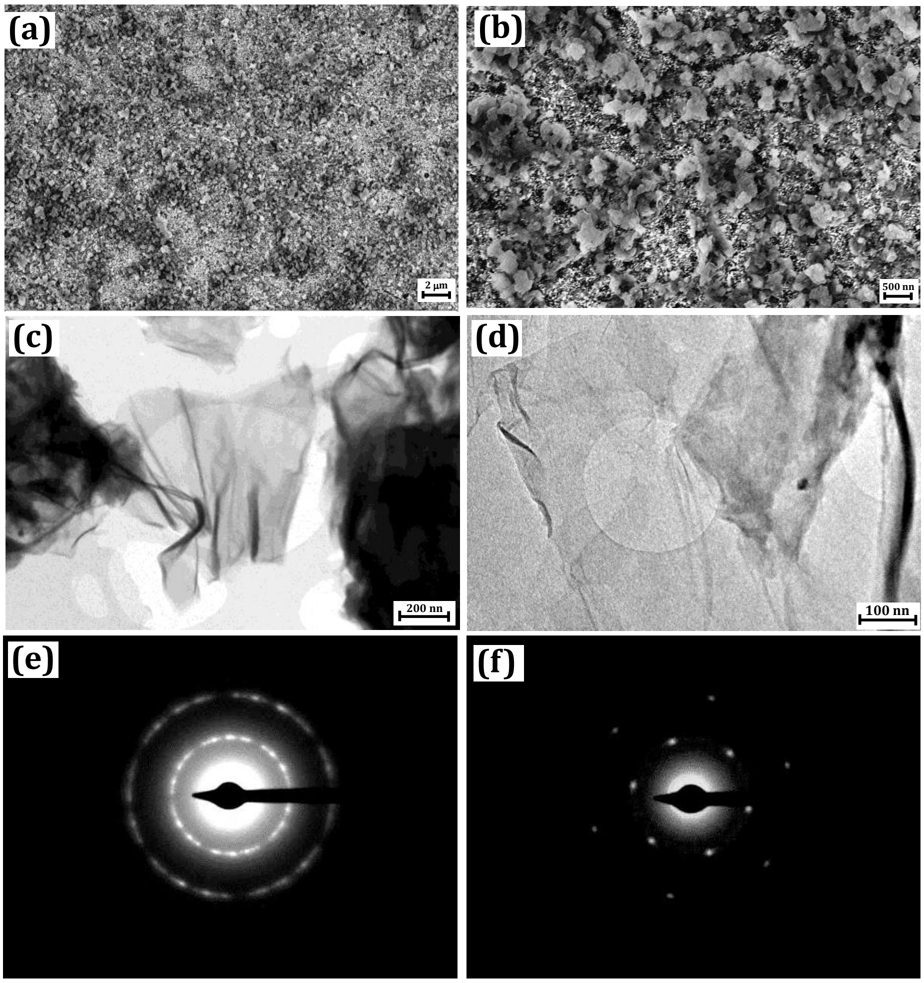

Figure: 3.10 Morphological characterization of GNFs (a, b) SEM images of GNFs on gold film with its magnified view (c, d) TEM images of nanoflakes of the graphene (e, f) electron diffraction pattern from two different areas on the GNFs sample.

The ring like diffraction patter (Figure 3.10e) indicates near-polycrystalline nature, which comes from the multiple GNF together, where spotty pattern (Figure 3.10f) reveals the presence of single sheet of GNF. The spot patterns correspond to the hexagonal pattern of a flake indicates the single crystalline nature. To confirm the presence of graphitic phase and the quality of the prepared flakes, Raman spectroscopy, which is extremely sensitive technique for carbon phase identification[132–134] has been carried out (Figure 3.11a). The Raman spectrum shows two peaks at 1348, and 1581 cm^{-1} corresponding to D- & G- bands respectively as typically observed for graphitic systems[134,135].

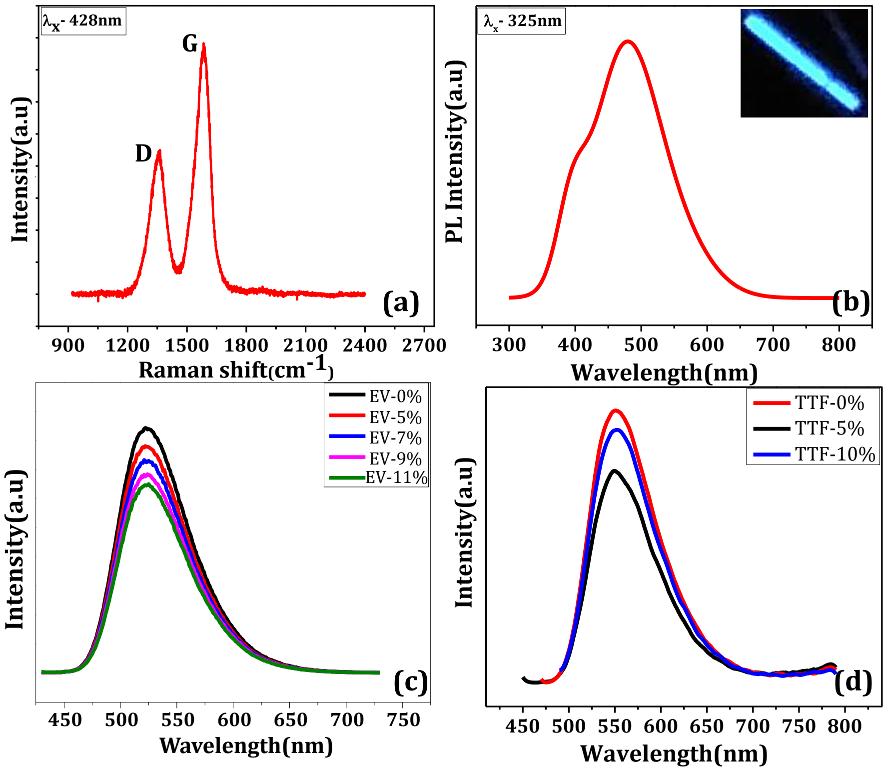

Figure: 3.11 (a) Raman spectrum of as prepared GNFs powder (b) Photoluminescence spectrum of GNFs in DMF with excitation wavelength 325 nm with inset showing the actual photograph during PL measurement (c, d) fluorescence quenching of GNFs by interacting with viologen and TTF.

The D-peak corresponds to sp^3 -hybridized carbon atoms originating from defects and G-peak arises from sp^2 -hybridized carbon atoms with intensity ratio of D- & G-peaks (D/G ratio) manifesting the crystalline nature (quality) and defects present in graphene-based nanoflakes. The strong G-peak with relatively low intense D-peak indicates low disorder in the GNFs[136]. D/G ratio for GNFs is obtained to be 0.56, which is quiet small as compared to the typically observed values for large sheets of graphene oxide predicting the presence of a good quality graphene structures. A blue luminescence (Figure 3.11b) on excitation at the 325 nm absorption band is another typical signature of GNFs which is observed from our sample as well showing a peak at 465 nm (i.e, with a Stokes shift of 140 nm or 1.15 eV compare to excitation source) [137]. Origin of the strong PL from GNFs is due to free zigzag sites on the boundaries[138]. In general, most of the carbon nanoparticles exhibits excitation-dependent luminescent, with increasing excitation wavelength, luminescent peak shift toward higher energy side accompanied by reduction in intensity[138]. Additionally, when the excitation wavelength is changed from 320 to 420 nm, the PL peak shifts to longer wavelengths and its intensity decreases rapidly[137]. As discussed above, the current work relies on the interaction of GNFs with viologen and TTF, thus it is important to establish the existence of such an interaction. Fluorescence spectroscopy can be used to identify such interactions between two compounds[131] which are GNFs and EV^{2+} in the present case. Figure 3.11c & 3.11d shows that the fluorescence intensity of GNFs decreases with increasing concentration of EV^{2+} and TTF respectively. Quenching in the fluorescence intensity (Figure 3.11c) of GNFs is due to electron density reduction as the electron deficient EV^{2+} withdraw electron in all likelihood from GNFs. Analogous effect of fluorescence quenching is observed in GNFs-TTF (Figure 3.11d). Collectively, it is revealed that GNFs interacts nicely with both the molecules which proves that, as hypothesized, GNFs may provide an excellent foundation for the highly stable and durable EC-Gel (EV^{2+}-GNF-

TTF) for over-all improvement of the device performance as will be shown later on.

3.2.2 Device mechanism

To monitor electron transportation between redox active species anchored with GNFs, and to establish role of each constituent in the EC-Gel, electrochemical measurement have been performed (Figure 3.12). For better understanding, cyclic voltammetry (CV) measurements of EC-gel has been carried out for multiple cycles at a given scan rate of 50mV/s (Figure 3.12a) to check stability along with scan rate dependent CV at different scan rates varying between 10mV/s & 80mV/s (Figure 3.12b). The overall range of potential on working electrode (WE) with reference to Ag/AgCl electrode have been divided into forward(anodic) and reverse(cathodic) scans. The first two peaks in the forward scan (Figure 3.12a & 3.12b) are observed due to oxidation of TTF at ~ 0.5V and ~0.8V[129]. In the reverse scan a small peak appears around -0.56V (Figure 3.12a) which corresponds to single-electron reduction of EV, resulting in creation of its free radical cation ($EV^{+\bullet}$). By going further in this scan, around -1.0 V there is an observation of current kink riding on a near-linear region that also coincides with the GNFs reduction which means that GNFs start getting reduced to GNF(e^-). The representation GNF(e^-) means that the electron involved in GNF reductions get stored within its 2D network as reported by *Bridewell et al.*[139] Finally the second reduction of EV takes place near -1.2 V to result in EV^0 ($EV^{+\bullet} \rightarrow EV^0$). The electron storing property of GNF is also evident from two observations in the CV curve (Figure 3.12a & 3.12b). Firstly absence of oxidation peaks of $EV^{+\bullet}$ in the voltage sweep from -1.5 to 0 V which otherwise is expected around -0.3 V (inset Figure 3.12a) after the second viologen reduction peak. Second observation in support of abovementioned conclusion is the zero current in the sweep region of -0.8V to 0V. The zero current means that the electron generated after oxidation of $EV^{+\bullet}$ has not been returned to the electrode thus getting stored in the GNF network. This appears to be the most likely case because GNFs remains the only destination for the electrons to go if not returned to the electrode. On the other hand finite current flows (no zero current) if the sweep voltage is restricted to-0.6V that means GNFs were not allowed to store the electrons as it take place at -1.0 V as discussed above. In this case the electrons are returned to the electrode to result in the oxidation peak in Figure 3.12. This establishes the electron storing property of GNFs.

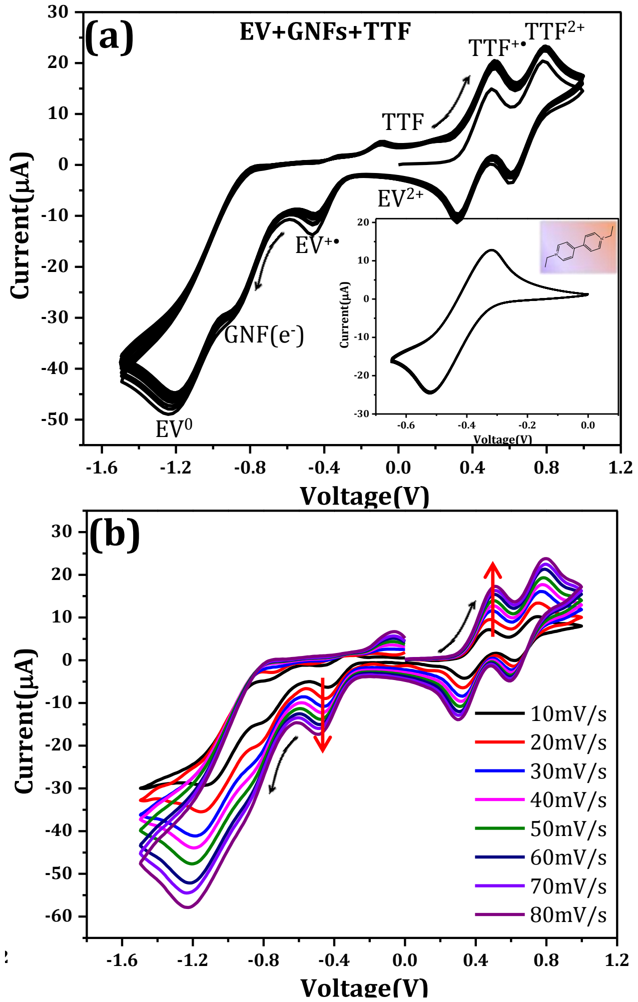

Figure: 3.12 Cyclic-voltammetric response of EC-gel with (a) multiple cycles at scan rate of 50mV/s with inset showing the CV for viologen alone, (b) different scan rate.

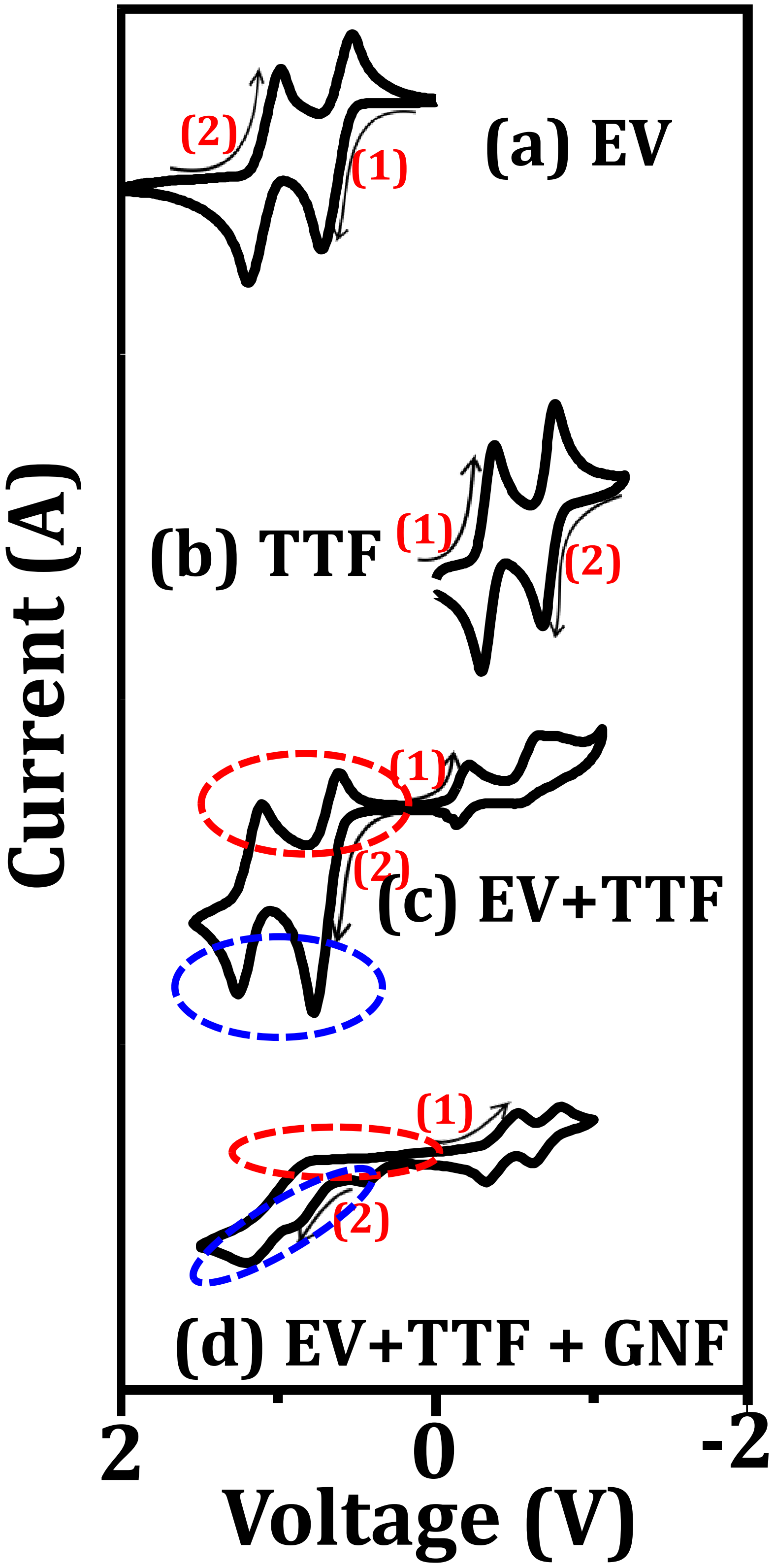

Figure: 3.13 CV curves for (a) only EV, (b) only TTF, (c) EV+TTF and (d) EC-Gel (containing EV+TTF+GNF)

In the next forward scan (Figure 3.12a) the intensity of first oxidation peak of TTF (0.56 V) increases noticeably as compared to that in the first cycle (prior to the reverse scan). In all likelihood, this increase in the oxidation (peak) current is due to more number of TTF molecules getting oxidized in later cycles as compared to the first cycle by taking electrons from the GNF network stored in the previous sweep.

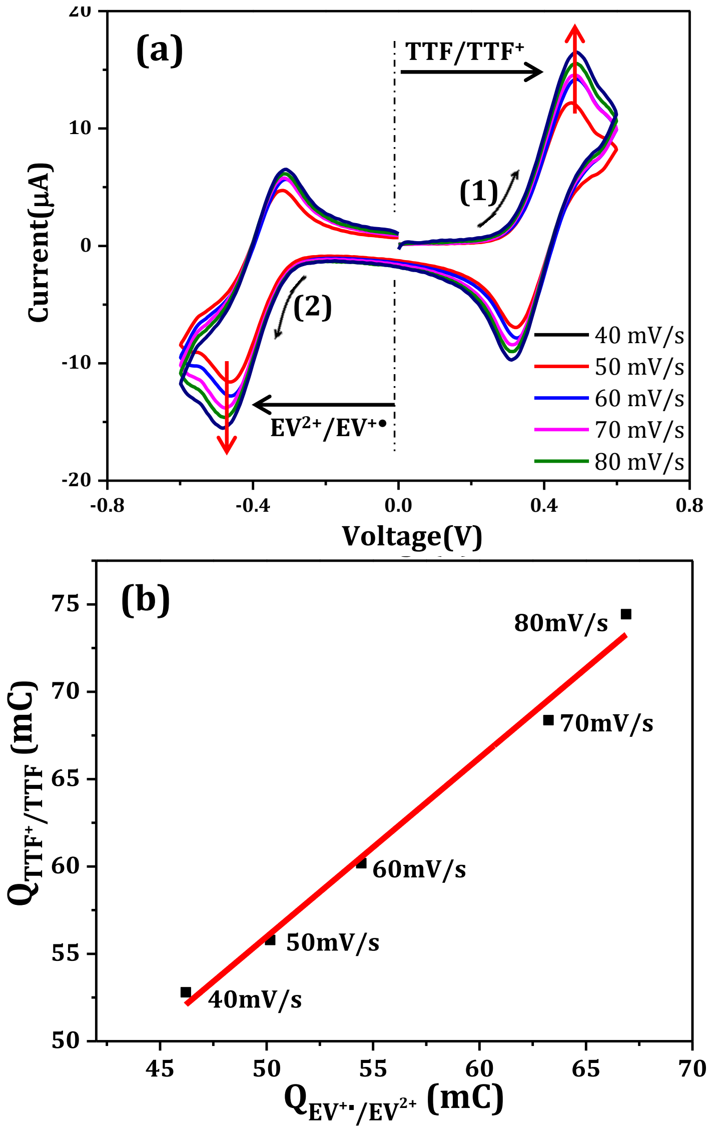

Figure: 3.14 (a) CV curves for EC-Gel in smaller scan window and (b) relationship between charge involved in EV reduction (EV^{2+}/EV^{+}) v/s TTF oxidation (TTF/TTF^{+})

GNFs enhance the TTF oxidation peak from which one can infer that GNFs can provide excess electron to the TTF. Abovementioned CV measurements based study of cooperative behavior between $EV^{2+}/EV^{+\bullet}$ and TTF/TTF^{+} with GNFs reveals that GNFs work as facilitator for shuttling of electrons from one molecule to the other. Scan rate dependent CV curves show reversible behavior of the system where EV/TTF/GNF are present in the form of EC-Gel showing consistent behavior with increasing peaks intensities (Figure 3.12b). For more clarity, we have plotted individual CV curves systematically for comparison in a single graph (Figure 3.13), one can clearly visualize the effect of presence of GNFs in the gel (c, d). The voltammograms follow the same pattern at all scan rates and exhibit reversibility during the voltage scan over the wide potential range. Before the fabrication of final device, stability of EC-Gel has been checked by recording multiple cycles from which charge calculation, required for the EV reduction and TTF oxidation, have been done corresponding to different scan rate CV curves (Figure 3.14a). The obtained results show a linear relationship (Figure 3.14b) between the charge involved in EV reduction (EV^{2+}/EV^{+}) to the charge involved in TTF oxidation (TTF/TTF^{+}). A linear behavior in Figure 3.14b reveals the presence of balance in charge transfer between both redox reactions. It means that the EC behavior of a device involving the EC-Gel as the building block will lead to an overall improvement in device repeatability and stability as the device in the form of electrode/EC-Gel/electrode appears to be complete. To explain the molecular arrangement within the device under operational condition, schematic figure has been presented to show alinement and random nature during coloring and bleaching state of the device (Figure 3.15).

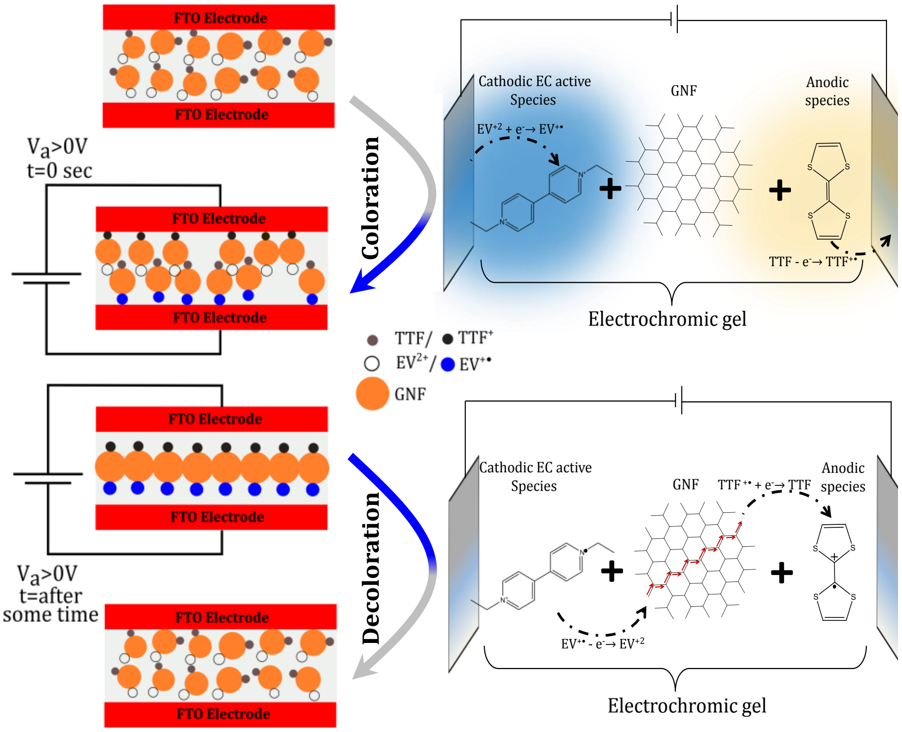

Figure: 3.15 Schematic representation of redox induced coloration-decoloration process (left panel) along with electron movement during coloring and bleaching of the device (right panel).

3.2.3 Device performance

Figure 3.16 shows the schematic representation of device fabrication with all steps involved along with the actual optical images of the fabricated device without and with bias. In the present study, a simple frame has been used in step 2 (Figure 3.16) for ease in carrying out in-situ spectroscopic measurements however a patterned layer of choice can also be used to fabricate a device. In-situ UV–Vis absorption spectra from the fabricated device (Figure 3.17a) show variation in absorbance as a function of applied bias. No change in absorbance can been observed upto an applied bias of -0.6 V meaning no color change is expected upto this voltage. No absorbance below this voltage (-0.6V) means all light gets transmitted through the device when seen in white light and appears transparent. On increasing the bias above -0.6 V, the device starts showing a weak absorption hump around 590 nm, which later appears as proper absorbance maximum at bias values of -1.5 V.

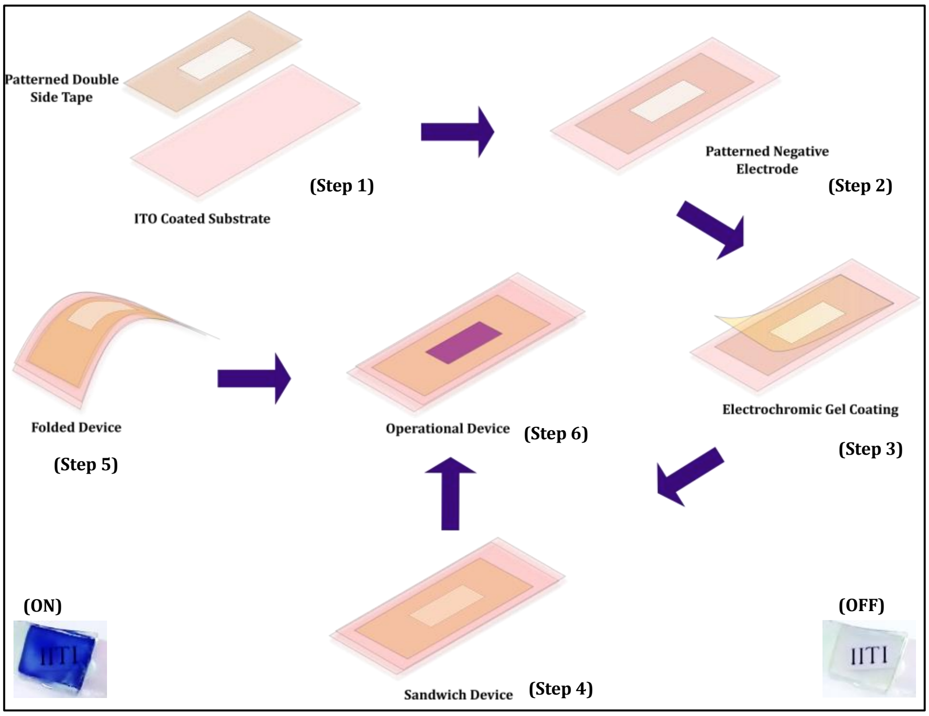

Figure: 3.16 Schematic portraiture of step by step fabrication process of ECD. The operation of the device carried out by applying −1.6 V, inset shows actual device.

As evident from Figure 3.17a, the device color change is associated with the increase in 590 nm absorbance and is in consonance with each-other as the device appears bluish on application of negative bias. It is now an established fact that a negative bias generates $EV^{+\bullet}$ as discussed above and has been verified by several others using spectroscopic tools[29,101,140]. Hence it can be concluded that the bias generated $EV^{+\bullet}$ are responsible for the color change and hence the associated absorbance change. The intermediate spectra of absorbance correspond to different contrast of the perceived color. Time taken to change the color (absorbance) under applied bias decides the speed of the device. Time dependent variation in 590 nm absorbance under -1.5V bias and corresponding current through the device have been shown in Figure 3.17b. It is evident from Figure 3.17b that it takes approximately 450ms for the device to change the color to appear opaque. The accompanying increase in current also indicates that more charge is flowing during this duration, which is generated due to the reduction of viologen under this bias.

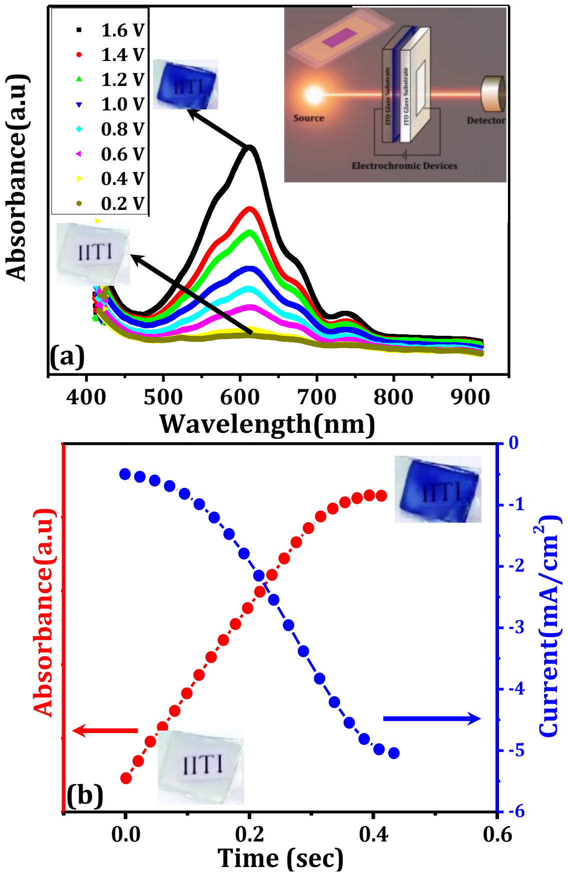

Figure: 3.17(a) Bias-induced modulation of UV−Vis absorption spectra of ECD along with actual images (b) variation in 590 nm absorbance (red) as a function time with corresponding current (blue) flowing in the device. Inset shows photographs of the device in the bleached (left) and colored (right) states.

All the above observations are in good agreement with each other and it seems that the ECD fabricated using the EC-Gel is faster than the reported ones where different paradigm (material combination) with EC-Gel as active component has been used. The variation in absorbance (corresponding to 590 nm) with time (Figure 3.17b) needs to be reversed fast as well after bias removal and this cycle ought to be repeatable for the device to be used in real. It has been observed from the UV-Vis spectrum, transmission (corresponding to 590 nm) of the device changes from 84% to 35% (Figure 3.18a) which gives the transmission change (ΔT~49%) with the coloration speed of 400 ms (same as depicted in Figure 3.17b). The bleaching time[8] of the device is ~ 900ms, which is quit less in comparison with other devices reported so-far[29,141,142]. Due to smaller bleaching time overall speed of the device is high, it shows nearly five cycles of coloration/decoloration within 10 second. Additionally, device stability during operation has also been checked. For this purpose, an asymmetric square wave (with duty cycle of 11 %) of voltage with OFF and ON pulse of magnitude 0 & 1.6 V (with appropriate polarity) was used to operate the device. The device's repeatability of transmission switching under ambient conditions can be seen in Figure 3.18a. The ECD shows switching between color and bleached states for upto 2500 cycles (Figure 3.18b). A change in current density corresponding to the voltage-controlled absorbance is also repeatable (Y-axis of Figure 3.18b). The maximum (5mA/cm^2) and minimum (-5mA/cm^2) current densities of the device are stable throughout 2500 color-bleach cycle. Stability in cyclic performance of the present device is high compare to the other reports [123,125–127,143] and has been summarized in Table 3.1. Longer stability of the device indicates that electrical conductivity of the EC-gel was maintained likely due to the presence of GNFs which not only provides forum for quick storage of the electron (during coloration) generated after reduction of viologen and later to be dissipated (during bleaching)

---

[8] Time taken by the device to change the state from color sate to transparent state.

quickly after removal of bias. This way graphene in the EC-Gel appears to be playing the key role in making the EC-Gel based ECD faster. For quick quantification, the electrochromic efficiency of the present device has been calculated using following Eq. 3.2 and found to be 208 $(C/cm^2)^{-1}$ which is two times better than the reported values for traditional ECD.

$$\eta_{CE}(\lambda) = \frac{\Delta OD(\lambda)}{Q} \tag{3.2}$$

Where ΔOD (λ) is optical density defined as $log\ (T_{bleach}/T_{color})$ and 'Q' is charge expressed in terms of coulombs per unit electrode area.

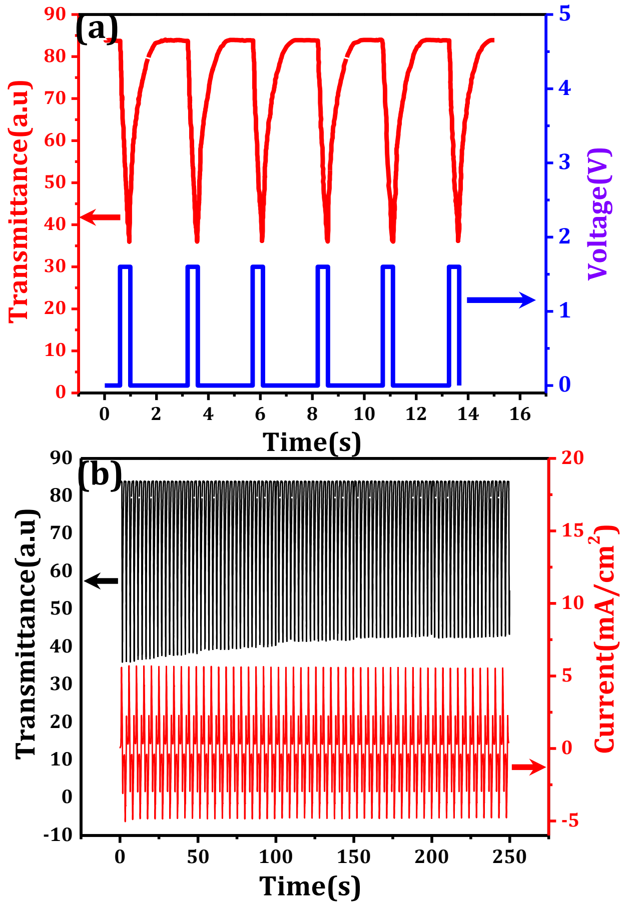

Figure: 3.18 Device characteristics **(a)** transmission cycles (red curve) of the device operating in response to the voltage cycle (blue) **(b)** Stability analysis of the device shows transmission spectra (black) and current density (red) as function of time . All transmittance are corresponding to 590 nm.

Table: 3.1 Comparison table include various parameters of electrochromism based previous reports

S.No	Device Composition	Coloration Efficiency (cm^2/C)	Coloration Cycling (per 100 second)	Reference
1.	EV–GNFs–TTF	208	~50	**This work**
2.	MV–EMI–TFSI–Fc	105	~5	Moon et al.[144]
3.	HV–BMI–TFSI–Fc	78	~1	Moon et al.[145]
4.	PEDOP–IL–RGO	477	~6	Reddy et al.[126]
5.	PEDOT:PSS–WO3	82	~2	Ling et al.[146]
6.	PANI-core/shell	206	~17	Zhang et al.[147]
7.	MV–GQDs	65	~6	Hwang et al.[127]
9.	EV-alone	75	~5	Mishra et al.[29]
11.	Poly(butyl viologen)	157	~5	Fan et al.[148]
12.	Viologen–ITO	140	~30	Nakajima et al.[149]

3.3 Summary

After understanding the fundamental mechanism of color change by fabricating simple device using viologen alone gel and stabilizing by in-situ spectroelectrochemistry and in-situ Raman studies various improvement have been done in the electrochromic gel by incorporating TTF counter supporting agent and GNFs flakes as facilitating material to improve the device efficiency. On the whole, a faster and efficient electrochromism has been displayed here using EV-GNFs-TTF, EC-gel as compared to others reported in literature. Performance of the device fabricated later has been compared with the earlier-one has better efficiency of 208 (cm^2/C). Along with the efficiency speed of the device also improved significantly, due to the presence of the GNFs which support the ballistic transportation of carrier.

Chapter 4

Inorganic Core-Shell Hetero Nanostructured Junction: Efficient Electrochromism

In this chapter, pure inorganic material based hetero-nanostructure of transition metal oxides have been explored for efficient electrochromism. Suitably designed heterostructured TiO_2/Co_3O_4 -core/shell nanorods array has been observed to exhibit improved electrochromic properties as compared to the nanostructures of either of the oxides when used individually. The core-shell nanostructures have been grown on an FTO coated glass substrate by preparing TiO_2 nanorods through hydrothermal reaction followed by electrodeposition growth of Co_3O_4 shell layer. These core-shells also exhibit stable and power efficient bias induced color changes between transparent (sky blue) and opaque (dark brown) state.[9]

---

[9] *Mishra et al.,* **ACS Appl. Energy Mater.**, (2018) 1, pp 790–798

4.1 Hetero-nanostructures

In the era of increasing demand for alternate energy/power sources, materials with capability of energy storage must be explored to meet this challenge in the field of supercapacitor and batteries. In the global context, materials not only with better efficiency but also with multifunctional operations need to be identified to address the future requirements. Nanomaterials, especially one-dimensional (1D) core/shell nano-arrays, have flashed great interest recently due to their enhanced physical and chemical properties as compared to its bulk counterparts[8,24,150–155]. The core-shell structures often possess different electronic properties from either of the constituents which make them eligible for application in areas of global interests including energy harvesting[154,156]. While synthesis of such kind of materials remains one of the issues to be addressed, choice of materials to be used in combination (in the form of core/shell) is also a matter of discussion and is mainly application oriented. Developing controlled protocols for the synthesis of hetrostructured core/shell porous nanorods is essential for developing new economic materials for high-performance electronic applications. One of the most important aspects, while choosing materials for energy application, is to look for large active surface area and short diffusion path lengths for charge carriers (electrons and ions) which are essential criteria mainly for efficient electrochemical energy storage purposes[154]. An extremely high active surface area can be achieved through miniaturization of materials where increased surface to volume ratio are obtained inherently by reducing the material dimension. A nano core-shell structure can help address the latter requirement also by appropriately choosing the core-shell combination so that it results in a heterojunction. The effective width will then be decided by the shell thickness or the effective junction width whichever dominates[157]. A smaller width may have an additional advantage in achieving high capacitance and thus such materials can serve as supercapacitors. This approach for obtaining higher capacitance is otherwise not possible by using single nanomaterial even in the nanostructured form.

Generally, two-step synthesis protocols are used for the fabrication of self-supported core/shell nanorods[152,154]. The core/shell nanorods are prepared by constructing a nanorod core backbone followed by coating with the shell material. This method needs to combine different methods such as sputtering, hydrothermal technique, electrodeposition etc. to prepare core/shell nanorods arrays. Various types of core/shell nanowire arrays whose core or shell materials consist of metals, oxides, carbon, hydroxides, semiconductors, and polymers like core/shell of semiconductor @ semiconductor, semiconductor @ metal, metal @ polymer have been studied rigorously in past[154,158]. Transition metal oxides such as Co_3O_4, NiO, and TiO_2 are scientifically & technologically important materials for the applications in electrochemical energy storage[158,159], chemical sensing[160,161], catalysis[162,163], and electrochromism[96,164]. Well-defined core/shell nanostructure fabrication and obtaining tunable functions remain as the major challenges when it comes to the realization in the form of device. In recent years some progress has been made for developing cost-effective and controllable hetero-nanostructure by simple methods[165]. Still, there exists no simple and high-efficient method to synthesize transition metal oxide core/ shell nanostructure arrays. Electrochromism is one of the inherent properties of the transition metal oxides such as WO_3, Co_3O_4, MoO_3, V_2O_5, NiO, and TiO_2.

As discussed earlier, electrochromism is the reversible change of color of material induced by application of an electrical current or a potential difference. The color appears of the any material depends upon the optical properties during the electrochromism these properties gets altered on the bias application. In contrast to the electrochromism of organic molecules, as discussed in chapter 3, various inorganic TMO can be incorporated in electrochromic as well as supercapacitive energy storage device makes them intelligent dual applicable material[166–171]. Supercapacitor (discussed in latter chapter) that changes its color during charging and discharging would be a smart energy efficient device to fulfill both the requirements. Concept of combining electrochromic & supercapacitor become possible due to conducting transparent glass electrodes as the replacement of conventional substrate like nickel foam or carbon.

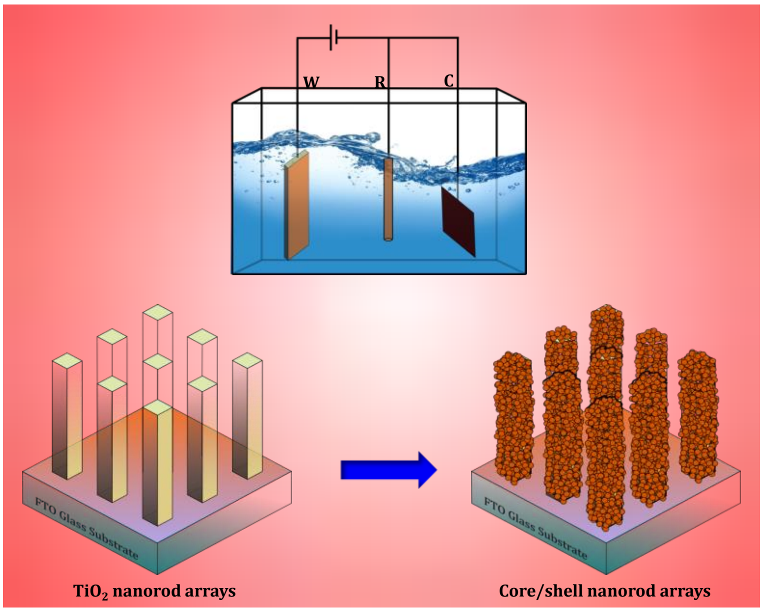

Figure: 4.1 Schematic illustration showing synthesis of core (TiO_2)/shell (Co_3O_4) nanowire on FTO coated glass substrate.

In this chapter, oxides of two metals belonging to the fourth period of periodic table (Ti & Co) have been combined by growing shell of the latter on the Ti core to explore its suitability in bifunctional application. A two-step methodology, hydrothermal followed by electrodeposition have been employed to synthesized such a core shell nanostructures which makes a hetero-junction between the two oxides. It has been shown that the synthesized nanostructures prove to be an efficient electrode for the abovementioned dual application. This has been done by addressing issues associated with Co_3O_4, which is one of the least studied materials as far as its electrochromic properties are concerned. In the core shell nanostructures, hydrothermally grown TiO_2 core provide the vertically aligned nanorods with high surface area, allows the electrolyte to penetrate and shorten the ions diffusion length, which can not be compromised in energy storage. Moreover, the TiO_2 nanorods are able to reduce the refractive index and improve optical transparency, which is very important in electrochromic application. Synthesis of TiO_2 nanorods and core shell nanostructures along with its characterizations has been discussed in chapter 2 in detail.

4.2 Structural study

The two-steps involved in the synthesis of core/shell nanostructures include hydrothermal growth of TiO_2 nanorods and electrodeposited Co_3O_4 shell. TiO_2 nanorods grown single crystalline on conducting FTO electrode used as backbone for the growth of Co_3O_4. The electrodeposition process deposits $Co(OH)_2$ precursor film as a result of following electrochemical reaction[158]:

$$NO_3^- + H_2O + 2e^- \rightarrow NO_2^- + 2OH^- \qquad \text{(R-4.1)}$$

$$Co^{2+} + 2OH^- \rightarrow Co(OH)_2 \qquad \text{(R-4.2)}$$

After the above reactions (R-4.1 & R-4.2) it is expected that cobalt based shell will get deposited on the single crystalline TiO_2 as schematically presented in Figure 4.1. The $Co(OH)_2$ produced as a result of reaction R-4.2 converts to Co_3O_4 after annealing step as described in chapter 2. The appearance of the resultant sample was clean and homogeneous in texture which is an indication that the typical shell nanostructures have covered the entire surface of TiO_2 nanorods backbone. Morphological analysis of the nanostructures have been carried out using SEM as shown in

Figure 4.2 showing SEM images of bare TiO_2 and Co_3O_4@ TiO_2 core shell nanorods grown on the FTO substrate.

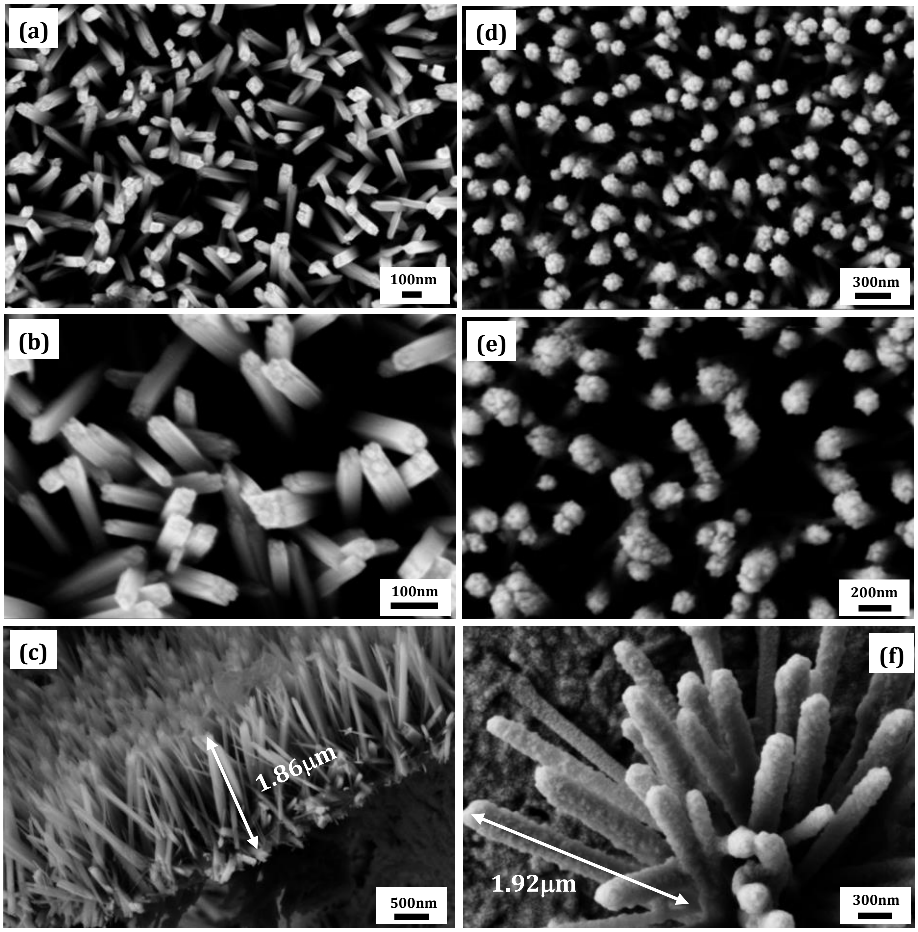

Figure: 4.2 SEM images of TiO_2 nanowire array in top view (a, b) and cross-sectional view (c), TiO_2/ Co_3O_4 core/shell nanowire array grown on FTO substrate in top view (d, e) and with tilt angle of 45 ^{0} (f).

The average diameter of TiO_2 nanorods is around 60 nm (Figure 4.2a&b) and length less than 2 μm (Figure 4.2c) as apparent from top-view and cross-sectional SEM images. Various parameters like uniformity and density of the structures can be visualized from the top view of the both bare TiO_2 and its core-shell SEM images. After electrochemical deposition, TiO_2 nanorods get coated with Co_3O_4 to make core shell nanostructures of size (diameter) around 200nm (Figure 4.2e) and length less than 2 μm (Figure 4.2f). Uniform and homogeneous coating of the shell layer on the TiO_2

core would be supporting for electrochromic performance. Further, to develop more clarity on the heterogeneous nanostructures phases, elemental color mapping proves to be an important tool for core/shell nanostructures analysis.

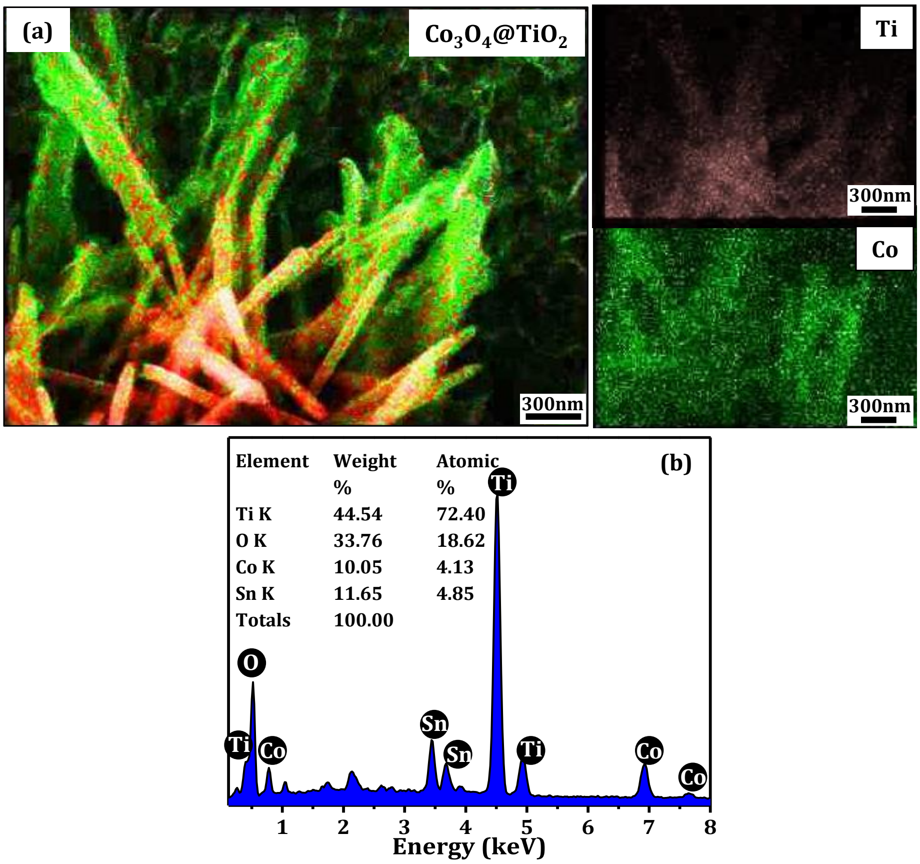

Element	Weight %	Atomic %
Ti K	44.54	72.40
O K	33.76	18.62
Co K	10.05	4.13
Sn K	11.65	4.85
Totals	100.00	

Figure: 4.3 (a, b) Energy dispersive x-ray along with elemental mapping where Ti and Co are represented as red and green colors respectively.

Figure 4.3a shows the color mapped images of both elements separately and in combination recreated for clarity. To confirm constituents present in the core-shell structures, energy-dispersive X-ray spectroscopy (EDX) was carried out which reveals heterostructures of titanium- cobalt oxides (Figure 4.3b). Further, to understand the growth mechanism of Co_3O_4, we have checked the electrodepotion of Co_3O_4 on various current densities there corresponding SEM images shown in Figure 4.4.

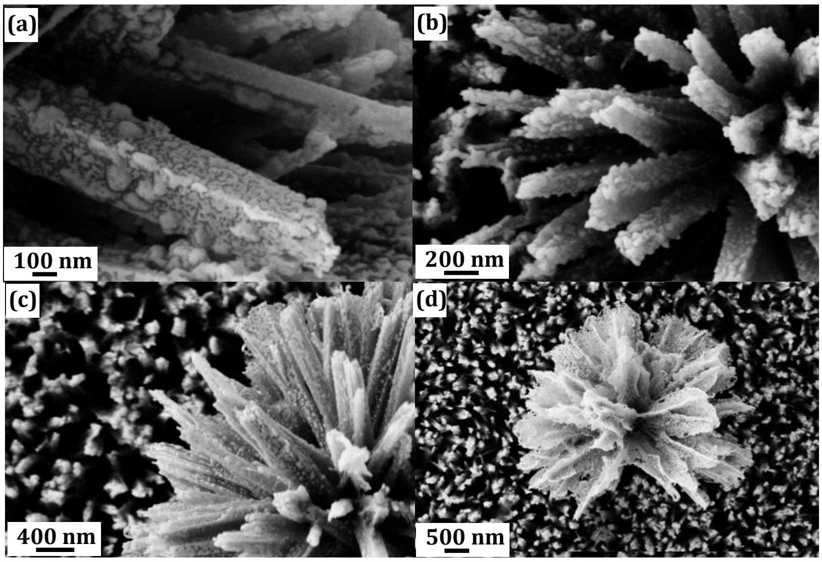

Figure: 4.4 SEM of TiO_2/Co_3O_4 –core/shell nanostructures, electrodeposition of shell on the application of current of (a) -0.1 mA (b) -0.2 mA (c) -0.4mA (d) -0.5 mA for 5 minutes.

For better understanding of microstructure of these structures, TEM has been carried out as shown in Figure 4.5 (a, b). The crystallinity of the prepared TiO_2 and Co_3O_4 @ TiO_2 nanorods are also visible from TEM images shown. Figure 4.5c shows HRTEM image of TiO_2 nanorods showing rods of a few tens of nanometers single crystalline nature. The TiO_2 NRs have even sides and rough top surface with single crystalline rutile phase grown in [001] direction with the fringe width of 3.02 Å. Uniform lattice parameters illustrate growth of the nanorods in a single plane, which is clearly depicted from the FFT image (obtained using ImageJ) consisting of light spots well aligned in a single line. Figure 4.5d shows the HRTEM image of the core/shell nanostructures in which TiO_2 nanorods have been covered with the Co_3O_4 shell. The HRTEM image of the core shell structure clearly shows the two planes on the rods, depicting two different materials with different fringe size and orientation. In case of the core-shell, the fringe size of the grown shell is around 2.41 Å. Corresponding FFT images confirms that the material has fringes in two mutually perpendicular directions.

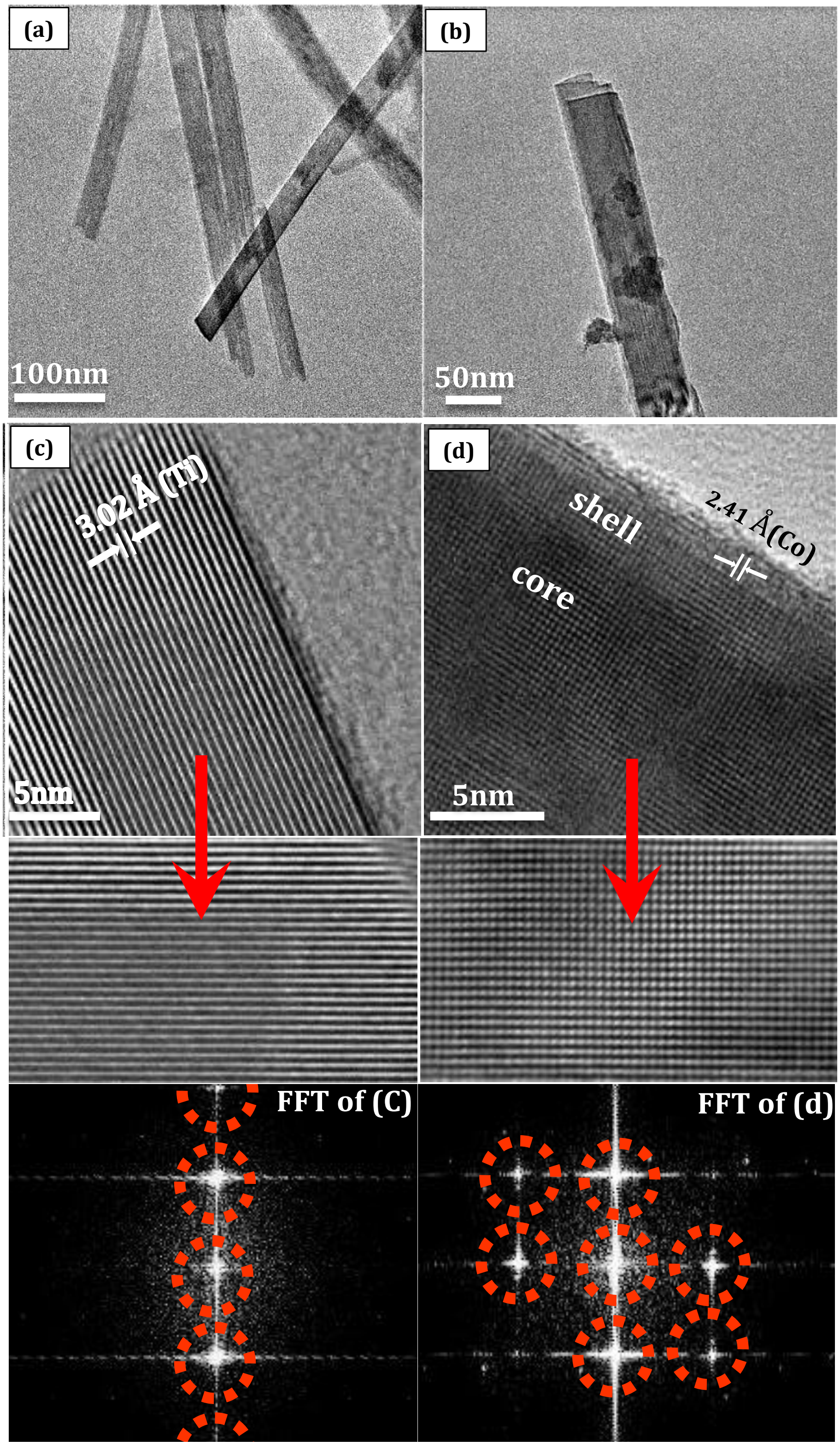

Figure: 4.5 (a, b) TEM images of TiO_2 nanorods and TiO_2/Co_3O_4 core/shell nanostructures (c, d) shows HRTEM image of the same and there corresponding FFT images.

Further spectroscopic studies have been carried out from the prepared core shell structures and shown in Figure 4.6. Material structural analysis has been carried out using Raman scattering and X-ray diffraction (XRD). Three Raman peaks around 225 cm^{-1} (weak), 446 cm^{-1} (strong) and 610 cm^{-1} (strong) in Figure 4.6a from TiO_2 nanorod array represents the O-Ti-O bending and the Ti-O stretching modes and corresponds to the TiO_2[172] which is consistent with the microscopy data discussed above. The Raman spectrum from cobalt oxide (Figure 4.6a) shows four optical-phonon vibrational modes at 465 cm^{-1} (moderate), 503 cm^{-1} (moderate), 604 cm^{-1} (low) and 663 cm^{-1} (strong).

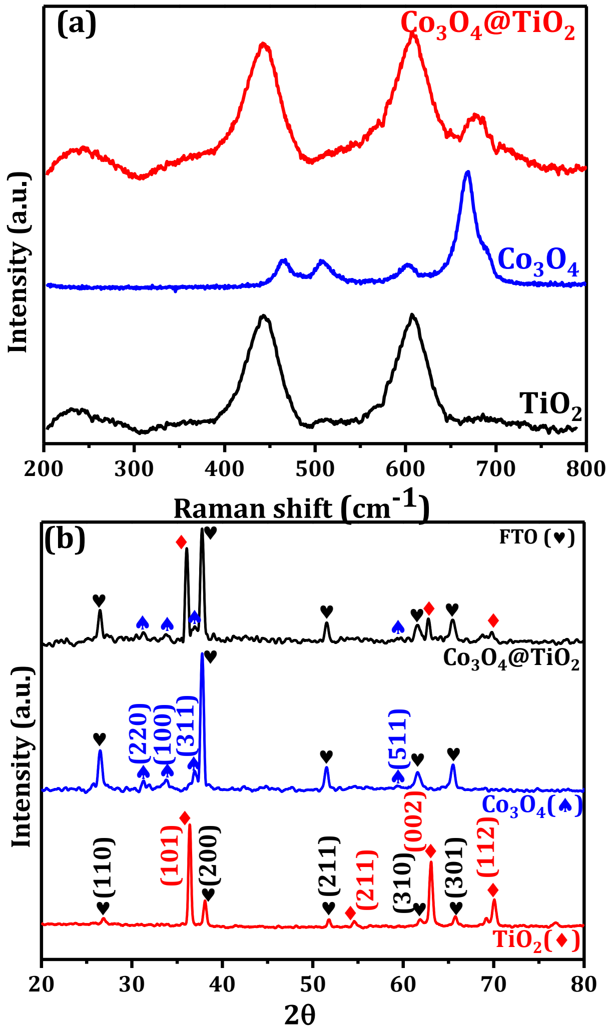

Figure: 4.6 Spectroscopic analysis of prepared core-shell NSs where (a) Raman spectra, (b) X-ray Diffraction patterns.

Raman spectrum from core/shell nanostructure shows combination of TiO_2 and Co_3O_4 modes as expected with some low intensity Raman peaks of cobalt oxide invisible as it get merged inside the strong peaks of TiO_2 nanorod array. The XRD pattern (Figure 4.6b) reveal the presence of crystalline TiO_2 (JCPDS 88–1175) corresponding to indexed planes (♦) which is in consonance with the HRTEM image (Figure 4.5c). XRD patters from Co_3O_4 on the FTO electrode show some week peaks (♠) compared to the intense FTO peaks (♥) because the structures prepared by electrodeposition techniques shows less crystalline nature in general. Where the top spectra of Figure 4.6b corresponds to core-shell nanorod array, confirms the presence of their related phases where Co_3O_4 is present in its spinel phase (JCPDS 42-1467).

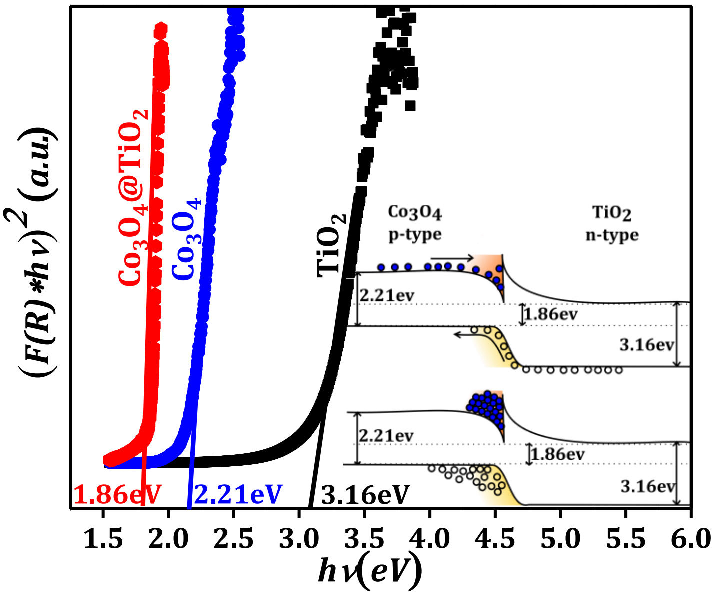

Figure: 4.7 Tauc plot obtained from diffuse reflectance spectroscopy with their corresponding band structures.

In order to investigate the band structure of the prepared structures, UV–Vis spectroscopy has been performed and for the relative band gap calculation their Tauc plots has been obtained as shown in Figure 4.7. Bandgap energies of the TiO_2 nanorods, the TiO_2/Co_3O_4 core/shell nanorods and pure Co_3O_4 films were calculated to be 3.16 eV, 1.86 eV and 2.21 eV respectively (Figure

4.7). It is evident here that the bandgap of core-shell nanostructures lie below that of both the materials, which shows the core-shell affects the properties of either of the material. This observation does not seem very correct intuitionally but is consistent with the available literature[152] and can be understood using the band diagram in the inset of Figure 4.7. Lower bandgap of the core-shell deposited on an FTO conducting electrode indicates an improvement in the charge transfer and overall improvement in performance when employed for electrochemical applications as will be discussed below.

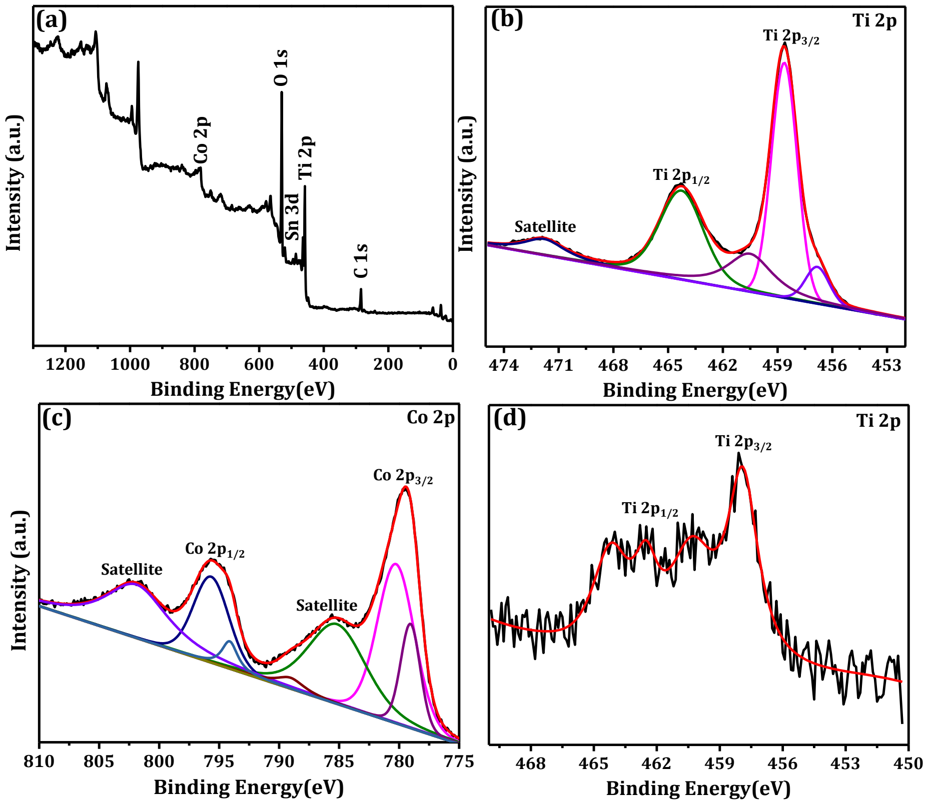

Figure: 4.8 X-ray photoemission consisting of (a) survey scan (b) TiO_2 deep scan (c) Co_3O_4 deep scan (d) TiO_2 scan by sputtered Co_3O_4 from core/shell.

The oxidation states and constituents present in the grown core/shell were analyzed via high-resolution X-ray photospectroscopy XPS as shown in Figure 4.8(a, b, c, d). The XPS survey scan confirms the presence of TiO_2 and Co_3O_4 phases along with the tin (Sn) peaks as contributed by the FTO substrate. The XPS survey and deep scans of titanium (Ti) and cobalt (Co) are shown in Figure 4.8 (a-d) respectively. Figure 4.8b, shows high resolution scan of Ti-2p shell taken from the bare TiO_2 nanorods, combined with three peaks where two major peaks at 459.0 eV and 464.5 eV correspond to Ti-$2p_{3/2}$ and Ti-$2p_{1/2}$, along with satellite peaks. In case of cobalt, Co-2p region (Figure 4.8c) contains total four peaks in which two are sharp (high intensity) peaks and remaining are satellite peaks. Major peaks are corresponding to Co-$2p_{3/2}$ (780 eV) and Co-$2p_{1/2}$ (796 eV). The cobalt oxidation states are highly related to the energy gaps between the Co-2p main peak and satellite peaks. Oxides, such as CoO, Co_2O_3 and Co_3O_4, exhibit Co-$2p_{3/2}$ peaks at nearly similar positions of 780.3, 779.9 and 779.3 eV respectively, due to the very similar Co-2p binding energies for both Co^{2+} and Co^{3+} makes it difficult to identify the oxidation state of Co ions from the binding energy alone. The strong satellite peaks and the splitting (energy difference) of the $2p_{1/2}$ & $2p_{3/2}$ orbital will be the deciding parameters for the oxidation state of the Co ion. The presence of weak shakeup satellites at 785.3 and 802.2 eV, which indicate that the Co atom is in oxidation state of 3+. In addition, the measured Δ value is 15.4 eV. Spectra given in Figure 4.8d, shows the Ti-2p XPS spectra record for core-shell nanorods by sputtering out the Co_3O_4.

4.3. Electrochromic behaviors

Oxides of titanium (TiO_2) and cobalt (Co_3O_4) are known for their electrochromic properties by virtue of their redox state dependent absorption[173,174]. Though studied extensively, both of these have serious demerits like poor cycle life when either of the two is used as the sole electrochromic agent. Being an inorganic material, TiO_2 shows required modulation in its optical properties at very high voltage[173] whereas it is hard to control the redox reaction in Co_3O_4 during the electrochromic applications along with the controllability it's very hard to grow stable structures on the FTO or ITO electrode due to lower adhesiveness. The core-shell structures deposited substrates have been studied here for potential use in electrochromism.

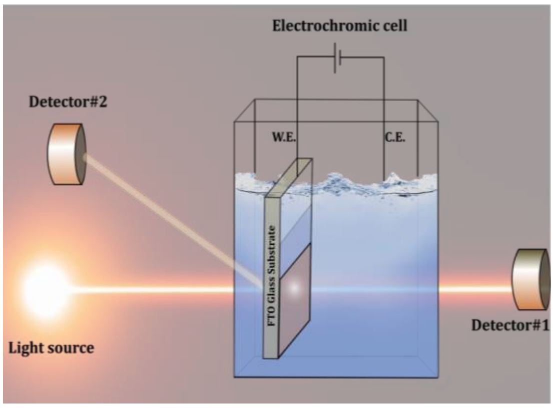

Figure: 4.9 Schematic illustration of electrochromic characterization using UV-Vis spectroscopy.

The electrochromic nature of the prepared device has been investigated by carrying out electrochemical measurements in quartz cell by using deposited FTO as working electrode, platinum wire as the counter and Hg/HgCl as reference electrode in three-electrode system with 1M KOH electrolyte solution. Figure 4.9 illustrates the setup used to carry out the electrochromic measurements. Detector#1 and detector#2 were used for transmittance and reflectance measurements respectively. Figure 4.10 shows various electrochromic characterization of the fabricated electrode including setup used during the measurement, diffused reflectance spectra, cycling, stability and efficiency calculation. Figure 4.10a shows the change in the reflectance spectra of working electrode (core-shell) as a result of applied bias of 1V (black curve) as compared to the as-prepared electrode (red curve). In OFF state, the sample reflects almost all colors out of which 410nm (blue) and 550 nm (green) wavelengths showing more prominent reflections. As a consequence of this blue-green primary color mixture, transparent sky-blue (magenta) color is apparent from the electrochromic device in OFF state (inset image of Figure 4.10d). When potential on the working electrode increases, it starts getting brownish in color with almost no reflection and eventually becomes opaque as shown in the corresponding actual images. Inset images correspond to the actual photographs of the electrode in its bleached (OFF, without bias) and colored (ON, with bias) states.

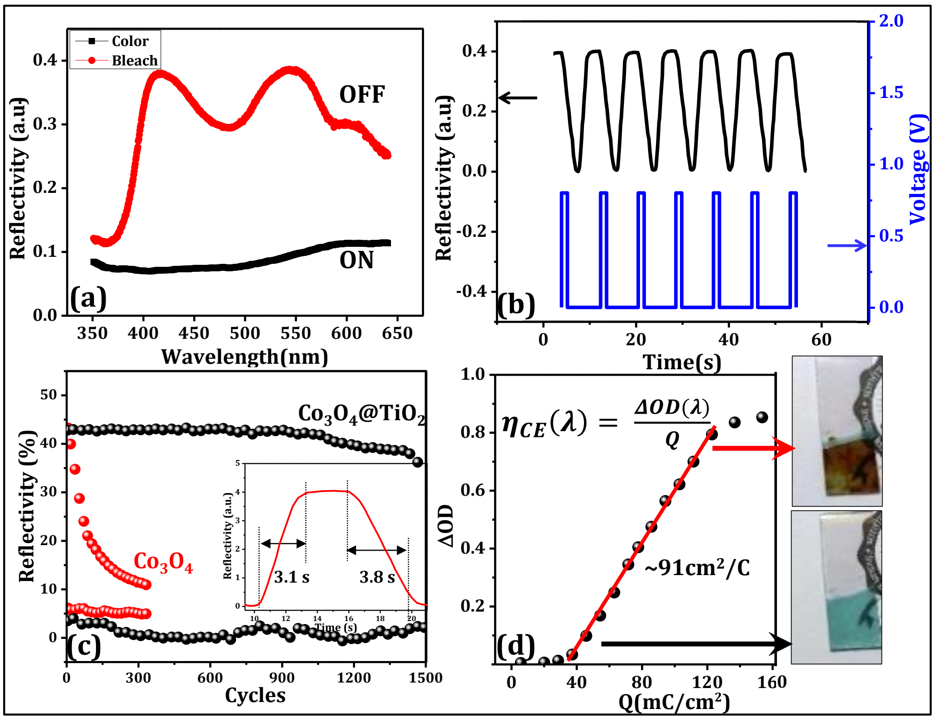

Figure: 4.10 (a) Reflectivity spectra of electrode in its ON (with bias) and OFF states (without bias) (b) ON & OFF cycling of reflectivity with corresponding bias of the electrode recorded at 422 nm, (c) stability test with response time analysis, (d) optical density (OD) of the electrode at 422 nm as a function of charge density and their corresponding images of the electrode.

It is worth mentioning here that the electrochromic experiment has been done from the core-shell structures prior to the annealing step. The image, corresponding to the ON state has been captured by pulling out the electrode after turning the device ON. To understand the cyclic nature of the fabricated electrode we have done in-situ measurement of the reflectivity changes by calibrating it with the absorption spectra with applied bias. Figure 4.10b shows bias induced switching between color and bleached states of the electrode. Furthermore, repeatability of the electrochromism has been checked upto 1500 cycles, which show core shell nanostructure array is more stable compare to their individual forms (red curve in Figure 4.10c). Cyclic change in the reflectance spectra has been recorded corresponding to 422.6 nm wavelength, which shows prominent change in the reflection (Figure 4.10b) with applied potential of 0.8 Volt. For quantitative analysis, coloration efficiency has been obtained by drawing a plot between changes in optical density as the function of charge required (Figure 4.10d).

$$\eta = \frac{\boldsymbol{Change\ in\ reflectance}(\Delta \boldsymbol{R})}{\boldsymbol{Current\ density}(\boldsymbol{J}) * \boldsymbol{time}(\boldsymbol{t})} \tag{4.1}$$

where ΔR is the change in reflectivity by application of potential and current flow through the circuit is denoted by J (current density). Time requred during the swtching of reflectance is signified by ‘t’. The coloration effciency (Eq. 4.1) is obtained to be ~91cm^2/C and color contrast ratio is ~80% (Figure 4.11).

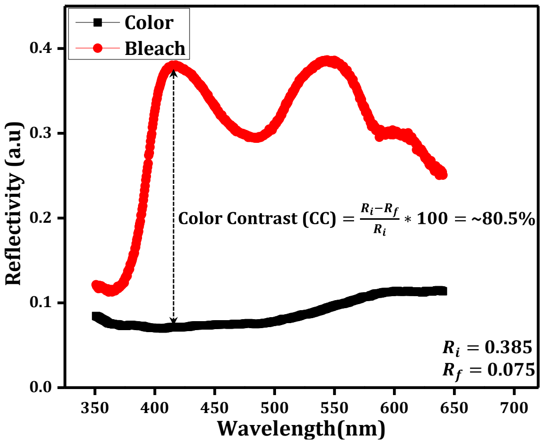

Figure: 4.11 Color Contrast ratio calculation of the fabricated electrode.

Above results reveal that the fabricated core-shell electrode shows very stable and power efficient (working at less than one volt bias) electrochromic properties as compared to oxides of titanium or cobalt alone. The advantage of using core-shell nanorods is good adhesion of Co_3O_4 on uniform and dense aligned TiO_2 nanorods. Single crystalline core nanorod array works as scaffolding for the cobalt oxide shell for controlling the charge transportation between the conducting electrode and electrolyte. Additionally, high surface area of nanorods reduces the biasing potential required to change the color of the cobalt substance. On the application of bias, during the voltage sweep between 0 to 0.8 V, the outer layer of the nanostructures made-up of cobalt, start getting reduced by taking negative ions present in the electrolyte. Comparison of electrochromic performance of other NSs has been summarized in Table 4.1

Table: 4.1 Comparison table include various parameters of electrochromism based previous reports

S. No.	Material	Electrochromic Coloration Efficiency (cm^2/C)	Reference No.
1.	NiO	63.2	Chen et al.[151]
2.	$NiO@TiO_2$	60.6	Cai et al.[152]
3.	$PANI@TiO_2$	37.1	Cai et al.[175]
4.	$WO_3@TiO_2$	67.5	Cai et al.[176]
5.	Co_3O_4	29	Xia et al.[177]
7.	$WO_3@TiO_2$	82[10]	Gil et al.[178]
8.	$Co_3O_4@TiO_2$	91	Present work[179]

---

[10] Represents "Reflection difference (ΔR)" in percentage.

4.4 Summary

Suitably designed nanorod array of TiO_2/Co_3O_4 core/shell shows superior electrochromic properties as a result of typical nature of the core-shell junction and miniaturization. The core-shell nanorods grown on FTO coated glass substrate by combining hydrothermal and electrodeposition techniques. Availability of high surface area, due to nano dimensional material with aligned rods, allows the electrolyte to penetrate and shorten the ions diffusion length to help improving electrochemical activity. Factors that increase the charge dynamics at the heterojunction formed between TiO_2/Co_3O_4 at the nanoscale. The core-shell structures also show power-efficient and stable electrochromism with a reflectivity variation of ~40% corresponding to 422.6 nm wavelength giving a coloration efficiency of ~91 cm^2/C. The color change between sky blue transparent state and dark brown opaque state take place with application of bias of as low as 0.8V and shows good cycle life of more than 1500 cycles. The fabricated active electrode composed with unique nanostructures is a promising for electrochromic device, which may have a profound impact on everyday life in the future which makes a way for the realization of energy saving self-sustained electronic devices.

Chapter 5

Hybrid Core/Shell Nanostructures: Improved Electrochromism

In this chapter, a combination of organic/inorganic based hybrid-nanostructures has been discussed to show as building block for an electrochromic display. Hybrid nanostructures' based array deigned using transition metal and conducting polymer show improved electrochromic properties like efficiency and stability with color tuneability. Here transition metal, nickel oxide's nanopetals (NPs) has been used as backbone for conducting polymer, polyaniline (PANI) nano-hemisphericals (NHs) to be deposited as shell. A specially designed two-step synthesis methodology has been used for the material fabrication, NPs deposited on FTO electrode using hydrothermal technique where electro-polymerization was used for the PANI deposition. The coaxial NPs/NHs core/shell arrays exhibit remarkable electrochromic performance compared to their individual ones. Device based on these hybrid nanostructures show power efficient optical switching from transparent to opaque with fast response.[11]

---

[11] *Mishra et al.,* **ACS Appl. Nano Mater**., (2018) X, pp XX–XX

5.1 Hybrid core-shell nanostructures

In current electronic devices nanoscience and nanotechnology has delivered its promises upto a great extent especially in the field of optoelectronics, materials science[180–184]. One of the most convincing reasons for this ongoing success story is related to the application specific (nano-) material design and there implementation in various devices. In current scenario, new nanomaterials need to be designed by adopting a dual approach where these can be used for potential application directly in energy storage and making other electronic devices power efficient. This will address the increasing demands by making good energy storage/generating devices and reducing the power consumption in other electronic devices. An electrochromic display is a very important device and efforts are going on in developing novel materials to be used for power efficient applications[124,144,185]. Device based on electrochemical activity show interesting behavior by controlling nanoscale architecture of the active material on the working electrode[186,187]. Among these, electrochromism of the fabricated electrode is one promising technologies, having various potential application in the current era of advancement from automobile to smart buildings to display system and many more[27,188]. Various organic, inorganic and their combinations as gel forms[124,144,185] & conducting polymers can be used as the active materials shows efficient electrochromic properties.

Currently conducting polymers are in increasing demand due to its biocompatibility, solution processable and inexpensive nature. Conducting polymer nanostructures exhibits high electrical conductivity, large surface area, short path lengths for the ions transport and superior electrochemical activity compare to their bulk counter parts which make them suitable for various applications[189–191]. Hence, primary focus to develop novel and multifunctional materials in one hand, and sustainable technologies on the other, for the sake of the same, several successful approaches have been explored to develop conducting polymer nanostructures. Along with CP its hybrid combination with inorganic nanostructures shows their combined properties during various applications[189,190]. At the same time tuning in the nano scale morphology prove to be very efficient in electrochemical based application such as supercapacitors[192,193], electrochromic displays[24,194], water-splitting[195–197], sensors[198–200] etc. Along with the general properties of these hybrid nanostructures, their tunable structures prove them as the out-standing functional segments or building blocks for various nanomaterials based devices[150,201]. The nanowire or nanofiber type shell of electrochromic active CP on TMO shows variation in color as a result of electric bias. It would be interesting to see the effect of morphology of polymer-shell on a TMO. Though expected to show different behavior, it would be interesting to look for an inorganic/organic combination with appropriate morphology which can result in transparent/opaque switching as a result of bias. This can be achieved even in the form of a device by using these hybrid nanostructures grown on electrode stack with the other appropriate electrode. The significance of growing these special kinds of hybrid nanostructures to improve the performance of various parameters of the electrochromic device like stability, color contrast ratio and optical modulation. In some previous existing reports, we found the combination of nickel and PANI for the electrochromic application with limited performance. Xia *et al*[202] has grown the NiO nanostructures on ITO electrode by chemical bath deposition method. Generally, structures grown by this methods show less adhesive nature with ITO electrode. When one is employing them in device perturbations, it shows limited cycling performance and most of the structures get peeled off from the electrode during the operation. Along with this some reports show poor electrochromic behavior of cheese like NiO nanostructures in combined with PANI due to less surface area for the electrochemical activity that diminished the color contrast appearance[203].

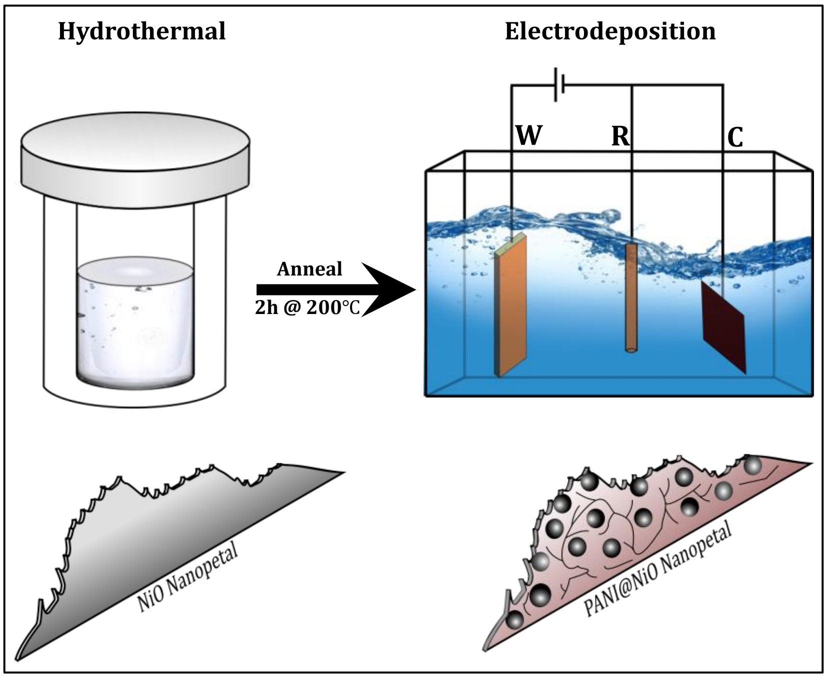

Figure: 5.1 Schematic presentation of two-step synthesis process of EC-electrode preparation combined of hydrothermal and electrodepotion.

The current chapter is based on attempts of significant enhancement in the electrochromic properties observed by designing a hybrid core-shell nanostructures with novel morphology where rose petal like NiO-NPs are covered with PANI nano-hemispheres (NHs) as shown in Figure 5.1 schematically. The NiO-NPs have been fabricated, by hydrothermal method as described in chapter 2, on a conducting FTO film coated glass substrate where conducting polymer based nano-hemispheres have been synthesis by electrodeposition method. A new preparation recipe (as described in chapter 2) has been adopted for the synthesis. A typical morphology of the hybrid nano core-shell is obtained which shows improved optical modulation in the electrochromism compared to their parental materials. Combination of both the materials and their morphologies (nanopetals covered by nano-hemispheres) on conducting and transparent FTO substrate provide excellent platform to enhance electrochromism in the device form. Switching between a transparent and opaque state can take place rather than switching between two colored states where contrast is always a concern addressing which a power efficient electrochromic device has been demonstrated.

5.2 Nickel Oxide (NiO)/Polyaniline (PANI) nano core-shell

The typical hydrothermal method for the synthesis of NiO NPs using $Ni(NO_3)_2$ as the nickel source, ammonium solution as the precipitant, potassium persulfate as the growth promoter which can be illustrated using following reactions[155].

$$Ni(NO_3)_2 + 2NH_4OH \rightarrow Ni(OH)_2 + 2NH_4NO_3 \qquad \text{(R 5.1)}$$

$$2Ni(OH)_2+K_2S_2O_8+2OH^-+H_2O \rightarrow 2NiOOH.H_2O+2SO_4^-+2H_2O \qquad \text{(R 5.2)}$$

During annealing:

$$NiOOH.H_2O + e^- \rightarrow Ni(OH)_2 + OH^- \qquad \text{(R 5.3)}$$

$$Ni(OH)_2 \rightarrow NiO + H_2O \qquad \text{(R 5.4)}$$

Here potassium persulfate ($K_2S_2O_8$) plays a key role during the formation of NiO NPs. In reaction (R 5.2), $K_2S_2O_8$ acts as an oxidant to drive the whole reaction and facilitate the heterogeneous nucleation. Without potassium persulfate, no NiO NPs will be formed on the substrates. Structural and morphological studies of nickel oxides nanostructures and polyaniline (PANI) coated NiO-NSs array have been carried out using scanning & transmission electron microscopies (SEM & TEM) and AFM. Figure 5.2(a) & (b) shows SEM and AFM image, respectively, of NiO nanostructures grown in the petals like shape, which can be seen in inset showing the magnified view of the same. The nanostructures, grown on flat transparent conducting surface are dense and uniform, which is essential for the electrochromic application, as has been intended for.

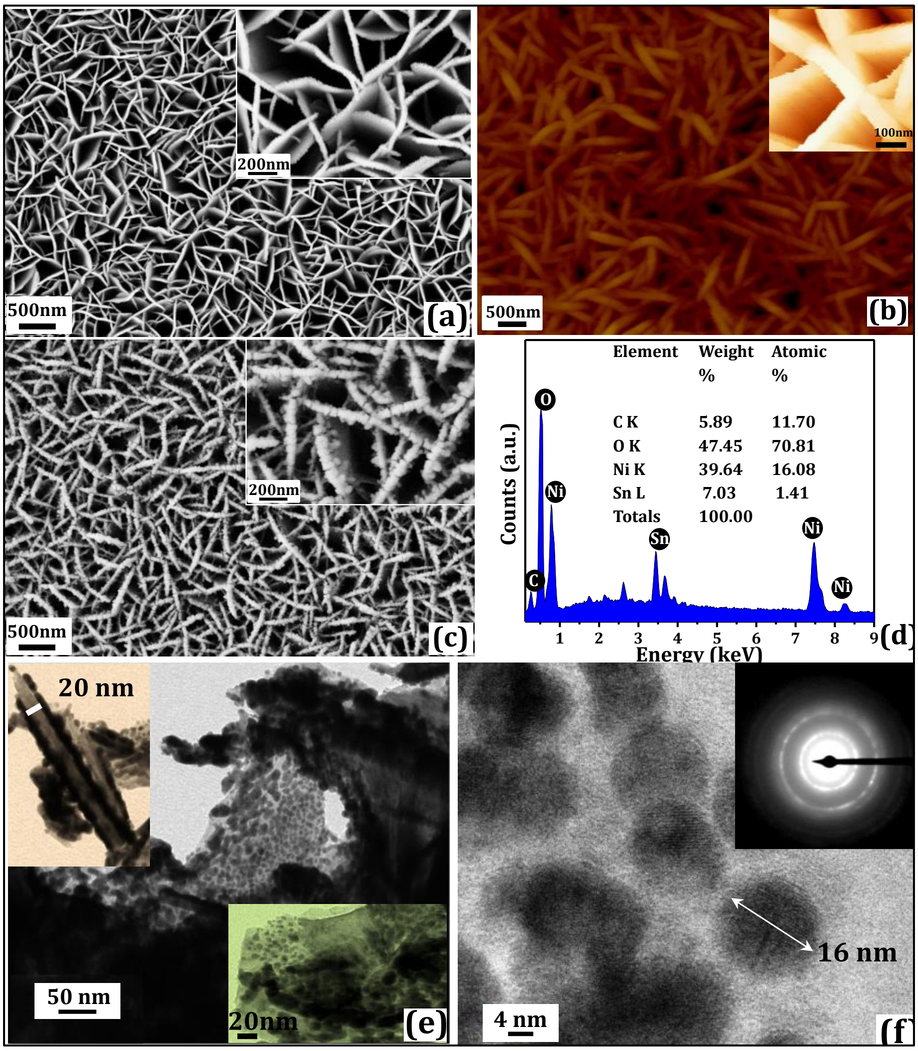

Element	Weight %	Atomic %
C K	5.89	11.70
O K	47.45	70.81
Ni K	39.64	16.08
Sn L	7.03	1.41
Totals	100.00	

Figure: 5.2 Surface morphologies of NiO nanopetals as seen using (a) SEM & (b) AFM along with their magnified views in insets (c) combined PANI and NiO in the form NHs @NPs (d) EDX spectra of the same along with (e) TEM and (f) HRTEM images, inset show diffraction pattern of present NHs.

Figure 5.2c shows the electro-polymerized PANI on the NiO NPs array. The hemispherical shaped look, resembling with the schematic (Figure 5.1), is obtained due to hetero-nuclear growth of PANI on NiO-NPs. This unique kind of morphology has been obtained by using growing methodology which is "initial current-pulse electrodeposition" followed by constant current mode deposition. The prepared nanostructures consist of elements Ni, C, O and Sn as apparent from corresponding peaks in energy dispersive x-ray (EDX) spectrum (Figure 5.2d), which reveals that NiO NPs and PANI NHs are present on the FTO electrode (source of Sn). Additionally, the information about size and shape of the grown nanostructures has been obtained using TEM. The TEM (Figure 5.2e) microstructures of the PANI@NiO on single nanopetal show grown hemispherical shaped PANI on the petal. The images in inset have been recorded from the cross section of a petal giving information about the width (white scale) and thickness of the grown PANI shell. The average width of the petals is around ~20nm on to which ~ 7-10 nm thick layer of PANI-NHs is deposited. Figure 5.2f shows a high resolution image of the same giving information about NHs present on the both sides of the petal. The size of the present NHs is around 14-20 nm (diameter). Effect of deposition time has been checked for hydrothermally deposited NiO petals. Figure 5.3 shows SEM images of NiO-NPs obtained when deposition of 2 hours to 5 hours was used which shows that as the deposition time increases density and thickness of the petals increases. Uniformity of the grown nanopetals on FTO electrode and its adhesiveness have been checked by peeling-off the film from electrode shown in SEM images in Figure 5.4a which looks well uniform from the bottom side and dense. Cross-sectional SEM image of the same is provided in Figure 5.4b to give the idea about the height of the petals. We have also checked the variations in the morphologies of the conducting polymer by electrodepositing it on to various substrates. Figure 5.5 show morphology obtained after electropolymerization of aniline on three different substrates FTO, NiO petals in flower shape and fiber of carbon which show different morphologies on each of these. On the FTO electrode it gets deposited very dense but not uniform whereas on petal it show hemispherical shape and wire like structure on the carbon fibers.

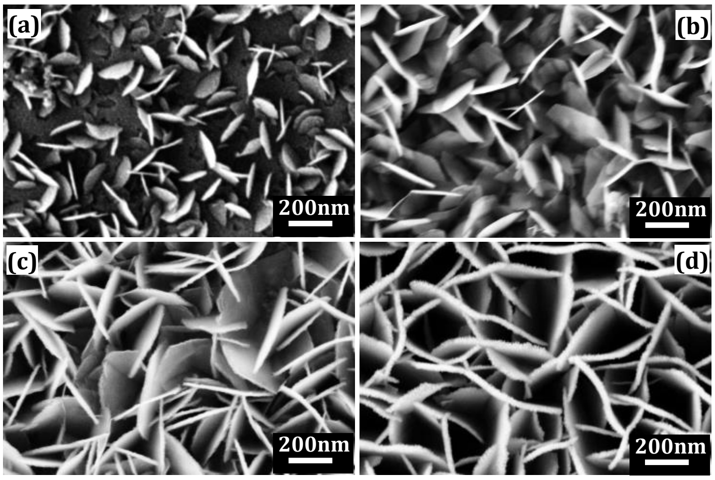

Figure: **5.3** Surface morphologies of NiO nanopetals grown by hydrothermal process with deposition time of (a) 2 hrs. (b) 3 hrs. (c) 4 hrs. and (d) 5 hrs.

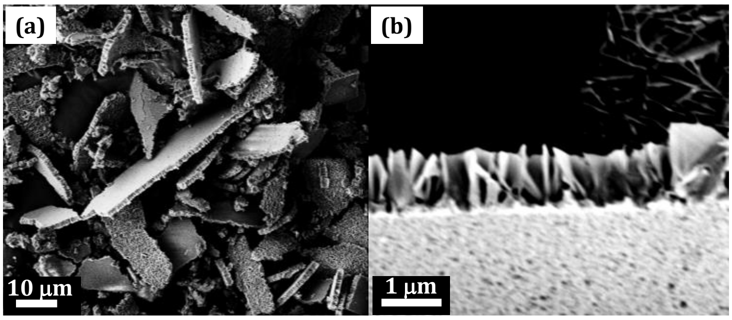

Figure: **5.4** SEM image (a) NiO-NPs film scratch-off from the FTO substrate (b) cross-sectional view of NPs.

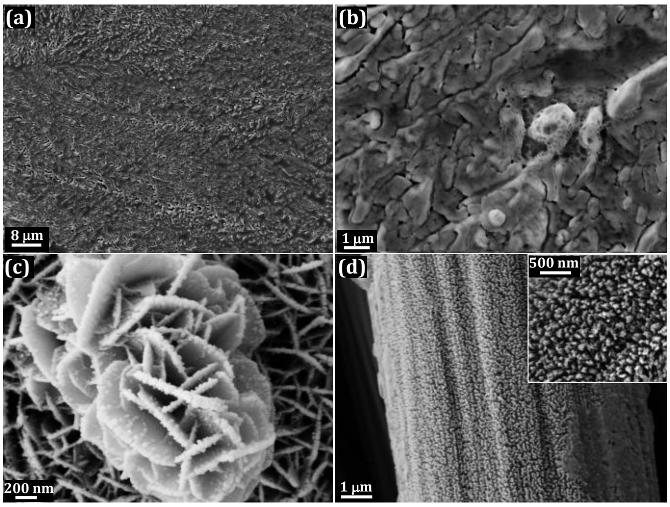

Figure: **5.5** SEM images of PANI grown on (a, b) FTO electrode (c) NiO nanopetals flower (d) carbon fiber

After microscopic study of the grown nanostructures spectroscopic study have been carried out to check Molecular composition and available bonding of PANI nano-hemisphere covered NiO. Raman spectroscopy from the prepared hybrid structures along with the constituents' nanostructure has been used to characterize (Figure 5.6a).

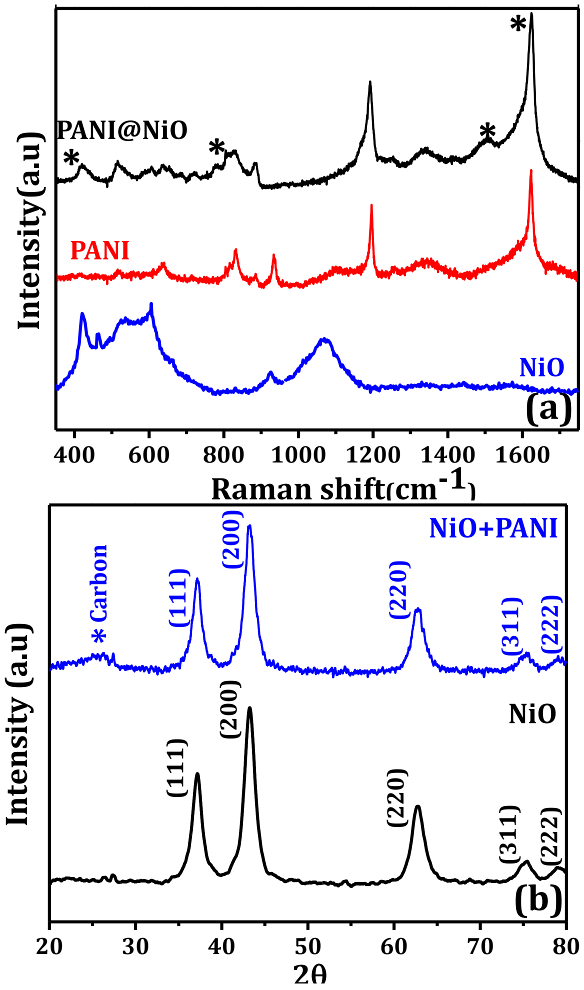

Figure: 5.6 (a) Raman spectra and (b) X-ray diffraction of EC materials.

Characteristic peaks (red curve) corresponding to PANI can be seen at 1623 cm^{-1} (C-C stretching) and 1529 cm^{-1} (C-N vibration). Peaks at 827cm^{-1} and 415cm^{-1} gives the information about the C–H bending, whereas other peaks at 1396, 1340, 1262, 1195 and 514 wavenumbers appear due to benzene ring distortion[204]. This spectrum can be compared with Raman spectrum of NiO NPs (blue curve in Figure 5.6a), two Raman peaks observed at 470 and 550 cm^{-1} corresponding to Ni–O bending and stretching modes, respectively, which are the characteristic peaks of NiO[205]. Figure 5.6b shows XRD pattern from NiO NPs and PANI@NiO showing diffraction peaks, in the order of decreasing XRD peak intensities, at 43°, 37°, 63°, 76° and 79° respectively. The peak positions and their relative intensities are in good agreement with the face centered cubic (FCC) structure of NiO-NPs revealing a crystalline nature of the NPs. In the presence of shell of PANI, XRD spectra show an additional broad hump around 23° due to the presence of carbon in amorphous state (from PANI).

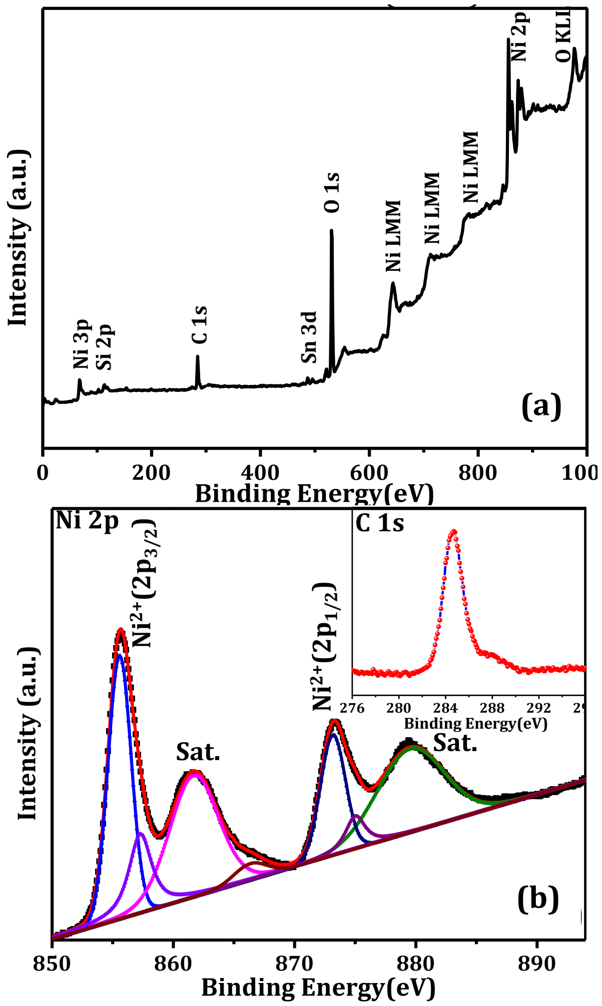

Figure: 5.7 (a) X-ray photospectroscopy survey scan and (b) deep scan of the Ni 2p and C 1s.

X-ray photoelectron spectroscopy (XPS) has been performed for the analysis of constituents and surface chemical compositions of NiO nanopetals. The XPS survey scan (Figure 5.7a) depicts composition of nickel and oxygen with the substrate peak contribution from tin (Sn) which is consistent with the EDX results. Both the characteristic Ni 2p peaks are observed at about 855.7eV ($2p_{3/2}$) and 873.4eV ($2p_{1/2}$) in high-resolution scan (Figure 5.7b). The deconvoluted spectrum contains overall seven peaks, two stronger peaks along with their satellite (weak) peaks. The carbon peak in the inset appears from PANI coated NiO NPs.

5.3 Electrochromism in NiO/PANI core-shell

Electrochemical properties of the abovementioned electrodes have been studied by carrying out cyclic voltammetry in typical three-electrode system at a scan rate of 50mV/s where fabricated electrode was used as the working electrode & SCE and Pt wire as the reference & counter electrodes respectively. Figure 5.8(a), the CV plot obtained during polymerization on aniline, gives the information about the oxidation state/potential. During the forward scan of the given cycle two major anodic peaks A_1 and A_2 were observed, which corresponds to the three states of the aniline as follows Leucoemeraldine salt (LS), Emeraldine salt (ES) and Pernigraniline (PG) [191]. In the reverse scan, the corresponding counter redox peaks appear as C_1 and C_2 due to reduction (Figure 5.8a). Along with two peaks A_1 and A_2 there is one small peak in between is correspond to the deformation of radical cation into the quinoid form. The CV scan of NiO-NPs alone shows only one redox couples A_3 and C_3 (Figure 5.8b) corresponding to the Ni^{+2} and Ni^{+3}. On the other hand, the CV scan with the PANI-NHs@NiO-NPs as the working electrode show an improved performance in terms of increased current density by a factor of ~100 (Figure 5.8c) as compared to their individual forms (Figure 5.8a & 5.8b).

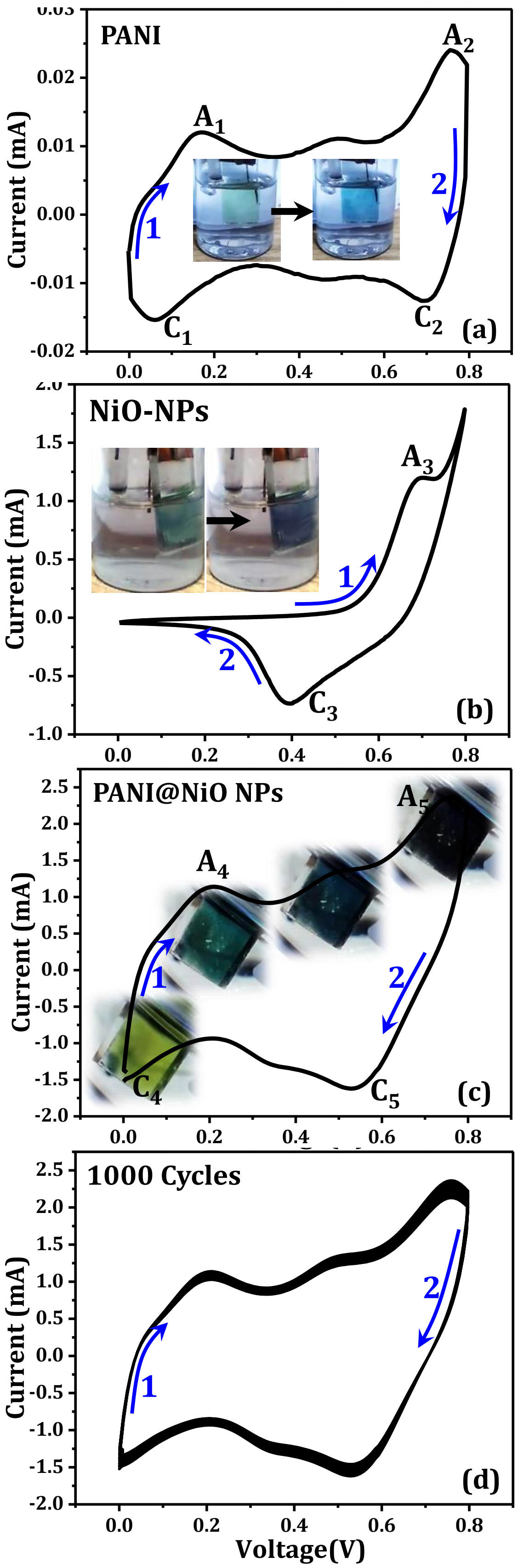

Figure: 5.8 CV measurement of synthesis material using SCE reference electrode (a) PANI (b) NiO-NPs (c) combination of both (d) show cyclic stability of the same.

A color variation of the working electrode (the fabricated substrate) is also evident during CV scan (Figure 5.8c) of the fabricated electrode corresponding to a given redox peak signifies that each state of the aniline shows different color and is reversible. Stability of the fabricated electrode has been tested to check electrochemical performance through multiple CV scans showing good cyclic stability upto 1000 cycles (Figure 5.8d). The improvement in the current density for NHs@NPs electrode is due to increased surface area of the active material available for interacting with the electrolyte. Overall, the combination of both materials shows improved coloration with viability of color tuneability within a bias range of only one volt.

The bias induced color switching of the fabricated electrodes characterized using electrochemical cell and has been validated using in-situ optical absorption studies in two electrode systems. Figure 5.9a shows the experimental set-up used for carrying out in-situ optical measurements using UV-Vis spectroscopy where quartz cuvette was used as the electrochemical cell with necessary electrode arrangements. The electrolyte consists of 1 M KOH with saturated calomel electrode (SCE) and Pt-wire electrode used as the reference and counter electrodes respectively. Figure 5.9b, shows the potential dependent absorption spectra of bare NiO-NPs electrode placed inside the electrochemical cell. An overall increase in absorption of all the wavelength in the whole spectral range (300-1000 nm) can be seen which signify variation in contrast of the electrode from being transparent to opaque rather than giving an appearance of a particular color. Inset image show actual electrode color appeared while in the biased and unbiased state given in Figure 5.8c. Figure 5.9c, shows the electrochromic behavior of PANI, which changes it color from transparent yellow to blue (Figure 5.8a), however remains transparent, during the operation due to lower contrast.

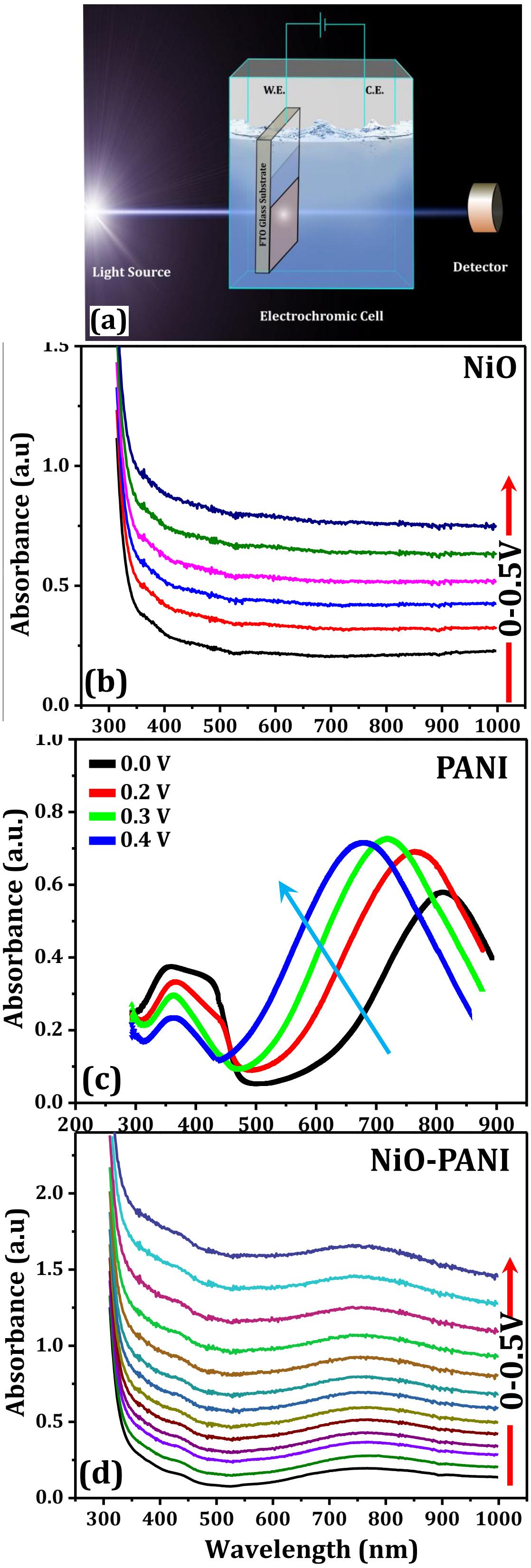

Figure: 5.9 (a) Experimental arrangement for carrying out in-situ optical measurements by applying varying bias in two electrode system with different working electrode as (b) NiO-NPs, (c) PANI and (d) PANI-NHs@NiO-NPs.

In PANI there are some intermediate redox states, initially in its reduced state LE show light yellow color, intermediate oxidize state show green color and finally gets converted into opaque state (as shown in inset of Figure 5.8c). During the electropolymerization aniline passes through various redox stats are as follows: LB→ES→EB→PS

$$PANI+ClO^{-}_{4} \rightarrow PANI^{+}(ClO^{-}_{4})+e^{-} \qquad (R\ 5.5)$$

$$ES^{+} \leftrightarrow (EB^{+})+(ClO^{-}_{4})+ H^{+} \qquad (R\ 5.6)$$

$$EB+ClO^{-}_{4} \rightarrow (EB^{+})(ClO^{-}_{4})+e^{-} \qquad (R\ 5.7)$$

Where reactions R 5.5 and R 5.7 correspond to the A_1 and A_2 peaks and R 5.6 show the protonation of Emeraldine salt into base. The absorption spectra of PANI alone deposited on FTO electrode with different bias given in Figure 5.9c show two peaks at 350 nm (low absorbance) and 800 nm (high absorbance) in zero-bias condition. With increasing applied bias (between zero to 0.5 V), higher absorbance peak show blue shift and enhancing the absorbance further. On the other hand the low absorbance peak did not show any significant shift in the peak position however a bias induced decrease in the absorbance was very clear as evident from Figure 5.9c. The bias induced diminishing of low intensity peak signify change of color from light yellow to sky blue as can be seen visually as well in the inset image Figure 5.8a. Though an appreciable color switching is observed, the color contrast in PANI is poor with no color tuning. Figure 5.9d shows the electrochromic behavior of hybrid fabricated electrode consisting of PANI(NHs)@NiO(NPs) with applied bias by keeping the electrode in the electrochemical cell. It can be observed from the UV-Vis spectra (Figure 5.9d) that the bias induced changes in absorption spectra much higher as compared to their individual forms (Figure 5.9b & 5.9c) in the same potential window. The change in absorption is consistent with the actual images (shown in Figure

5.8c), which shows a switching form transparent (yellowish) to opaque (dark brownish) with some intermediate colors.

5.4 Electrochromic device with NiO/PANI core-shell

To investigate the possibility of the above mentioned fabricated electrode in being used as an actual device, the electrode has been tested under device type condition by preparing a prototype electrochromic device in a sandwiched geometry. Steps involved in device fabrication have been discussed in chapter 2 in detail and can be summarized in the form of schematic in Figure 5.10.

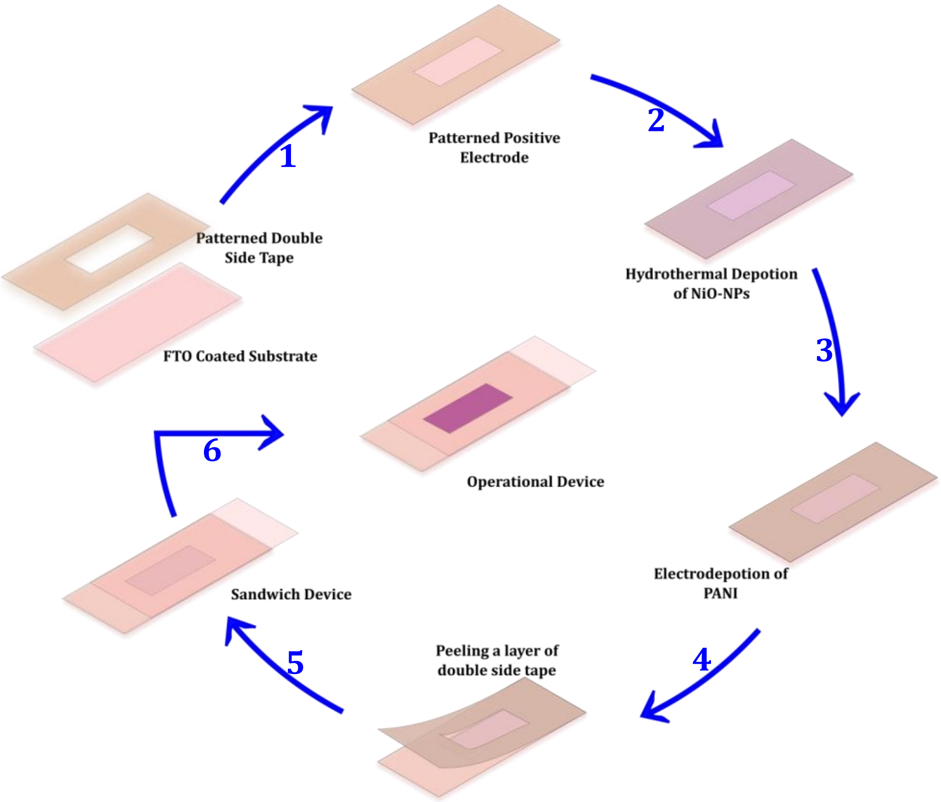

Figure: 5.10 Schematic presentation of different sequence followed during electrochromic device fabrication.

To evaluate the electrochromic properties of the fabricated solid-state device, NHs @ NPs grown on FTO electrode stick with other bare FTO electrode used as counter to enable the bias application to the electrochromic device.

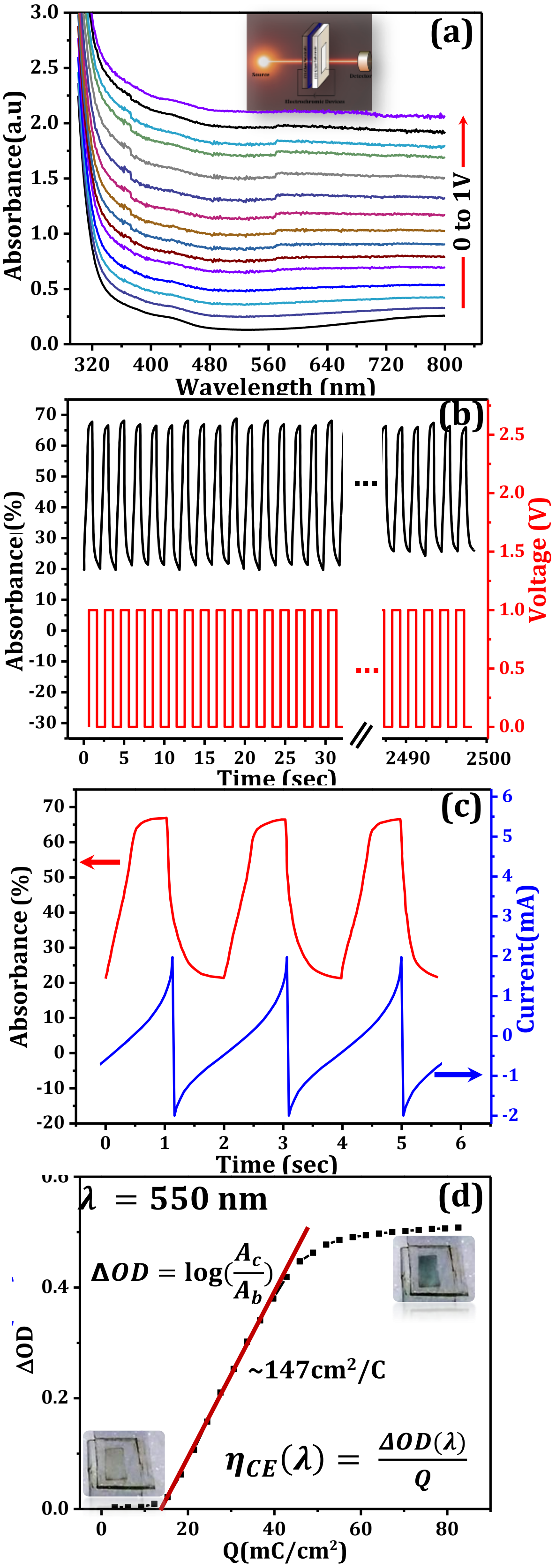

Figure: 5.11 (a) Absorption spectra variation vs bias, inset: set-up (b) cyclic stability of color switching device vs potential (c) current response of the same (d) OD and CE calculation.

In-situ bias induced optical property variation, optical constants' (optical density & coloration efficiency) measurement and cyclic repeatability of the electrochromic device has been investigated and shown in Figure 5.11. Measurements have also been carried out to calculate color contrast ratio and chronoamperometric response from the fabricated device**.** A bias induced change in absorption spectra from the electrochromic device, in the bias window of 0 to 1V, is shown in Figure 5.11a when measured in arrangement shown in the inset. It is evident from Figure 5.11a that the absorbance of the device increases by more than 20 times for the whole visible wavelength window. It indicates a switching of the device between transparent to opaque states reversibly. Cyclability and reversibility of the device has been studied by applying square wave pulses of 1 Volt. Corresponding change in the absorbance (for 550 nm) is shown in Figure 5.11b for 1000 cycles (2500 s). The device appears to switch between 22% to 67% absorbance in its OFF and ON states respectively. The amperometric response of the device, which gives the information about the current flowing through the device during the operation, has been provided in Figure 5.11c for fewer cycles for clarity. This has been used to estimate the corresponding charge flow (Q) while the bias induced color switching take place. Optical density (OD) and coloration efficiency ($\boldsymbol{\eta}$) of the device is the measure of power consumption by the device, have been calculated from its electrochromic performance, shown in Figure 5.11d, through following equations.

$$\boldsymbol{OD(\lambda) = log\left(\frac{1}{A_\lambda}\right)} \tag{5.1}$$

$$\boldsymbol{CE(\eta) = \frac{\Delta OD(\lambda)}{Q}} \tag{5.2}$$

where, A_λ is the absorbance for a given value of wavelength (550 nm in the present case). By calculating change in the optical density (ΔD) from Eq. 5.1 in ON and OFF state of the device $\boldsymbol{\eta}$ can be obtain from Eq. 5.2 the slope of the ΔOD (v/s) Q plot, given in Figure 5.11d. The color switching of the electrochromic device can be visualized from the actual images given in the inset of Figure 5.11d. CE ($\boldsymbol{\eta}$), which should be high for a power efficient electrochromic device, is estimated to be ~147 cm^2/C for the present device. The value is comparatively higher than the other devices fabricated when either organic or inorganic electrochromic materials were used alone. It seems that a hybrid electrochromic device made using inorganic/organic hybrid material is more efficient as compared to the individual ones.

5.5 Summary

Hydrothermally grown NiO nanopetals covered with electrodeposited PANI on an FTO electrode shows power efficient electrochromic properties as compared to the individual ones in an electrochemical cell as well as in the device form. Overall increase in surface area due to coverage of thin PANI over fine NiO NPs is the likely reason for improvement in the overall electrochromic performance of the electrode. An electrochromic electrode having only PANI or NiO-NPs show very poor color contrast in the colored and bleach state, which can be improved when PANI covered NiO NPs are used. The PANI@NiO electrodes shows great adhesion stability due to the inorganic NPs of NiO provides solid template foundation for polymer (PANI) growth. Eased electrons transport through the inorganic/organic nano interface along with higher surface area of PANI nanostructures increase the ion diffusion. The beauty of NiO/PANI core-shell electrochromic behavior is in its switching between transparent to opaque states rather than colored state as evident from bias induced increased absorption of whole visible spectrum with minimum bias of one volts resulting in absorption modulation of more than 45% (for 550 nm) and coloration efficiency of more than 145 cm^2/C.

Chapter 6

Special Nanostructures: Applications beyond Electrochromism

In this chapter, non-electrochromic related device-oriented applications of different nanostructures have been reported. These applications include supercapacitive properties of Ti, Co based metal oxides core-shell and field emission & glucose sensing properties of NiO nanopetals. Metal oxide based core-shell nanostructure array have been reported here to exhibit energy storage properties and ultra-thin thorns like structures of NiO show enhanced field emission. The NiO nanopetals like nanostructures show glucose sensing properties. In chapter 4, TiO_2/Co_3O_4 core/shell nanostructures were discussed to show efficient electrochromic display. The same structure also shows supercapacitive applications as will be discussed here.[12] In chapter 5, it was discussed how NiO nanopetals template is used to grow the nanostructures of PANI conducting polymer and prove to be very efficient in electrochromic application. It will also be reported here that the prepared NiO nanopetals are mesoporous in nature and show excellent electrochemical glucose sensing.[13,14]

---

[12] *Mishra et al.,* **ACS Appl. Energy Mater**., (2018) 1, pp 790–798

[13] *Mishra et al.,* **J. Mater. chem. C,** (2017), 5, pp 9611-9618

[14] *Mishra et al.,* **Nanoscale Research Letters**, (2018), pp 13-16

6.1 Nanostructures for energy storage: Supercapacitors

Nanostructures based applications such as energy storage where supercapacitor becomes increasingly popular, work on the principle of electrochemical redox reactions. Benefit of using supercapacitor in energy conservation is its higher power density while shorter charging time remains as an additional advantage. Pseudocapacitors, another member in the family of capacitors, works on the principle of reversible redox reaction near the surface of active electrode within the electrochemical cell[206]. Transition metal oxide (TMO)[152,153] have many associated properties which allows them to be used in energy storage applications, along with various other organic counterparts[185,207,208], when used alone or in the form of core-shell nanostructures.

The core/shell nanorods are prepared by constructing a nanorod core backbone followed by coating with an appropriate shell material. This method needs to combine different methods such as sputtering, hydrothermal technique, electrodeposition etc. to prepare core/shell nanorods arrays. Various types of core/shell nanowire arrays whose core or shell materials consist of metals, oxides, carbon, hydroxides, semiconductors, and polymers like core/shell of semiconductor @ semiconductor, semiconductor @ metal, metal @ polymer have been studied rigorously in past[154,158]. Transition metal oxides such as Co_3O_4, NiO, and TiO_2 are scientifically & technologically important materials for the applications in electrochemical energy storage[158,159], chemical sensing[160,161], catalysis[162,163], and electrochromism[96,164]. Well-defined core/shell nanostructure fabrication and obtaining tunable functions remain as the major challenges when it comes to the realization in the form of device. In recent years some progress has been made for developing cost-effective and controllable hetero-nanostructure by simple methods[165]. Still, there exists no simple and high-efficient method to synthesize transition metal oxide core/ shell nanostructure arrays.

In this section, two metals oxide, Ti and Co, have been combined by growing shell of the latter on the Ti core to explore its suitability as a supercapacitor. The electrochromic property of the same structure has already been discussed in chapter 4, making it appropriate for multifunctional application. A two-step process involving hydrothermal followed by electrodeposition technique have been employed to synthesized such a core shell nanostructures which makes a hetero-junction between the two oxides. It has been shown that the synthesized nanostructures prove to be an efficient electrode for the abovementioned application. In the core shell nanostructures, hydrothermally grown TiO_2 core provide the vertically aligned nanorods with high surface area, allows the electrolyte to penetrate and shorten the ions diffusion length, which cannot be compromised in energy storage. Where more details have been discussed in the experimental and synthesis techniques in chapter 2

6.1.1 Supercapacitive property of TiO_2/Co_3O_4 core/shell

Microscopic and spectroscopic study of the prepared core-shell nanostructures discussed in the chapter 4. For potential application in supercapacitors, the electrochemical performance of the synthesized core/shell nanorod array has been studied using cyclic voltammetry (CV) and chronopotentiommetry (charge/discharge) measurements. Standard three-electrode electrochemical system was used for this purpose, where core-shell deposited FTO-glass substrate was used as the working electrode with Ag/AgCl and Pt-wire were used as reference- and counter- electrodes respectively in 1 M KOH solutions in the potential range of -0.4 V to 0.4V. Figure 6.1a shows the recorded CV curves of the $Co_3O_4@TiO_2$ core shell nanostructures grown on FTO coated conducting glass at a scan rate of 50 mV/sec shows corresponding redox peaks. CV curve of the core shell nanostructures recorded with varying scan rates show the capacitive nature of the material with liner behavior with scanrate during operation in Figure 6.1b. The capacitive behavior of the designed nanomaterials comes from the redox reactions between Co^{3+} and Co^{4+}. Interestingly the Co_3O_4 electrodeposited film, exposed to the electrolyte, exhibits two redox peaks couples A_1/C_1 & A_2/C_2 shown in Figure 6.1a.

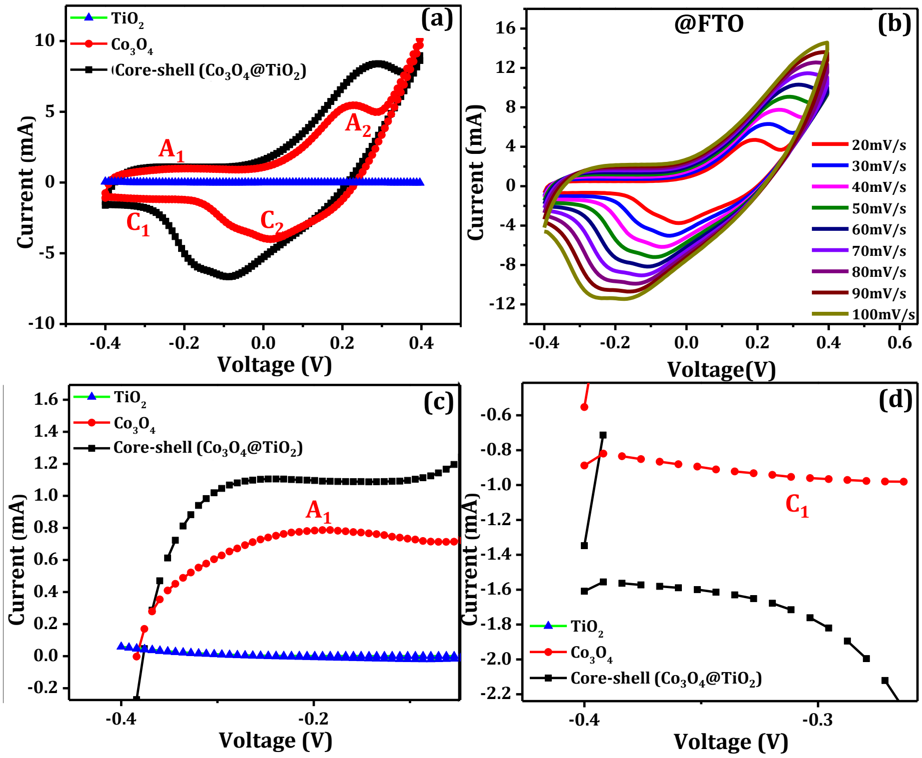

Figure: **6.1** (a) Anodic and cathodic peak analysis Co_3O_4 with and without the presence of TiO_2 nanorod array (b) CV curves of the TiO_2/ Co_3O_4-core/shell nanostructures at different scan rates (c, d) zoomed section of corresponding redox peaks spectra recorded in 1M KOH solution with scan rate of 50mV/sec (1 M KCL Ag/AgCl as reference electrode).

The first redox couple A_1/C_1 corresponds to the conversion between Co(II)/ Co(III) whereas A_2 could occur at higher potential range with C_2 present in the cathodic process represent the conversion of Co(III)/Co(IV). Cobalt oxide, when deposited on TiO_2 nanorod, does not show first redox peak in CV scan Figure 6.1(c, d). This interesting phenomenon is indicating that the cobalt oxide nanostructures, grown on the single-crystalline TiO_2, does not possess much active sites and ions entangled within the hetrostructure which is favorable condition improve overall supercapacitive behavior of the electrode. It is also noticeable that the Co_3O_4@TiO_2 core/shell nanostructures fabricated electrode exhibits higher current densities compared to their individual forms, indicating that the heterostructures composite film has higher electrochemical activity (Figure 6.1a).

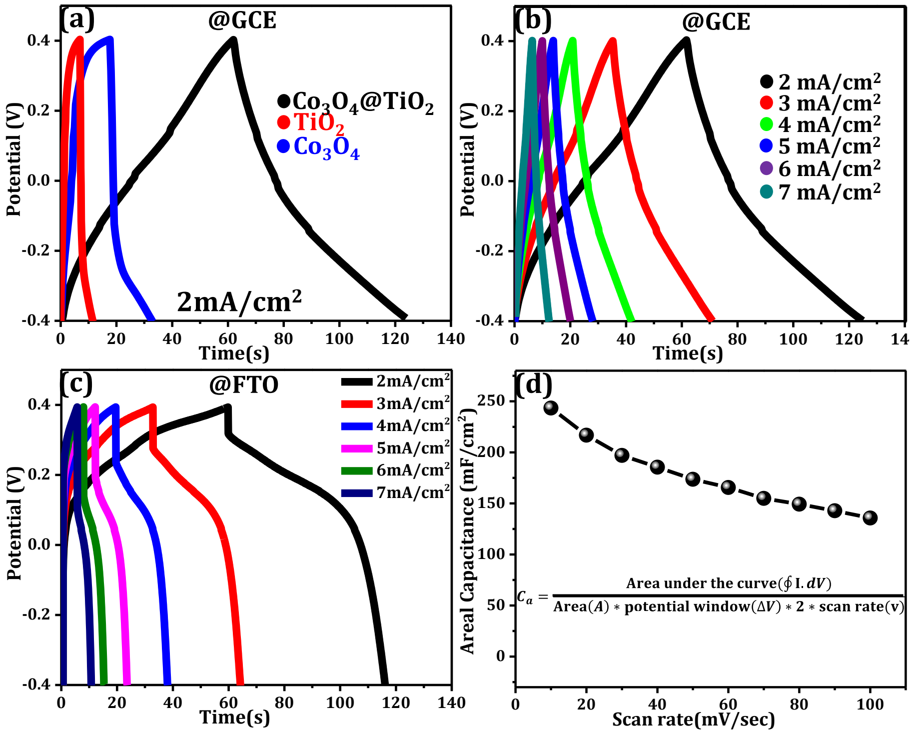

Figure: **6.2** (a) Galvanostatic charge-discharge curves of the core shell and their parental materials on glassy carbon electrode (b, c) charge-discharge study of the core shell array with various current densities on GCE and FTO electrodes, (d) areal capacitance of fabricated electrode as a function of scan rate.

Galvanostatic charge–discharge (CD) study of the fabricated core-shell nanostructures on glassy carbon electrode (GCE) as well as FTO electrode has been carried out. Figure 6.2a shows the superior behavior of core shell nanostructures as compared to their parental materials. Figure 6.2b & 6.2c presenting the charging and discharging curves of the core shell nanostructures on GCE and FTO substrate at various current densities, which shows nearly similar charging and discharging time except the IR drop which is present when the material is on an FTO substrate (Figure 6c). The IR drop in case of FTO electrode is higher because of the FTO-core-shell Schottky junction effect. On the other hand, the same core shell nanostructure when peeled-off from FTO surface show nearly negligible drop (Figure 6.2b) when tested using a GCE. Areal capacitance (C_a) of core/shell nanostructures, obtained from the CV curve at various scan rates, is shown in figure 6.1d, as obtained using following formula (Eq. 6.1), was found to be ~173.4 mF/cm^2 at the scan rate of 50mV/sec.

$$\mathbf{C_a = \frac{Charge(Q)}{Area(A)*potential\ window(\Delta V)}} \tag{6.1}$$

where, C_a is areal capacitance, A is active surface area, ΔV is potential range. The effective working area dipped into the electrolyte and the mass loading of the electrode are 0.35cm^2 and 0.242 mg/cm^2 respectively. The CD curve is important as time constant (τ), mass loaded (m) and active area (A), can be obtained from this which provides information about the specific capacitance of the electrode material. Another parameter in the characterization of supercapacitor, specific capaciance (C_s), is calculated by following Eq. 6.2 and found to be 341.88 F/g.

$$\boldsymbol{C_s = \frac{I*\Delta t}{m*\Delta V}} \tag{6.2}$$

where, current density (I), Δt is dicharging time, 'm' is loaded mass per unit area and ΔV is potential range. Variation in areal capacitance as a function of scan rate (Figure 6.2d) shows a reciprocal relationship between the two. Stability of the capacitive behavior is another important parameter in supercapacitive studies. The areal capacitance has been calculated and shows little variation (Figure 6.3) in its value at the end of 5000th cycle indicating a stable capacitive behavior. Changes in the CV curve from 1st to 100th scans and 5000th scan can be seen in the inset of Figure 6.3. There can be seen some change in the peaks intensity but the overall negligible modulation <3% in the area under the curve further confirms the stability and robustness of the material for supercapacitive application.

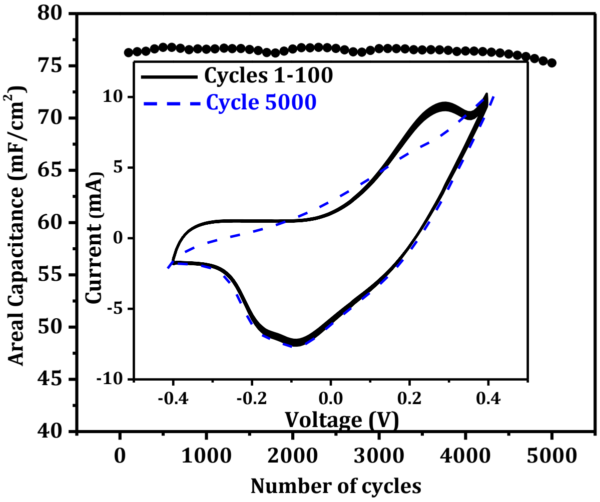

Figure: **6.3** Stability test of areal capacitance with multiple cycles CV curve at 50mV/sec.

Possible origin of the above-mentioned observed improved supercapacitive behvior of core-shell structures, as evident from high aerial and specific capacitance values, can be understood as follows. Apart from the increased surfece area resulted due to low-dimension, very small effective device width is also likely to play a role in giving the very high capacitance values as evident from the supercapacitive bahaviour (Figure 6.1) of core-shell. It is known that a hetero-junction at the TiO_2/Co_3O_4 core-shell structure is formed[160,161] which restricts the movement of electrons by confining them near the core-shell junction. The electrons quasitrapped near the junction needs energy for conduction and thusususlly remains stagnent and maintains the charged state of the capacitor until discharged intentionally by connecting a load which prompts the trapped electrons to flow and to constitute the current through the circuit. Under this geometry, the capacitence will be dominated either by the thickness of the shell or the width of the junction (if the core-shell thickness is very high). In the present situation, the reduction in effective capacitor width due to very thin shell thickness (chapter 4) in addition to increased effective surface area appears to be likely reasons for the manyfold imrpovement in the supercapacitivie behaviour of TiO_2/Co_3O_4 core-shell electrode. The current study establishes that metal oxides core-shell structure has capacity to be used for supercapacitive applications.

6.2 Nanostructures as better field emitters

Beginning of the current century has witnessed foundation of great breakthroughs in the field of optics, electronics and optoelectronics achieved by designing novel materials in their nanostructured form[209–211]. Nanostructures (NSs) of semiconductors as well as oxides (usually insulating in the bulk form) exhibit extremely important properties in numerous applications like electrochromism[152], memory[140] devices and sensing[212,213] and many others. Various NSs of carbon, silicon and oxides have been studied very extensively for last couple of decades for application in field emission (FE) in an endeavor to get a FE based display device[76,77,214,215]. Other than the display devices, the FE, a quantum mechanical tunneling phenomena is of great interest, due to its application in devices such as microwave device, x-ray source etc.[69,70] One dimensional (1D) materials such as nanotubes, rods, wires and needles are having high aspect ratio that provide local electric field enhancement[71] which is a favorable condition for FE. Similarly two dimensional (2D) materials such as nanosheets, wells, plates have novel and unique physical and chemical properties[72]. High surface area to volume ratio with nanoscale thickness makes them suitable for a given applications by exploiting the appropriate property of the NSs[73]. Nanosheets, another 2D materials, can get arranged like flower petals (nanopetals)[74]. If these NSs (wires or petals) are well aligned, very good FE is theoretically possible irrespective of the material however, the FE efficiency and ease with which FE can take place may vary and makes a topic of research as has been investigated covering a variety of materials in their different nano forms[75].

Carbon, in the form of nanotubes and nanoflakes, has been established as a landmark material for field emission[76–81]. In-spite of being one of the well-studied systems, carbon NSs based FE devices are not available commercially[77]. This has forced scientists to start quest for another material that are good field emitters, parallely, if not as an alternative to the carbon based field emitters. Nickel based materials[82] and different oxides[83,84] are amongst materials which have been studied in search for good field emitting materials other than elemental nanomaterials like carbon[81] and silicon[71]. Nickel oxide (NiO), a combination of above two, has drawn attentions in recent years due to its dielectric properties attributed to its wide band gap[216]. Additionally, recent studies from NiO, widely studied for various applications in electrochromism[24], gas sensing[217], p-type transparent conducting electrodes[73,218], also include investigation of its optical and emission properties[219]. Similarly, hexagonal shaped nanopetals composed of multilayer mesoporous nickel oxide films grown by precipitating hydroxides followed by calcination process, shows excellent electrochemical capacitance[220]. Such an application spread of NiO has been welcomed and being explored for electron field emission properties and seems to have promise as it is relatively easier to fabricate by various routes including traditional hydrothermal process and recently reported[220] novel two-step strategy to fabricate NiO nanoplatelets. Vertically aligned cone-shaped NiO nanowires, fabricated using a simple technique, exhibits a field emission properties[219] with threshold field of ~6500 V/mm and turn on field of ~11500 V/mm giving rise to a field enhancement factor of ~ 2000. The abovementioned FE parameters from a few hundred nanometers thick NiO nanowires are comparable to those reported for well aligned carbon nanotubes. For wider acceptability of field emission application a better turn-on and threshold field is required and methods to achieve the same should be investigated. The characteristic of the FE, a quantum mechanical tunneling effect, of any material is dependents on its structural, chemical, mechanical, electrical and thermal properties[221,222]. In addition, work function ($\emptyset$) and surrounding conditions such as vacuum, temperature and distance between the electrodes play an important role. The stability of a FE current is ascertain by the consistency in the $\emptyset$ along the surface of the emitter. This may vary under the influence of the adsorption of external gas molecules and migration of the material from the emitter[222]. Methods to improve FE include increasing pulse voltage induced electric field, improving the vacuum system and moderate heating of the cathode to protect it from adsorption of residual gases[223]. Recent study reveals the role of surface morphology in the field emission properties from CdS NSs[224]. Other players in controlling the field emission properties include the nanostructures' size and its aspect ratio etc[71,77]. Appropriate modifications in surface morphologies that can take care of these aspects may lead to improved FE properties upto an extent to make it possible to bring FE device to a reality and this makes the basis of current study.

The current section of the chapter reports an observation of significant enhancement in the FE properties from rose petal like NiO NSs covered with ultrathin nanothorn like structures. The NiO NSs fabricated, by hydrothermal method,[24] on a conducting FTO film coated glass substrate shows three orders of magnitude better turn on field and threshold fields as compared to the previous reports on NiO[219]. Details about the synthesis of these nanostructures have been discussed in chapter 2 (section 2.5.8). The modifications induced by morphology (nanothorn covered well aligned NiO NSs) and the design (presence of conducting FTO film) introduces certain perturbations in the system that addresses the bottleneck issues associated with limited FE properties from metal oxide NSs. Observed improvement in the FE properties have been explained based on the adequate understanding of physics by considering various aspects of material and how it gets affected by the induced perturbations in and around the NiO NSs. Where more of details have been discussed in the experimental and synthesis techniques of chapter 2

6.2.1 NiO nanothorns: Structural Properties

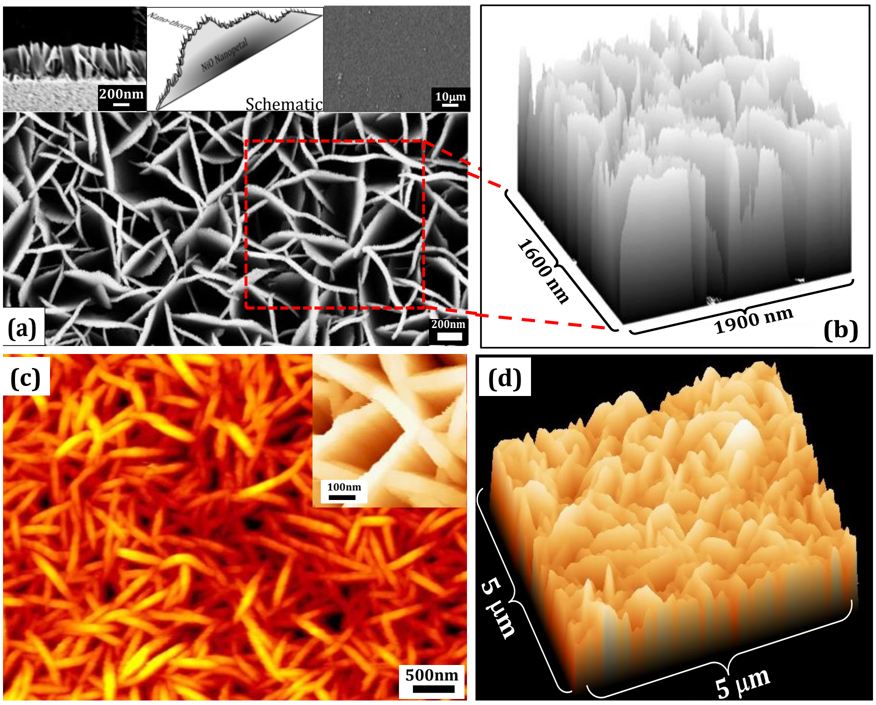

Figure: 6.4 Rose-petal type NiO NSs can we seen by (a) SEM with it cross-sectional image (left inset), nanopetals schematic in mid-inset and uniform wider area of about hundred microns (right inset) (b) 3D surface plot obtained from a portion on SEM micrograph using Image-J software. (c, d) 2D and 3D AFM images of the same.

Microstructural details and morphology of NiO nanostructures have been studied using scanning electron microscope (SEM). Figure 6.4a shows very dense rose-petal like structures of NiO which have been grown on the FTO film on a flat glass substrate. Very fine thorn like structures on the top of the petal, favorable for field emission, can be visualized by the Figure 6.4b processed SEM image using "Image-J' software. AFM images of the same have been given in Figure 6.4(c, d) confirming the presence of petal like structures. Thickness of each petal is around 25-30 nm. We have discussed more on the microscopic study of the synthesized morphology in the chapter 5 (section 5.2). The density and uniformity of the film can be appreciated from the right inset in Figure 6.4a which shows that hundreds of microns wide area can be uniformly deposited with such kind of nanoflakes covered with nano thorn on the top edge. Cross-sectional view of the NiO NSs can be seen in left inset (Figure 6.4a) shows vertical alignment and the height of the petals. Alignment and uniformity of the film grown on the FTO substrate can be seen from scratched-off parts of the film by SEM images given in Figure 5.4a in chapter 5 showing very well grown film well connected to the substrate. X-ray photoelectron spectroscopy (XPS) has already been performed to check constitutes (Figure 5.7a&b in chapter 5) in the sample which confirms the presence of Ni & O in the prepared samples under study. It is necessary to identify the phase of the film to ensure any physical property associated with the material thus, UV-Vis spectroscopy and X-ray diffraction (XRD) have been carried out for this purpose. XRD pattern (Figure 6.5a) clearly shows diffraction peaks, in the order of decreasing XRD peak intensities, at 43°, 37°, 63°, 76° and 79° respectively. The peak positions and their relative intensities are in good agreement with the face centered cubic (FCC) structure of NiO-NSs revealing a crystalline nature of the NSs[225].

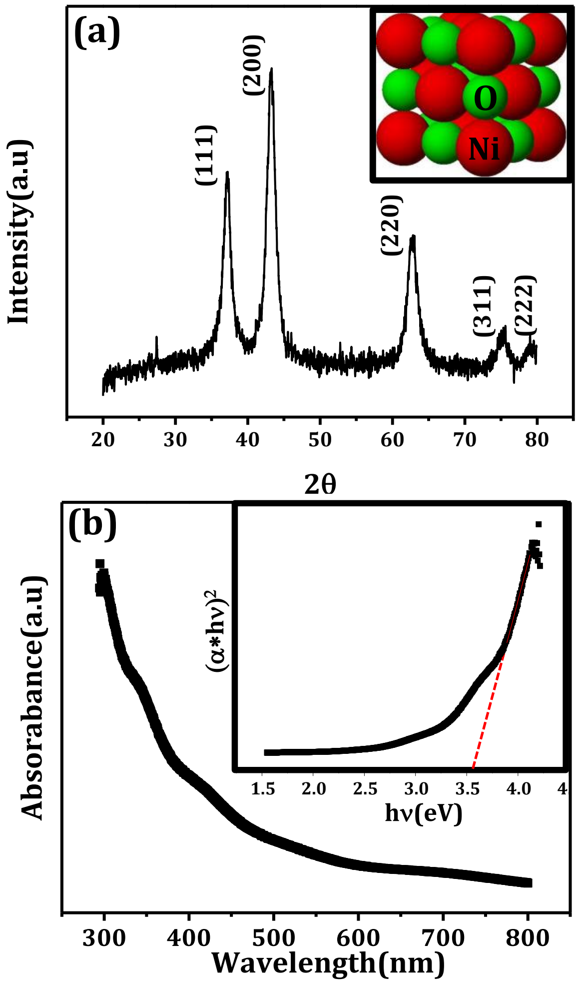

Figure: 6.5 (a) XRD pattern of NiO-NPs. Indexing predicts an FCC structure as represented in inset. (b) UV-Vis absorption spectrum of NiO NSs with Tauc-plot in the inset showing the band gap estimation.

UV-Vis absorption spectrum (Figure 6.5b) of NiO NSs and corresponding Tauc-plot of the same (Figure 6.5b inset) has been employed to estimate the optical band gap (E_g). The optical band gap of NiO-NPs film calculated from the TP is observed to be approximately 3.61 eV, which is consistent with the values reported earlier[152]. From the above discussion it has been established that the sample contains FCC-structured, crystalline, dense, well aligned nano-petals of NiO which is covered with very fine (nano-) thorns of size of a few nanometers making it an ideal candidate for electron field emission applications. With the band gap value handy, it will be easier to understand the inherent physical process and mechanism for controlling the emission and fabrication of a cold cathode FE device.

6.2.2 NiO Nanothorns: Improved Field Emission

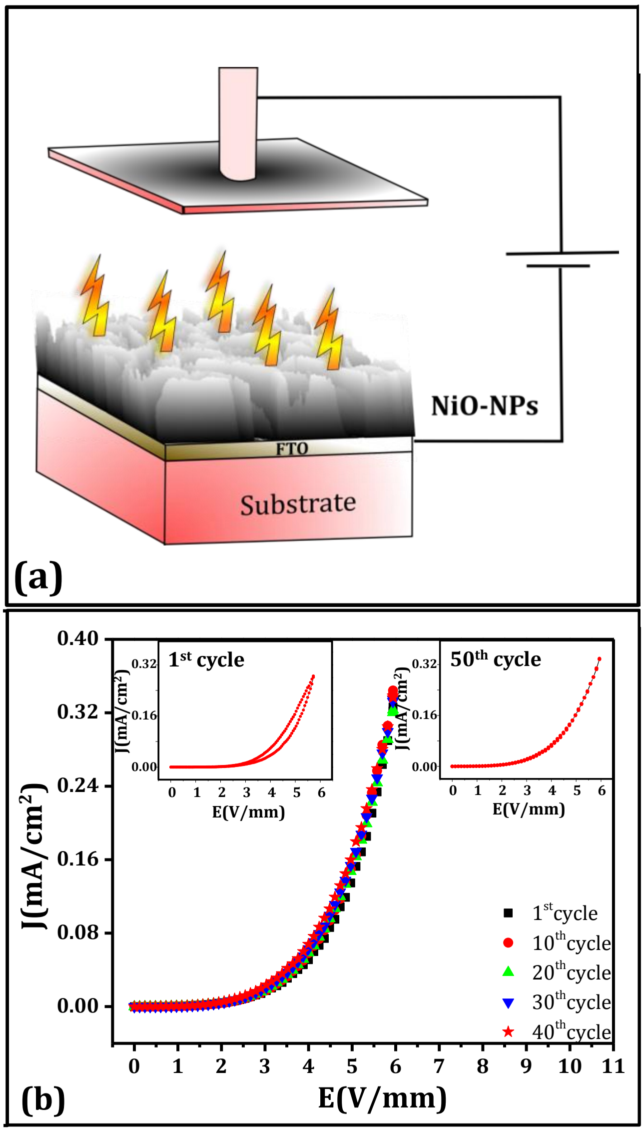

Figure: 6.6 (a) Schematic illustration of parallel plate field emission measurement set-up (b) field emission (J-E plot) obtained from NiO-NPs@FTO at various cycles. Insets show J-E curves on 1st and 50th cycle.

The electron FE measurement has been done in vacuum with NiO NSs sample mounted on cathode and placing the anode with suitably applied bias to initiate the FE. Figure 6.6 shows the schematic of the geometry used for FE measurement and the corresponding field emission (J-E) results. Schematic illustration of the geometry (Figure 6.6a) depicts the ejection of electrons (field emission) from the NiO NSs, deposited on conducting FTO film, as a result of appropriate bias applied to the top electrode. The FTO film not only acts as the electrode to bias the NiO NSs but also may provide electrons due to its conducting nature. The 3D structures of SEM images NiO NPs on the FTO layer, works as cathode for the emission, shown in Figure 6.6a. The FE from NiO NSs (Figure 6.6b) has been characterized by measuring the macroscopic current density (J) versus macroscopic electric field. As the bias at NiO-NPs@FTO cold cathode and Cu plate anode increases, it is expected that NPs starts emitting electrons after a threshold value (to be defined later) as a result of tunneling of electrons from the NiO NSs to the cathode through the vacuum gap (0.5 mm in the present case). Figure 6.6b clearly shows a fairly high noticeable current (mA) flows with an applied bias of a few volts which will be calculated quantitatively later on. It is apparent from figure 6.6b that at the electric field of around 3 V/mm sufficiently large numbers of electrons start tunneling out from the surface of cold cathode. This electric field appears to be very small as compared to various other nanostructured material reported so far[84,226,227]. Another term important in characterizing the FE properties is the "turn on field" which is traditionally defined as the field required to get a FE current of 10 $\mu A/cm^2$. The observed turn on field is found to be 1.2 mV/μm (or 1.2V/mm) which is very less as compared to other NiO NSs[71,219]. The observed turn-on field is at least thousand times (three orders of magnitude) better than the cone shaped NiO nanorods fabricated by Zhang et al[219] using hydrothermal method. Explanation for the observed low turn-on field will be discussed in the later sections.

From application point of view, stability is one of the key parameters to be discussed. We have done FE study for multiple cycles as demonstrated in Figure 6.6b which shows FE in 1st, 10th, 20th, 30th and 40th cycle exhibiting consistency in emission current. In each cycle, emission current retains its value, which is an evidence of cathodic stability. Furthermore, FE plots in first cycle and 50th cycle have been shown in the insets of Figure 6.6b separately for comparison. During the cyclic measurement an interesting phenomenon was observed. During the first cyclic scan when voltage goes from initial to final and again returning back to the initial value a hysteresis appears in the 'J-E curve' (left inset Figure 6.6b). It is evident from the insets of the Figure 6.6b that hysteresis is present in the first cycles but as the cycle proceeds, it disappears without changing the value of turn-on field and corresponding current values. This gives an indication that the field emission stabilizes after a few cycles. Hysteresis in the field emission has been seen very frequently in carbon based NSs like graphene or CNTs [228–231]. Players involved in the observed hysteresis in J-E curve include electrostatic alignment, captivity of carrier in deep layers, absorption & de-absorption of gas molecules etc. [232] has been well discussed. Hysteresis in J-E curve (Figure 6.6b) from NiO might be also due to the above-discussed phenomena as probability of absorption/deabsorption of gas molecules is higher here as it depends upon the morphology, structures and high surface area to volume ratio. In addition to this NiO is well known for its gas sensing properties which support the above claim[72] that it has capability of absorbing various gases and other suitable materials in order to be sensed. The absorbing property of NiO NSs is also supported by the fact that the hysteresis disappears (Figure 6.6b, right inset) after a few cycles when kept in vacuum for some time as that helps in removing the adsorbed gases etc.

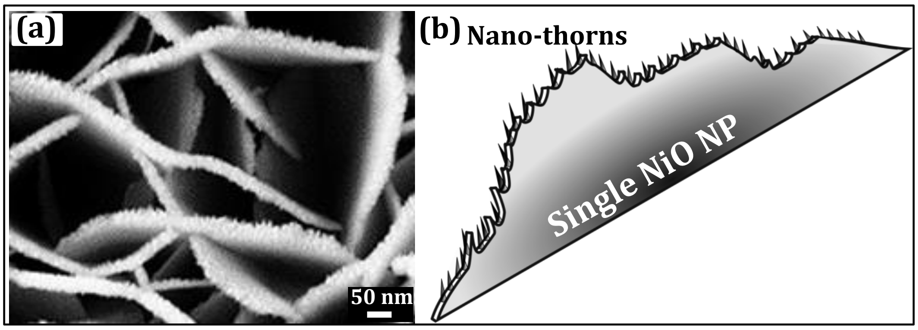

Figure: 6.7 (a) SEM image of the NIO NSs (b) schematic illustration of a single nanopetal contacting thorn like structures on the top of it.

Though it is very enthusiastic to achieve such a low turn-on field, reason for the same must be understood. As the FE properties are dependent on the nanowire diameter and morphology, the likely reason for the low turn-on field may be related to the same in our case also which is supported by the SEM images (Figure 6.4a**).** Figure 6.7a shows SEM image, where thickness of each petal is around 25-30 nm with sharp needle like edges (schematic shown in Figure 6.7b) on the top of it provide higher local electric field enhancement. The extremely fine NSs on the top of NiO nanopetals have multiple advantages that improve the FE properties as explained below. As mentioned earlier, the FE works on the principle of quantum tunneling from the surface through a vacuum gap under the influence of electric field thus depends on the potential barrier and its width. Which means that, tunneling barrier width is one of the important parameters to be addressed if one needs to get FE as per one's choice. In FE, electrons, having higher energy than the work function, can escape by overcrossing the barrier and those with lower energy needs stronger electric field to overcome the attractive force of the nuclei and tunnel through the barrier by surpassing the same[233].

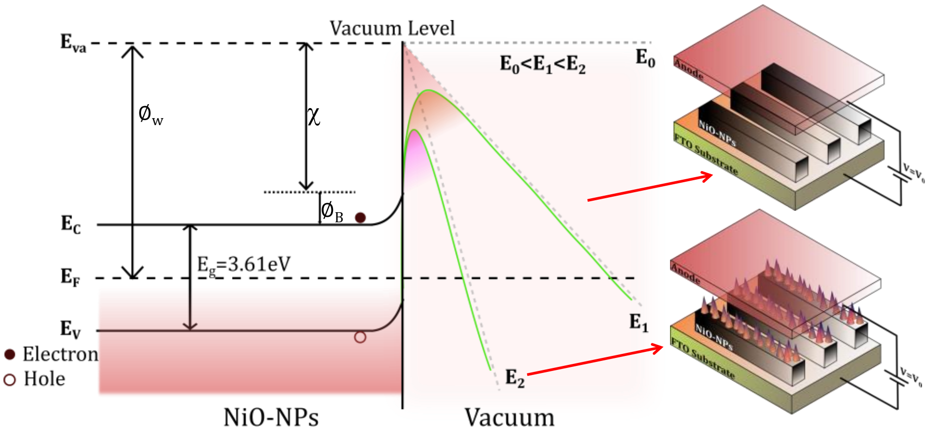

Figure: 6.8 Band-diagram of NiO-NPs along with favorable bias conditions for tunneling. Where, E_C- bottom of conduction band; E_F- Fermi level; E_V- top of valance band.

The process of FE and various players involved in the process can be understood using a schematic given in Figure 6.8, which shows various energy levels and their relative positions/alignment. With no bias applied (thermionic and photo emission case) an additional amount of energy (χ) is required so that electron is free to move. For FE, depending on the applied bias, the effective vacuum level gets modified as shown by dotted lines (for two different field values) for the ideal situations. As a result, the applied bias perturbs the situation in such a way that now a relatively thinner width needs to be tunneled for electron emission. It is also evident from Figure 6.8 that the width of the potential barrier decreases as a result of increasing field.

In Figure 6.8, actual energy pattern for two different electric fields are represented by solid green lines. Voltage applied for both the conditions is same but resulting in two different effective electric fields due to sample morphological variations as shown in right side of the Figure 6.8 (block diagram). The actual potential profile, as a result of applied field in such systems, is different from the ideal ones and must be taken into account while understanding the FE properties. The energy state path followed by an electron, emitted by the barrier tunneling as a function of separation (x) from cathode[222] is given by.

$$e\emptyset = e\emptyset_{work} - \frac{e^2}{16\pi\epsilon_0 x} - eEx \qquad (6.3)$$

where, $e\emptyset$ is electric potential energy of an electron $\emptyset_{work}$ and ϵ_0 represent the work function and permittivity of the material respectively. 'E' is the applied electric field during the emission. Schematic diagrams in Figure 6.8 shows the energy levels in the absence (E_0) and presence of two different electric fields E_1 and E_2 with $E_1 < E_2$ at the interface of vacuum and NiO NSs. Solid green lines (curved) show the typical plot of Eq. 6.3 for two different values of E. The slanted dotted lines accompanying these green lines represent their corresponding ideal counterpart as discussed above. It is interesting to see that the real situation (green solid lines), obtained using Eq. 6.3, is more favorable for FE as the barrier height and width both are smaller. It is worth mentioning here that the two situations (corresponding to the two electric fields) can be obtained by using the same bias (voltage) under two different sample morphologies as shown in the diagram next to the green lines. This can be elaborated as follows. The ultrathin nanothorns present in our samples effectively enhance electric field around the finer structures. As a consequence, a given applied bias voltage results in a higher effective electric field for samples containing nanothorns as compared to samples without them. This way the nanothorns present on the NiO NSs give rise to an effect similar to "lightening-conductor" making a relatively stronger electric field available for easy field emission in the nanothorn covered NiO NSs[76,234].

It is clearly evident from the schematic (Figure 6.8) that for stronger electric field, there is a reduction in barrier height and barrier width which means that the electrons not only need to be pushed upto a shorter distance to make it free (for emission) but also will require relatively lesser energy to cross the barrier. Both of these effects play an important role in achieving the low turn on values. Moreover, electrons enclosed in a strongly confined system (as in nanothorns of a few nanometers only) will possess more energy as compared to a weekly confined system (as in nanorods of a few tens of nanometers or nanoflakes without nanothorns). Thus the electrons, that already have higher energies, would need further lesser energy to cross the potential barrier before it is attracted by an applied electric field to initiate the FE. This way a morphological variation induced three fold constructive perturbations is present in a system containing nanothorns which improves the FE from the nanothorn covered NiO nanopetals deposited on conducting FTO film which provides plenty of electrons.

To be more conclusive about the stability of emission electric field for conjugate cycles and corresponding emission current have been plotted as a function of time as shown in Figure 6.9a & 6.9b respectively for eight cycles. Figure 6.9a shows electric field variation by ramping between 0 to 6 V and the corresponding current density variation is shown in Figure 6.9b for the same number of cycles. Insets in Figure 6.9 show the E-T and J-T cycle plots for 100 minutes (~50 cycles). It is interesting to see that initially there was lesser emission current which gets saturated to a value of around 0.32mA/cm^2 as the cycle proceeds. The current stabilization with time in vacuum also seems in accordance with the disappearing hysteresis in J-E curve (Figure 6.6b insets) as a consequence of removal of adsorbed gases. Another important aspect is the repeatability of field emission that can be turned ON and OFF for more than 50 cycles.

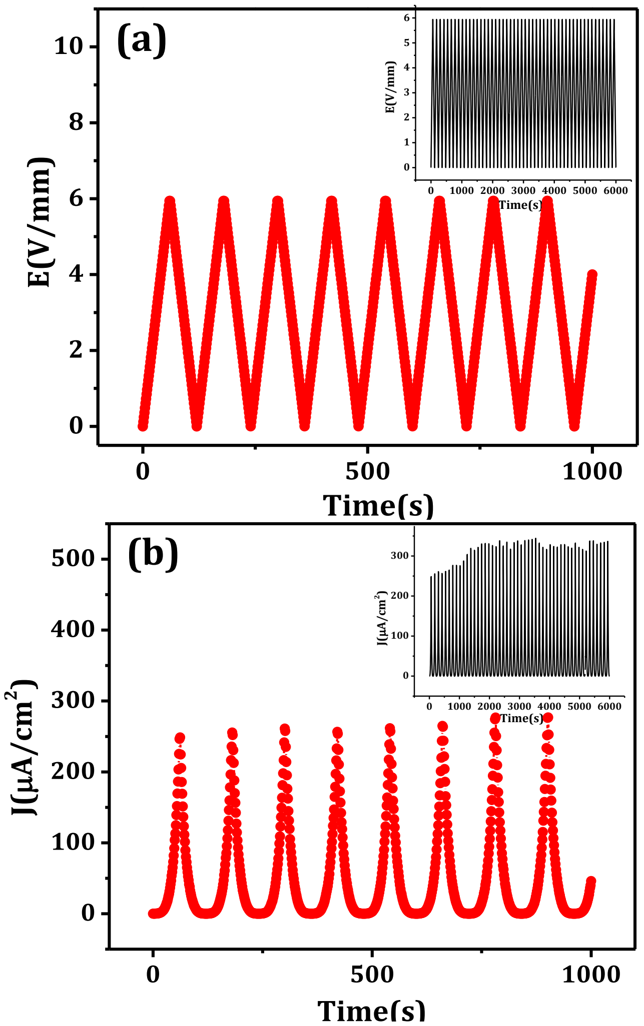

Figure: 6.9 (a) Electric field cycles in the range 0 to 6 V/mm with time (b) Corresponding emission current. Insets show the cycling for longer time duration.

The FE properties of NiO NSs have also been analyzed using the Fowler-Nordheim (FN) framework by fitting the FE data with the following FN Eq. 6.4:

$$J = A\emptyset^{-1}\beta^2E^2e^{\frac{-B\emptyset^{\frac{3}{2}}}{\beta E}} \tag{6.4}$$

where ‘A’ and ‘B’ are the temperature independent constants with ($A=1.54x10^{-6}$ A.eV/V^2 and $B=6.83x10^3$ $eV^{-3/2}$ V/μm). ‘β’ is the field-enhancement factor and J, E are the emission current density and applied electric field respectively. Figure 6.10 shows the FN plot, which is obtained by plotting $\ln(J/E^2)$ vs 1/E for various cycles from the same sample recorded consequently. The little variation in the plots with respect to the cycling number has already been discussed above. It is evident from Eq. 6.4 that the FN plot is a linear function, when $ln(J(E)/E^2)$ is plotted as a function of $1/E$, with slope equal to $(-\frac{B\emptyset^{\frac{3}{2}}}{\beta})$ whose fitting with the experimental FE emission data (discrete points in Figure 6.10 inset) has been used for the calculation of field enhancement factor (β) and threshold field (E_{th}).

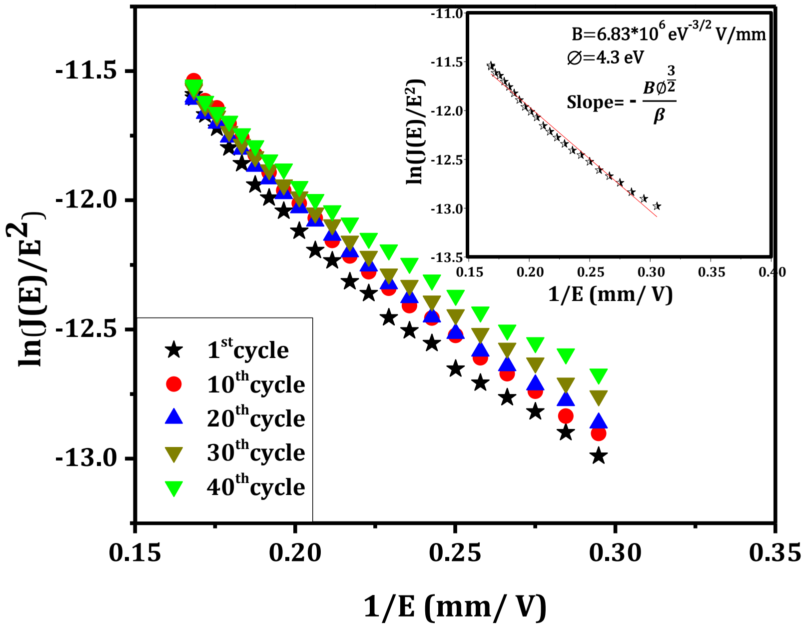

Figure: 6.10 Fowler-Nordheim fitting of the experimental FE data obtained from the NiO NFs. Inset shows the fitting, which has been used for β calculation.

Linear fitting (solid line in Figure 6.10 inset) of the FN curve gives a straight line with the slope of 10.66 giving a 'β' value of 5713 thousand. It is also clear that intercept of FN equation is a measure of the threshold electric field (E_{th}) which comes out to be 2.94 V/mm. The observed enhancement factor and threshold electric field are thousand times better than the reported values[219] for NiO nano rods where reported values are $\beta \sim 2000$ and $E_{th} \sim 4000$ V/mm. The improved FE properties in the present case are due to the effective improvement in the system due to typical nature of surface morphology containing ultrathin nanothorns present on NiO NSs. The surface microstructure mediated improvement in FE properties is consistent with the ones reported in literature.

6.3 Nanomaterial based glucoses sensing

Diabetes is a chronic disease in which glucose level increases in blood and if undiagnosed and untreated, can be very lethal and eventually may lead to death[235,236]. Different therapy regimes in the management of diabetes include drugs' dose adjustment according to the level of glucose in the blood as a result of compromised insulin level, the main cause of the disease. Hence, accurate and reliable glucose sensor to monitor the level in the blood is the most important parameter in managing diabetes. Generally, glucose sensor works on the use of an enzyme, glucose oxidase (GOx), which converts glucose into gluconic acid and H_2O_2[237–241]. The concentration of glucose is determined by monitoring the number of electrons flowing through electrode for the formation of hydrogen in the form of peroxide[242]. In enzymatic biosensors quantitative sensing is done by controlling the potential and measuring the current as a result of substance (to be sensed) reacting with the active area of the material (acting as sensor) on the working electrode. Enzymatic glucose sensors, working on the same principle, display high sensitivity to glucose. Limitations with these sensors include their shorter life span, the environmental conditions such as temperature, pH value and toxicity of the chemical used. To address these issues many metal oxide based non-enzymatic glucose sensors have been developed in recent time[243–248]. The sensing mechanism of these non-enzymatic glucose sensors is based on oxidation of glucose, by metal-oxide ion near the surface of the electrode, to gluconolactone. In electrochemical sensing cyclic voltammetry roves to be an efficient technique due to its high sensitivity at low detection limits, accurate quantitative analysis and fast and clear characterization[249,250]. These oxide based glucose sensors certainly have potential to be used in real diagnosis and needs further study.

There are increasing interests on fabrication of electrodes with low-cost metal-oxide materials, such as NiO, CuO, TiO_2, ZnO and composites which can show high sensitivity toward glucose by improving electro-catalytic activity[251–258]. When it comes to reaction based sensing, nanomaterials could be of interest as they can provide more surface area for reaction and hence better sensing. In recent times, a variety of materials in nanostructured form have shown great potential in sensing, electronics, and optoelectronics[8,208,259]. Established fact about nanostructures is the capability of tailoring a physical property by changing its size and/or morphology which gives the versatility to the nanomaterials to be used in diverse applications. Hence, for sensors also design of electrodes surface is one of the key parameters. Amongst plenty, Ni-based nanomaterials exhibit remarkable properties, such as catalysis[73,260,261] and high sensitivity due to large surface-to-volume ratio. An economic yet sensitive glucose sensor can be a reality with NiO nanostructure based sensors by appropriately designing the device and synthesizing the material. In this paper, a working electrode consisting of petal like NiO nanostructures for glucose sensing via electrochemical study have been fabricated to be used as the active compound. Fluorine doped tin oxide (FTO) coated conducting glass substrate has been used to grow the NiO nanostructures (NSs) by hydrothermal technique. Where more of details have been discussed in the experimental and synthesis techniques of chapter 2

Microstructural details and morphology of NiO NSs have been studied using electron microscopy and atomic force microscopy (AFM). In previous section of field emission we have shown very dense rose-petal like structures grown on the FTO coated conducting glass substrate. In microscopic analysis thickness of these petals is approximately 25-30 nm with cross sectional height is around ~1μm. The film is dense and uniform over more than hundred microns.

6.3.1 NiO nanopetals structural study

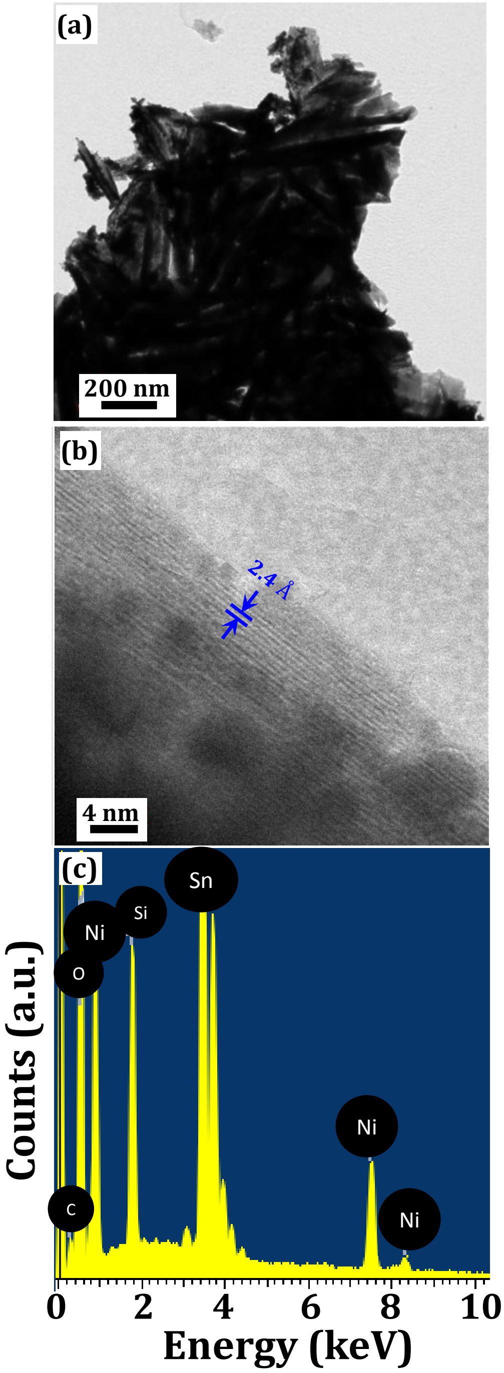

Figure: 6.11 (a) TEM image of the multiple NiO nanopetals (b) HRTEM image of a petal and their corresponding diffraction pattern (c) EDX spectra for elemental conformation.

The uniformity over larger areas makes it eligible for better sensing applications. TEM micrograph and constituents present of these NiO-NSs have been recorded by HRTEM and EDAX. Figure 6.11 clearly demonstrate that NiO nanopetal with uniformly distributed lattice of gap 2.4 Å in given HRTEM image (Figure 6.11b). In EDX spectra present element can be obtain the presence of Sn and Si peaks correspond to the FTO coated glass substrate (Figure 6.11c). The oxidation states of the present element can be checked by X-ray photoelectron spectroscopy (XPS). XPS is performed for the surface analysis and chemical compositions of NiO nanopetals. The XPS survey scan (Figure 6.12a) depicts composition of nickel and oxygen with the substrate peak of tin (Sn) which is consistent with the EDX results. Two characteristic Ni 2p peaks are observed at about 855.7eV ($2p_{3/2}$) and 873.4eV ($2p_{1/2}$) in high resolution scan (Figure 6.12b). The deconvoluted spectrum contains seven peaks with two stronger peaks at 855.7 and 873.4 eV correspond to Ni^{2+} in Ni–O bonds, with two satellite (weak) peaks[151]. Above mentioned morphological and structural characterization of prepared substrate predicts the presence of low dimensional petal like structures of NiO and the same will be investigated for possible glucose sensing properties. As mentioned earlier, basis of the sensing mechanism is the reactivity of glucose with NiO thus needing higher surface areas, which should be analyzed before investigating the sensing properties. The specific surface area and other parameters, like type of isotherm, average pore size, total pore volume have been obtain by the N_2 adsorption/desorption using BET method. Figure 6.12c reveals type-IV isotherm and type-H3 hysteresis when measured[252] at 77 K with the relative pressure range of $0.025 \leq P/P_0 \leq 1.00$. The measured surface area, estimated by BET and Langmuir methods in the P/P_0 range of 0.05-0.30, is found to be 114.936m^2/g and pore size distribution around 3.7 nm. This indicates NiO NPs are mesoporous with relatively uniform pore size distribution. The total pore volume in the sample is found to be 0.267 cm^3/g estimated at a relative pressure (P/P_0) of 0.99.

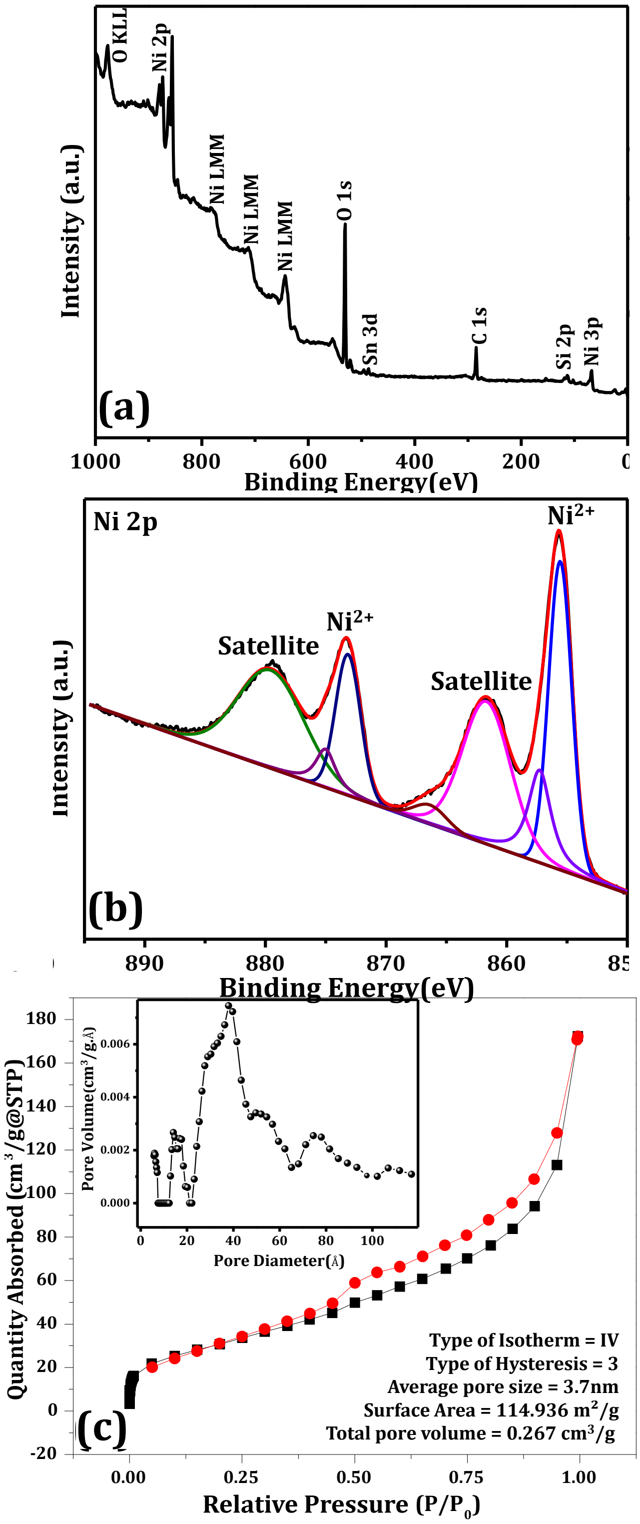

Figure: 6.12 Chemical states analysis of the fabricated NiO nanopetals using XPS (a) survey scan (b) deep scan of 2p Ni (c) BET isotherm measurement by N_2 adsorption/desorption.

6.3.2 NiO Nanopetals for electrochemical sensing

An adequate surface appears available for glucose sensing of the NiO-NPs has been studied below using electrochemical CV measurements as shown in Figure 6.13. For CV measurements, a three-electrode system has been employed with NiO-NPs@FTO sample as working electrode, Ag/AgCl (1 M KCl) and platinum wire used as reference and counter electrodes respectively. Figure 6.13a shows I-V curves with different voltage sweep rates varying between 10 mV/s and 100mV/s. It is evident from Figure 6.13a that a current of ~0.25 mA/cm^2 was flowing at scan rate of 10mV/s (black curve) and increases to 2.5 mA/cm^2 when scan rate was increased to 100mV/s (light green curve). A ten times current increase by increasing the scan rate by ten times means a linear variation between the two. Such a linear variation in current as a function of scan rate, as evident in Figure 6.13a inset, is most often assigned to be originating due to a surface controlled reaction and will be better for sensing applications. For sensing study, CV measurements have been carried out with NiO NSs film as working electrode (NiO-NPs@FTO) at a scan rate of 50mV/s with (red) and without (black) glucose, in the presence of 0.1M NaOH electrolyte as shown in Figure 6.13b. The CV plots recorded at different scan rates in the presence of glucose have also been shown is Figure 6.13c which also shows increased current values as compared to non-glucose case and further increases with increasing scan rates. This scan rate dependent CV curves in Figure 6.13c are consistent with the discussions above pertaining to the glucose sensing and surface controlled reaction. As can be seen from black and red curves in Figure 6.13b, a reaction peak current observed, indicating that NiO-NPs@FTO electrode undergoes the redox reaction in the potential range of 0.0 to 0.6V.

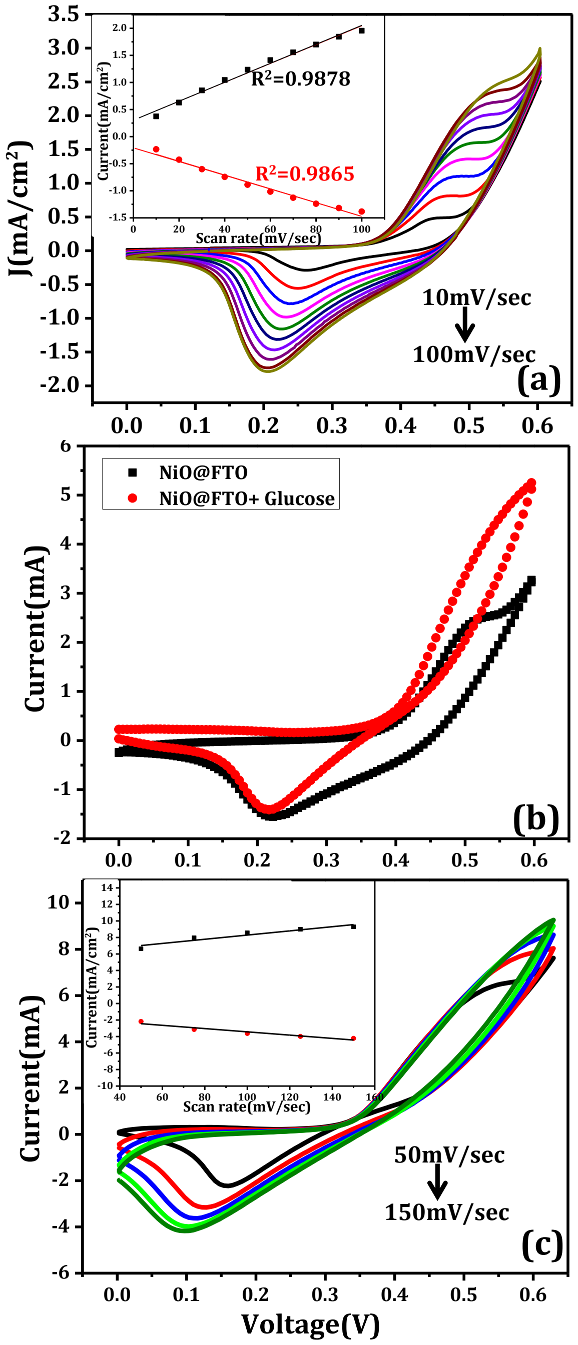

Figure: 6.13 (a) Cyclic voltammetry (CV) of NiO-NPs@FTO on various scan-rates (b) Electrochemical glucose (10µM) sensing using CV technique (c) CV scan of NiO-NPs@FTO electrode in presence of glucose at various scan rates. Insets in (a) and (c) show a linear variation of current as a function of scan rate.

The peak current value gets doubled in the presence of glucose, i.e, the current of NiO-NPs@FTO electrode with glucose is larger than the one without glucose which can be attributed to oxidation of glucose molecule immobilized within larger surface area of the NiO NSs. This appears to be the most likely mechanism of glucose sensing as can be supported by the following redox reactions taking place at appropriate sites.

$$NiO+H_2O \rightarrow NiOOH \quad (R\ 6.1)$$

$$NiOOH + glucose \rightarrow NiO + H_2O_2 + gluconolactone \quad (R\ 6.2)$$

$$gluconolactone \rightarrow gluconic\ acid \quad (R\ 6.3)$$

$$gluconic\ acid + H_2O \rightarrow gluconate^- + H^+ \quad (R\ 6.4)$$

During CV measurement, Ni^{2+} oxidizes into Ni^{3+} by aqueous electrolytic solution present in the cell at NiO-NPs@FTO electrode (reaction R 6.1). Oxidized Ni^{3+} work as catalyst for glucose, and oxidizes glucose by reducing itself (reaction R 6.2). On oxidation, glucose converts to gluconolactone which consequently gets converted immediately to gluconic acid (reaction R 6.3) and this compound reacts with water molecules to form gluconate and hydronium ions (reaction R 6.4). These ions near the surface of working electrode result in increased current as detectable signal with a very good specific sensitivity of 3.9μA/μM/cm^2.

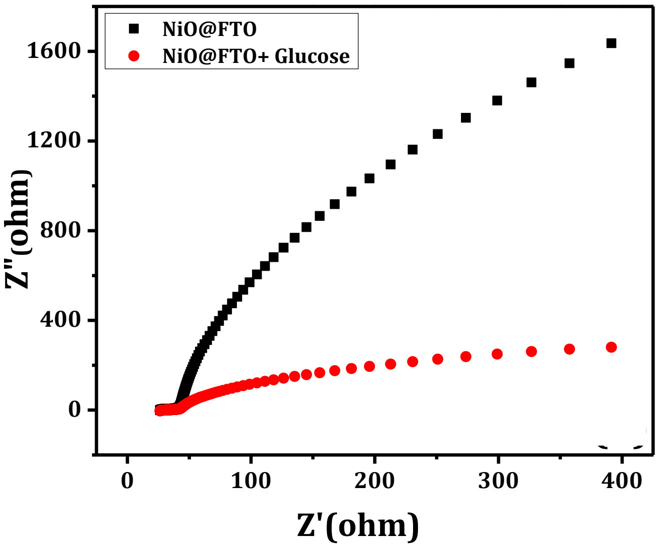

Figure: 6.14 Electrochemical impedance spectroscopy (EIS) to show glucose sensing.

Further to support the “glucose-doping” induced enhancement in electric conductivity, electrochemical impedance spectroscopy (EIS) of NiO NPs fabricated working electrode has been measured with and without glucose (Figure 6.14). A single depressed semicircle in the high frequency region and an inclined line in the low frequency region can be seen in the Nyquist (cole-cole) plot in Figure 6.14.

Generally, the high frequency semicircle shows the electrochemical reaction impedance between the glucose present in the electrolytic solution and NiO nanostructure interface. Whereas inclined line in the lower frequency region shows the active material (NiO) and conducting electrode interface impedance[262]. Effect of glucose on the cole-cole plot in Figure 6.14 is clearly distinguishable and thus the same measurement can be utilized to sense the presence of glucose. This clearly exhibits the glucose sensing property of the material which is nanopetal shaped NiO NSs.

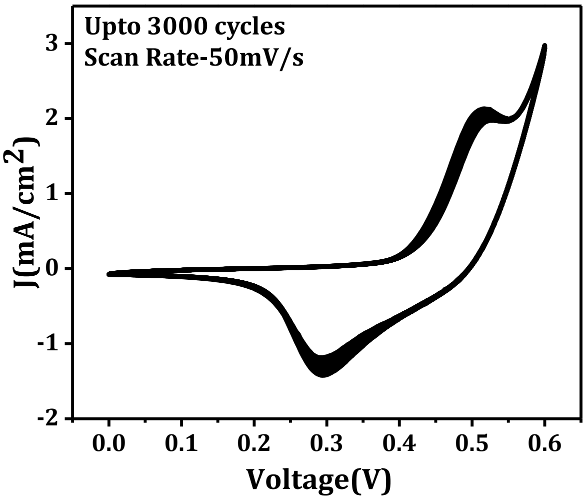

Figure: 6.15 Repeatability test of the fabricated electrode sensor upto 3000 cycles at the scan rate of 50mV/sec.

The electrode is very stable as tested by repeating the CV scans for 3000 cycles (Figure 6.15). The repeatability of a device is one of the important parameters for effective performance as real sensor. Figure 6.16a is the electrochemical cell for the glucose sensing through CV and amperometric techniques. Figure 6.16b corresponds to CV scan of NiO-NPs@FTO in the presents of various glucose concentrations from 100μM-1.2mM. Figure 6.16c shows linear relation of glucose concentration with current density having a linear fitting factor (R^2) of 0.9948.

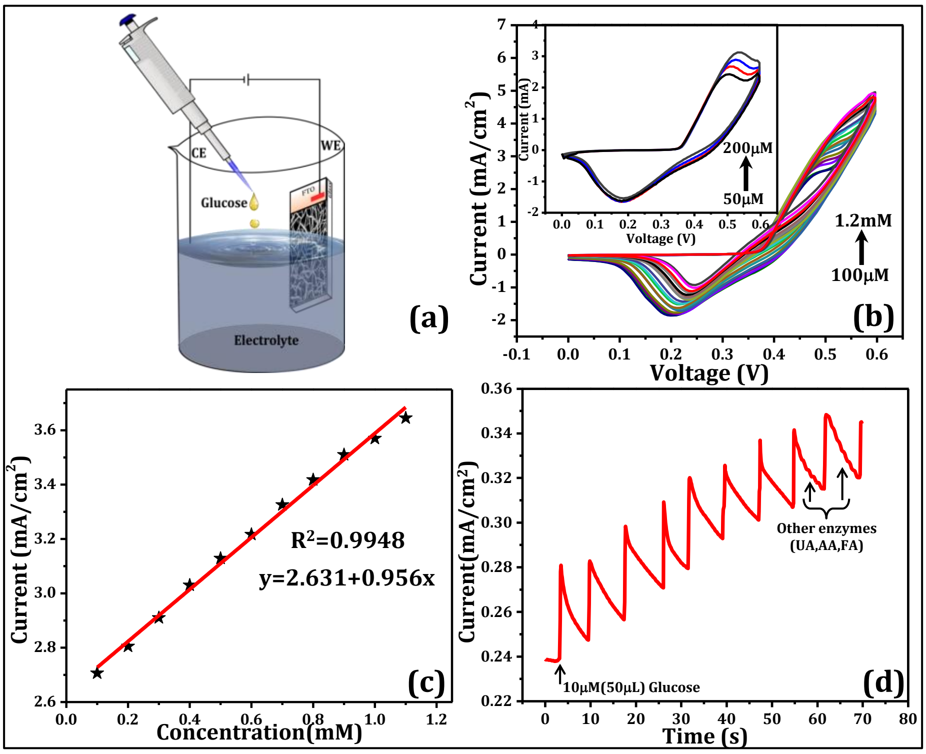

Figure: 6.16 (a) Schematic illustration of electrochemical glucose sensing setup using NiO-NPs@FTO as working electrode with supporting electrolyte NaOH (0.1M) (b) sequential glucose addition of 50μM during CV scan with its magnifying view in the inset (c) linear relation of glucose concentration with current (d) amperometric response (at +0.5V) on 10μM glucose addition.

Figure 6.16d shows amperometric behavior of NiO-NPs@FTO electrode on addition of aqueous glucose solution of different amounts in 0.1 M NaOH electrolyte as sensed at +0.5V. At this bias, the NiO-NPs@FTO electrode exhibits systematic changes in the current when 50μl glucose solution of concentration 1μM is added in the electrolyte. Further, to illustrate the exclusive glucose sensing behavior, effect of other compounds present with glucose like uric acid (UA), ascorbic acid (AA), folic acid (FA) were checked by carrying out control experiments. Responses of the mentioned species at various concentrations were studied by adding these enzymes at 57th and 65th second (arrow marked in figure 6.16d) which do not show any significant changes in the current during amperometric measurement whereas glucose was sensed when added in between at 60th second. Another important observation is the reduction in current after glucose induced spike, which makes the sensor reusable. The NiO NSs electrode shows very good sensitivity as compared to various other sensor electrodes as can be seen in Table 6.1, which summarizes some of the recent glucose sensing electrodes. A superior sensitivity of the NiO NSs based electrode (bottom row in Table 6.1) makes NiO nanopetal based electrode a good candidate for glucose sensing applications on which further studies can be done on real samples like blood or foods as applicable.

Table: 6.1 Comparison of sensing parameters used in the present study as compared to other reports

Type of Electrode	**Sensitivity (μA/μM/cm²)**	**Detection Potential (V)**	**Reference**
Ti/TiO2 nanotube array/Ni	0.20	0.55	Wang et al.[244]
Ni nano-sphere/RGO	0.15	0.46	Yang et al.[263]
Ni nanoparticles loaded MWCNT	1.44	0.40	Nie et al.[264]
Ni nanoparticles loaded carbon nanofibers	0.42	0.60	Liu et al.[265]
3D porous Ni nanonetwork	2.90	0.50	Niu et al.[266]
NiO-NPs@FTO	3.90	0.50	Present work

6.4 Summary

Suitably designed nanorod array of TiO_2/Co_3O_4 core/shell shows superior supercapacitive properties. The single crystalline core of TiO_2 provide excellent platform for the Co_3O_4 shell. Nanorod array grown on FTO glass substrate by combining, hydrothermal and electrodeposition methods, show improved supercapacitive behavior with a high areal capacitance of 240 mF/cm^2 at a scan rate of 10 mV/s. In addition to this, a high specific capacitance of 344.88 F/g is also observed, clearly demonstrating improved energy storage with superior cyclic stability for more than 5000 cycles.

Uniform and vertically aligned NiO-NPs structures, grown on very flat, conducting surface (FTO coated glass), show sharp needles like structures on the top edges of the flakes. Modification in device geometry and surface micro- (nano-) structure has been found to play the key role in addressing the bottlenecks in achieving an efficient field emission. A power efficient and stable field emission, in terms of threshold and turn-on fields, has been observed from these NiO-NPs with field enhancement factor of approximately five million and threshold field of 3V/mm as estimated by analyzing the FE data (J-E plot) within the frame work of Fowler-Nordheim (FN).

The abovementioned well-aligned, dense nickel oxide nanopetals are mesoporous in nature and has been tested for glucose sensing applications. The hydrothermally grown nanopetals covered with immobilized glucose, shows detection of wide range of glucose concentrations with good linearity and high sensitivity of 3.9μA/μM/cm^2 at 0.5 V operating potential. Detection limit of as low as 1μM and a fast response time of less than 1s was observed. The glucose sensor electrode possesses good anti-interference ability, stability, repeatability & reproducibility and shows inert behavior towards ascorbic acid, uric acid and dopamine acid making it a perfect non-enzymatic glucose sensor.

Chapter 7

Conclusions and Future Scope

Major conclusions of the research work reported in this thesis are being summarized below along with the scope for future extension of the work:

7.1 Conclusions and summary

7.1.1 Electrochromic materials and Devices

- Working mechanism of an electrochromic device can be understood by designing device in simple geometry and planning neat experiments.
- In-situ investigations, such and UV-Vis and Raman spectroscopies, have been carried out on the device during its operational conditions to establish the exact working principle of bias induced color switching and factors controlling it.
- In-situ UV-Vis spectroscopy shows how the optical properties of the device change by increasing doping induced by electrical bias on the material.
- In-situ Raman spectroscopy prove to be the handy tool to track the molecular changes or redox states of the active material participate in the electrochromism. It revealed that interfacial redox layers play the key role in showing the color switching in electrochromic devices.
- Special nanostructures of both organic and inorganic materials have been incorporated to make an

electrochromic device with better perform in terms of speed and power utilization.

- Graphene nanoflakes (GNFs) have been synthesized and incorporated within the electrochromic device, which provide the channel to shuttle the carrier from working to the counter electrode very fast and improve the overall switching speed of the device.
- Prepared nanostructures having geometry of core-shell where n-type TiO_2 is used as core and p-type Co_3O_4 as shell form heterojunction. Prepared electrode show stable electrochromism with a reflectivity variation of ~40% and coloration efficiency is ~91 cm^2/C, higher compare to their parental material.
- Along with heterojunction hybrid nanostructures have also been prepared in coplanar core-shell form. Nickel oxides core, incorporated with the conducting polymers PANI shows improved electrochromic absorption modulation ~55% (for 550 nm) and coloration efficiency of 145 cm^2/C.

7.1.2 Other functional applications of nanomaterials

- Apart from the electrochromic application, the prepared nanostructures show multifunctional application such as energy storage, field emission and electrochemical sensing of glucose.
- Prepared nanostructures having geometry of core-shell where n-type TiO_2 used as core and p-type Co_3O_4 as shell form heterojunction. Improved supercapacitive behavior with areal capacitance of 240 mF/cm^2 (@10mV/s) and specific capacitance of 344.88 F/g is observed with cyclic stability for more than 5000 cycles.
- Vertically aligned NiO-NPs structures grown on flat conducting surface show power efficient and stable field emission with threshold field of ~3V/mm.

- Above mentioned nickel oxide nanopetals, mesoporous in nature, show electrochemical sensitivity of 3.9μA/μM/cm^2 toward glucose with lowest detection limit of 1μM.

7.2 New findings of reported in the thesis

- Core origin of the bias induced color switching in electrochromic devices, especially where organic materials are used as active component, has been established based on interfacial redox mechanism.
- The perceived colors' origin in an electrochromic device has been explained through gradual Raman spectroscopic variations in electrochromism of viologen.
- An electrochromic gel, prepared by combining three different materials, chosen appropriately to perform an identified role individually, has been developed while searching for faster electrochromism.
- Nanostructures of conducting polymer on inorganic nanostructure were prepared which shows efficient electrochromic behavior with higher color contrast as compared to individual ones.
- Mesoporous nickel oxide nanopetals have been designed for ultrasensitive glucose sensing and improved field electron emission.
- TiO_2/Co_3O_4 core-shell nanorods have been designed and its bi-functional role has been established in better energy storage & electrochromism.

7.3 Future scope of work

The research work carried out in this thesis can be extended further keeping the following points in mind:

- Fabrication of ultrafast display with switching of coloration and decoloration state within 100ms.
- Apart from the speed, power consumption is also one of the biggest challenges currently which needs to be reduced in future devices and needs to be worked out. This can be done by choosing appropriate materials.
- Color tuneability within a single device as the function of varying potential can make device more advance and lot of other application can be associated like memory. A multi-level memory and electrochromic device can be a possibility.
- Fabrication of device in large scale needs to be carried out for commercialization.
- Incorporating electrochromic device can be used with some other device such as solar cell, energy storage device for their multifunctional application.
- If keeping in mind merits and demerits of both the organic and inorganic materials incorporated into single device which exhibit simultaneous cathodic or anodic coloration in the same voltage window, optical contrast and efficiency can be maximized
- Thermal and electrochemical stability of the polymer electrolyte stability will reflect product safety, recyclability and shelf-life.
- Recent developments in nanotechnology open new avenues for integrating multiple functional materials into composites and novel form for efficient applications.
- A deeper understanding of nano and microstructure-property relationships for chromogenic materials is

required to improve color neutrality, switching rate, bleached/colored state contrast, and durability.

- In electrochromic windows, knowledge of charge transport kinetics and chemical reactions at electrode-electrolyte interfaces is still lacking. Current challenges demands, more theoretical and experimental investigations on materials and device engineering and this can be explored.

The thesis can be concluded with the following lines:

"Science never solves a problem without creating ten more….."

--George Bernard Shaw

Appendix

A.1 Effect of electric field

To discount the effect of the electric field induced structural change in the material during the operation of the electrochromic device, control experiment have been carried out by sandwiching EV+PEO gel between two glass substrates coated with ITO facing opposite to each other. Figure A.1 shows the schematic of the experiment set-up used. The biasing condition does not provide electrons to the molecule (for possible reduction) but do provide field for any field-related structural change. No color change observed upto a bias voltage of 50 V, which suggests that the observed color switching is not related to field induced structural changes and more likely reason being the transmission change due to redox process.

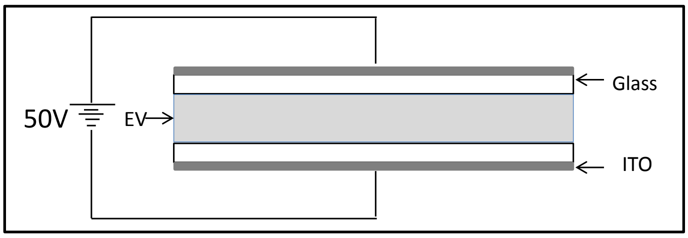

Figure: A.1 Schematic illustration of electric field effect testing.

A.2 Chemical reduction of EV

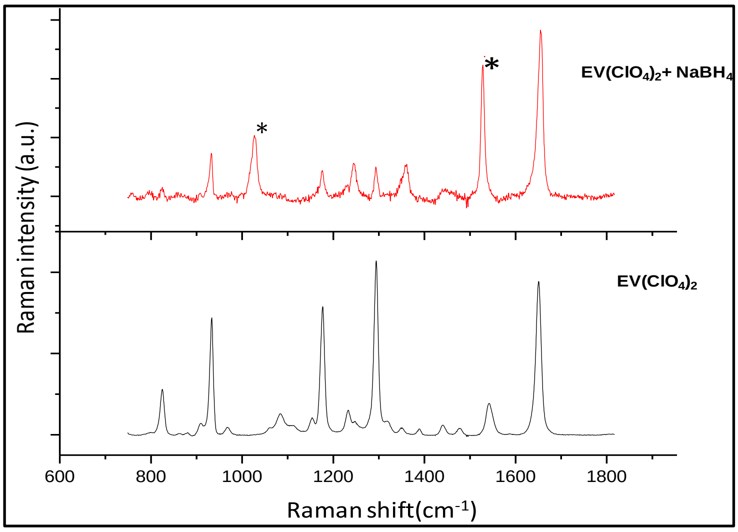

Figure: A.2 Raman scattering spectra of pure ethyl viologen (powder) and its chemically reduced form.

A.3 Raman spectra of intermediate states

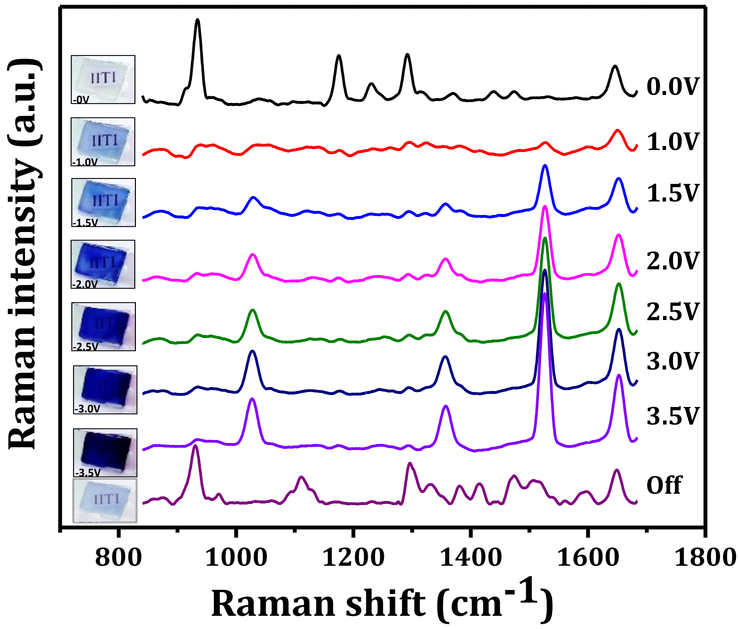

Figure: A.3 Raman spectra records the gradual changes in species with perceive color.

A.4 Open face geometry device

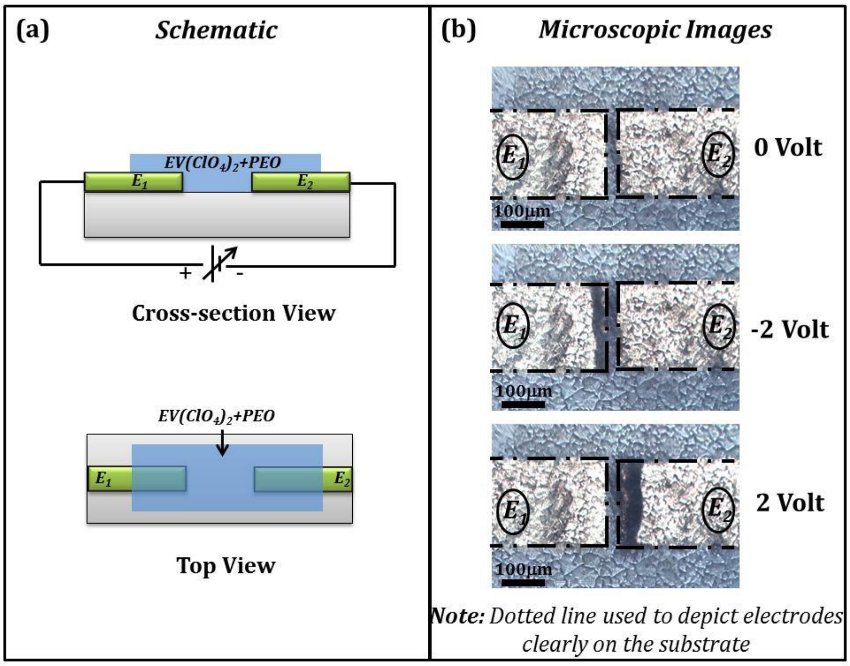

Note: Dotted line used to depict electrodes clearly on the substrate

Figure: A.4 Operation of electrochromic device in open face geometry.

A.5 FTIR spectra of EV

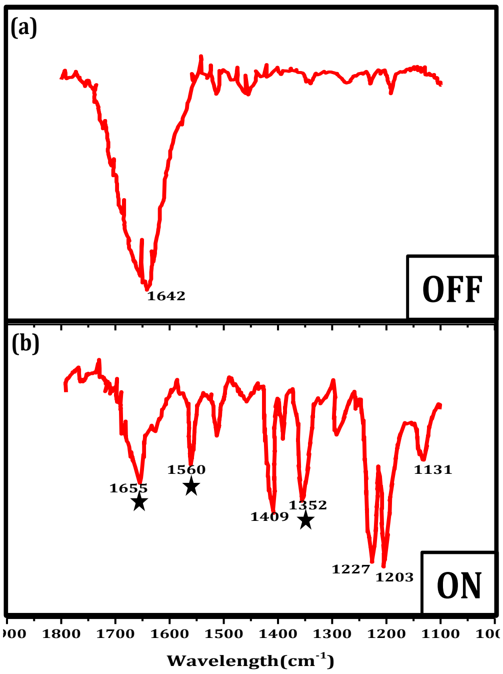

Figure: A.5 FTIR spectra of $EV(ClO_4)_2$ in acetonitrile in (a) OFF and (b) ON state.

A.6 Electrochromic as wavelength filter

This work is based on the application of electrochromic device as wavelength filter. Wavelength filtering is one of the potential applications having use in numerous fields such as automobile sector. Figure A.6 shows block diagram presentation of the filtering process along with the spectra filtered wavelength. Currently work is under consideration and in the process of patent application.

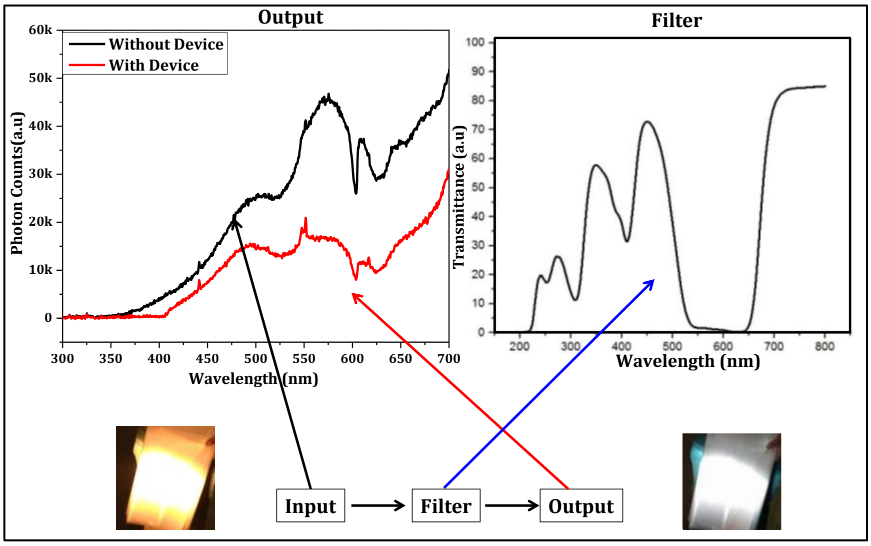

Figure: A.6 Schematic combine with spectroscopy to show the arrangement we have develop to filter the input light.

Reference

[1] S. Najmaei, Z. Liu, W. Zhou, X. Zou, G. Shi, S. Lei, B.I. Yakobson, J.-C. Idrobo, P.M. Ajayan, J. Lou, Vapour phase growth and grain boundary structure of molybdenum disulphide atomic layers, Nat. Mater. 12 (2013) 754–759. doi:10.1038/nmat3673.

[2] J. Abraham, K.S. Vasu, C.D. Williams, K. Gopinadhan, Y. Su, C.T. Cherian, J. Dix, E. Prestat, S.J. Haigh, I.V. Grigorieva, P. Carbone, A.K. Geim, R.R. Nair, Tunable sieving of ions using graphene oxide membranes, Nat. Nanotechnol. 12 (2017) 546. doi:10.1038/nnano.2017.21.

[3] J. Lahann, Environmental nanotechnology: Nanomaterials clean up, Nat. Nanotechnol. 3 (2008) 320–321. doi:10.1038/nnano.2008.143.

[4] M. Zahn, Magnetic colloid petroleum oil spill clean-up of ocean surface, depth, and shore regions, 2012. https://patents.google.com/patent/US8945393B2/en (accessed February 18, 2018).

[5] R. Gupta, Q. Xiong, C.K. Adu, U.J. Kim, P.C. Eklund, Laser-Induced Fano Resonance Scattering in Silicon Nanowires, Nano Lett. 3 (2003) 627–631. doi:10.1021/nl0341133.

[6] R. Kumar, H.S. Mavi, A.K. Shukla, V.D. Vankar, Photoexcited Fano interaction in laser-etched silicon nanostructures, J. Appl. Phys. 101 (2007) 064315. doi:10.1063/1.2713367.

[7] D.M. Sagar, J.M. Atkin, P.K.B. Palomaki, N.R. Neale, J.L. Blackburn, J.C. Johnson, A.J. Nozik, M.B. Raschke, M.C. Beard, Quantum Confined Electron–Phonon Interaction in Silicon Nanocrystals, Nano Lett. 15 (2015) 1511–1516. doi:10.1021/nl503671n.

[8] S. Mishra, P. Yogi, S.K. Saxena, V. Kumar, R. Kumar, Fano Scattering: Manifestation of Acoustic Phonons at the

Nanoscale, J. Phys. Chem. Lett. 7 (2016) 5291–5296. doi:10.1021/acs.jpclett.6b02090.

[9] L.V. Wang, S. Hu, Photoacoustic Tomography: In Vivo Imaging from Organelles to Organs, Science. 335 (2012) 1458–1462. doi:10.1126/science.1216210.

[10] P. Lai, L. Wang, J.W. Tay, L.V. Wang, Photoacoustically guided wavefront shaping for enhanced optical focusing in scattering media, Nat. Photonics. 9 (2015) 126–132. doi:10.1038/nphoton.2014.322.

[11] L. Wang, C. Zhang, L.V. Wang, Grueneisen Relaxation Photoacoustic Microscopy, Phys. Rev. Lett. 113 (2014) 174301. doi:10.1103/PhysRevLett.113.174301.

[12] Y. Liu, M. Pharr, G.A. Salvatore, Lab-on-Skin: A Review of Flexible and Stretchable Electronics for Wearable Health Monitoring, ACS Nano. 11 (2017) 9614–9635. doi:10.1021/acsnano.7b04898.

[13] Y. Yang, N. Sun, Z. Wen, P. Cheng, H. Zheng, H. Shao, Y. Xia, C. Chen, H. Lan, X. Xie, C. Zhou, J. Zhong, X. Sun, S.-T. Lee, Liquid-Metal-Based Super-Stretchable and Structure-Designable Triboelectric Nanogenerator for Wearable Electronics, ACS Nano. (2018). doi:10.1021/acsnano.8b00147.

[14] C. Yan, W. Kang, J. Wang, M. Cui, X. Wang, C.Y. Foo, K.J. Chee, P.S. Lee, Stretchable and Wearable Electrochromic Devices, ACS Nano. 8 (2014) 316–322. doi:10.1021/nn404061g.

[15] D. Son, J.H. Koo, J.-K. Song, J. Kim, M. Lee, H.J. Shim, M. Park, M. Lee, J.H. Kim, D.-H. Kim, Stretchable Carbon Nanotube Charge-Trap Floating-Gate Memory and Logic Devices for Wearable Electronics, ACS Nano. 9 (2015) 5585–5593. doi:10.1021/acsnano.5b01848.

[16] J.H. Koo, S. Jeong, H.J. Shim, D. Son, J. Kim, D.C. Kim, S. Choi, J.-I. Hong, D.-H. Kim, Wearable Electrocardiogram Monitor Using Carbon Nanotube Electronics and Color-Tunable

Organic Light-Emitting Diodes, ACS Nano. 11 (2017) 10032–10041. doi:10.1021/acsnano.7b04292.

[17] B. Xie, C. Yang, Z. Zhang, P. Zou, Z. Lin, G. Shi, Q. Yang, F. Kang, C.-P. Wong, Shape-Tailorable Graphene-Based Ultra-High-Rate Supercapacitor for Wearable Electronics, ACS Nano. 9 (2015) 5636–5645. doi:10.1021/acsnano.5b00899.

[18] S. Kabiri Ameri, R. Ho, H. Jang, L. Tao, Y. Wang, L. Wang, D.M. Schnyer, D. Akinwande, N. Lu, Graphene Electronic Tattoo Sensors, ACS Nano. 11 (2017) 7634–7641. doi:10.1021/acsnano.7b02182.

[19] Y.J. Park, S.-K. Lee, M.-S. Kim, H. Kim, J.-H. Ahn, Graphene-Based Conformal Devices, ACS Nano. 8 (2014) 7655–7662. doi:10.1021/nn503446f.

[20] M. Gueltig, H. Ossmer, M. Ohtsuka, H. Miki, K. Tsuchiya, T. Takagi, M. Kohl, High Frequency Thermal Energy Harvesting Using Magnetic Shape Memory Films, Adv. Energy Mater. 4 (2014) n/a-n/a. doi:10.1002/aenm.201400751.

[21] T. Lv, Z. Cheng, D. Zhang, E. Zhang, Q. Zhao, Y. Liu, L. Jiang, Superhydrophobic Surface With Shape Memory Micro/Nanostructure and Its Application in Rewritable Chip for Droplet Storage, ACS Nano. 10 (2016) 9379–9386. doi:10.1021/acsnano.6b04257.

[22] K.-H. Lee, J.-H. Lee, H.-D. Kang, B. Park, Y. Kwon, H. Ko, C. Lee, J. Lee, H. Yang, Over 40 cd/A Efficient Green Quantum Dot Electroluminescent Device Comprising Uniquely Large-Sized Quantum Dots, ACS Nano. 8 (2014) 4893–4901. doi:10.1021/nn500852g.

[23] K.-H. Lee, C.-Y. Han, H.-D. Kang, H. Ko, C. Lee, J. Lee, N. Myoung, S.-Y. Yim, H. Yang, Highly Efficient, Color-Reproducible Full-Color Electroluminescent Devices Based on Red/Green/Blue Quantum Dot-Mixed Multilayer, ACS Nano. 9 (2015) 10941–10949. doi:10.1021/acsnano.5b05513.

[24] X. Xia, D. Chao, X. Qi, Q. Xiong, Y. Zhang, J. Tu, H. Zhang, H.J. Fan, Controllable Growth of Conducting Polymers Shell for Constructing High-Quality Organic/Inorganic Core/Shell Nanostructures and Their Optical-Electrochemical Properties, Nano Lett. 13 (2013) 4562–4568. doi:10.1021/nl402741j.

[25] P.M. Beaujuge, J.R. Reynolds, Color Control in π-Conjugated Organic Polymers for Use in Electrochromic Devices, Chem. Rev. 110 (2010) 268–320. doi:10.1021/cr900129a.

[26] V.K. Thakur, G. Ding, J. Ma, P.S. Lee, X. Lu, Hybrid Materials and Polymer Electrolytes for Electrochromic Device Applications, Adv. Mater. 24 (2012) 4071–4096. doi:10.1002/adma.201200213.

[27] Y. Wang, E.L. Runnerstrom, D.J. Milliron, Switchable Materials for Smart Windows, Annu. Rev. Chem. Biomol. Eng. 7 (2016) 283–304. doi:10.1146/annurev-chembioeng-080615-034647.

[28] S.K. Deb, Optical and photoelectric properties and colour centres in thin films of tungsten oxide, Philos. Mag. J. Theor. Exp. Appl. Phys. 27 (1973) 801–822. doi:10.1080/14786437308227562.

[29] S. Mishra, H. Pandey, P. Yogi, S.K. Saxena, S. Roy, P.R. Sagdeo, R. Kumar, Interfacial redox centers as origin of color switching in organic electrochromic device, Opt. Mater. 66 (2017) 65–71. doi:10.1016/j.optmat.2017.01.030.

[30] C.M. Amb, A.L. Dyer, J.R. Reynolds, Navigating the Color Palette of Solution-Processable Electrochromic Polymers, Chem. Mater. 23 (2011) 397–415. doi:10.1021/cm1021245.

[31] P. Chandrasekhar, B.J. Zay, T. McQueeney, G.C. Birur, V. Sitaram, R. Menon, M. Coviello, R.L. Elsenbaumer, Physical, chemical, theoretical aspects of conducting polymer electrochromics in the visible, IR and microwave regions,

Synth. Met. 155 (2005) 623–627. doi:10.1016/j.synthmet.2005.08.015.

[32] P. Chandrasekhar, B.J. Zay, T. McQueeney, A. Scara, D. Ross, G.C. Birur, S. Haapanen, L. Kauder, T. Swanson, D. Douglas, Conducting Polymer (CP) infrared electrochromics in spacecraft thermal control and military applications, Synth. Met. 135–136 (2003) 23–24. doi:10.1016/S0379-6779(02)00682-3.

[33] A.L. Dyer, C.R.G. Grenier, J.R. Reynolds, A Poly(3,4-alkylenedioxythiophene) Electrochromic Variable Optical Attenuator with Near-Infrared Reflectivity Tuned Independently of the Visible Region, Adv. Funct. Mater. 17 (2007) 1480–1486. doi:10.1002/adfm.200601145.

[34] K. Liu, J. Varghese, J.Y. Gerasimov, A.O. Polyakov, M. Shuai, J. Su, D. Chen, W. Zajaczkowski, A. Marcozzi, W. Pisula, B. Noheda, T.T.M. Palstra, N.A. Clark, A. Herrmann, Controlling the volatility of the written optical state in electrochromic DNA liquid crystals, Nat. Commun. 7 (2016) 11476. doi:10.1038/ncomms11476.

[35] S.K. Deb, Opportunities and challenges in science and technology of WO3 for electrochromic and related applications, Sol. Energy Mater. Sol. Cells. 92 (2008) 245–258. doi:10.1016/j.solmat.2007.01.026.

[36] R.J. Mortimer, Electrochromic Materials, Annu. Rev. Mater. Res. 41 (2011) 241–268. doi:10.1146/annurev-matsci-062910-100344.

[37] S.K. Deb, A Novel Electrophotographic System, Appl. Opt. 8 (1969) 192–195. doi:10.1364/AO.8.S1.000192.

[38] C.G. Granqvist, Oxide electrochromics: An introduction to devices and materials, Sol. Energy Mater. Sol. Cells. 99 (2012) 1–13. doi:10.1016/j.solmat.2011.08.021.

[39] C.-P. Li, C. Engtrakul, R.C. Tenent, C.A. Wolden, Scalable synthesis of improved nanocrystalline, mesoporous tungsten

oxide films with exceptional electrochromic performance, Sol. Energy Mater. Sol. Cells. 132 (2015) 6–14. doi:10.1016/j.solmat.2014.08.014.

[40] A.C. Dillon, A.H. Mahan, R. Deshpande, P.A. Parilla, K.M. Jones, S.-H. Lee, Metal oxide nano-particles for improved electrochromic and lithium-ion battery technologies, Thin Solid Films. 516 (2008) 794–797. doi:10.1016/j.tsf.2007.06.177.

[41] J.M. Wang, X.W. Sun, Z. Jiao, Application of Nanostructures in Electrochromic Materials and Devices: Recent Progress, Materials. 3 (2010) 5029–5053. doi:10.3390/ma3125029.

[42] G. Boschloo, D. Fitzmaurice, Electron Accumulation in Nanostructured TiO2 (Anatase) Electrodes, J. Phys. Chem. B. 103 (1999) 7860–7868. doi:10.1021/jp983040m.

[43] S.-H. Lee, C.E. Tracy, Y. Yan, J.R. Pitts, S.K. Deb, Solid-State Nanocomposite Electrochromic Pseudocapacitors, Electrochem. Solid-State Lett. 8 (2005) A188–A190. doi:10.1149/1.1861050.

[44] M.R.J. Scherer, U. Steiner, Efficient Electrochromic Devices Made from 3D Nanotubular Gyroid Networks, Nano Lett. 13 (2013) 3005–3010. doi:10.1021/nl303833h.

[45] D. Wei, M.R.J. Scherer, C. Bower, P. Andrew, T. Ryhänen, U. Steiner, A Nanostructured Electrochromic Supercapacitor, Nano Lett. 12 (2012) 1857–1862. doi:10.1021/nl2042112.

[46] P.M. Beaujuge, J.R. Reynolds, Color Control in π-Conjugated Organic Polymers for Use in Electrochromic Devices, Chem. Rev. 110 (2010) 268–320. doi:10.1021/cr900129a.

[47] J. Jensen, M. Hösel, A.L. Dyer, F.C. Krebs, Development and Manufacture of Polymer-Based Electrochromic Devices, Adv. Funct. Mater. 25 (2015) 2073–2090. doi:10.1002/adfm.201403765.

[48] P.M. Beaujuge, S. Ellinger, J.R. Reynolds, The donor–acceptor approach allows a black-to-transmissive switching

polymeric electrochrome, Nat. Mater. 7 (2008) 795. doi:10.1038/nmat2272.

[49] J.-M. Tarascon, M. Armand, Issues and challenges facing rechargeable lithium batteries, Nature. (2001). doi:10.1038/35104644.

[50] M.G. Kim, J. Cho, Reversible and High-Capacity Nanostructured Electrode Materials for Li-Ion Batteries, Adv. Funct. Mater. 19 (2009) 1497–1514. doi:10.1002/adfm.200801095.

[51] C. Liu, F. Li, L.-P. Ma, H.-M. Cheng, Advanced Materials for Energy Storage, Adv. Mater. 22 (2010) E28–E62. doi:10.1002/adma.200903328.

[52] L. Mai, L. Xu, C. Han, X. Xu, Y. Luo, S. Zhao, Y. Zhao, Electrospun Ultralong Hierarchical Vanadium Oxide Nanowires with High Performance for Lithium Ion Batteries, Nano Lett. 10 (2010) 4750–4755. doi:10.1021/nl103343w.

[53] G. Derrien, J. Hassoun, S. Panero, B. Scrosati, Nanostructured Sn–C Composite as an Advanced Anode Material in High-Performance Lithium-Ion Batteries, Adv. Mater. 19 (2007) 2336–2340. doi:10.1002/adma.200700748.

[54] Y.-G. Guo, J.-S. Hu, L.-J. Wan, Nanostructured Materials for Electrochemical Energy Conversion and Storage Devices, Adv. Mater. 20 (2008) 2878–2887. doi:10.1002/adma.200800627.

[55] Y. Wang, G. Cao, Developments in Nanostructured Cathode Materials for High-Performance Lithium-Ion Batteries, Adv. Mater. 20 (2008) 2251–2269. doi:10.1002/adma.200702242.

[56] P. Simon, Y. Gogotsi, Materials for electrochemical capacitors, Nat. Mater. 7 (2008) 845–854. doi:10.1038/nmat2297.

[57] J.R. Miller, P. Simon, Electrochemical Capacitors for Energy Management, Science. 321 (2008) 651–652. doi:10.1126/science.1158736.

[58] M.M. Shaijumon, F.S. Ou, L. Ci, P.M. Ajayan, Synthesis of hybrid nanowire arrays and their application as high power supercapacitor electrodes, Chem. Commun. 0 (2008) 2373–2375. doi:10.1039/B800866C.

[59] J.-H. Kim, K. Zhu, Y. Yan, C.L. Perkins, A.J. Frank, Microstructure and Pseudocapacitive Properties of Electrodes Constructed of Oriented NiO-TiO2 Nanotube Arrays, Nano Lett. 10 (2010) 4099–4104. doi:10.1021/nl102203s.

[60] C. Yu, C. Masarapu, J. Rong, B. Wei, H. Jiang, Stretchable Supercapacitors Based on Buckled Single-Walled Carbon-Nanotube Macrofilms, Adv. Mater. 21 (2009) 4793–4797. doi:10.1002/adma.200901775.

[61] L.L. Zhang, X.S. Zhao, Carbon-based materials as supercapacitor electrodes, Chem. Soc. Rev. 38 (2009) 2520–2531. doi:10.1039/B813846J.

[62] C.-C. Hu, K.-H. Chang, M.-C. Lin, Y.-T. Wu, Design and Tailoring of the Nanotubular Arrayed Architecture of Hydrous RuO2 for Next Generation Supercapacitors, Nano Lett. 6 (2006) 2690–2695. doi:10.1021/nl061576a.

[63] P.-C. Chen, G. Shen, Y. Shi, H. Chen, C. Zhou, Preparation and Characterization of Flexible Asymmetric Supercapacitors Based on Transition-Metal-Oxide Nanowire/Single-Walled Carbon Nanotube Hybrid Thin-Film Electrodes, ACS Nano. 4 (2010) 4403–4411. doi:10.1021/nn100856y.

[64] L. Hu, M. Pasta, F. La Mantia, L. Cui, S. Jeong, H.D. Deshazer, J.W. Choi, S.M. Han, Y. Cui, Stretchable, Porous, and Conductive Energy Textiles, Nano Lett. 10 (2010) 708–714. doi:10.1021/nl903949m.

[65] X. Dong, W. Shen, J. Gu, L. Xiong, Y. Zhu, H. Li, J. Shi, MnO2-Embedded-in-Mesoporous-Carbon-Wall Structure for Use as Electrochemical Capacitors, J. Phys. Chem. B. 110 (2006) 6015–6019. doi:10.1021/jp056754n.

[66] A.E. Fischer, K.A. Pettigrew, D.R. Rolison, R.M. Stroud, J.W. Long, Incorporation of Homogeneous, Nanoscale MnO2 within Ultraporous Carbon Structures via Self-Limiting Electroless Deposition: Implications for Electrochemical Capacitors, Nano Lett. 7 (2007) 281–286. doi:10.1021/nl062263i.

[67] H. Wang, H.S. Casalongue, Y. Liang, H. Dai, Ni(OH)2 Nanoplates Grown on Graphene as Advanced Electrochemical Pseudocapacitor Materials, J. Am. Chem. Soc. 132 (2010) 7472–7477. doi:10.1021/ja102267j.

[68] R. Liu, S.B. Lee, MnO2/Poly(3,4-ethylenedioxythiophene) Coaxial Nanowires by One-Step Coelectrodeposition for Electrochemical Energy Storage, J. Am. Chem. Soc. 130 (2008) 2942–2943. doi:10.1021/ja7112382.

[69] Y. Saito, S. Uemura, Field emission from carbon nanotubes and its application to electron sources, Carbon. 38 (2000) 169–182. doi:10.1016/S0008-6223(99)00139-6.

[70] J.-H. Deng, L.-N. Deng, R.-N. Liu, A.-L. Han, D.-J. Li, G.-A. Cheng, Vapor–solid preparation of densely distributed and small-sized graphene nanoflakes on one-dimensional nanomaterials for low-field and highly stable field emission, Carbon. 102 (2016) 1–9. doi:10.1016/j.carbon.2016.02.026.

[71] V. Kumar, S.K. Saxena, V. Kaushik, K. Saxena, A.K. Shukla, R. Kumar, Silicon nanowires prepared by metal induced etching (MIE): good field emitters, RSC Adv. 4 (2014) 57799–57803. doi:10.1039/C4RA11093E.

[72] P.V. Kamat, Photochemistry on nonreactive and reactive (semiconductor) surfaces, Chem. Rev. 93 (1993) 267–300. doi:10.1021/cr00017a013.

[73] B.A. Nail, J.M. Fields, J. Zhao, J. Wang, M.J. Greaney, R.L. Brutchey, F.E. Osterloh, Nickel Oxide Particles Catalyze Photochemical Hydrogen Evolution from Water—Nanoscaling Promotes P-Type Character and Minority Carrier Extraction, ACS Nano. 9 (2015) 5135–5142. doi:10.1021/acsnano.5b00435.

[74] S.K. Srivastava, A.K. Shukla, V.D. Vankar, V. Kumar, Growth, structure and field emission characteristics of petal like carbon nano-structured thin films, Thin Solid Films. 492 (2005) 124–130. doi:10.1016/j.tsf.2005.07.283.

[75] R.L. McCreery, Chemical monolayer field emitter device, US7019449 B2, 2006. http://www.google.com/patents/US7019449 (accessed April 4, 2017).

[76] A. Pandey, A. Prasad, J.P. Moscatello, M. Engelhard, C. Wang, Y.K. Yap, Very Stable Electron Field Emission from Strontium Titanate Coated Carbon Nanotube Matrices with Low Emission Thresholds, ACS Nano. 7 (2013) 117–125. doi:10.1021/nn303351g.

[77] A. Pandey, A. Prasad, J.P. Moscatello, Y.K. Yap, Stable Electron Field Emission from PMMA–CNT Matrices, ACS Nano. 4 (2010) 6760–6766. doi:10.1021/nn100925g.

[78] M.S. Dresselhaus, Recent Advances in Carbon Nanotube Science and Applications, ACS Nano. 4 (2010) 4344–4349. doi:10.1021/nn101845f.

[79] P.S. Weiss, A Conversation with Prof. Mildred Dresselhaus: A Career in Carbon Nanomaterials, ACS Nano. 3 (2009) 2434–2440. doi:10.1021/nn901147q.

[80] J.F. Rodriguez-Nieva, M.S. Dresselhaus, L.S. Levitov, Thermionic Emission and Negative dI/dV in Photoactive Graphene Heterostructures, Nano Lett. 15 (2015) 1451–1456. doi:10.1021/nl502522q.

[81] J.F. Rodriguez-Nieva, M.S. Dresselhaus, J.C.W. Song, Enhanced Thermionic-Dominated Photoresponse in Graphene Schottky Junctions, Nano Lett. 16 (2016) 6036–6041. doi:10.1021/acs.nanolett.6b01965.

[82] D. Wu, C. Zhang, S. Xu, Y. Zhu, D. Xiong, P. Guo, Y. Wu, R. Qi, R. Huang, L. Wang, P.K. Chu, Nitrogen-doped multilayered nanographene derived from Ni3C with efficient electron field emission, J. Mater. Chem. C. 4 (2016) 9251–9260. doi:10.1039/C6TC03264H.

[83] X. Zhou, Z. Zhang, Y. Wang, Ce3+ and Tb3+ singly- and co-doped MgGd4Si3O13 for ultraviolet light emitting diodes and field emission displays, J. Mater. Chem. C. 3 (2015) 3676–3683. doi:10.1039/C4TC02807D.

[84] K.K. Naik, R. Khare, D. Chakravarty, M.A. More, R. Thapa, D.J. Late, C.S. Rout, Field emission properties of ZnO nanosheet arrays, Appl. Phys. Lett. 105 (2014) 233101. doi:10.1063/1.4903271.

[85] Carl Zeiss Supra 55 Variable Pressure Field Emission Scanning Electron Microscope (VP FE-SEM) Electron microscope | Red, (n.d.). http://eqdb.nrf.ac.za/equipment/microscope/carl-zeiss-supra-55-variable-pressure-field-emission-scanning-electron (accessed January 19, 2018).

[86] FEI Tecnai G2 20 TWIN Transmission Electron Microscope | www.bionand.es, (n.d.). http://www.bionand.es/equipment/fei-tecnai-tem (accessed January 19, 2018).

[87] MultiMode 8 - Overview - Performance AFMs | Bruker - MultiMode 8 | Bruker, Bruker.com. (n.d.). https://www.bruker.com/products/surface-and-dimensional-analysis/atomic-force-microscopes/multimode-8-hr/overview.html (accessed January 19, 2018).

[88] Research Microscope/Research Microscopes, (n.d.). http://www.radicalindia.com/Research-Microscope.html (accessed January 19, 2018).

[89] LabRAM HR Evolution - HORIBA, (n.d.). http://www.horiba.com/scientific/products/raman-spectroscopy/raman-spectrometers/raman-microscopes/hr-evolution/labram-hr-evolution-17309/?L=titletx_horibafeuserregister_pi1%5Bcmd%5D (accessed January 19, 2018).

[90] Agilent | Cary 60 UV-Vis, (n.d.). https://www.agilent.com/en/products/uv-vis-uv-vis-nir/uv-vis-uv-vis-nir-systems/cary-60-uv-vis (accessed January 19, 2018).

[91] Intelligent X-ray diffraction (XRD) system | Rigaku, (n.d.). https://www.rigaku.com/en/products/xrd/smartlab (accessed January 19, 2018).

[92] Home, (n.d.). http://www.specs.de/cms/front_content.php?idcat=209 (accessed January 19, 2018).

[93] Keithley Potentiostats | Tektronix, (n.d.). https://www.tek.com/potentiostats (accessed January 19, 2018).

[94] S. Stankovich, D.A. Dikin, R.D. Piner, K.A. Kohlhaas, A. Kleinhammes, Y. Jia, Y. Wu, S.T. Nguyen, R.S. Ruoff, Synthesis of graphene-based nanosheets via chemical reduction of exfoliated graphite oxide, Carbon. 45 (2007) 1558–1565. doi:10.1016/j.carbon.2007.02.034.

[95] B. Liu, E.S. Aydil, Growth of Oriented Single-Crystalline Rutile TiO2 Nanorods on Transparent Conducting Substrates for Dye-Sensitized Solar Cells, J. Am. Chem. Soc. 131 (2009) 3985–3990. doi:10.1021/ja8078972.

[96] X.H. Xia, J.P. Tu, J. Zhang, J.Y. Xiang, X.L. Wang, X.B. Zhao, Cobalt Oxide Ordered Bowl-Like Array Films Prepared by

Electrodeposition through Monolayer Polystyrene Sphere Template and Electrochromic Properties, ACS Appl. Mater. Interfaces. 2 (2010) 186–192. doi:10.1021/am900636g.

[97] I. Horcas, R. Fernández, WSXM: A software for scanning probe microscopy and a tool for nanotechnology, Rev. Sci. Instrum. 78 (2007) 013705. doi:10.1063/1.2432410.

[98] C.A. Schneider, W.S. Rasband, K.W. Eliceiri, NIH Image to ImageJ: 25 years of image analysis, Nat. Methods. 9 (2012) 671–675. doi:10.1038/nmeth.2089.

[99] R. Kwok, XPS Peak Fitting Program for WIN95/98 XPSPEAK Version 4.1. Department of Chemistry, The Chinese University of Hong Kong, (n.d.).

[100] Flowchart Maker & Diagramming Software, Microsoft Visio, (n.d.). https://products.office.com/en-in/visio/flowchart-software (accessed February 21, 2018).

[101] B. Liu, A. Blaszczyk, M. Mayor, T. Wandlowski, Redox-Switching in a Viologen-type Adlayer: An Electrochemical Shell-Isolated Nanoparticle Enhanced Raman Spectroscopy Study on Au(111)-(1×1) Single Crystal Electrodes, ACS Nano. 5 (2011) 5662–5672. doi:10.1021/nn201307g.

[102] B. Han, Z. Li, T. Wandlowski, A. Błaszczyk, M. Mayor, Potential-Induced Redox Switching in Viologen Self-Assembled Monolayers: An ATR–SEIRAS Approach, J. Phys. Chem. C. 111 (2007) 13855–13863. doi:10.1021/jp073208g.

[103] L. Michaelis, E.S. Hill, THE VIOLOGEN INDICATORS, J. Gen. Physiol. 16 (1933) 859–873.

[104] M. Mohammad, Methyl viologen neutral MV. 1. Preparation and some properties, J. Org. Chem. 52 (1987) 2779–2782. doi:10.1021/jo00389a025.

[105] J.J. Yang, M.D. Pickett, X. Li, D.A.A. Ohlberg, D.R. Stewart, R.S. Williams, Memristive switching mechanism for metal/oxide/metal nanodevices, Nat. Nanotechnol. 3 (2008) 429–433. doi:10.1038/nnano.2008.160.

[106] J. Yao, Z. Sun, L. Zhong, D. Natelson, J.M. Tour, Resistive Switches and Memories from Silicon Oxide, Nano Lett. 10 (2010) 4105–4110. doi:10.1021/nl102255r.

[107] C. Lu, Q. Fu, S. Huang, J. Liu, Polymer Electrolyte-Gated Carbon Nanotube Field-Effect Transistor, Nano Lett. 4 (2004) 623–627. doi:10.1021/nl049937e.

[108] M.J. Panzer, C.D. Frisbie, Polymer Electrolyte-Gated Organic Field-Effect Transistors: Low-Voltage, High-Current Switches for Organic Electronics and Testbeds for Probing Electrical Transport at High Charge Carrier Density, J. Am. Chem. Soc. 129 (2007) 6599–6607. doi:10.1021/ja0708767.

[109] M.J. Panzer, C.D. Frisbie, Polymer Electrolyte Gate Dielectric Reveals Finite Windows of High Conductivity in Organic Thin Film Transistors at High Charge Carrier Densities, J. Am. Chem. Soc. 127 (2005) 6960–6961. doi:10.1021/ja051579+.

[110] A. Das, S. Pisana, B. Chakraborty, S. Piscanec, S.K. Saha, U.V. Waghmare, K.S. Novoselov, H.R. Krishnamurthy, A.K. Geim, A.C. Ferrari, A.K. Sood, Monitoring dopants by Raman scattering in an electrochemically top-gated graphene transistor, Nat. Nanotechnol. 3 (2008) 210–215. doi:10.1038/nnano.2008.67.

[111] J. Lee, L.G. Kaake, J.H. Cho, X.-Y. Zhu, T.P. Lodge, C.D. Frisbie, Ion Gel-Gated Polymer Thin-Film Transistors: Operating Mechanism and Characterization of Gate Dielectric Capacitance, Switching Speed, and Stability, J. Phys. Chem. C. 113 (2009) 8972–8981. doi:10.1021/jp901426e.

[112] J.D. Yuen, A.S. Dhoot, E.B. Namdas, N.E. Coates, M. Heeney, I. McCulloch, D. Moses, A.J. Heeger, Electrochemical Doping in Electrolyte-Gated Polymer Transistors, J. Am. Chem. Soc. 129 (2007) 14367–14371. doi:10.1021/ja0749845.

[113] C. Pozo-Gonzalo, M. Salsamendi, A. Viñuales, J.A. Pomposo, H.-J. Grande, Highly transparent electrochromic plastic device that changes to purple and to blue by increasing the

potential, Sol. Energy Mater. Sol. Cells. 93 (2009) 2093–2097. doi:10.1016/j.solmat.2009.01.010.

[114] A.J. Bard, A. Ledwith, H.J. Shine, Formation, Properties and Reactions of Cation Radicals in Solution, in: V.G. and D. Bethell (Ed.), Adv. Phys. Org. Chem., Academic Press, 1976: pp. 155–278. http://www.sciencedirect.com/science/article/pii/S0065316008602142 (accessed December 21, 2016).

[115] J.A. Farrington, A. Ledwith, M.F. Stam, Cation–radicals: oxidation of methoxide ion with 1,1′-dimethyl-4,4′-bipyridylium dichloride (paraquat dichloride), J. Chem. Soc. D. (1969) 259–260. doi:10.1039/C29690000259.

[116] W. Pryor, Free Radicals in Biology, Elsevier, 2012.

[117] H.T. van Dam, J.J. Ponjeé, Electrochemically Generated Colored Films of Insoluble Viologen Radical Compounds, J. Electrochem. Soc. 121 (1974) 1555–1558. doi:10.1149/1.2401732.

[118] C.M. Amb, A.L. Dyer, J.R. Reynolds, Navigating the Color Palette of Solution-Processable Electrochromic Polymers, Chem. Mater. 23 (2011) 397–415. doi:10.1021/cm1021245.

[119] LED ColorCalculator, (n.d.). https://www.sylvania.com/en-us/tools-and-resources/Pages/led-color-calculator.aspx (accessed March 15, 2016).

[120] Z.Q. Tian, W.H. Li, B.W. Mao, J.S. Gao, Surface-enhanced Raman spectroscopic studies on structural dynamics of coadsorption of thiourea and ClO4− at Ag electrodes, J. Electroanal. Chem. 379 (1994) 271–279. doi:10.1016/0022-0728(94)87148-5.

[121] F.M. Raymo, R.J. Alvarado, E.J. Pacsial, D. Alexander, Electron Transport in Self-Assembled Bipyridinium Multilayers, J. Phys. Chem. B. 108 (2004) 8622–8625. doi:10.1021/jp036730l.

[122] T. Lu, T.M. Cotton, In situ Raman spectra of the three redox forms of heptylviologen at platinum and silver electrodes: counterion effects, J. Phys. Chem. 91 (1987) 5978–5985. doi:10.1021/j100307a033.

[123] J.R. Jennings, W.Y. Lim, S.M. Zakeeruddin, M. Grätzel, Q. Wang, A Redox-Flow Electrochromic Window, ACS Appl. Mater. Interfaces. 7 (2015) 2827–2832. doi:10.1021/am508086u.

[124] E. Hwang, S. Seo, S. Bak, H. Lee, M. Min, H. Lee, An Electrolyte-Free Flexible Electrochromic Device Using Electrostatically Strong Graphene Quantum Dot–Viologen Nanocomposites, Adv. Mater. 26 (2014) 5129–5136. doi:10.1002/adma.201401201.

[125] J. Palenzuela, A. Viñuales, I. Odriozola, G. Cabañero, H.J. Grande, V. Ruiz, Flexible Viologen Electrochromic Devices with Low Operational Voltages Using Reduced Graphene Oxide Electrodes, ACS Appl. Mater. Interfaces. 6 (2014) 14562–14567. doi:10.1021/am503869b.

[126] B.N. Reddy, M. Deepa, A.G. Joshi, A.K. Srivastava, Poly(3,4-Ethylenedioxypyrrole) Enwrapped by Reduced Graphene Oxide: How Conduction Behavior at Nanolevel Leads to Increased Electrochemical Activity, J. Phys. Chem. C. 115 (2011) 18354–18365. doi:10.1021/jp205551k.

[127] E. Hwang, S. Seo, S. Bak, H. Lee, M. Min, H. Lee, An Electrolyte-Free Flexible Electrochromic Device Using Electrostatically Strong Graphene Quantum Dot–Viologen Nanocomposites, Adv. Mater. 26 (2014) 5129–5136. doi:10.1002/adma.201401201.

[128] L. Zhao, L. Zhao, Y. Xu, T. Qiu, L. Zhi, G. Shi, Polyaniline electrochromic devices with transparent graphene electrodes, Electrochimica Acta. 55 (2009) 491–497. doi:10.1016/j.electacta.2009.08.063.

[129] A.J. Olaya, P. Ge, J.F. Gonthier, P. Pechy, C. Corminboeuf, H.H. Girault, Four-Electron Oxygen Reduction by Tetrathiafulvalene, J. Am. Chem. Soc. 133 (2011) 12115–12123. doi:10.1021/ja203251u.

[130] R. Oliveira, S. Groni, C. Fave, M. Branca, F. Mavré, D. Lorcy, M. Fourmigué, B. Schöllhorn, Electrochemical activation of a tetrathiafulvalene halogen bond donor in solution, Phys. Chem. Chem. Phys. 18 (2016) 15867–15873. doi:10.1039/C6CP02219G.

[131] S. Roy, S.K. Saxena, S. Mishra, P. Yogi, P.R. Sagdeo, R. Kumar, Evidence of bovine serum albumin-viologen herbicide binding interaction and associated structural modifications, J. Mol. Struct. 1139 (2017) 447–454. doi:10.1016/j.molstruc.2017.03.058.

[132] M. Kalbac, H. Farhat, J. Kong, P. Janda, L. Kavan, M.S. Dresselhaus, Raman Spectroscopy and in Situ Raman Spectroelectrochemistry of Bilayer 12C/13C Graphene, Nano Lett. 11 (2011) 1957–1963. doi:10.1021/nl2001956.

[133] O. Frank, M.S. Dresselhaus, M. Kalbac, Raman Spectroscopy and in Situ Raman Spectroelectrochemistry of Isotopically Engineered Graphene Systems, Acc. Chem. Res. 48 (2015) 111–118. doi:10.1021/ar500384p.

[134] C. Cong, T. Yu, R. Saito, G.F. Dresselhaus, M.S. Dresselhaus, Second-Order Overtone and Combination Raman Modes of Graphene Layers in the Range of 1690–2150 cm−1, ACS Nano. 5 (2011) 1600–1605. doi:10.1021/nn200010m.

[135] M.S. Dresselhaus, A. Jorio, M. Hofmann, G. Dresselhaus, R. Saito, Perspectives on Carbon Nanotubes and Graphene Raman Spectroscopy, Nano Lett. 10 (2010) 751–758. doi:10.1021/nl904286r.

[136] J. Lee, K. Kim, W.I. Park, B.-H. Kim, J.H. Park, T.-H. Kim, S. Bong, C.-H. Kim, G. Chae, M. Jun, Y. Hwang, Y.S. Jung, S. Jeon, Uniform Graphene Quantum Dots Patterned from Self-

Assembled Silica Nanodots, Nano Lett. 12 (2012) 6078–6083. doi:10.1021/nl302520m.

[137] D. Pan, J. Zhang, Z. Li, M. Wu, Hydrothermal Route for Cutting Graphene Sheets into Blue-Luminescent Graphene Quantum Dots, Adv. Mater. 22 (2010) 734–738. doi:10.1002/adma.200902825.

[138] S. Zhu, J. Zhang, C. Qiao, S. Tang, Y. Li, W. Yuan, B. Li, L. Tian, F. Liu, R. Hu, H. Gao, H. Wei, H. Zhang, H. Sun, B. Yang, Strongly green-photoluminescent graphene quantum dots for bioimaging applications, Chem. Commun. 47 (2011) 6858–6860. doi:10.1039/C1CC11122A.

[139] V.L. Bridewell, C.J. Karwacki, P.V. Kamat, Electrocatalytic Sensing with Reduced Graphene Oxide: Electron Shuttling between Redox Couples Anchored on a 2-D Surface, ACS Sens. 1 (2016) 1203–1207. doi:10.1021/acssensors.6b00377.

[140] R. Kumar, R.G. Pillai, N. Pekas, Y. Wu, R.L. McCreery, Spatially Resolved Raman Spectroelectrochemistry of Solid-State Polythiophene/Viologen Memory Devices, J. Am. Chem. Soc. 134 (2012) 14869–14876. doi:10.1021/ja304458s.

[141] B. Gadgil, P. Damlin, E. Dmitrieva, T. Ääritalo, C. Kvarnström, ESR/UV-Vis-NIR spectroelectrochemical study and electrochromic contrast enhancement of a polythiophene derivative bearing a pendant viologen, RSC Adv. 5 (2015) 42242–42249. doi:10.1039/C5RA04618A.

[142] V. Jain, M. Khiterer, R. Montazami, H.M. Yochum, K.J. Shea, J.R. Heflin, High-Contrast Solid-State Electrochromic Devices of Viologen-Bridged Polysilsesquioxane Nanoparticles Fabricated by Layer-by-Layer Assembly, ACS Appl. Mater. Interfaces. 1 (2009) 83–89. doi:10.1021/am8000264.

[143] B.-H. Chen, S.-Y. Kao, C.-W. Hu, M. Higuchi, K.-C. Ho, Y.-C. Liao, Printed Multicolor High-Contrast Electrochromic Devices,

ACS Appl. Mater. Interfaces. 7 (2015) 25069–25076. doi:10.1021/acsami.5b08061.

[144] H.C. Moon, T.P. Lodge, C.D. Frisbie, Solution Processable, Electrochromic Ion Gels for Sub-1 V, Flexible Displays on Plastic, Chem. Mater. 27 (2015) 1420–1425. doi:10.1021/acs.chemmater.5b00026.

[145] H.C. Moon, C.-H. Kim, T.P. Lodge, C.D. Frisbie, Multicolored, Low-Power, Flexible Electrochromic Devices Based on Ion Gels, ACS Appl. Mater. Interfaces. 8 (2016) 6252–6260. doi:10.1021/acsami.6b01307.

[146] H. Ling, J. Lu, S. Phua, H. Liu, L. Liu, Y. Huang, D. Mandler, P. See Lee, X. Lu, One-pot sequential electrochemical deposition of multilayer poly(3,4-ethylenedioxythiophene):poly(4-styrenesulfonic acid)/tungsten trioxide hybrid films and their enhanced electrochromic properties, J. Mater. Chem. A. 2 (2014) 2708–2717. doi:10.1039/C3TA14781A.

[147] S. Zhang, G. Sun, Y. He, R. Fu, Y. Gu, S. Chen, Preparation, Characterization, and Electrochromic Properties of Nanocellulose-Based Polyaniline Nanocomposite Films, ACS Appl. Mater. Interfaces. 9 (2017) 16426–16434. doi:10.1021/acsami.7b02794.

[148] M.-S. Fan, S.-Y. Kao, T.-H. Chang, R. Vittal, K.-C. Ho, A high contrast solid-state electrochromic device based on nano-structural Prussian blue and poly(butyl viologen) thin films, Sol. Energy Mater. Sol. Cells. 145 (2016) 35–41. doi:10.1016/j.solmat.2015.06.031.

[149] R. Nakajima, Y. Yamada, T. Komatsu, K. Murashiro, T. Saji, K. Hoshino, Electrochromic properties of ITO nanoparticles/viologen composite film electrodes, RSC Adv. 2 (2012) 4377–4381. doi:10.1039/C2RA01090A.

[150] S. Mishra, P. Yogi, S.K. Saxena, J. Jayabalan, P. Behera, P.R. Sagdeo, R. Kumar, Significant field emission enhancement in

ultrathin nano-thorn covered NiO nano-petals, J. Mater. Chem. C. (2017). doi:10.1039/C7TC01949A.

[151] Y. Chen, Y. Wang, P. Sun, P. Yang, L. Du, W. Mai, Nickel oxide nanoflake-based bifunctional glass electrodes with superior cyclic stability for energy storage and electrochromic applications, J. Mater. Chem. A. 3 (2015) 20614–20618. doi:10.1039/C5TA04011F.

[152] G. Cai, J. Tu, D. Zhou, L. Li, J. Zhang, X. Wang, C. Gu, Constructed TiO2/NiO Core/Shell Nanorod Array for Efficient Electrochromic Application, J. Phys. Chem. C. 118 (2014) 6690–6696. doi:10.1021/jp500699u.

[153] J. Zhang, G. Cai, D. Zhou, H. Tang, X. Wang, C. Gu, J. Tu, Co-doped NiO nanoflake array films with enhanced electrochromic properties, J. Mater. Chem. C. 2 (2014) 7013–7021. doi:10.1039/C4TC01033G.

[154] J. Liu, J. Jiang, C. Cheng, H. Li, J. Zhang, H. Gong, H.J. Fan, Co3O4 Nanowire@MnO2 Ultrathin Nanosheet Core/Shell Arrays: A New Class of High-Performance Pseudocapacitive Materials, Adv. Mater. 23 (2011) 2076–2081. doi:10.1002/adma.201100058.

[155] X. Xia, Y. Zhang, D. Chao, C. Guan, Y. Zhang, L. Li, X. Ge, I.M. Bacho, J. Tu, H.J. Fan, Solution synthesis of metal oxides for electrochemical energy storage applications, Nanoscale. 6 (2014) 5008–5048. doi:10.1039/C4NR00024B.

[156] K. Wang, J. Chen, W. Zhou, Y. Zhang, Y. Yan, J. Pern, A. Mascarenhas, Direct Growth of Highly Mismatched Type II ZnO/ZnSe Core/Shell Nanowire Arrays on Transparent Conducting Oxide Substrates for Solar Cell Applications, Adv. Mater. 20 (2008) 3248–3253. doi:10.1002/adma.200800145.

[157] B.G. Streetman, S. Banerjee, Solid State Electronic Devices, Pearson Prentice Hall, 2006.

[158] X. Xia, J. Tu, Y. Zhang, J. Chen, X. Wang, C. Gu, C. Guan, J. Luo, H.J. Fan, Porous Hydroxide Nanosheets on Preformed Nanowires by Electrodeposition: Branched Nanoarrays for Electrochemical Energy Storage, Chem. Mater. 24 (2012) 3793–3799. doi:10.1021/cm302416d.

[159] X. Xia, J. Tu, Y. Mai, X. Wang, C. Gu, X. Zhao, Self-supported hydrothermal synthesized hollow Co3O4 nanowire arrays with high supercapacitor capacitance, J. Mater. Chem. 21 (2011) 9319–9325. doi:10.1039/C1JM10946D.

[160] L. Zhang, Z. Gao, C. Liu, Y. Zhang, Z. Tu, X. Yang, F. Yang, Z. Wen, L. Zhu, R. Liu, Y. Li, L. Cui, Synthesis of TiO2 decorated Co3O4 acicular nanowire arrays and their application as an ethanol sensor, J. Mater. Chem. A. 3 (2015) 2794–2801. doi:10.1039/C4TA06440B.

[161] Y.Q. Liang, Z.D. Cui, S.L. Zhu, Z.Y. Li, X.J. Yang, Y.J. Chen, J.M. Ma, Design of a highly sensitive ethanol sensor using a nano-coaxial p-Co3O4/n-TiO2 heterojunction synthesized at low temperature, Nanoscale. 5 (2013) 10916–10926. doi:10.1039/C3NR03616B.

[162] I.S. Cho, Z. Chen, A.J. Forman, D.R. Kim, P.M. Rao, T.F. Jaramillo, X. Zheng, Branched TiO2 Nanorods for Photoelectrochemical Hydrogen Production, Nano Lett. 11 (2011) 4978–4984. doi:10.1021/nl2029392.

[163] Y. Liang, Y. Li, H. Wang, J. Zhou, J. Wang, T. Regier, H. Dai, Co3O4 nanocrystals on graphene as a synergistic catalyst for oxygen reduction reaction, Nat. Mater. 10 (2011) 780–786. doi:10.1038/nmat3087.

[164] G. Luo, K. Shen, J. Zheng, C. Xu, CdS modified TiO2 films showing multicolor switching and enhanced optical contrast, J. Mater. Chem. C. 4 (2016) 9085–9093. doi:10.1039/C6TC02815B.

[165] H. Wang, A.L. Rogach, Hierarchical SnO2 Nanostructures: Recent Advances in Design, Synthesis, and Applications, Chem. Mater. 26 (2014) 123–133. doi:10.1021/cm4018248.

[166] J. Zhao, Y. Tian, Z. Wang, S. Cong, D. Zhou, Q. Zhang, M. Yang, W. Zhang, F. Geng, Z. Zhao, Trace H2O2-Assisted High-Capacity Tungsten Oxide Electrochromic Batteries with Ultrafast Charging in Seconds, Angew. Chem. Int. Ed. 55 (2016) 7161–7165. doi:10.1002/anie.201602657.

[167] A.M. Österholm, D.E. Shen, A.L. Dyer, J.R. Reynolds, Optimization of PEDOT Films in Ionic Liquid Supercapacitors: Demonstration As a Power Source for Polymer Electrochromic Devices, ACS Appl. Mater. Interfaces. 5 (2013) 13432–13440. doi:10.1021/am4043454.

[168] Z. Xie, X. Jin, G. Chen, J. Xu, D. Chen, G. Shen, Integrated smart electrochromic windows for energy saving and storage applications, Chem. Commun. 50 (2013) 608–610. doi:10.1039/C3CC47950A.

[169] G. Cai, P. Darmawan, X. Cheng, P.S. Lee, Inkjet Printed Large Area Multifunctional Smart Windows, Adv. Energy Mater. 7 (2017) n/a-n/a. doi:10.1002/aenm.201602598.

[170] W. Kang, M.-F. Lin, J. Chen, P.S. Lee, Highly Transparent Conducting Nanopaper for Solid State Foldable Electrochromic Devices, Small. 12 (2016) 6370–6377. doi:10.1002/smll.201600979.

[171] G. Cai, P. Darmawan, M. Cui, J. Wang, J. Chen, S. Magdassi, P.S. Lee, Highly Stable Transparent Conductive Silver Grid/PEDOT:PSS Electrodes for Integrated Bifunctional Flexible Electrochromic Supercapacitors, Adv. Energy Mater. 6 (2016) n/a-n/a. doi:10.1002/aenm.201501882.

[172] Y. Kim, H.M. Hwang, L. Wang, I. Kim, Y. Yoon, H. Lee, Solar-light photocatalytic disinfection using

crystalline/amorphous low energy bandgap reduced TiO_2, Sci. Rep. 6 (2016) srep25212. doi:10.1038/srep25212.

[173] M. Barawi, L. De Trizio, R. Giannuzzi, G. Veramonti, L. Manna, M. Manca, Dual Band Electrochromic Devices Based on Nb-Doped TiO2 Nanocrystalline Electrodes, ACS Nano. 11 (2017) 3576–3584. doi:10.1021/acsnano.6b06664.

[174] C.N.P. da Fonseca, M.-A. De Paoli, A. Gorenstein, The electrochromic effect in cobalt oxide thin films, Adv. Mater. 3 (1991) 553–555. doi:10.1002/adma.19910031107.

[175] G. Cai, J. Tu, D. Zhou, J. Zhang, Q. Xiong, X. Zhao, X. Wang, C. Gu, Multicolor Electrochromic Film Based on TiO2@Polyaniline Core/Shell Nanorod Array, J. Phys. Chem. C. 117 (2013) 15967–15975. doi:10.1021/jp4056939.

[176] G.F. Cai, D. Zhou, Q.Q. Xiong, J.H. Zhang, X.L. Wang, C.D. Gu, J.P. Tu, Efficient electrochromic materials based on TiO2@WO3 core/shell nanorod arrays, Sol. Energy Mater. Sol. Cells. 117 (2013) 231–238. doi:10.1016/j.solmat.2013.05.049.

[177] X.H. Xia, J.P. Tu, J. Zhang, J.Y. Xiang, X.L. Wang, X.B. Zhao, Cobalt Oxide Ordered Bowl-Like Array Films Prepared by Electrodeposition through Monolayer Polystyrene Sphere Template and Electrochromic Properties, ACS Appl. Mater. Interfaces. 2 (2010) 186–192. doi:10.1021/am900636g.

[178] K.R. Reyes-Gil, Z.D. Stephens, V. Stavila, D.B. Robinson, Composite WO3/TiO2 Nanostructures for High Electrochromic Activity, ACS Appl. Mater. Interfaces. 7 (2015) 2202–2213. doi:10.1021/am5050696.

[179] S. Mishra, P. Yogi, P.R. Sagdeo, R. Kumar, TiO2–Co3O4 Core–Shell Nanorods: Bifunctional Role in Better Energy Storage and Electrochromism, ACS Appl. Energy Mater. 1 (2018) 790–798. doi:10.1021/acsaem.7b00254.

[180] B. Göhler, V. Hamelbeck, T.Z. Markus, M. Kettner, G.F. Hanne, Z. Vager, R. Naaman, H. Zacharias, Spin Selectivity in Electron

Transmission Through Self-Assembled Monolayers of Double-Stranded DNA, Science. 331 (2011) 894–897. doi:10.1126/science.1199339.

[181] M. Grätzel, Photoelectrochemical cells, Nature. (2001). doi:10.1038/35104607.

[182] C. Jia, A. Migliore, N. Xin, S. Huang, J. Wang, Q. Yang, S. Wang, H. Chen, D. Wang, B. Feng, Z. Liu, G. Zhang, D.-H. Qu, H. Tian, M.A. Ratner, H.Q. Xu, A. Nitzan, X. Guo, Covalently bonded single-molecule junctions with stable and reversible photoswitched conductivity, Science. 352 (2016) 1443–1445. doi:10.1126/science.aaf6298.

[183] S. Nakamura, M. Senoh, S. Nagahama, N. Iwasa, T. Yamada, T. Matsushita, H. Kiyoku, Y. Sugimoto, InGaN Multi-Quantum-Well-Structure Laser Diodes with Cleaved Mirror Cavity Facets, Jpn. J. Appl. Phys. 35 (1996) L217. doi:10.1143/JJAP.35.L217.

[184] L.-F. Chen, Y. Lu, L. Yu, X.W. (David) Lou, Designed formation of hollow particle-based nitrogen-doped carbon nanofibers for high-performance supercapacitors, Energy Environ. Sci. 10 (2017) 1777–1783. doi:10.1039/C7EE00488E.

[185] S. Mishra, P. Yogi, S.K. Saxena, S. Roy, P.R. Sagdeo, R. Kumar, Fast electrochromic display: tetrathiafulvalene–graphene nanoflake as facilitating materials, J. Mater. Chem. C. (2017). doi:10.1039/C7TC02913F.

[186] C. Xia, Q. Jiang, C. Zhao, M.N. Hedhili, H.N. Alshareef, Selenide-Based Electrocatalysts and Scaffolds for Water Oxidation Applications, Adv. Mater. 28 (2016) 77–85. doi:10.1002/adma.201503906.

[187] C. Xia, H. Liang, J. Zhu, U. Schwingenschlögl, H.N. Alshareef, Active Edge Sites Engineering in Nickel Cobalt Selenide Solid Solutions for Highly Efficient Hydrogen Evolution, Adv. Energy Mater. 7 (2017) n/a-n/a. doi:10.1002/aenm.201602089.

[188] V.K. Thakur, G. Ding, J. Ma, P.S. Lee, X. Lu, Hybrid Materials and Polymer Electrolytes for Electrochromic Device Applications, Adv. Mater. 24 (2012) 4071–4096. doi:10.1002/adma.201200213.

[189] X. Xia, D. Chao, Z. Fan, C. Guan, X. Cao, H. Zhang, H.J. Fan, A New Type of Porous Graphite Foams and Their Integrated Composites with Oxide/Polymer Core/Shell Nanowires for Supercapacitors: Structural Design, Fabrication, and Full Supercapacitor Demonstrations, Nano Lett. 14 (2014) 1651–1658. doi:10.1021/nl5001778.

[190] J.-X. Feng, H. Xu, S.-H. Ye, G. Ouyang, Y.-X. Tong, G.-R. Li, Silica–Polypyrrole Hybrids as High-Performance Metal-Free Electrocatalysts for the Hydrogen Evolution Reaction in Neutral Media, Angew. Chem. Int. Ed. 56 (2017) 8120–8124. doi:10.1002/anie.201702934.

[191] K. Wang, J. Huang, Z. Wei, Conducting Polyaniline Nanowire Arrays for High Performance Supercapacitors, J. Phys. Chem. C. 114 (2010) 8062–8067. doi:10.1021/jp9113255.

[192] J. Liu, J. Jiang, C. Cheng, H. Li, J. Zhang, H. Gong, H.J. Fan, Co3O4 Nanowire@MnO2 Ultrathin Nanosheet Core/Shell Arrays: A New Class of High-Performance Pseudocapacitive Materials, Adv. Mater. 23 (2011) 2076–2081. doi:10.1002/adma.201100058.

[193] Y. Chen, Y. Wang, P. Sun, P. Yang, L. Du, W. Mai, Nickel oxide nanoflake-based bifunctional glass electrodes with superior cyclic stability for energy storage and electrochromic applications, J. Mater. Chem. A. 3 (2015) 20614–20618. doi:10.1039/C5TA04011F.

[194] G. Cai, J. Tu, D. Zhou, L. Li, J. Zhang, X. Wang, C. Gu, Constructed TiO2/NiO Core/Shell Nanorod Array for Efficient Electrochromic Application, J. Phys. Chem. C. 118 (2014) 6690–6696. doi:10.1021/jp500699u.

[195] W. Mtangi, F. Tassinari, K. Vankayala, A. Vargas Jentzsch, B. Adelizzi, A.R.A. Palmans, C. Fontanesi, E.W. Meijer, R. Naaman, Control of Electrons' Spin Eliminates Hydrogen Peroxide Formation During Water Splitting, J. Am. Chem. Soc. 139 (2017) 2794–2798. doi:10.1021/jacs.6b12971.

[196] Y.-R. Liu, X. Shang, W.-K. Gao, B. Dong, X. Li, X.-H. Li, J.-C. Zhao, Y.-M. Chai, Y.-Q. Liu, C.-G. Liu, In situ sulfurized CoMoS/CoMoO4 shell–core nanorods supported on N-doped reduced graphene oxide (NRGO) as efficient electrocatalyst for hydrogen evolution reaction, J. Mater. Chem. A. 5 (2017) 2885–2896. doi:10.1039/C6TA10284K.

[197] T. An, Y. Wang, J. Tang, W. Wei, X. Cui, A.M. Alenizi, L. Zhang, G. Zheng, Interlaced NiS2–MoS2 nanoflake-nanowires as efficient hydrogen evolution electrocatalysts in basic solutions, J. Mater. Chem. A. 4 (2016) 13439–13443. doi:10.1039/C6TA05022K.

[198] P. Si, S. Ding, J. Yuan, X.W. (David) Lou, D.-H. Kim, Hierarchically Structured One-Dimensional TiO2 for Protein Immobilization, Direct Electrochemistry, and Mediator-Free Glucose Sensing, ACS Nano. 5 (2011) 7617–7626. doi:10.1021/nn202714c.

[199] J. Zhang, X. Yu, W. Guo, J. Qiu, X. Mou, A. Li, H. Liu, Construction of titanium dioxide nanorod/graphite microfiber hybrid electrodes for a high performance electrochemical glucose biosensor, Nanoscale. 8 (2016) 9382–9389. doi:10.1039/C6NR01360K.

[200] S. Mishra, P. Yogi, P.R. Sagdeo, R. Kumar, Mesoporous Nickel Oxide (NiO) Nanopetals for Ultrasensitive Glucose Sensing, Nanoscale Res. Lett. 13 (2018) 16. doi:10.1186/s11671-018-2435-3.

[201] S. Mishra, P. Yogi, S.K. Saxena, V. Kumar, R. Kumar, Fano Scattering: Manifestation of Acoustic Phonons at the

Nanoscale, J. Phys. Chem. Lett. 7 (2016) 5291–5296. doi:10.1021/acs.jpclett.6b02090.

[202] X.H. Xia, J.P. Tu, J. Zhang, X.L. Wang, W.K. Zhang, H. Huang, A highly porous NiO/polyaniline composite film prepared by combining chemical bath deposition and electro-polymerization and its electrochromic performance, Nanotechnology. 19 (2008) 465701. doi:10.1088/0957-4484/19/46/465701.

[203] A.C. Sonavane, A.I. Inamdar, H.P. Deshmukh, P.S. Patil, Multicoloured electrochromic thin films of NiO/PANI, J. Phys. Appl. Phys. 43 (2010) 315102. doi:10.1088/0022-3727/43/31/315102.

[204] N. Kurra, R. Wang, H.N. Alshareef, All conducting polymer electrodes for asymmetric solid-state supercapacitors, J. Mater. Chem. A. 3 (2015) 7368–7374. doi:10.1039/C5TA00829H.

[205] G. Cai, J. Tu, J. Zhang, Y. Mai, Y. Lu, C. Gu, X. Wang, An efficient route to a porous NiO/reduced graphene oxide hybrid film with highly improved electrochromic properties, Nanoscale. 4 (2012) 5724–5730. doi:10.1039/C2NR31397A.

[206] J. Liang, Z. Fan, S. Chen, S. Ding, G. Yang, Hierarchical NiCo2O4 Nanosheets@halloysite Nanotubes with Ultrahigh Capacitance and Long Cycle Stability As Electrochemical Pseudocapacitor Materials, Chem. Mater. 26 (2014) 4354–4360. doi:10.1021/cm500786a.

[207] S. Mishra, H. Pandey, P. Yogi, S.K. Saxena, S. Roy, P.R. Sagdeo, R. Kumar, Live spectroscopy to observe electrochromism in viologen based solid state device, Solid State Commun. 261 (2017) 17–20. doi:10.1016/j.ssc.2017.05.020.

[208] S. Mishra, H. Pandey, P. Yogi, S.K. Saxena, S. Roy, P.R. Sagdeo, R. Kumar, Interfacial redox centers as origin of color switching in organic electrochromic device, Opt. Mater. 66 (2017) 65–71. doi:10.1016/j.optmat.2017.01.030.

[209] Z.W. Pan, Z.R. Dai, Z.L. Wang, Nanobelts of Semiconducting Oxides, Science. 291 (2001) 1947–1949. doi:10.1126/science.1058120.

[210] M.H. Huang, S. Mao, H. Feick, H. Yan, Y. Wu, H. Kind, E. Weber, R. Russo, P. Yang, Room-Temperature Ultraviolet Nanowire Nanolasers, Science. 292 (2001) 1897–1899. doi:10.1126/science.1060367.

[211] H. Zeng, W. Cai, P. Liu, X. Xu, H. Zhou, C. Klingshirn, H. Kalt, ZnO-Based Hollow Nanoparticles by Selective Etching: Elimination and Reconstruction of Metal−Semiconductor Interface, Improvement of Blue Emission and Photocatalysis, ACS Nano. 2 (2008) 1661–1670. doi:10.1021/nn800353q.

[212] X.-C. Dong, H. Xu, X.-W. Wang, Y.-X. Huang, M.B. Chan-Park, H. Zhang, L.-H. Wang, W. Huang, P. Chen, 3D Graphene–Cobalt Oxide Electrode for High-Performance Supercapacitor and Enzymeless Glucose Detection, ACS Nano. 6 (2012) 3206–3213. doi:10.1021/nn300097q.

[213] H.S.-Y. Cho, J.H. Nickel, R.S. Williams, J. Roh, J. Park, C. Hyejung, M.S. Joo, J. Moon, C.-G. Lee, Y.S. Sohn, J.T. Kim, Non-volatile resistive memory cells, EP2880689 A4, 2016. http://www.google.ch/patents/EP2880689A4 (accessed March 31, 2017).

[214] H. Liu, Q. Zhao, Y. Li, Y. Liu, F. Lu, J. Zhuang, S. Wang, L. Jiang, D. Zhu, D. Yu, L. Chi, Field Emission Properties of Large-Area Nanowires of Organic Charge-Transfer Complexes, J. Am. Chem. Soc. 127 (2005) 1120–1121. doi:10.1021/ja0438359.

[215] H. Gan, H. Liu, Y. Li, Q. Zhao, Y. Li, S. Wang, T. Jiu, N. Wang, X. He, D. Yu, D. Zhu, Fabrication of Polydiacetylene Nanowires by Associated Self-Polymerization and Self-Assembly Processes for Efficient Field Emission Properties, J. Am. Chem. Soc. 127 (2005) 12452–12453. doi:10.1021/ja053352k.

[216] G.T. Tyuliev, K.L. Kostov, XPS/HREELS study of NiO films grown on Ni(111), Phys. Rev. B. 60 (1999) 2900–2907. doi:10.1103/PhysRevB.60.2900.

[217] X. Song, L. Gao, S. Mathur, Synthesis, Characterization, and Gas Sensing Properties of Porous Nickel Oxide Nanotubes, J. Phys. Chem. C. 115 (2011) 21730–21735. doi:10.1021/jp208093s.

[218] D. Lee, D. Paeng, H.K. Park, C.P. Grigoropoulos, Vacuum-Free, Maskless Patterning of Ni Electrodes by Laser Reductive Sintering of NiO Nanoparticle Ink and Its Application to Transparent Conductors, ACS Nano. 8 (2014) 9807–9814. doi:10.1021/nn503383z.

[219] Z. Zhang, Y. Zhao, M. Zhu, NiO films consisting of vertically aligned cone-shaped NiO rods, Appl. Phys. Lett. 88 (2006) 033101. doi:10.1063/1.2166479.

[220] C. Yuan, J. Li, L. Hou, L. Yang, L. Shen, X. Zhang, Facile growth of hexagonal NiO nanoplatelet arrays assembled by mesoporous nanosheets on Ni foam towards high-performance electrochemical capacitors, Electrochimica Acta. 78 (2012) 532–538. doi:10.1016/j.electacta.2012.06.044.

[221] K.L. Jensen, D.A. Shiffler, J.J. Petillo, Z. Pan, J.W. Luginsland, Emittance, surface structure, and electron emission, Phys. Rev. Spec. Top. - Accel. Beams. 17 (2014) 043402. doi:10.1103/PhysRevSTAB.17.043402.

[222] D.H. Dowell, J.F. Schmerge, Quantum efficiency and thermal emittance of metal photocathodes, Phys. Rev. Spec. Top. - Accel. Beams. 12 (2009) 074201. doi:10.1103/PhysRevSTAB.12.074201.

[223] H. Gundel, J. Hańderek, H. Riege, Time-dependent electron emission from ferroelectrics by external pulsed electric fields, J. Appl. Phys. 69 (1991) 975–982. doi:10.1063/1.347290.

[224] T. Zhai, X. Fang, Y. Bando, Q. Liao, X. Xu, H. Zeng, Y. Ma, J. Yao, D. Golberg, Morphology-Dependent Stimulated Emission and Field Emission of Ordered CdS Nanostructure Arrays, ACS Nano. 3 (2009) 949–959. doi:10.1021/nn800895k.

[225] JCPDS Card: 47-1049, (n.d.).

[226] G. Rosenman, D. Shur, Electron emission from ferroelectrics, J. Appl. Phys. 88 (2000) 6109–6161. doi:10.1063/1.1319378.

[227] Y.W. Zhu, T. Yu, F.C. Cheong, X.J. Xu, C.T. Lim, V.B.C. Tan, J.T.L. Thong, C.H. Sow, Large-scale synthesis and field emission properties of vertically oriented CuO nanowire films, Nanotechnology. 16 (2005) 88. doi:10.1088/0957-4484/16/1/018.

[228] J. Chen, B. Yang, X. Liu, J. Yang, X. Yan, Field electron emission from pencil-drawn cold cathodes, Appl. Phys. Lett. 108 (2016) 193112. doi:10.1063/1.4949563.

[229] J. Chen, J. Li, J. Yang, X. Yan, B.-K. Tay, Q. Xue, The hysteresis phenomenon of the field emission from the graphene film, Appl. Phys. Lett. 99 (2011) 173104. doi:10.1063/1.3655912.

[230] J. Chen, L. Cui, D. Sun, B. Yang, J. Yang, X. Yan, Enhanced field emission properties from aligned graphenes fabricated on micro-hole patterned stainless steel, Appl. Phys. Lett. 105 (2014) 213111. doi:10.1063/1.4902971.

[231] E. Cazalas, I. Childres, A. Majcher, T.-F. Chung, Y.P. Chen, I. Jovanovic, Hysteretic response of chemical vapor deposition graphene field effect transistors on SiC substrates, Appl. Phys. Lett. 103 (2013) 053123. doi:10.1063/1.4816426.

[232] C. Li, G. Fang, X. Yang, N. Liu, Y. Liu, X. Zhao, Effect of adsorbates on field emission from flame-synthesized carbon nanotubes, J. Phys. Appl. Phys. 41 (2008) 195401. doi:10.1088/0022-3727/41/19/195401.

[233] R.H. Fowler, L. Nordheim, Electron Emission in Intense Electric Fields, Proc. R. Soc. Lond. Ser. Contain. Pap. Math. Phys. Character. 119 (1928) 173–181.

[234] Z. Yang, W. Yan, J. Lv, K. Qian, Y. Zhang, J. Liu, J. Ai, T. Guo, E. Chen, L. Hu, A simple spraying process greatly enhanced field emission of novel T-ZnO-supported CNT emitters, J. Mater. Chem. C. 4 (2016) 1658–1664. doi:10.1039/C5TC03507D.

[235] T.Y. Wong, C.M.G. Cheung, M. Larsen, S. Sharma, R. Simó, Diabetic retinopathy, Nat. Rev. Dis. Primer. 2 (2016) 16012. doi:10.1038/nrdp.2016.12.

[236] R. Iable, Diabetic kidney disease, Nat. Rev. Dis. Primer. 1 (2015) 15038. doi:10.1038/nrdp.2015.38.

[237] Y. Xiang, Y. Lu, Using personal glucose meters and functional DNA sensors to quantify a variety of analytical targets, Nat. Chem. 3 (2011) 697–703. doi:10.1038/nchem.1092.

[238] H. Lee, T.K. Choi, Y.B. Lee, H.R. Cho, R. Ghaffari, L. Wang, H.J. Choi, T.D. Chung, N. Lu, T. Hyeon, S.H. Choi, D.-H. Kim, A graphene-based electrochemical device with thermoresponsive microneedles for diabetes monitoring and therapy, Nat. Nanotechnol. 11 (2016) 566–572. doi:10.1038/nnano.2016.38.

[239] A. Heller, B. Feldman, Electrochemical Glucose Sensors and Their Applications in Diabetes Management, Chem. Rev. 108 (2008) 2482–2505. doi:10.1021/cr068069y.

[240] G.T. Chandran, X. Li, A. Ogata, R.M. Penner, Electrically Transduced Sensors Based on Nanomaterials (2012–2016), Anal. Chem. 89 (2017) 249–275. doi:10.1021/acs.analchem.6b04687.

[241] J. Bai, B. Zhou, Titanium Dioxide Nanomaterials for Sensor Applications, Chem. Rev. 114 (2014) 10131–10176. doi:10.1021/cr400625j.

[242] J. Wang, Electrochemical Glucose Biosensors, Chem. Rev. 108 (2008) 814–825. doi:10.1021/cr068123a.

[243] Y. Lin, F. Lu, Y. Tu, Z. Ren, Glucose Biosensors Based on Carbon Nanotube Nanoelectrode Ensembles, Nano Lett. 4 (2004) 191–195. doi:10.1021/nl0347233.

[244] C. Wang, L. Yin, L. Zhang, R. Gao, Ti/TiO2 Nanotube Array/Ni Composite Electrodes for Nonenzymatic Amperometric Glucose Sensing, J. Phys. Chem. C. 114 (2010) 4408–4413. doi:10.1021/jp912232p.

[245] J. Xu, N. Xu, X. Zhang, B. Gao, B. Zhang, X. Peng, J. Fu, P.K. Chu, K. Huo, In situ fabrication of Ni nanoparticles on N-doped TiO2 nanowire arrays by nitridation of NiTiO3 for highly sensitive and enzyme-free glucose sensing, J. Mater. Chem. B. 5 (2017) 1779–1786. doi:10.1039/C6TB02784A.

[246] J. Xu, N. Xu, X. Zhang, P. Xu, B. Gao, X. Peng, S. Mooni, Y. Li, J. Fu, K. Huo, Phase separation induced rhizobia-like Ni nanoparticles and TiO2 nanowires composite arrays for enzyme-free glucose sensor, Sens. Actuators B Chem. 244 (2017) 38–46. doi:10.1016/j.snb.2016.12.088.

[247] G. Başkaya, Y. Yıldız, A. Savk, T.O. Okyay, S. Eriş, H. Sert, F. Şen, Rapid, sensitive, and reusable detection of glucose by highly monodisperse nickel nanoparticles decorated functionalized multi-walled carbon nanotubes, Biosens. Bioelectron. 91 (2017) 728–733. doi:10.1016/j.bios.2017.01.045.

[248] Q. Qian, Q. Hu, L. Li, P. Shi, J. Zhou, J. Kong, X. Zhang, G. Sun, W. Huang, Sensitive fiber microelectrode made of nickel hydroxide nanosheets embedded in highly-aligned carbon nanotube scaffold for nonenzymatic glucose determination, Sens. Actuators B Chem. 257 (2018) 23–28. doi:10.1016/j.snb.2017.10.110.

[249] J. Wang, L. Xu, Y. Lu, K. Sheng, W. Liu, C. Chen, Y. Li, B. Dong, H. Song, Engineered IrO2@NiO Core–Shell Nanowires for Sensitive Non-enzymatic Detection of Trace Glucose in

Saliva, Anal. Chem. 88 (2016) 12346–12353. doi:10.1021/acs.analchem.6b03558.

[250] M. Saraf, K. Natarajan, S.M. Mobin, Non-enzymatic amperometric sensing of glucose by employing sucrose templated microspheres of copper oxide (CuO), Dalton Trans. 45 (2016) 5833–5840. doi:10.1039/C6DT00670A.

[251] P. Si, S. Ding, J. Yuan, X.W. (David) Lou, D.-H. Kim, Hierarchically Structured One-Dimensional TiO2 for Protein Immobilization, Direct Electrochemistry, and Mediator-Free Glucose Sensing, ACS Nano. 5 (2011) 7617–7626. doi:10.1021/nn202714c.

[252] H. Tian, M. Jia, M. Zhang, J. Hu, Nonenzymatic glucose sensor based on nickel ion implanted-modified indium tin oxide electrode, Electrochimica Acta. 96 (2013) 285–290. doi:10.1016/j.electacta.2013.02.096.

[253] Z.H. Ibupoto, K. Khun, J. Lu, M. Willander, The synthesis of CuO nanoleaves, structural characterization, and their glucose sensing application, Appl. Phys. Lett. 102 (2013) 103701. doi:10.1063/1.4795135.

[254] J.X. Wang, X.W. Suna, A. Wei, Zinc oxide nanocomb biosensor for glucose detection, Appl. Phys. Lett. 88 (2006) 233106. doi:10.1063/1.2210078.

[255] S.Y. Tee, E. Ye, P.H. Pan, C.J.J. Lee, H.K. Hui, S.-Y. Zhang, L.D. Koh, Z. Dong, M.-Y. Han, Fabrication of bimetallic Cu/Au nanotubes and their sensitive, selective, reproducible and reusable electrochemical sensing of glucose, Nanoscale. 7 (2015) 11190–11198. doi:10.1039/C5NR02399H.

[256] Y. Mu, D. Jia, Y. He, Y. Miao, H.-L. Wu, Nano nickel oxide modified non-enzymatic glucose sensors with enhanced sensitivity through an electrochemical process strategy at high potential, Biosens. Bioelectron. 26 (2011) 2948–2952. doi:10.1016/j.bios.2010.11.042.

[257] X. Liu, W. Yang, L. Chen, J. Jia, Three-Dimensional Copper Foam Supported CuO Nanowire Arrays: An Efficient Non-enzymatic Glucose Sensor, Electrochimica Acta. 235 (2017) 519–526. doi:10.1016/j.electacta.2017.03.150.

[258] S.Y. Tee, C.P. Teng, E. Ye, Metal nanostructures for non-enzymatic glucose sensing, Mater. Sci. Eng. C. 70 (2017) 1018–1030. doi:10.1016/j.msec.2016.04.009.

[259] J.Y.T. Chan, S.Y. Ang, E.Y. Ye, M. Sullivan, J. Zhang, M. Lin, Heterogeneous photo-Fenton reaction on hematite (α-Fe2O3){104}, {113} and {001} surface facets, Phys. Chem. Chem. Phys. 17 (2015) 25333–25341. doi:10.1039/C5CP03332B.

[260] W.L. Kwong, C.C. Lee, J. Messinger, Scalable Two-Step Synthesis of Nickel–Iron Phosphide Electrodes for Stable and Efficient Electrocatalytic Hydrogen Evolution, J. Phys. Chem. C. 121 (2017) 284–292. doi:10.1021/acs.jpcc.6b09050.

[261] E.J. Popczun, J.R. McKone, C.G. Read, A.J. Biacchi, A.M. Wiltrout, N.S. Lewis, R.E. Schaak, Nanostructured Nickel Phosphide as an Electrocatalyst for the Hydrogen Evolution Reaction, J. Am. Chem. Soc. 135 (2013) 9267–9270. doi:10.1021/ja403440e.

[262] P.F. Méndez, J.R. López, U. López-García, J. Manríquez, C. Frontana, F.J. Rodríguez, L.A. Godínez, Voltammetric and Electrochemical Impedance Spectroscopy Study of Prussian Blue/Polyamidoamine Dendrimer Films on Optically Transparent Electrodes, J. Electrochem. Soc. 164 (2017) H85–H90. doi:10.1149/2.1041702jes.

[263] D. Yang, P. Liu, Y. Gao, H. Wu, Y. Cao, Q. Xiao, H. Li, Synthesis, characterization, and electrochemical performances of core-shell Ni(SO4)0.3(OH)1.4/C and NiO/C nanobelts, J. Mater. Chem. 22 (2012) 7224–7231. doi:10.1039/C2JM30237C.

[264] H. Nie, Z. Yao, X. Zhou, Z. Yang, S. Huang, Nonenzymatic electrochemical detection of glucose using well-distributed

nickel nanoparticles on straight multi-walled carbon nanotubes, Biosens. Bioelectron. 30 (2011) 28–34. doi:10.1016/j.bios.2011.08.022.

[265] Y. Liu, H. Teng, H. Hou, T. You, Nonenzymatic glucose sensor based on renewable electrospun Ni nanoparticle-loaded carbon nanofiber paste electrode, Biosens. Bioelectron. 24 (2009) 3329–3334. doi:10.1016/j.bios.2009.04.032.

[266] X. Niu, M. Lan, H. Zhao, C. Chen, Highly Sensitive and Selective Nonenzymatic Detection of Glucose Using Three-Dimensional Porous Nickel Nanostructures, Anal. Chem. 85 (2013) 3561–3569. doi:10.1021/ac3030976.